

**METAL CATALYSED TRANSFER
HYDROGENATION, DEHYDROGENATION AND
RACEMISATION OF AMINES**

David John Taylor

PhD

The University of York

Chemistry

December 2010

ABSTRACT

This thesis describes the study of the fundamental mechanisms relating to asymmetric transfer hydrogenation (ATH) of imines and the transfer dehydrogenation and racemisation of secondary amines by Cp*Rh and Cp*Ir complexes. A series of 16-electron complex of the type Cp*M(XNC₆H₄NX') (where M = Rh or Ir and X, X' = H or Ts) have been synthesised, fully characterised and demonstrated to be active catalysts for the transfer hydrogenation of imines. The crystal structures of the complexes reveal structural features that are important in understanding their unique ability to act as transfer hydrogenation catalysts including a remarkable trend in the M-N bond lengths, indicative of M-NH π -bonding and the absence of M-NTs π -bonding which has several implications for catalysis. The complexes allowed catalytic studies without the need for 18-electron precursors, as is the case for the more widely used Noyori-type Cp*M(Cl)(TsNCHPhCHPhNH₂) (where M = Rh or Ir) ATH complexes. We observed key intermediates in the mechanism by NMR spectroscopy such as an 18-electron formate complex, Cp*Rh(OCHO)(TsNC₆H₄NH₂) and the 18-electron Rh(III) hydride complex, Cp*Rh(H)(TsNC₆H₄NH₂). An 18-electron chloride precursor complex, Cp*Rh(Cl)(TsNC₆H₄NH₂) was also characterised by X-ray crystallography. DFT calculations were used to support our observations and an “outer-sphere” mechanism for the transfer hydrogenation of imines is proposed. We also studied the mechanism of a dimeric Cp*Ir diiodide complex, [Cp*Ir(I)₂]₂ that is capable of amine racemisation under *mild* conditions and characterised several key intermediates including an ammine-coordinated complex, Cp*Ir(I)₂(NH₃) which itself was demonstrated to be equally active for the racemisation process under identical conditions; amine bound complexes of the type Cp*M(X)₂(PhCH₂NHMe) (where M = Rh, Ir and X = Cl, I) proposed to be the first step in the mechanism; an imine-coordinated Cp*Ir diiodide complex characterised by ¹H/¹⁵N HSQC and the reversible hydrogenation of this complex by addition of molecular hydrogen to form the corresponding amine. A mechanism based on the current evidence for the racemisation of amines using the [Cp*Ir(I)₂]₂ catalyst is proposed. Finally, we describe a method for producing hyperpolarised carbon dioxide gas by using the Cp*Rh(Cl)(TsNCHPhCHPhNH₂) ATH catalyst to catalytically decompose a pre-hyperpolarised solution of natural abundance formic acid, which was observed by ¹³C NMR spectroscopy.

TABLE OF CONTENTS

Abstract	i
List of Contents	ii
List of Figures	viii
List of Tables.....	xvii
List of Abbreviations and Symbols.....	xviii
Acknowledgements	xxiii
Author's Declaration.....	xxiv

Chapter One: Introduction

1.1 Chirality	1
1.2 Mechanisms of C=N and C=O Reduction in Transfer Hydrogenation.....	3
1.2.1 Direct Hydrogen Pathway.....	5
1.2.2 Hydridic Route.....	7
1.2.3 Metal-ligand bifunctional catalysis.....	8
1.3 Organometallic Catalysts based on Ru, Rh and Ir for ATH of Imines	9
1.3.1 Shvo's catalyst	11
1.3.2 Noyori-Ikariya type catalysts.....	16
1.4 Transfer Dehydrogenation	21
1.5 Outline of Thesis.....	28
1.6 References.....	29

Chapter Two: Synthesis and Structure of 16-electron Cp*Rh(III) and Cp*Ir(III) complexes for Transfer Hydrogenation

2.1 Introduction.....	34
2.1.1 16-electron Cp*Rh(III) and Cp*Ir(III) air and water stable complexes	35
2.1.2 Grace's Complex, Cp*Rh(TsNC ₆ H ₄ NH) which is catalytically active.....	37
2.1.3 Evidence of redirection of π -bonding from M-NH and M-NTs groups	38
2.1.4 Related 16-electron complexes stabilised by π -donation.....	39
2.1.5 π -stabilised unsaturation.....	40
2.1.6 Aims of the Chapter	42

2.2 Results and Discussion	43
2.2.1 Synthesis of monosulphonylated <i>o</i> -phenylenediamine ligands	43
2.2.2 Synthesis of disulphonylated <i>o</i> -phenylenediamine ligands	46
2.2.3 Synthesis of “16-electron” rhodium and iridium(III) complexes	47
2.2.4 MO analysis of Cp*Rh(HNC ₆ H ₄ NH) and Cp*Rh(HNCHPhCHPhNH)	51
2.2.5 X-ray crystallography characterisation of rhodium(III) complexes	54
2.2.6 X-ray crystallography characterisation of iridium(III) complexes	57
2.2.7 DFT calculations for π -bonding in Cp*Rh(III) complexes.....	59
2.2.8 Electronic configuration of 16-electron Cp*Rh complexes.....	61
2.2.9 Synthesis and characterisation of 4,5-disubstituted 16-e complexes.....	63
2.3 Summary	64
2.4 Supporting NMR data	65
2.4.1 Cp*Rh(TsNC ₆ H ₄ NH).....	65
2.4.2 Cp*Rh(TsNC ₆ H ₄ NTs).....	67
2.4.3 Cp*Rh(HNC ₆ H ₄ NH).....	69
2.4.4 Cp*Ir(TsNC ₆ H ₄ NH).....	70
2.4.5 Cp*Ir(TsNC ₆ H ₄ NTs).....	72
2.4.6 4,5-dimethyl- <i>N</i> ¹ -tosylbenzene-1,2-diamine	73
2.4.7 4,5-dichloro- <i>N</i> ¹ -tosylbenzene-1,2-diamine	75
2.4.8 Cp*Rh(TsNC ₆ H ₂ (CH ₃) ₂ NH).....	76
2.5 References	78

Chapter Three: A Mechanistic Study into Transfer Hydrogenation using 16-electron Cp*Rh and Cp*Ir Complexes

3.1 Introduction.....	80
3.1.1 Noyori’s “Outer-sphere” bifunctional mechanism	80
3.1.2 NPIL Pharma’s Cp*Rh and Cp*Ir catalysts	82
3.1.3 Reactivity of Cp*Rh(Cl)(TsNCHPhCHPhNH ₂) with formic acid	83
3.1.4 Ikaiya’s formato-amino complex	84
3.1.5 Rauchfuss and Heiden Mechanistic Work.....	88
3.1.6 Aims of the Chapter	90
3.2 Results and Discussion	91
3.2.1 Transfer hydrogenation of a cyclic imine with Cp*Rh complexes.....	91

3.2.2	Transfer hydrogenation of a cyclic imine with Cp*Ir complexes.....	93
3.2.3	Catalytic decomposition of formic acid.....	94
3.2.4	Catalytic activity of 4,5-dimethyl substituted Cp*Rh complexes	95
3.2.5	Synthesis and characterisation of Cp*Rh(Cl)(TsNC ₆ H ₄ NH ₂).....	96
3.2.6	Reactivity of Cp*Rh(TsNC ₆ H ₄ NH) with formic acid	101
3.2.7	Characterisation of the 18-electron hydride, Cp*Rh(H)(TsNC ₆ H ₄ NH ₂)... ..	103
3.2.8	DFT calculations on reaction of Cp*Rh complexes with formic acid.....	106
3.2.9	DFT calculations on reaction of Cp*Rh complexes with methanol	110
3.3	Summary	111
3.4	Supporting NMR data	112
3.4.1	Cp*Rh(Cl)(TsNC ₆ H ₄ NH ₂).....	112
3.4.2	Cp*Rh(OCHO)(TsNC ₆ H ₄ NH ₂)	114
3.4.3	Cp*Rh(H)(TsNC ₆ H ₄ NH ₂).....	115
3.5	References.....	116

Chapter Four: A Study on an Amine Racemisation Catalyst

4.1	Introduction.....	119
4.1.1	Decomposition pathways of the amine racemisation catalyst	121
4.1.2	Using [Cp*Ir(NH ₃) ₃][I] ₂ for the synthesis of amines from NH ₃	122
4.1.3	Blacker <i>et al.</i> show that [Cp*IrI ₂] ₂ is a versatile catalyst	125
4.1.4	Aims of the Chapter	127
4.2	Results and Discussion	128
4.2.1	Synthesis, Isolation and Characterisation of Cp*IrI ₂ (NH ₃).....	128
4.2.2	Racemisation of sertraline with purified Cp*IrI ₂ (NH ₃) complex	132
4.2.3	Reactivity of [Cp*IrI ₂] ₂ with a secondary amine, PhCH ₂ NHMe.....	134
4.2.4	Reactivity of [Cp*Ir(I) ₂ (NH ₃)] with a secondary amine.....	138
4.2.5	Characterisation of Cp*Ir(Cl) ₂ (NH(Me)CH ₂ Ph)	139
4.2.6	Characterisation of Cp*Rh(Cl) ₂ (NH(Me)CH ₂ Ph)	140
4.2.7	Coordination of a secondary imine to the [Cp*IrI ₂] ₂ catalyst.....	142
4.2.8	Reactivity of coordinated imine with para-hydrogen <i>in-situ</i> NMR.....	146
4.2.9	Using [Cp*IrI ₂] ₂ with norbornene to dehydrogenate an amine	147
4.2.10	Proposed mechanism of amine racemisation using [Cp*IrI ₂] ₂	149
4.3	Summary	150

4.4 Supporting NMR data	151
4.4.1 Cp*IrI ₂ (NH ₃).....	151
4.4.2 Cp*Ir(I) ₂ (PhCH ₂ NHMe).....	152
4.4.3 Cp*Ir(Cl) ₂ (PhCH ₂ NHMe).....	153
4.4.4 Cp*Rh(Cl) ₂ (PhCH ₂ NHMe).....	154
4.4.5 Coordinated imine, Cp*Ir(I) ₂ [imine]	155
4.4.6 6,7-dimethoxy-1-methyl-3,4-dihydroisoquinoline at 248 K.....	157
4.5 References	159

Chapter Five: Using Asymmetric Transfer Hydrogenation Catalysts for the Production of Hyperpolarised Carbon Dioxide

5.1 Introduction.....	161
5.1.1 The Nuclear Spin	162
5.1.2 Nuclear Polarisation.....	163
5.1.3 Hyperpolarisation.....	164
5.1.4 The Dynamic Nuclear Polarisation (DNP) Method.....	165
5.1.5 Properties of potential ¹³ C imaging agents	166
5.1.6 Aims of the Chapter	166
5.2 Results and Discussion	167
5.2.1 Decomposition of formic acid by Cp*Rh ATH catalysts	167
5.2.2 Observation of CO ₂ from the decomposition of H ¹² CO ₂ H.....	168
5.2.3 Hyperpolarisation of ¹³ C-labelled triethylammonium formate solution....	169
5.3 Summary	172
5.4 References	173

Chapter Six: Conclusions and Future Work

6.1 Conclusions.....	174
6.2 Future Work	178

Chapter Seven: Experimental

7.1 General.....	179
7.1.1 General experimental methods	179

7.1.2 Physical Methods	180
7.1.3 Computational Details	180
7.2 Experimental procedures for Chapter Two.....	181
7.2.1 <i>N</i> -tosyl-1,2-diaminobenzene.....	181
7.2.2 <i>N</i> -tosyl-4,5-dimethyl-1,2-diaminobenzene	181
7.2.3 <i>N</i> -tosyl-4,5-dichloro-1,2-diaminobenzene.....	182
7.2.4 <i>N</i> -tosyl-9,10-diaminophenanthrene	182
7.2.5 <i>N</i> -(2'-amino-1,1'-binaphthyl-2-yl)-4-methylbenzenesulfonamide.....	183
7.2.6 <i>N</i> -Dansyl-1,2-diphenylethylenediamine	184
7.2.7 Ditosyl-1,2-diaminobenzene	185
7.2.8 Cp*Rh(TsNC ₆ H ₄ NH) (1a).....	186
7.2.9 Cp*Rh(TsNC ₆ H ₄ NTs) (1b).....	186
7.2.10 Cp*Rh(HNC ₆ H ₄ NH) (1c).....	187
7.2.11 Cp*Rh(TsNC ₆ H ₂ (CH ₃) ₂ NH)	188
7.2.12 Cp*Ir(TsNC ₆ H ₄ NH) (1d)	188
7.2.13 Cp*Ir(TsNC ₆ H ₄ NTs) (1e).....	189
7.3 Experimental procedures for Chapter Three.....	190
7.3.1 Catalytic hydrogenation of a secondary imine.....	190
7.3.2 General procedure for catalytic runs.....	191
7.3.3 Catalytic run for 4,5-dimethyl substituted Cp*Rh complex	192
7.3.4 Cp*Rh(Cl)(TsNC ₆ H ₄ NH ₂) (2a)	192
7.3.5 Cp*Rh(HCOO)(TsNC ₆ H ₄ NH ₂) (3a).....	192
7.3.6 Cp*Rh(H)(TsNC ₆ H ₄ NH ₂) (4a)	193
7.4 Experimental procedures for Chapter Four.....	194
7.4.1 Cp*Ir(I) ₂ (NH ₃)	194
7.4.2 Cp*Ir(I) ₂ (PhCH ₂ NHMe)	195
7.4.3 Cp*Ir(Cl) ₂ (PhCH ₂ NHMe).....	195
7.4.4 Cp*Rh(Cl) ₂ (PhCH ₂ NHMe).....	196
7.4.5 Cp*Ir(I) ₂ (6,7-dimethoxy-1-methyl-3,4-dihydroisoquinoline)	197
7.4.6 Dehydrogenation of a secondary amine with [Cp*IrI ₂] ₂	197
7.5 Experimental procedures for Chapter Five	198
7.6 References.....	199

Appendix: X-ray crystallography data

A8.1	Crystal data for ditosylphenanthrene ligand.....	201
A8.2	Crystal data for Cp*Rh(TsNC ₆ H ₄ NTs) (1b)	204
A8.3	Crystal data for Cp*Rh(HNC ₆ H ₄ NH) (1c).....	207
A8.4	Crystal data for Cp*Ir(TsNC ₆ H ₄ NH) (1d)	211
A8.5	Crystal data for Cp*Ir(TsNC ₆ H ₄ NTs) (1e).....	214
A8.6	Crystal data for Cp*Rh(Cl)(TsNC ₆ H ₄ NH ₂) (2a).....	217
A8.7	Crystal data for Cp*Ir(I) ₂ (NH ₃).....	221
A8.8	Crystal data for Cp*Ir(I) ₂ (PhCH ₂ NHMe)	223
A8.9	Crystal data for Cp*Ir(Cl) ₂ (PhCH ₂ NHMe)	226
A8.10	Crystal data for Cp*Rh(Cl) ₂ (PhCH ₂ NHMe)	228

LIST OF FIGURES

Chapter One: Introduction

Figure 1	(S)-Alanine (left) and (R)-alanine (right) in zwitterionic form at neutral pH.....	1
Figure 2	Optical isomers of biologically active compounds can have significantly different effects such as Thalidomide (top), Asparagine (middle) and Benzopyryldiol (bottom)	3
Figure 3	Definition of transfer hydrogenation, where A = acceptor, DH_2 = hydrogen donor and [cat] = transition metal catalyst.....	4
Figure 4	The 6-membered transition state in the Meerwein-Ponndorf-Verley (MPV) reduction showing the direct hydrogen pathway	5
Figure 5	A highly enantioselective MPV reduction of <i>N</i> -phosphinoyl ketimines by (BINOL)Al(III) / 2-propanol and proposed pathway and transition states.	6
Figure 6	Transfer hydrogenation: dihydridic route	7
Figure 7	Transfer hydrogenation: monohydride route.....	8
Figure 8	Metal-ligand bifunctional catalysis proceeds through an “outer-sphere” mechanism	8
Figure 9	$Ru_3(CO)_{12}$ reported by Jones to catalyse the transfer hydrogenation of benzylideneanilines using isopropanol as the hydrogen source	9
Figure 10	X-ray structure of $(\mu-H)Ru_3(CO)_9(\mu_3-PhNCHPh)$, phenyl hydrogens omitted for clarity	10
Figure 11	Transfer hydrogenation of imines using as Ru(II) catalyst.....	10
Figure 12	The role of base to form the highly active $RuH_2(PPh_3)_3$ catalyst.....	10
Figure 13	Proposed mechanism of hydrogen transfer for $RuCl_2(PPh_3)_3$	11
Figure 14	Shvo catalyst and the equilibrium between A and B	12
Figure 15	Proposed “Outer-sphere” reaction for the carbonyl hydrogenation by means of the Shvo catalyst	13
Figure 16	The catalytic dehydrogenation of 1-(4-fluorophenyl)ethanol, using tetrafluorobenzoquinone as hydrogen acceptor.....	13
Figure 17	Hydrogenation of imine study.....	14

Figure 18	Bäckvall's proposal for a stepwise mechanism for the transfer hydrogenation of imines by Shvo's catalyst.	15
Figure 19	Molecular structure of Rh, Ir and Ru ATH catalysts	16
Figure 20	Proposed mechanism involving "outer-sphere" bifunctional hydrogen transfer for ketones.....	17
Figure 21	Stoichiometric reaction between Ru-hydride and imine does neither form any complex, nor reduce the substrate	19
Figure 22	Addition of acid is necessary for reduction of imine by the Ru-hydride.....	19
Figure 23	Mode of reduction of acetophenone (a) and potential modes of reduction of imine (b-d) in ATH by Ru, Ir and Rh TsDPEN catalyst.....	20
Figure 24	A diagram by Bäckvall showing imines as important intermediates: 1.) hydrogenation, 2.) Mannich, 3.) Strecker, 4.) imino-ene, 5.) addition, 6.) [2+2] addition, 7.) aza-Baylis-Hillman, 8.) aza-Diels-Alder.	21
Figure 25	Dehydrogenation of amines using Noyori's ruthenium catalyst.....	22
Figure 26	Shvo's catalyst and the reaction with <i>N</i> -methyl-substituted amine	23
Figure 27	Proposed mechanism for the ruthenium-catalyzed dehydrogenation of secondary amines	23
Figure 28	Cp* Iridium complexes containing (left) 2-hydroxypyridine and (right) 2-pyridonate ligands.....	24
Figure 29	Dehydrogenation of 1,2,3,4-tetrahydroquinolines catalyzed by a modified Cp*Ir complex	24
Figure 30	Hydrogenation of quinolines catalysed by complex 3	25
Figure 31	Formation of the hydride-bridged dinuclear Cp*Ir complex responsible for hydrogenation reaction and the formation of 3 by reaction of 4 and free ligand in the absence of hydrogen.....	25
Figure 32	Hydrogenation of imine with [Cp*IrHCl] ₂ catalyst	26
Figure 33	Overall Process for the Reversible and Repetitive Catalytic Dehydrogenation-Hydrogenation of imine using Cp*Ir pyridinate complexes.....	26

Chapter Two: Synthesis and Structure of 16-electron Cp*Rh(III) and Cp*Ir(III) Complexes for Transfer Hydrogenation

Figure 1	Cp*Rh and Cp*Ir complexes with amine or amino-alcohol ligands capable of π -bonding for ATH of ketones and imines, when HCl is eliminated.....	34
Figure 2	“Outer-sphere” bifunctional catalysis mechanism using 18-electron half-sandwich complexes. Complex B is capable of metal-ligand π -bonding.....	35
Figure 3	Three complexes first prepared by Maitlis with formally 16-electron configurations (left) Cp*Rh(HNC ₆ H ₄ NH), (middle) Cp*Rh(OC ₆ H ₄ NH), (right) Cp*Rh(OC ₆ H ₄ O).....	36
Figure 4	Two mutually perpendicular views of the molecular structure of Maitlis’ Cp*Rh(OC ₆ H ₄ O) complex	36
Figure 5	X-Ray structure of Cp*Rh(TsNC ₆ H ₄ NH) a complex which catalyses the transfer hydrogenation of imines	37
Figure 6	Rauchfuss’ work shows the protonation of Cp*Ir(TsNCHPhCHPhNH) at the NH group significantly changes the bonding between the iridium, NTs and NH groups.....	38
Figure 7	Cp*Rh(pin) complex and associated reactivity with catechol and 2,3-dimethylbutadiene. No reaction observed between Cp*Rh(OC ₆ H ₄ O) and 2,3-dimethylbutadiene, highlighting the stability of this 16-electron catecholate complex	39
Figure 8	π -donation at the X-ligand by lone pairs mitigates the coordinative unsaturation	40
Figure 9	Pyramidal and distorted trigonal bipyramidal structure.....	41
Figure 10	Angle between plane L-Ru-X and the Ru-Cp center	41
Figure 11	Total energy curves calculated by Eisenstein <i>et al.</i> for [CpRuH ₂] ₂ (2), CpRu(PH ₃)I (3a) and [CpRu(CO) ₂] ⁺ (4).....	42
Figure 12	Synthesis of <i>N</i> -tosyl-1,2-diaminobenzene (X = H) and 4,5-disubstituted <i>o</i> -phenylenediamine ligands (X = Cl and CH ₃).....	43
Figure 13	¹ H NMR spectrum (500 MHz, CDCl ₃ , 300 K) of <i>N</i> -tosyl-1,2-diaminobenzene	44
Figure 14	Other mono-tosylated ligands synthesised during this study	45

Figure 15	Synthesis of ditosylbenzene-1,2-diamine ligand.....	46
Figure 16	X-ray structure of ditosyl-9,10-diaminophenanthrene	46
Figure 17	Synthesis of complexes 1a-1e with formal 16e configurations	47
Figure 18	^1H NMR spectrum of $\text{Cp}^*\text{Rh}(\text{TsNC}_6\text{H}_4\text{NH})$ in dichloromethane- d_2	48
Figure 19	$^1\text{H}/^{103}\text{Rh}$ HSQC data for 1a , $\text{Cp}^*\text{Rh}(\text{TsNC}_6\text{H}_4\text{NH})$ in chloroform- d ($\delta_{\text{Rh}} = 2063$ ppm).....	49
Figure 20	UV-visible spectra of complexes 1a , 1b , 1d and 1e	50
Figure 21	MO representation of in-phase / out-of-phase interactions for the $\text{HNC}_6\text{H}_4\text{NH}$ system	51
Figure 22	MO diagram to show interaction of ligands with CpRh fragment, 4- electron repulsions.....	52
Figure 23	4-electron repulsions in A1c , A1b , B1c , B1b	53
Figure 24	Diagram for definition of angles θ_{oop} and θ_{tilt}	54
Figure 25	Two mutually perpendicular views of molecular structures of $\text{Cp}^*\text{Rh}(\text{TsNC}_6\text{H}_4\text{NH})$, 1a (top), $\text{Cp}^*\text{Rh}(\text{TsNC}_6\text{H}_4\text{NTs})$, 1b (middle) and $\text{Cp}^*\text{Rh}(\text{HNC}_6\text{H}_4\text{NH})$, 1c (bottom); hydrogens are omitted for clarity. Thermal ellipsoids shown at 50% probability	55
Figure 26	Two mutually perpendicular views of molecular structures of $\text{Cp}^*\text{Ir}(\text{TsNC}_6\text{H}_4\text{NH})$, 1d (top), $\text{Cp}^*\text{Ir}(\text{TsNC}_6\text{H}_4\text{NTs})$, 1e (middle) and $\text{Cp}^*\text{Ir}(\text{HNC}_6\text{H}_4\text{NH})$, 1f (bottom); hydrogens are omitted for clarity. Thermal ellipsoids shown at 50% probability	58
Figure 27	Comparison of calculated and observed bond lengths (\AA) for 1a , 1b and 1c	59
Figure 28	Optimised structures for 1a , 1b and 1c showing the 2p lone pairs on each nitrogen mixing with the $\text{Rh}(d_{xy})$ orbital and the C_6H_4 carbon orbital (HOMO-1)	60
Figure 29	In-phase and out-of-phase combination between unoccupied d_{yz} of Cp^*Rh and HOMO of diamido ligand	61
Figure 30	4,5-disubstituted complexes synthesised in this study	63

Chapter Three: A Mechanistic Study into Transfer Hydrogenation using 16-electron Cp*Rh and Cp*Ir Complexes

Figure 1	Ru-TsDPEN catalyst precursor 1 , true catalyst 2 and reactive intermediate 3	80
Figure 2	Shvo's catalyst and subsequent reaction with hydrogen and ketones.....	81
Figure 3	Catalytic cycle for the reduction of imine 8 to amine 9 with TEAF as the reducing agent, highlighting the roles of the 16 electron 'reactive intermediate' 6 and the 18-electron 'true catalyst' 7	82
Figure 4	Molecular structure of the cation of Grace's complex, $[\{\text{Cp}^*\text{Rh}\}_2(\mu\text{-H})(\mu\text{-Cl})(\mu\text{-HCO}_2)]$	83
Figure 5	Reaction of 16-electron (<i>p</i> -cymene)Ru[(<i>R,R</i>)-TsNCHPhCHPhNH] with formic acid at 243 K to give the formate complex.....	84
Figure 6	ORTEP view of (<i>p</i> -cymene)Ru(OCOCH ₃)[(<i>R,R</i> -TsNCHPhCHPhNH ₂)]	85
Figure 7	Morris' formate complex, <i>trans</i> -Ru(PPh ₃) ₂ (H)(tmen)(OCHO).....	86
Figure 8	Decarboxylation of the formate and kinetic data	87
Figure 9	Proposed catalytic cycle for the reduction of dioxygen with Cp*IrH(TsDPEN).....	89
Figure 10	Turnover number for the production of water in methylene chloride-d ₂ using 15 mol % of [Cp*Ir(X)(TsNCHPhCHPhNH ₂)] (where X = BAr ^F , BF ₄ ⁻ and NO ₃ ⁻) under 1 atm of H ₂ and O ₂	90
Figure 11	Transfer hydrogenation of 6,7-dimethoxy-1-methyl-3,4-dihydroisoquinoline with 1a using 5 equivalents of triethylamine: formic acid (2:5) in methanol-d ₄ at 300 K	91
Figure 12	Conversion of imine to amine (%) against time for various [1a]/substrate ratios	92
Figure 13	Rate of conversion of imine to amine against [1a] in methanol-d ₄ at 300 K.....	92
Figure 14	Rate of conversion of imine to amine using 1a (top, blue) 1b (middle, yellow) and 1c (bottom, pink) in methylene chloride-d ₂	93
Figure 15	Rate of conversion of the cyclic imine, 6,7-dimethoxy-1-methyl-3,4-dihydroisoquinoline to the corresponding amine using 1d and 1e in acetonitrile-d ₃	94

Figure 16	Rate of conversion of imine to amine against concentration of 4,5-dimethyl complex, Cp*Rh(TsNC ₆ H ₂ (Me) ₂ NH) in methanol-d ₄ at 300 K (125 mol amine h ⁻¹ per mol of catalyst)	95
Figure 17	Synthesis of 18-electron chloride ‘precursor’ complex from 1a and HCl in ether and methylene chloride-d ₂ at 193 K	96
Figure 18	¹ H NMR spectrum of 2a at 193 K, showing broad doublets for the two non-equivalent NH ₂ protons	97
Figure 19	Molecular structure of Cp*Rh(Cl)(TsNC ₆ H ₄ NH ₂), 2a (two molecules in asymmetric unit), hydrogens omitted except NH ₂	98
Figure 19^b	Two mutually perpendicular views of molecular structure of Cp*Rh(Cl)(TsNC ₆ H ₄ NH ₂), 2a , hydrogens omitted for clarity	98
Figure 20	Hydrogen bonding in, Cp*Rh(Cl)(TsNC ₆ H ₄ NH ₂), 2a	100
Figure 21	Extended hydrogen bonding in crystal packing structure	100
Figure 22	Synthesis of 18-electron formato-amino complex from 1a and formic acid or TEAF solution in methylene chloride-d ₂ at 193 K	101
Figure 23	¹ H NMR spectrum of formato-amino complex (with expanded aromatic region)	102
Figure 24	¹ H NMR spectrum of H _{2(g)} and HD _(g) evolved by warming formato-amino complex, 3a from 193 K to 300 K	103
Figure 25	Conversion of formato-amino to hydride complex	104
Figure 26	¹ H NMR of hydride peak for 4a in methylene chloride-d ₂ at 273 K	104
Figure 27	HSQC ¹ H- ¹⁰³ Rh for Cp*Rh(H)(TsNC ₆ H ₄ NH ₂), 4a	105
Figure 28	DFT calculations on hydrogenation of 1a , 1b and 1c with HCO ₂ H	106
Figure 29	DFT calculation on hydrogenation of Cp*Rh(XNCHPhCHPhNX)	107
Figure 30	DFT calculation of alternative pathway to 18-electron hydride from the 18-electron formato-amino complex	108
Figure 31	DFT calculation of hydrogenation of 16-electron iridium complexes by formic acid to produce 18-electron hydride complexes	109
Figure 32	DFT calculations show that hydrogenation of 1a , 1b and 1c with methanol-d ₄ are thermodynamically unfavourable	110

Chapter Four: A Study on an Amine Racemisation Catalyst

Figure 1	Racemisation of primary amines using Shvo's catalyst.....	119
Figure 2	Racemisation of (S)-1-methyl-1,2,3,4-tetrahydroisoquinoline	120
Figure 3	Structure of the Cp*Ir cyclometallated species indicating catalyst deactivation at higher temperatures.....	121
Figure 4	The immobilised [Cp*IrI ₂] ₂ complex.....	121
Figure 5	Synthesis of Cp*Ir-amine complexes from the corresponding Cp*Ir halide dimer and aqueous ammonia.....	122
Figure 6	N-alkylation of aqueous ammonia with benzyl alcohols catalysed by Cp*Ir-amine complexes under various conditions. The reaction was carried out with NH ₃ (1.0 mmol, 28% aqueous solution). Cp*Ir catalyst (1.0 mol % Ir), and benzyl alcohol (3.0 mmol). The percentage yields were determined by GC.....	123
Figure 7	Transfer hydrogenation of N-benzylidenebenzylamine carried out in the presence of the three halide ion catalysts, the highest yield was obtained using the iodide complex (yield = 70%)	123
Figure 8	A possible mechanism for the N-alkylation of aqueous ammonia with an alcohol and Cp*Ir-amine complex	124
Figure 9	Ir-Catalyzed Conversion of Benzaldehyde into 2-Phenylbenzoxazole using 1 mol% [Cp*IrI ₂] ₂	125
Figure 10	Acceptorless oxidation of Aldehydes to Benzoxazoles using the [Cp*IrI ₂] ₂ complex	126
Figure 11	Mechanism proposed by Blacker <i>et al.</i> for the conversion of aldehydes into benzazoles using the [Cp*IrI ₂] ₂ complex.....	127
Figure 12	Preparation of Cp*Ir(NH ₃)I ₂ from [Cp*IrI ₂] ₂ and NH _{3(g)}	128
Figure 13	X-ray crystallography structure of Cp*IrI ₂ (NH ₃).....	129
Figure 14	Structure of [Cp*Ir(NH ₃) ₃][I] ₂ developed by Fujita and co-workers....	130
Figure 15	UV-visible spectrum of Cp*IrI ₂ (NH ₃) in chloroform	131
Figure 16	Racemisation of sertraline catalysed by Cp*IrI ₂ (NH ₃).....	132
Figure 17	A graph to show the time profile of racemisation of sertraline with [Cp*IrI ₂] ₂ and the recycled ammonia catalyst, Cp*IrI ₂ (NH ₃).....	133
Figure 18	A graph to show time profile changes during a pulse experiment for the racemisation of sertraline with the recycled ammonia	

	catalyst, Cp*IrI ₂ (NH ₃), where the discontinuity corresponds to the second run with fresh substrate	133
Figure 19	Reaction of [Cp*IrI ₂] ₂ with <i>N</i> -methylbenzylamine at low temperature in methylene chloride-d ₂	134
Figure 20	¹ H NMR of Cp*Ir(PhCH ₂ NHMe)I ₂ in methylene chloride-d ₂ at 233 K.....	135
Figure 21	¹ H NMR of Cp*Ir(PhCH ₂ NHMe)I ₂ in methylene chloride-d ₂ showing the NH splitting pattern (doublet of quartets) at 233 K.....	135
Figure 22	UV-visible spectrum of [Cp*Ir(I) ₂ (PhCH ₂ NHMe)] in chloroform.....	136
Figure 23	X-ray crystallography structure for Cp*IrI ₂ [NH(Me)CH ₂ Ph]	137
Figure 24	Reaction of Cp*Ir(I) ₂ (NH ₃) with <i>N</i> -methylbenzylamine at low temperature in methylene chloride-d ₂	138
Figure 25	X-ray crystallography structure for Cp*IrCl ₂ (NH(Me)CH ₂ Ph).....	139
Figure 26	X-ray crystallography structure for Cp*RhCl ₂ (NH(Me)CH ₂ Ph).....	141
Figure 27	Epimerisation profile of (1 <i>S</i> ,4 <i>S</i>) sertraline to (1 <i>R</i> , <i>S</i> ,4 <i>S</i>)-sertraline with the [Cp*IrI ₂] ₂ catalyst and evidence for formation of corresponding imine over time.....	142
Figure 28	Coordination of a cyclic secondary imine to the [Cp*IrI ₂] ₂ complex...	143
Figure 29	Portion of the ¹ H / ¹⁵ N HMQC spectrum showing the crosspeak of the Cp* protons and the nitrogen of the coordinated imine at -219 ppm, (referenced to pyridine at 0 ppm).....	143
Figure 30	¹ H NMR spectrum of Cp*Ir(I) ₂ [6,7-dimethoxy-1-methyl-3,4-dihydroisoquinoline] at 248 K in methylene chloride-d ₂ and a schematic showing the conformation the isoquinoline ring adopts	144
Figure 31	Resonance structures for mer-[1]	145
Figure 32	Conversion between mer-[1] and mer-[2].....	145
Figure 33	Reaction of coordinated imine with 3 bar of <i>p</i> H ₂ in methylene chloride-d ₂ at 300 K to form coordinated amine.....	146
Figure 34	Postulated (iminium ion) iridium hydride intermediate.....	147
Figure 35	Quantitative conversion of amine to imine using [Cp*IrI ₂] ₂ and an excess of bicyclo[2.2.1]hept-2-ene in toluene-d ₈ at 353 K.....	148
Figure 36	Secondary amine at t = 0 at 300 K (bottom); Conversion of amine to imine after heating in toluene-d ₈ at 353K for 1 h (top).....	148
Figure 37	Proposed mechanism for racemisation of amines using [Cp*IrI ₂] ₂	149

Chapter Five: Using ATH Catalysts for the Production of Hyperpolarised CO₂

- Figure 1** Pictorial description by Goldman *et al.* of the orientation of the nuclei at thermal equilibrium and in the hyperpolarised state. In the figure, the magnetic field (B_0) is directed vertically upwards..... 163
- Figure 2** 600 MHz NMR spectrometer and Hypersense Nuclear polariser..... 165
- Figure 3** During the dynamic nuclear polarisation process, polarisation is transferred from the electrons of the doping material to the ¹³C nuclei by means of microwave irradiation (Golman *et al.*)..... 166
- Figure 4** The decomposition of formic acid in the presence of transfer hydrogenation catalysts 167
- Figure 5** Observation of a ¹³C CO₂ peak from decomposition of natural-abundance H¹²CO₂H 169
- Figure 6** ¹³C{¹H} NMR spectrum of hyperpolarised of H¹³CO₂H / Et₃N (2:5 TEAF solution) and ¹³CO₂(g)..... 170
- Figure 7** Arrayed 1D ¹³C{¹H} experiment showing decay of CO₂(g) signal 171
- Figure 8** Plot of signal-to-noise ratio for H¹³CO₂H and ¹³CO₂(g)..... 171

LIST OF TABLES

Chapter Two: Synthesis and Structure of 16-electron Cp*Rh(III) and Cp*Ir(III) Complexes for Transfer Hydrogenation

Table 1	UV-visible data values for 1a-1e	50
Table 2	X-ray diffraction data for 1a, 1b and 1c	56
Table 3	Selected Bond Lengths (Å) and Angles (deg) for free ligands	56
Table 4	Selected bond lengths and angles for 1d, 1e and 1f	57
Table 5	Values for the contributions of the Rh orbital to the composition of the nitrogen natural localised molecular orbital	61

Chapter Three: A Mechanistic Study into Transfer Hydrogenation using 16-electron Cp*Rh and Cp*Ir Complexes

Table 1	X-ray diffraction data for Cp*Rh(Cl)(TsNC ₆ H ₄ NH ₂), 2a	99
----------------	--	----

Chapter Four: A Study on an Amine Racemisation Catalyst

Table 1	X-ray crystallographic data for [Cp*Ir(I) ₂ (NH ₃)] and [Cp*Ir(NH ₃) ₃][I] ₂	129
Table 2	Molar extinction coefficients for [Cp*Ir(NH ₃)(I) ₂] in chloroform.....	131
Table 3	X-ray crystallographic data for [Cp*Ir(I) ₂ (PhCH ₂ NHMe)] and [Cp*Ir(I) ₂ (NH ₃)].....	137
Table 4	X-ray data for amine coordination complexes	140
Table 5	KBr-IR data for amine coordination complexes	141

Chapter Five: Using ATH Catalysts for the Production of Hyperpolarised CO₂

Table 1	Signal-to-noise calculation for the ¹³ C resonance of formic acid at δ 164.4 and carbon dioxide at δ 124.2.....	172
----------------	--	-----

LIST OF ABBREVIATIONS AND SYMBOLS

16e	16-electron
1D	1-Dimensional
2D	2-Dimensional
Å	Angstrom (1.0×10^{-10} m)
ABS	Absorbance
acac	Acetylacetonate
aq	Aqueous
Ar	Aryl
ATH	Asymmetric Transfer Hydrogenation
atm	Atmosphere
BAr ^F ₄	[B[3,5-(CF ₃) ₂ C ₆ H ₃] ₄] ⁻
BINAP	2,2'-bis(diphenylphosphanyl)-1,1'-binaphthyl
BINOL	1,1'-bi-2-naphthol
bpy	2,2'-bipyridine
br	broad
Bu <i>or</i> <i>n</i> -Bu	<i>n</i> -butyl
calcd	calculated
cat.	catalytic; catalyst (in schemes and tables)
CATHy	Chiral Asymmetric Transfer Hydrogenation
CIP	Cahn-Ingold-Prelog
cm ⁻¹	wavenumber(s)
Co(salen)	N,N'-Ethylenebis(salicylideniminato)cobalt(II)
COSY	Correlation Spectroscopy
Cp	cyclopentadienyl, C ₅ H ₅
Cp(cent)	Centroid of Cp ring
Cp*	pentamethylcyclopentadienyl, C ₅ (CH ₃) ₅
d	day(s); doublet (spectral)
DCM	dichloromethane
dd	doublet of doublets
de	diastereomeric excess
DFT	Density Functional Theory

dmpe	1,2-Bis(dimethylphosphino)ethane
DNP	Dynamic Nuclear Polarisation
dpbz	(Z)-1,2-Bis(diphenylphosphino)ethene
DPEN	1,2-diphenyl-1,2-ethylenediamine
dppb	1,4-Bis(diphenylphosphino)butane
dppe	1,2-Bis(diphenylphosphino)ethane
dppm	1,1-Bis(diphenylphosphino)methane
dppp	1,3-Bis(diphenylphosphino)propane
dt	doublet of triplets
E	energy
ee	enantiomeric excess
EHT	Extended Huckel Theory
EI	electron impact
eq	equation
equiv.	equivalent(s)
er	enantiomeric ratio
ESI	electrospray ionization
Et ₂ O	diethyl ether
Et ₃ N	triethylamine
FAB	fast atom bombardment
FD	field desorption
FDA	United States Food and Drug Administration
FID	free induction decay
FT	Fourier transform
g	gram(s)
GC	gas chromatography
h	hours(s)
HMBC	Heteronuclear Multiple Bond Coherence
HMQC	Heteronuclear Multiple Quantum Coherence
HOMO	highest occupied molecular orbital
HPLC	high-performance liquid chromatography
HRMS	high-resolution mass spectrometry
HSBC	Heteronuclear Single Bond Coherence

HSQC	Heteronuclear Single Quantum Coherence
Hz	hertz
<i>i</i> -Pr	isopropyl
<i>i</i> -PrOH	isopropyl alcohol / propan-2-ol
IR	infrared
<i>J</i>	Coupling constant
K	kelvin(s)
LMCT	ligand-to-metal charge transfer
LUMO	lowest unoccupied molecular orbital
m	multiplet (spectral)
M	molar (moles per liter)
m/z	mass-to-charge ratio
M ⁺	parent molecular ion
MeCN	acetonitrile
MeOH	methanol
MgSO ₄	magnesium sulfate
MHz	megahertz
min	minute(s); minimum
mL	milliliter
MLCT	metal-to-ligand charge transfer
mmol	millimole(s)
MO	molecular orbital
mol	mole(s)
MPV	Meerwein-Ponndorf-Verley
MRI	Magnetic Resonance Imaging
MRS	Magnetic Resonance Spectroscopy
MS	mass spectrometry
NBO	Natural Bond Orbital
NLMO	Natural Localized Molecular Orbital
NMR	Nuclear Magnetic Resonance
NOE	Nuclear Overhauser Effect
NOESY	Nuclear Overhauser Effect Spectroscopy
OAc	Acetoxy group

OMe	methoxy group
OPDA	<i>o</i> -phenylenediamine
ORTEP	Oak Ridge Thermal Ellipsoid Plot Program
OTf	trifluoromethanesulfonate (triflate)
<i>p</i> -cymene	1-methyl-4-(1-methylethyl)benzene
PEG	Polyethylene glycol
Ph	phenyl
Phen	1,10-phenanthroline
Pin	pinacolate
PMe ₃	trimethylphospine
PPh ₃	triphenylphospine
ppm	part(s) per million
q	quartet
quint	quintet
r.t.	room temperature
RECP	relativistic effective core potentials
R _f	retention factor (for TLC)
s	singlet (spectral); second(s)
S,S-Chiraphos	(S,S)-(-)-Bis(diphenylphosphino)butane
S/N	signal-to-noise ratio
SCRAM	Stirling's Catalytic Racemisation Alcohols and Amines
t	triplet
TEAF	triethylammonium formate
THF	tetrahydrofuran
TMEDA	tetramethylethylenediamine
Tmen	tetraethylethylenediamine
TOF	time-of-flight
TON	turnover number
Ts	tosyl / <i>p</i> -toluenesulfonyl
TsCl	tosyl chloride / <i>p</i> -toluenesulfonyl chloride
TsDPEN	N-tosyl-1,2-diphenyl-1,2-ethylenediamine
UV	ultraviolet
vis	visible

XRD	X-ray diffraction
δ	chemical shift
ϵ	molar extinction coefficient

ACKNOWLEDGEMENTS

I would never have been able to finish my dissertation without the guidance of my committee members and support from my family, friends and wife.

I would first like to thank my supervisors Professor Robin Perutz, Professor Simon Duckett and Dr John Blacker for their guidance and support during my PhD. I am extremely grateful to the EPSRC for funding and Piramal Healthcare for supporting an Industrial CASE Studentship.

I would also like to thank all the technical, workshop and stores staff in the department at York for their kind assistance throughout my project. Thank you to all past and present members of the Perutz and Duckett research groups and the team at Piramal Healthcare. Special gratitude goes out to Jonathon Holmes (The Duckett Group) who helped me collect NMR data on the Hypersense dynamic nuclear polarisation equipment for Chapter 5. Many thanks to the Eisenstein Group (University of Montpellier, France), especially Ainara Nova, who gave me kind permission to use the Density Functional Theory calculations she performed on my work in this thesis.

Finally, I owe my deepest gratitude to my wife, Cristin. She always stood by me, encouraging me all the way.

AUTHOR'S DECLARATION

I hereby declare that this submission is my own work and that, to the best of my knowledge and belief, it contains no material previously published or written by another person nor material which to a substantial extent has been accepted for the award of any other degree or diploma of the university or other institute of higher learning, except where due acknowledgment has been made in the text.

INTRODUCTION

1.1 Chirality

A chiral (or *optically active*) molecule is a type of molecule that lacks an internal plane of symmetry and has a non-superimposable mirror image, most commonly due to the presence of a stereogenic atom in which the four substituents attached to one of the carbon atoms are different.¹ This leads to two non-identical structures (or *enantiomers*) as shown in Figure 1. The origin of the term *optical activity* is derived from the interaction of chiral materials with polarized light. An enantiomer can be named by the direction in which it rotates the plane of polarized light. If it rotates the light clockwise, as seen by a viewer towards whom the light is travelling the enantiomer is labelled (+); the mirror-image is labelled (-). The property was first observed by Jean-Baptiste Biot in 1815 and Louis Pasteur deduced in 1848 that this phenomenon has a molecular basis.^{2,3} The enantiomers can also be differentiated from each other by using standard nomenclature such as the (*R*)/(*S*) system. It labels each stereogenic centre *R*- or *S*- according to a system by which its substituents are each assigned a priority, according to the Cahn-Ingold-Prelog priority rules (CIP), based on atomic number.^{4,5} A racemic mixture (or *racemate*) is one that has equal amounts of *R*- and *S*- enantiomers of a chiral molecule. Enantiomeric excess (or *ee*) is a measure for how much of one enantiomer is present compared to the other. For example, in a sample with 60% *ee* in *R*, the remaining 40% is a racemic mixture with 20% of *R* and 20% of *S*, so that the total amount of *R* is 80%.

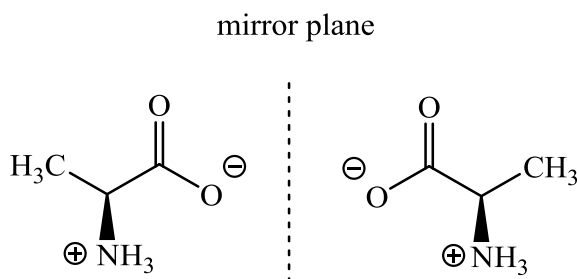


Figure 1 (S)-Alanine (left) and (R)-alanine (right) in zwitterionic form at neutral pH.

Enantiomers are equal in energy and have identical NMR and IR spectra and will migrate with identical R_f in thin layer chromatography and have identical retention time in HPLC. However, enantiomers can be separated when subjected to the influence of another chiral species.⁶ Many biologically active macromolecules are chiral and occur in nature in one enantiomeric form, including the naturally occurring amino acids (the building blocks of proteins) and sugars.⁷ Enzymes, which are chiral, often distinguish between two enantiomers of a chiral substrate. Consequently, optically active compounds are important in the fine-chemical, pharmaceutical and agrochemical industries.⁸ A biologically active compound interacts with its receptor in a chiral manner and the two enantiomers can have significantly different effects, such as the molecules shown in Figure 2. For example, (*R*)-Thalidomide has desirable sedative properties, while the (*S*)-enantiomer is teratogenic resulting in foetal malformations (however this interpretation must be considered carefully, because the (*R*)-enantiomer undergoes racemisation *in-vivo*).⁹ This highlights the problems that can arise from inappropriate molecular recognition, which should be avoided at all costs. In 1992, the United States Food and Drug Administration (FDA) introduced guidelines regarding ‘*racemic switches*’ to encourage the commercialisation of clinical drugs consisting of single enantiomers.¹⁰ Such marketing regulations for synthetic drugs have resulted in a significant increase in the proportion of single enantiomer drugs. Therefore, producing enantiomerically pure compounds in the development of pharmaceuticals, agrochemicals and flavours is a very significant endeavour. One category is enantiomerically pure amines which are highly important intermediates or building blocks for biologically active molecules. It is estimated that about 20% of drugs contain at least one amine chiral centre, so there is enormous demand for a variety of methods for the synthesis of optically active amines.¹¹ Development of truly efficient methods to achieve these transformations has been a great challenge for chemists in both academia and industry.

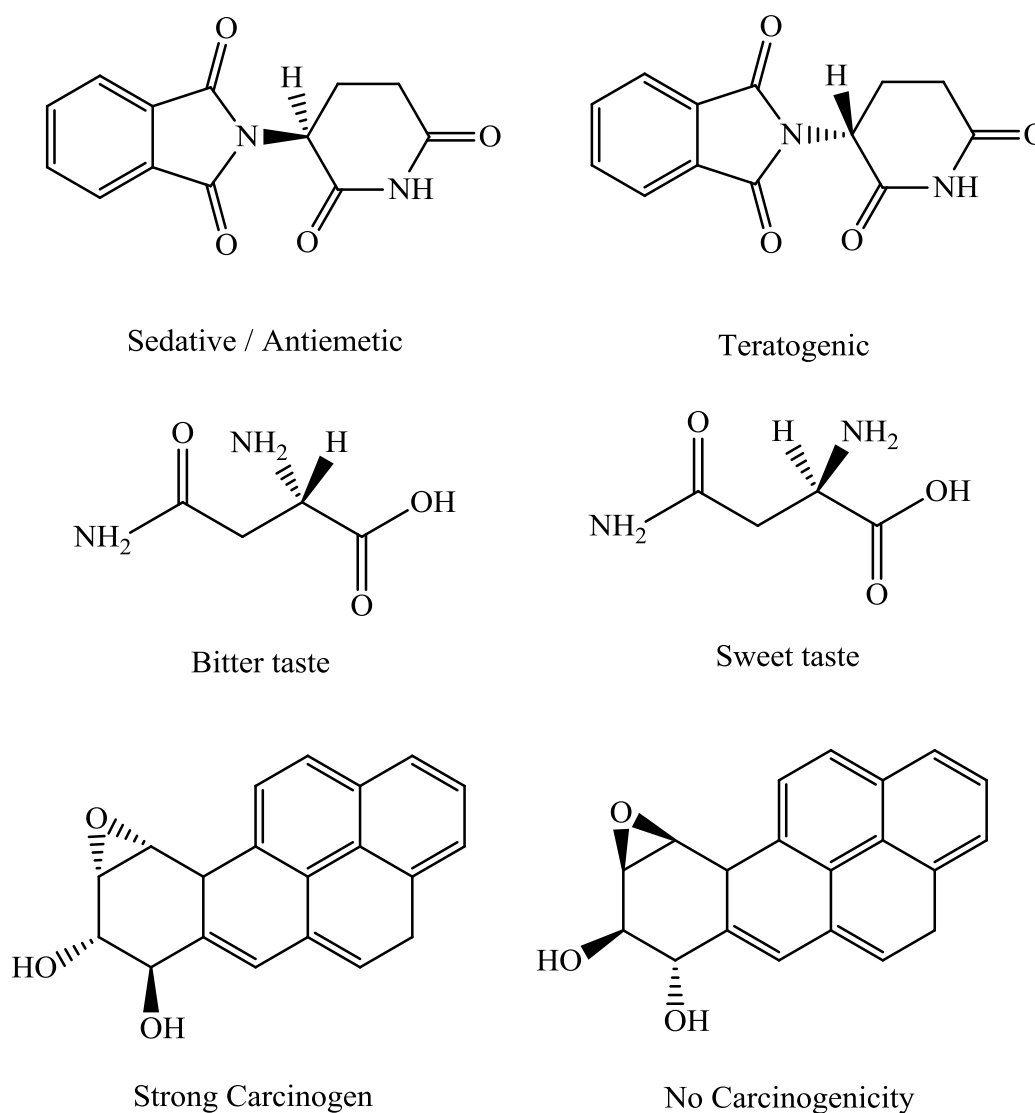


Figure 2 Optical isomers of biologically active compounds can have significantly different effects such as Thalidomide (top), Asparagine (middle) and Benzopyryldiol (bottom).

1.2 C=N and C=O Bond Reduction by Transfer Hydrogenation

Reduction of C=N and C=O bonds forming amines and alcohols, respectively is among the most fundamental molecular transformations.¹² The enantioselective hydrogenation of C=N and C=O double bonds using chiral transition metal complexes as the catalyst is one of the most useful methods for preparing optically active amines and alcohols. One method for achieving this is called Asymmetric

Transfer Hydrogenation (ATH) in which hydrogen is transferred to a molecule from a source other than gaseous H₂ using a chiral transition metal catalyst (Figure 3).

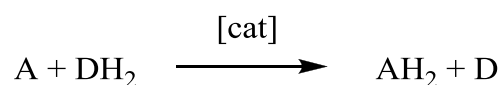


Figure 3 Definition of transfer hydrogenation, where A = acceptor, DH₂ = hydrogen donor and [cat] = transition metal catalyst.

In recent years this methodology has become rated second in order of importance immediately behind asymmetric hydrogenation with molecular hydrogen. The increasing success in industry and organic synthesis of this technique follows from its operational simplicity and reduction of risks associated with the use of an inflammable gas of high diffusibility. The transformation is carried out using isopropanol, formic acid or a formate salt as the hydrogen source. The most commonly, but not exclusively, used metals are ruthenium, rhodium and iridium.

1.2.1 Mechanisms of hydrogen transfer: Direct hydrogen pathway

The mechanism for the transfer hydrogenation of imines has been the subject of extended synthetic, computational and mechanistic studies. Hydrogen transfer reactions for the reduction of imines (and ketones) may proceed through a variety of different pathways and are divided into two broad classes. The first of these, Meerwein-Ponndorf-Verley (MPV) reduction or its reverse (Oppenauer oxidation) considers the case where a metal coordinates to both substrate and hydrogen source (typically isopropanol) and hydrogen transfer takes place via a six-centred transition state with concomitant formation of ketone (for example, acetone, if isopropanol is used) (Figure 4). This is referred to as the *direct hydrogen pathway* and is typically observed with metal catalysts that cannot readily form hydrides, such as metal alkoxides.¹³

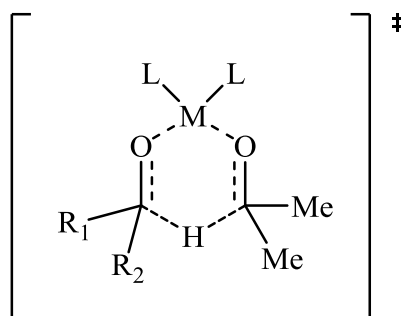


Figure 4 The 6-membered transition state in the Meerwein-Ponndorf-Verley (MPV) reduction showing the direct hydrogen pathway.

The MPV reduction reaction is very well established and implemented for the reduction of ketones through use of aluminium(III) salts. However, the literature on MPV-type reductions of imines is quite limited, but a very effective system based on Al(III) BINOL complexes has been reported (Figure 5).¹⁴ Although the BINOL / Al(III) system requires stoichiometric quantities of ligands and metal, both can be reused after the reaction and are inexpensive.

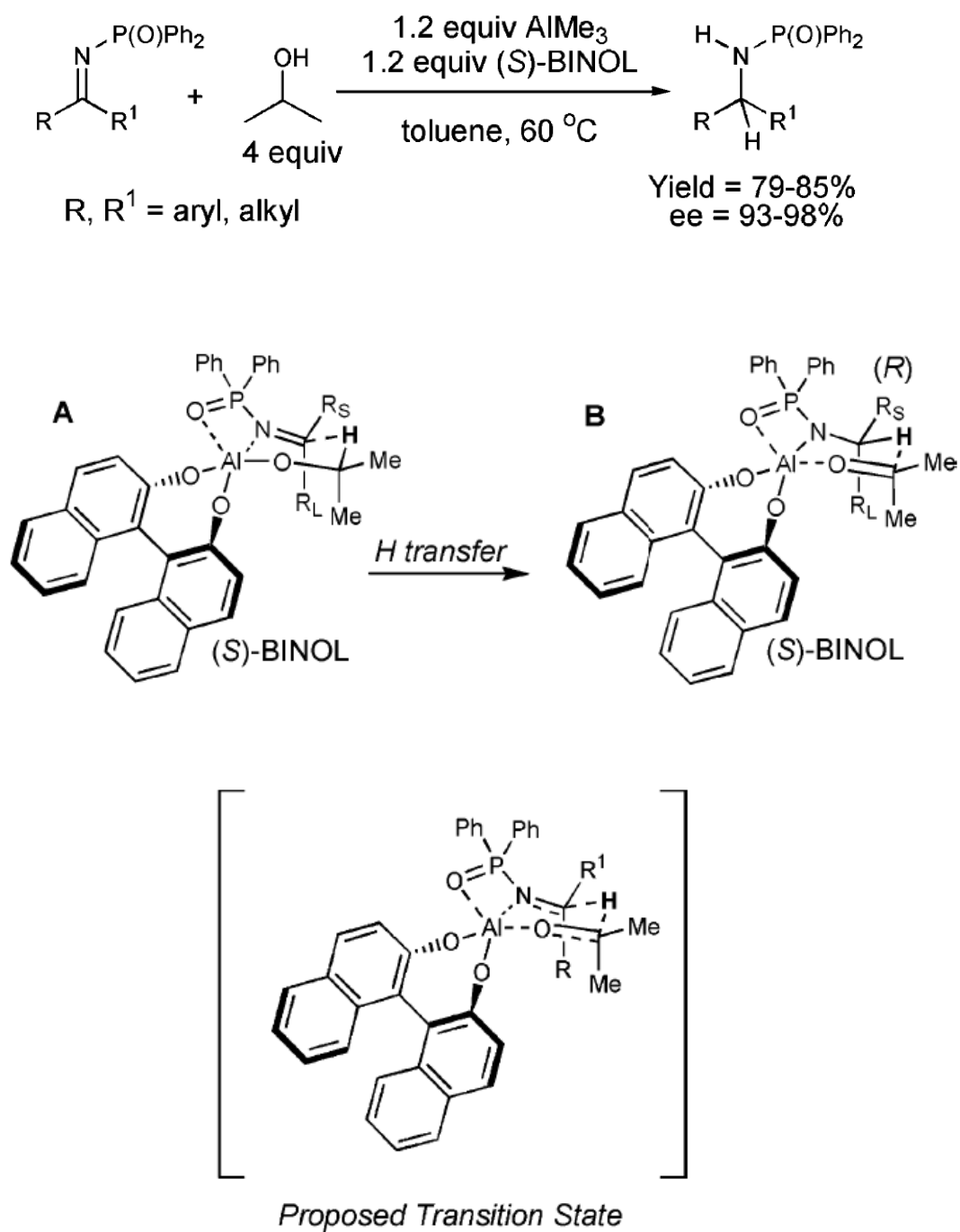


Figure 5 A highly enantioselective MPV reduction of *N*-phosphinoyl ketimines by (BINOL)Al(III) / 2-propanol and proposed pathway and transition states reported by Graves *et al.*¹⁴

1.2.2 Mechanisms of hydrogen transfer: hydridic route

Metals such as rhodium, ruthenium and iridium which can readily form metal hydrides favour an alternative mechanism, known as the “hydridic route” where a metal-hydride complex participates in the catalytic cycle. There are again several routes that exist for hydrogen transfer. For example, both hydrogen atoms may transfer to the metal to form an intermediate which then transfers the H atoms to the substrate (Figure 6).

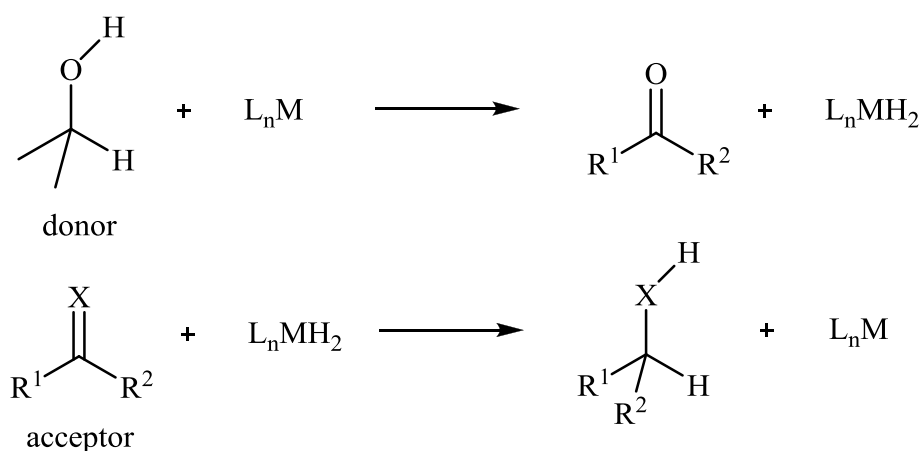


Figure 6 Transfer hydrogenation: dihydridic route

In the alternative monohydride mechanism, the substrate may interact directly with the metal centre. A hydride is then transferred to the carbon of the C=N bond and the nitrogen atom of the product then interacts directly with the metal atom. Loss of amine is facilitated by protonation to give the product and regenerate the catalyst which then re-enters the catalytic cycle (Figure 7).

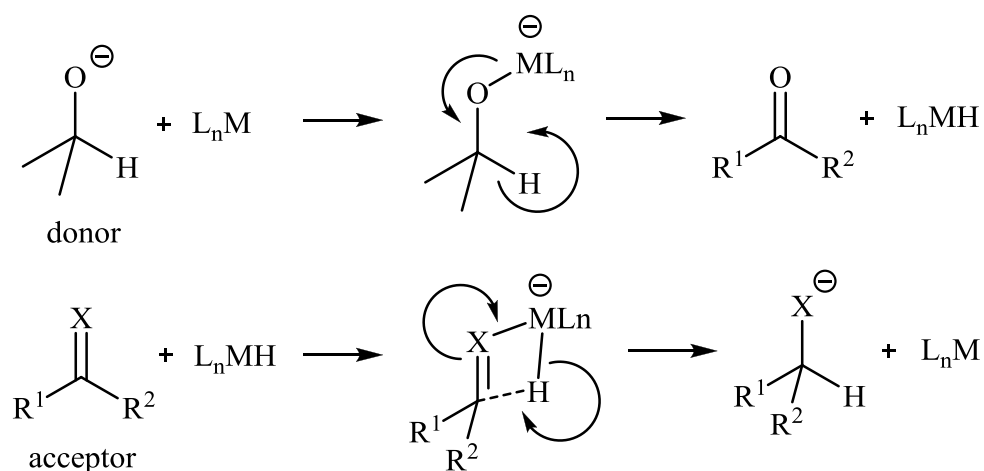


Figure 7 Transfer hydrogenation: monohydride route

1.2.3 Mechanisms of hydrogen transfer: metal-ligand bifunctional catalysis

A variation on the direct hydride mechanism, involving *metal ligand bifunctional catalysis*¹⁵ or what Morris has called *ligand assistance*¹⁶ is the situation where two hydrogen atoms are simultaneously transferred from the catalyst to the substrate in a six-membered transition state. In this mechanism, the substrate does not come into contact with the metal but is reduced through an “outer-sphere” mechanism (Figure 8).

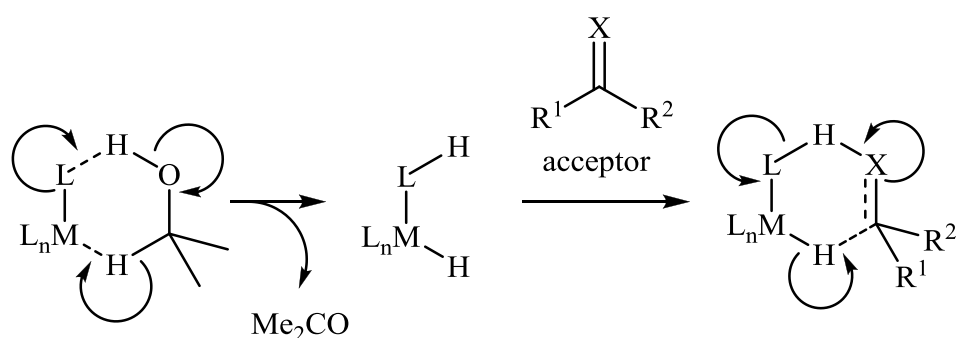


Figure 8 Metal-ligand bifunctional catalysis proceeds through an “outer-sphere” mechanism

The mechanism of transfer hydrogenation can be determined by racemisation of a chiral alcohol or amine containing a deuterium atom adjacent to the $\text{C}=\text{X}$ group. If

the dihydride mechanism operates then the deuterium level will drop to about 50% upon racemisation (where the OH or NH gains a corresponding amount of D label) because the two hydrogens in the metal hydride are equivalent. Whereas, if the monohydride mechanism is operating then the label will remain on the carbon atom because the mechanism demands that the donor atom be the same as the recipient atom for the hydride on the metal. In contrast to ketones, and in particular with respect to asymmetric reductions, the reduction of compounds containing C=N bonds has remained relatively underdeveloped. Unlike ketone reductions which have been the subject of extensive studies and optimisations, the mechanism of imine reduction is rather less fully developed and understood. However, some incisive studies have been completed.

1.3 Organometallic Catalysts Based on Ru, Rh and Ir for transfer hydrogenation of imines

In 1987, the ruthenium complex $\text{Ru}_3(\text{CO})_{12}$ was reported by Jones *et al.* to catalyse the transfer of hydrogen from isopropanol to benzylideneanilines (Figure 9).¹⁷ The active catalyst, $(\mu_2\text{-H})\text{Ru}_3(\text{CO})_9(\mu_3\text{-PhNCHPh})$ was isolated and characterised by X-ray crystallography (Figure 10). The X-ray crystallography structure of the active catalyst was found to be a complex of the imine substrate and a trimetallic hydride.

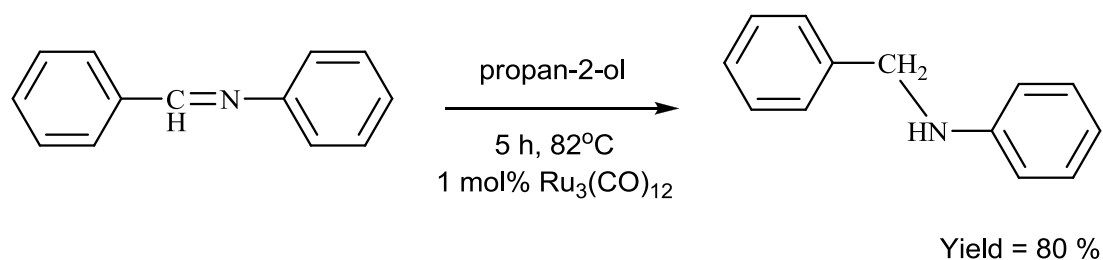


Figure 9 $\text{Ru}_3(\text{CO})_{12}$ reported by Jones to catalyse the transfer hydrogenation of benzylideneanilines using isopropanol as the hydrogen source.¹⁷

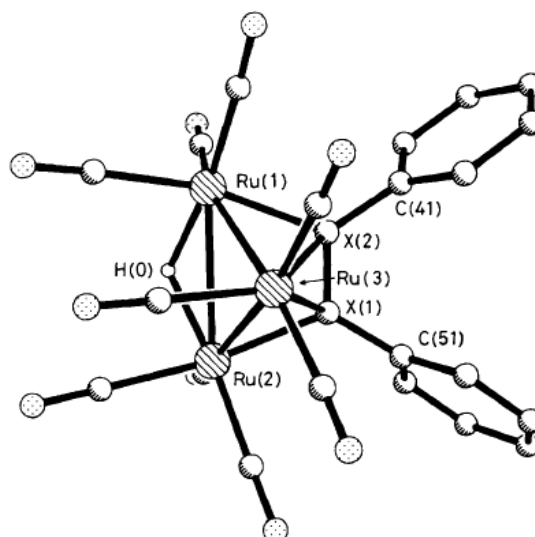


Figure 10 X-ray structure of $(\mu_2\text{-H})\text{Ru}_3(\text{CO})_9(\mu_3\text{-PhNCHPh})$, phenyl hydrogens omitted for clarity.

In 1992, a racemic imine reduction using the Ru complex $[\text{RuCl}_2(\text{PPh}_3)_3]$ as the catalyst and isopropanol as the hydrogen source was reported by Bäckvall (Figure 11).¹⁸ In this case, the role of base is to generate a highly active $\text{RuH}_2(\text{PPh}_3)_3$ catalyst from the dichloride via two consecutive alkoxide displacement- β -elimination sequences (Figure 12).

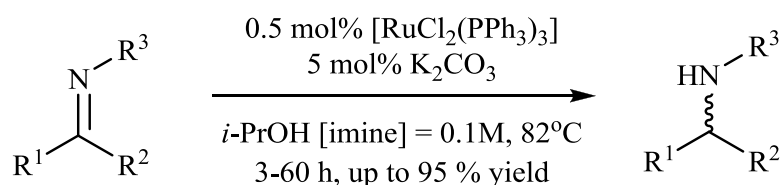


Figure 11 Transfer hydrogenation of imines using as Ru(II) catalyst

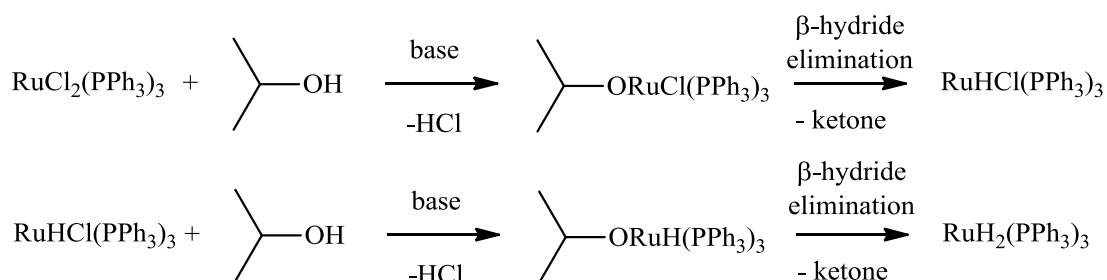


Figure 12 The role of base is to form the highly active $\text{RuH}_2(\text{PPh}_3)_3$ catalyst

The $[\text{RuH}_2(\text{PPh}_3)_3]$ complex was isolated and shown to be active for the C=N bond reduction without a requirement to add base.¹⁹ The mechanistic studies have shown that this reaction proceeds through the dihydride (*inner-sphere*) mechanism without ligand assistance (Figure 13).²⁰ Furthermore, the chlororuthenium monohydride was shown not to be reactive toward hydride addition to a C=X group and this was supported by theoretical calculations.

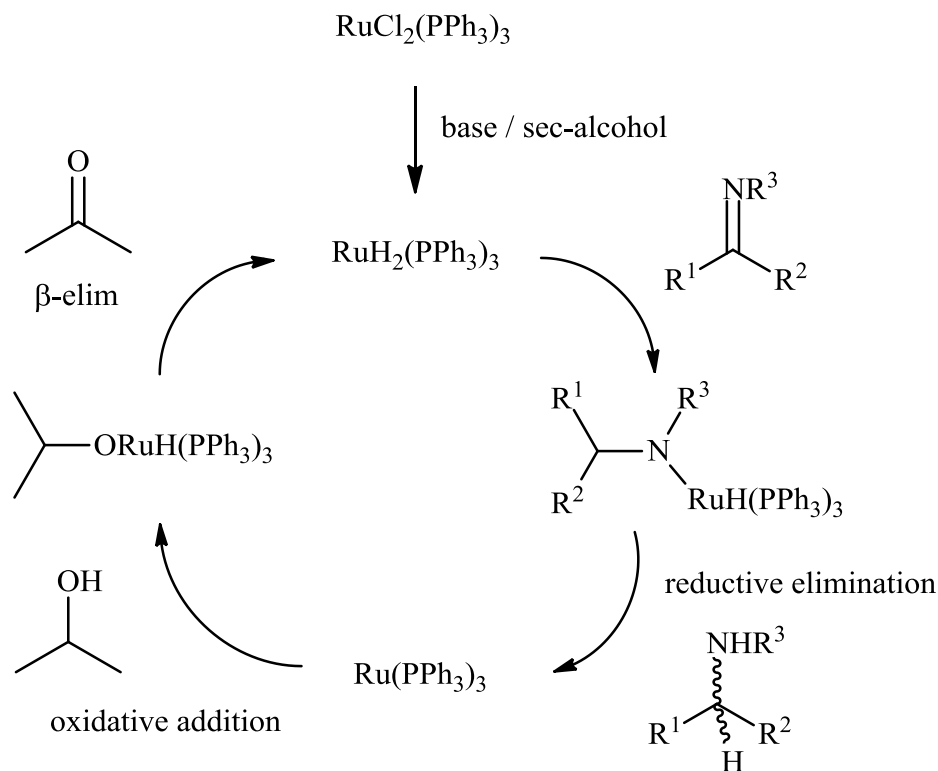


Figure 13 Proposed mechanism of hydrogen transfer for $\text{RuCl}_2(\text{PPh}_3)_3$

1.3.1 Shvo's catalyst

A number of other catalysts have been used for imine transfer hydrogenation such as the Shvo diruthenium catalyst, probably the very first example of a metal-ligand bifunctional catalyst.^{21,22,23,24} The Shvo catalyst is one of the most popular hydrogen-transfer catalysts due to its great versatility. It has proved to be an effective catalyst for the hydrogenation of carbonyl compounds,^{25,26} transfer hydrogenation of ketones and imines,^{27,28} oxidation of alcohols and amines^{29,30,31,32,33} and the racemisation of alcohols and amines.^{34,35,36} Dissociation of the dimer to form hydride **A**, the active

hydrogenating species and coordinatively unsaturated **B**, the active dehydrogenating species, is necessary to activate the complex (Figure 14) and is usually achieved by heating above 100°C. This equilibrium is what makes Shvo's catalyst so versatile in hydrogen-transfer processes. While **A** can be isolated, **B** is very unstable; however its existence has been demonstrated by trapping with PPh₃.

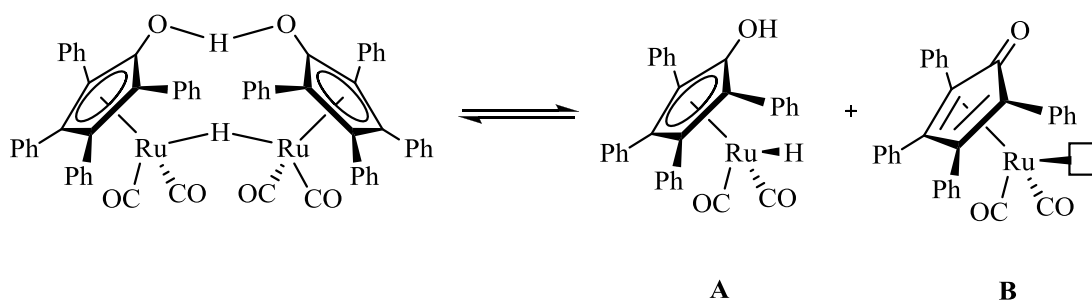


Figure 14 Shvo catalyst and the equilibrium between **A** and **B**

The reaction mechanism for the hydrogen-transfer process is a matter of controversy. Studies by Casey³⁷ by means of primary deuterium isotope effects on the hydrogenation of PhCHO via the reducing form (**A**) of the Shvo tolyl analogue catalyst, $[2,5\text{-Ph}_2\text{-3,4-Tol}_2(\eta^5\text{-C}_4\text{COH})\text{Ru}(\text{CO})_2\text{H}]$, concluded that carbonyl hydrogenation is concerted without substrate coordination (outer-sphere, Figure 15); this conclusion was also supported by DFT calculations by the same authors.³⁸ Bäckvall using a similar methodology, also reported a concerted mechanism for the catalytic dehydrogenation of an alcohol, 1-(4-fluorophenyl)ethanol using tetrafluorobenzoquinone as the hydrogen acceptor and **B** (Figure 16).³⁹ In this case he found the rate to be first order in both alcohol and metal complex. Individual isotope effects all support a mechanism involving concerted transfer of both hydrogens of the alcohol to the ruthenium complex in agreement with Casey's proposals.

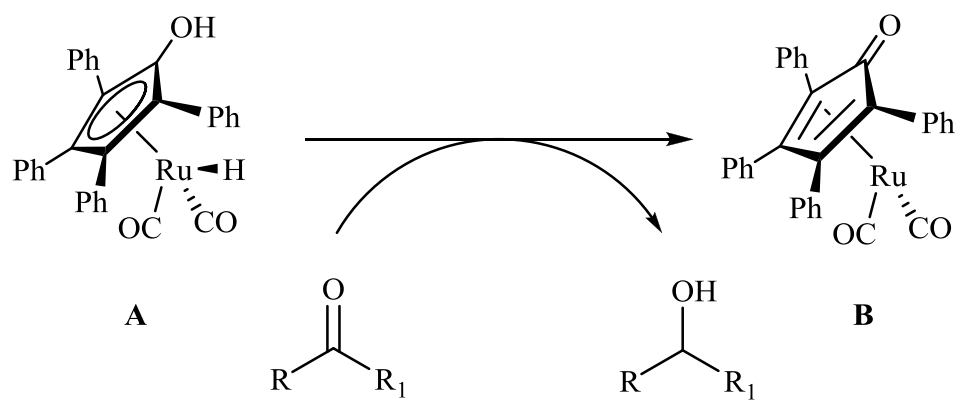


Figure 15 Proposed "Outer-sphere" reaction for the carbonyl hydrogenation by means of the Shvo catalyst.^{37,38}

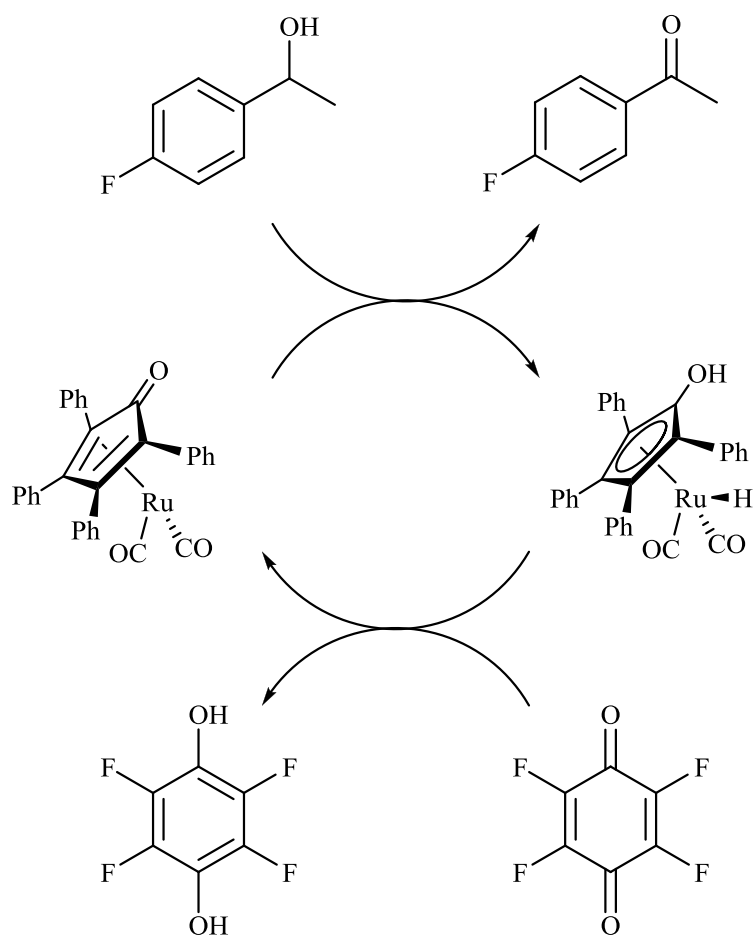


Figure 16 The catalytic dehydrogenation of 1-(4-fluorophenyl)ethanol, using tetrafluorobenzoquinone as hydrogen acceptor.³⁹

For the transfer dehydrogenation of the amine N-phenyl-1-phenylethylamine using 2,6-dimethoxybenzoquinone as hydrogen acceptor, Bäckvall found kinetic deuterium isotope effects of $k_{\text{CHNH}}/k_{\text{CDNH}} = 3.24 \pm 0.16$, $k_{\text{CHNH}}/k_{\text{CHND}} = 1.39 \pm 0.13$, $k_{\text{CHNH}}/k_{\text{CDND}} = 3.26 \pm 0.25$, $k_{\text{CDNH}}/k_{\text{CDND}} = 1.01 \pm 0.12$ and $k_{\text{CHND}}/k_{\text{CDND}} = 2.33 \pm 0.38$.³² These data suggest that cleavage of the CH bond of the amine is rate determining, but cleavage of the NH bond is not. This is not consistent with the concerted transfer seen with carbonyl / alcohol systems. Bäckvall suggested that the substrate coordinates to the metal via a η^5 - η^3 ring slippage of the aromatic ligand, followed by simultaneous β -hydride addition and a proton transfer to the unsaturated organic substrate (inner-sphere mechanism, Figure 15).

This was followed up by an experiment studying the transfer hydrogenation of the imine, N-phenyl-[1-(4-methoxyphenyl)ethylidene]amine where the product of the reaction is a Ru-amine complex (Figure 17).⁴⁰

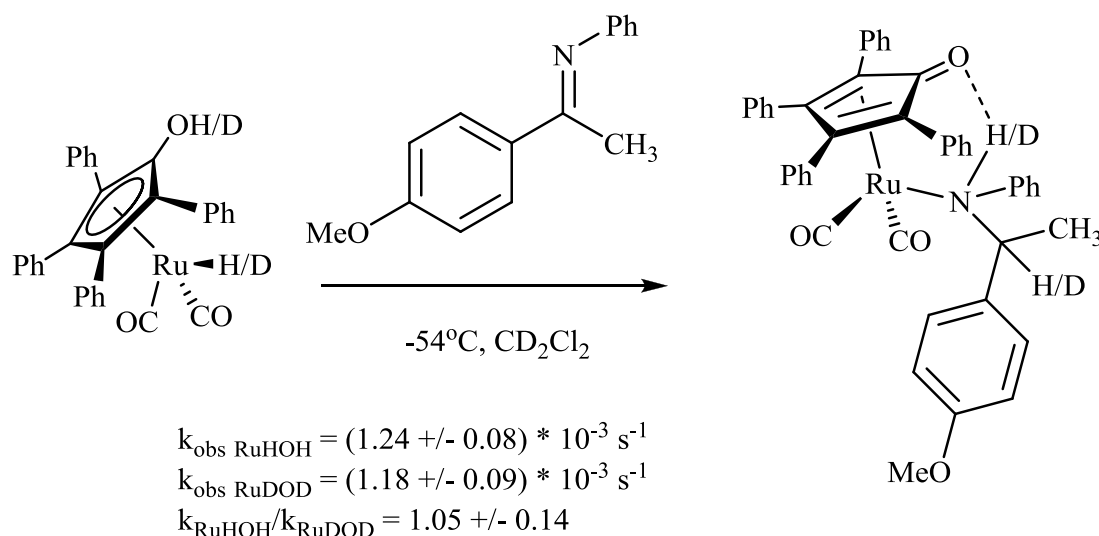


Figure 17 Hydrogenation of imine study

The negligible double isotope effect ($k_{\text{HH}}/k_{\text{DD}} = 1.05$) of the reaction suggested no bond to hydrogen is either broken or formed in the rate determining step leading to a more detailed mechanistic suggestion (Figure 18); reversible η^5 - η^3 ring slip, followed by coordination of the imine and fast hydrogen transfer leads to an amine complex with its Cp ring η^2 -coordinated, this quickly rearranges to the final 18-electron amine product with the Cp ring η^4 -coordinated.

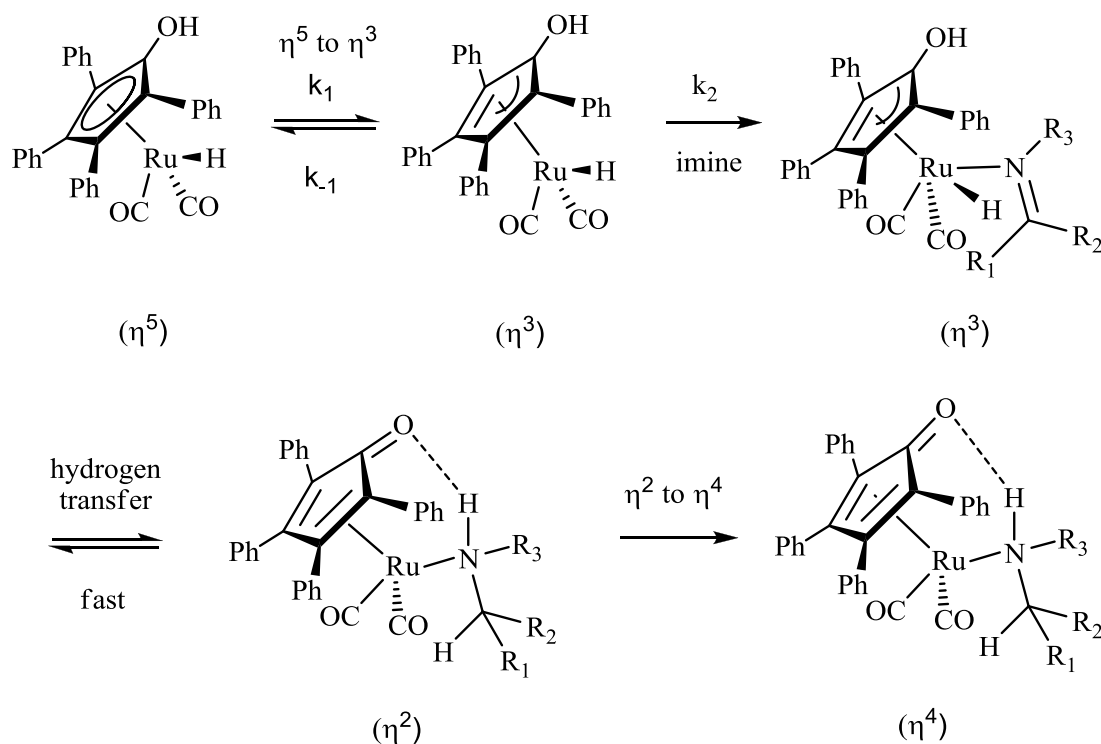


Figure 18 Bäckvall's proposal for a stepwise mechanism for the transfer hydrogenation of imines by Shvo's catalyst.

In imine hydrogenation although trapping experiments have provided additional information, they again have led to opposite conclusions concerning the mechanism. In ketone hydrogenation, this approach is not possible because of the high lability of alcohol complexes.⁴¹ The mechanism of Shvo's catalyst for transfer hydrogenation of imines has been one of the most controversial regarding the nature of hydrogen transfer. The "inner-sphere / outer-sphere" dichotomy in the hydrogenation of polar bonds such as C=O and C=N functional groups is commonly found in recent literature. In addition to experimental work, theoretical calculations were fundamental in studying the process, including some controversy. Recently, from the overall theoretical analysis of Comas-Vives *et al.*, it can be concluded that the concerted outer-sphere mechanism is nearly 10 kcal mol⁻¹ lower in energy than the lowest energy barrier reported in the inner-sphere mechanism. Therefore, theoretical analysis supports the concerted outer-sphere mechanism for both the imine and ketone hydrogenation using Shvo's catalyst.⁴²

1.3.2 Asymmetric Transfer Hydrogenation (ATH) catalysts

In the 1970's, the groups of Ohkubo and Sinou demonstrated that by combining $\text{RuCl}_2(\text{PPh}_3)_3$ with a chiral monophosphine ligand, they were able to form a chiral transition metal catalyst capable of asymmetric transfer hydrogenation.^{43,44} Since their discovery several other catalytic systems for ATH have been developed including Pfaltz's iridium,⁴⁵ Genet's ruthenium,⁴⁶ Lemaire's rhodium⁴⁷ and Evans' samarium⁴⁸ systems. However, these systems all had the major drawback of enantioselectivity rarely exceeding 90% ee's.

A major breakthrough in transition-metal-catalysed ATH was made by Noyori and co-workers in 1995. They developed half-sandwiched ruthenium(II) catalysts such as $[(\text{arene})\text{Ru}(\text{Cl})(\text{TsNCHPhCHPhNH}_2)]$ with chelating monotosylated 1,2-diamines or amino alcohols (Figure 19); these catalysts were discovered to be highly efficient and enantioselective for the reduction of ketones with isopropyl alcohol or $\text{HCO}_2\text{H}/\text{Et}_3\text{N}$ azeotrope (TEAF) as the hydrogen source.⁴⁹ Subsequently, Mao and Baker reported the use of the isolable $[\text{Cp}^*\text{Rh}^{\text{III}}(\text{Cl})(\text{TsNCHPhCHPhNH}_2)]$ catalyst.⁵⁰ This catalyst showed comparable yields and ee's, but greater activity, reactions taking generally tens of minutes with Rh, as opposed to several hours in the case of Ru. $[\text{Cp}^*\text{Rh}(\text{Cl})(\text{TsNCHPhCHPhNH}_2)]$ and $[\text{Cp}^*\text{Ir}(\text{Cl})(\text{TsNCHPhCHPhNH}_2)]$ catalysts are also the basis of patents granted by Avecia Ltd (now Piramal Healthcare) (Figure 19).^{51,52}

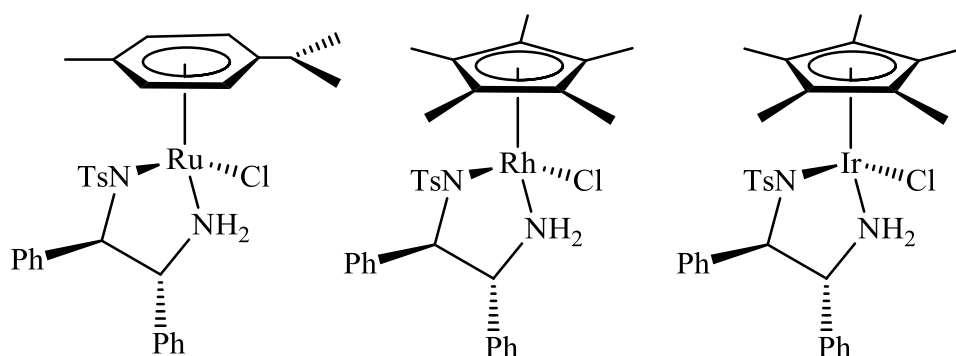


Figure 19 Molecular structures of Ru(II), Rh(III) and Ir(III) ATH catalysts

Noyori demonstrated that these systems require primary or secondary amine functionality, as catalysts with tertiary amine functions are inactive.⁵³ Combined with similar features in his asymmetric hydrogenation catalyst *trans*-(BINAP)Ru(DPEN)Cl₂ led Noyori to propose that these catalysts proceed through a metal-ligand bifunctional catalysis mechanism⁵⁴ (Figure 20, Step 1: In-situ formation of the 18-electron chloride complex with base; Step 2: Abstraction of HCl by base to form a 16-electron amido complex; Step 3: Transfer Hydrogenation of the 16-electron complex by isopropyl alcohol to form the 18-electron hydride complex and acetone; Step 4: Transfer of hydrogen from the 18-electron complex to a ketone (in an outer-sphere asymmetric addition depending on the stereochemical configuration of the monotosylated diamine ligand) and formation of a chiral secondary alcohol with regeneration of the 16-electron amido complex). The mechanism of hydrogen transfer for ketones is now relatively well established. Mechanistic and computational studies have provided strong support for the ATH “outer-sphere” mechanism, as classified by Morris,⁵⁵ in which two hydrogen atoms are transferred to a substrate via a six-membered transition state. A π /CH interaction between a hydrogen atom on the η^6 -arene of the complex and the aromatic ring of a substrate with a value of ca. 8.6 kJ mol⁻¹ is pivotal to the control of the absolute product stereochemistry (Figure 23a). This effect operates even more strongly through a methyl group on the η^6 -arene (*p*-cymene) or the Cp* ligand of the catalyst; value ca. 12.3 kJ mol⁻¹.⁵⁶ However this requires that the substrate contains a suitably located aromatic ring. “Dialkyl” ketones are reduced in much lower enantioselectivity.

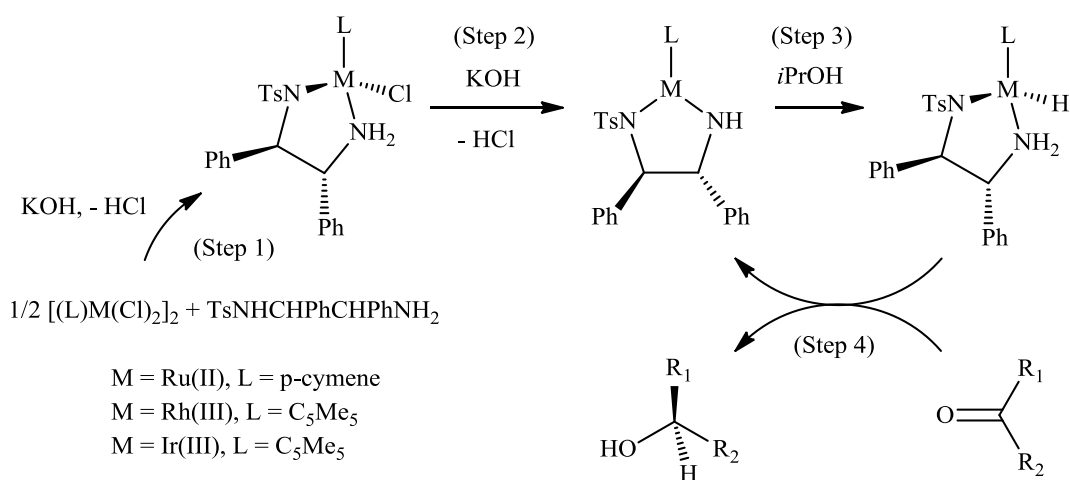


Figure 20 Proposed mechanism involving “outer-sphere” ATH of ketones

With monotosylated diamine ligands, imine substrates require the use of formic acid as the hydrogen donor. The mechanistic studies described above all focus on the IPA / KOH hydrogen donor system; much less is known of the mechanisms operating with the analogous Rh and Ir systems, the use of formic acid as a hydrogen donor or about reduction of imine substrates. Ikariya has studied the action of formic acid on the 16-electron ruthenium complex, [(p-cymene)Ru(TsNCHPhCHPhNH)] by NMR spectroscopy and presented evidence that the hydride is formed via a short-lived formate complex.^{57,58} The reversibility of this process was demonstrated by subjecting the hydride species at 10 atm of CO₂ at -78°C which produced formic acid and regenerated the 16-electron complex. Wills has demonstrated that Ru hydride formation can be the limiting factor in catalysis.⁵⁹

Bäckvall has demonstrated that the Ru(II)-TsDPEN hydride species, which reacts fast with ketones, does not react with imines (Figure 21).⁶⁰ However, when an acid is added in the latter case a fast reduction occurs (Figure 22). These results support an ionic mechanism for the reduction of imines by the Ru ATH catalyst, where the substrate is pre-activated by protonation prior to hydrogen transfer. To confirm that formic acid was not acting as a hydrogen donor, Bäckvall performed the hydrogenation of imines with different Brønsted acids and one Lewis acid. The acids promoted the hydrogenation in excellent yields, particularly tetrafluoroboric acid, trifluoroacetic acid and acetic acid (Figure 22). This further supports their proposal that the role of the acid was to activate the imine.

An ionic mechanism has also been proposed by Norton and Bullock for the hydrogenation of ketones (aldehydes) and imines by different transition metal catalysts of the general formula $[(\eta^5\text{-C}_5\text{R}_5)\text{RuH}(\text{L-L})]$ where L-L = dppe, dppe, dpbz, dppp, dppb, (S,S)-Chiraphos, dmpe.⁶¹

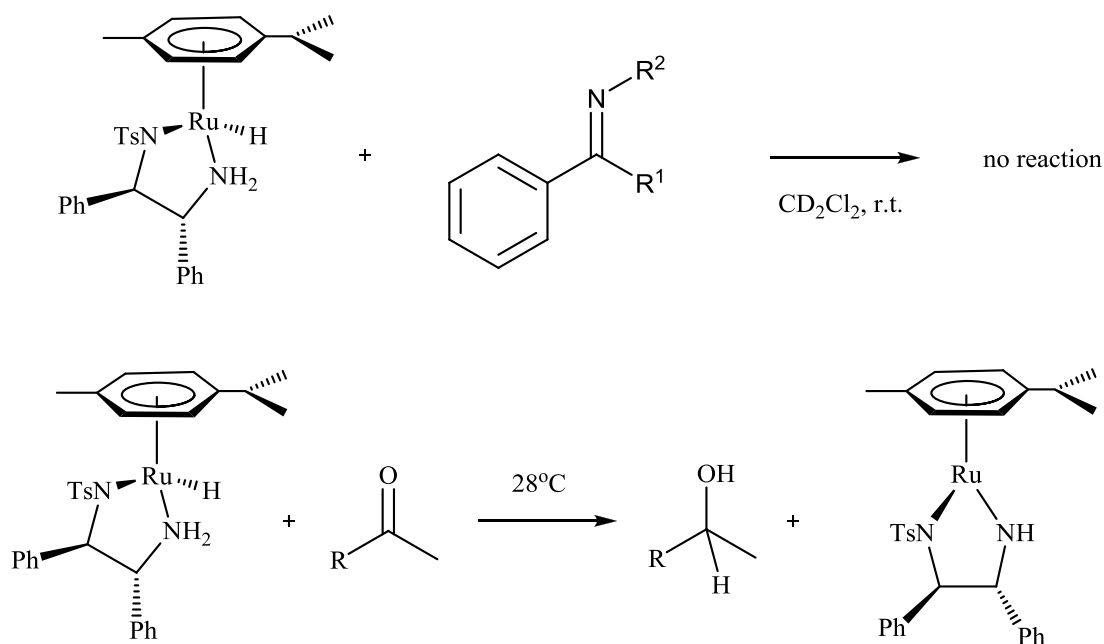


Figure 21 Stoichiometric reaction between Ru-hydride and imine does neither form any complex, nor reduce the substrate.

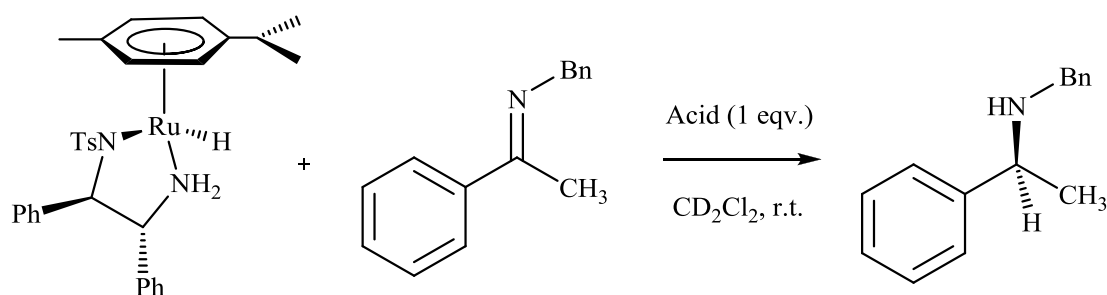


Figure 22 Addition of acid is necessary for reduction of imine by the Ru-hydride complex.

Wills *et al.* have recently proposed alternative explanations where the iminium is reduced through a six-membered transition state but oriented such that the relative positions of alkyl and aryl groups are reversed (Figure 23c). They also considered a process where the imine is reduced through an ionic mechanism in which the C=N

bond of an iminium cation is oriented away from the NH of the amine of the ligand (Figure 23d) and without involvement of a six-membered transition state.⁶² This would allow the analogous CH/ π interaction to operate while delivering the correct (observed) enantiomer of the reduction product. N-alkylated TsDPEN derivatives bearing a small alkyl group were found to be highly efficient ligands in Ru(II) complexes for ATH of imines. Wills *et al.* discuss how a larger alkyl group significantly reduced the activity, although high ee's were still obtained. An X-ray crystallography structure of the N-benzyl derivative revealed a conformation that permitted hydrogen transfer through a six-membered transition state (Figure 23c).

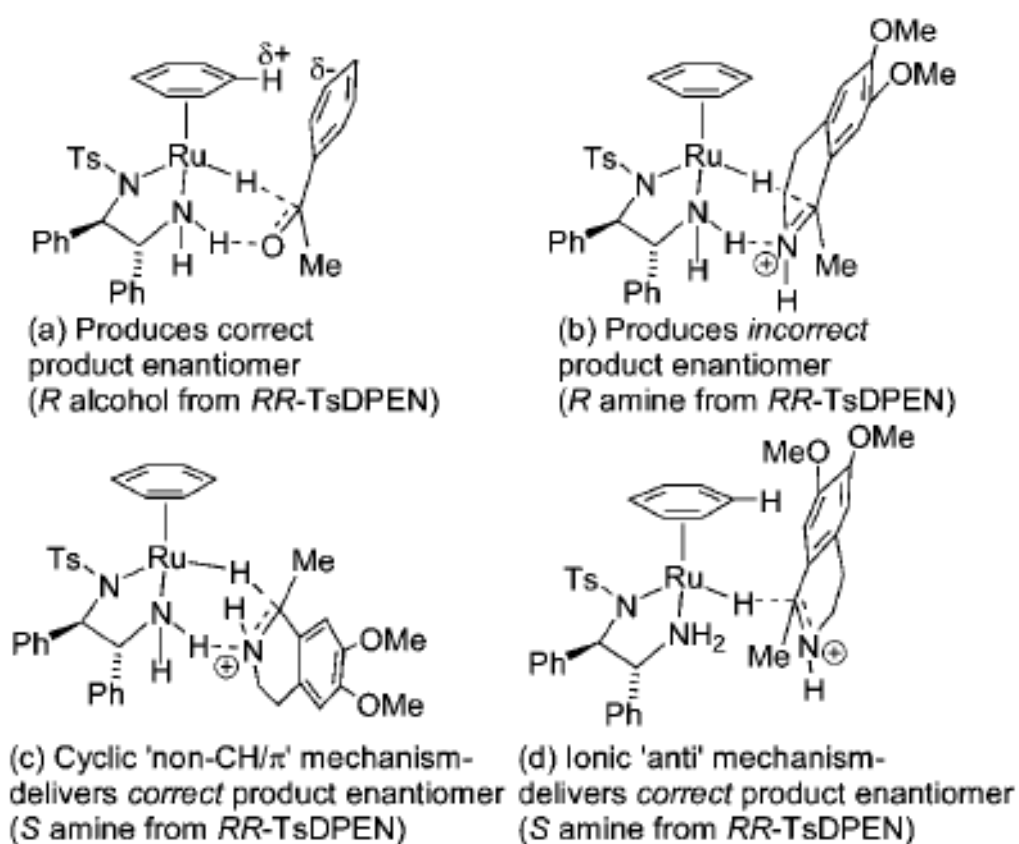


Figure 23 Mode of reduction of acetophenone (a) and potential modes of reduction of imine (b-d) in ATH by Ru TsDPEN catalysts.⁶²

Since only Figure 23d permits what is known to be an important CH/ π interaction and given the evidence for the involvement of a protonated imine in the reduction reaction, Will's *et al.* suggest this could be considered a viable model for further investigations into the precise mechanism by which ATH of imines operate.

1.5 Transfer Dehydrogenation

Oxidation reactions are fundamental in organic chemistry.⁶³ Many oxidations that are still used today require stoichiometric quantities of metal-based oxidants such as dichromate ions, permanganate ions, manganese dioxide, silver oxide and lead tetraacetate. This is extremely wasteful both environmentally and economically.⁶⁴ For example, imines can be formed by the oxidation of amines and are used extensively as intermediates in organic synthesis because they can act as electrophilic reagents in many different reactions such as reductions, additions, condensations and cycloadditions (Figure 24).⁶⁵ Therefore, the development of transition-metal catalysts to achieve efficient oxidations is highly desirable.

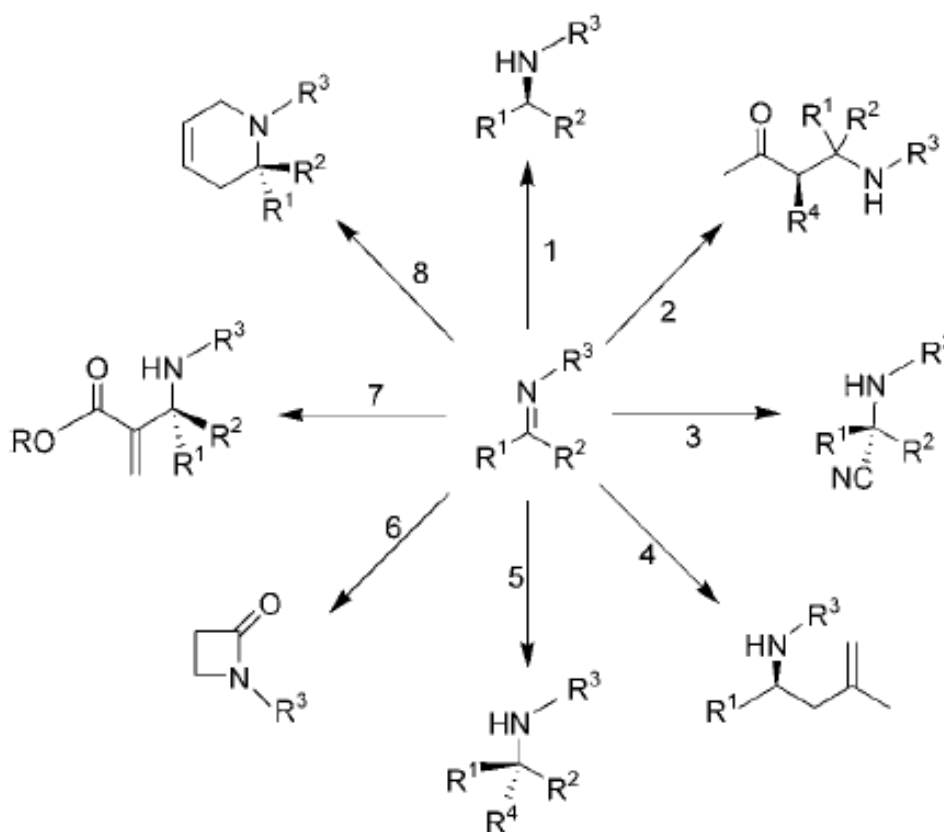


Figure 24 A diagram by Bäckvall,⁶⁵ showing imines as important intermediates for: 1.) hydrogenation,⁶⁶ 2.) Mannich,⁶⁷ 3.) Strecker,⁶⁸ 4.) imino-ene,⁶⁹ 5.) addition,⁷⁰ 6.) [2+2] addition,⁷⁰ 7.) aza-Baylis-Hillman,⁷¹ 8.) aza-Diels-Alder.⁷²

The Noyori-type ATH catalysts such as (p-cymene)Ru(Cl)(TsNCHPhCHPhNH₂), Cp*Rh(Cl)(TsNCHPhCHPhNH₂) and Cp*Ir(Cl)(TsNCHPhCHPhNH₂) described in Section 1.3.2 are effective catalysts for the transfer hydrogenation of imine substrates under catalytic conditions. The principle of microscopic reversibility indicates that it should be possible to use these types of catalyst under appropriate catalytic conditions to dehydrogenate amines to produce imines; in this case the amine would act as the hydrogen donor in tandem with a suitable hydrogen acceptor such as a ketone substrate. Bäckvall *et al.* showed that by employing Noyori's ruthenium catalyst,⁷³ 10% of the corresponding imine could be isolated. Although this was a low yield, it did prove the concept that dehydrogenation of amines was occurring (Figure 25).

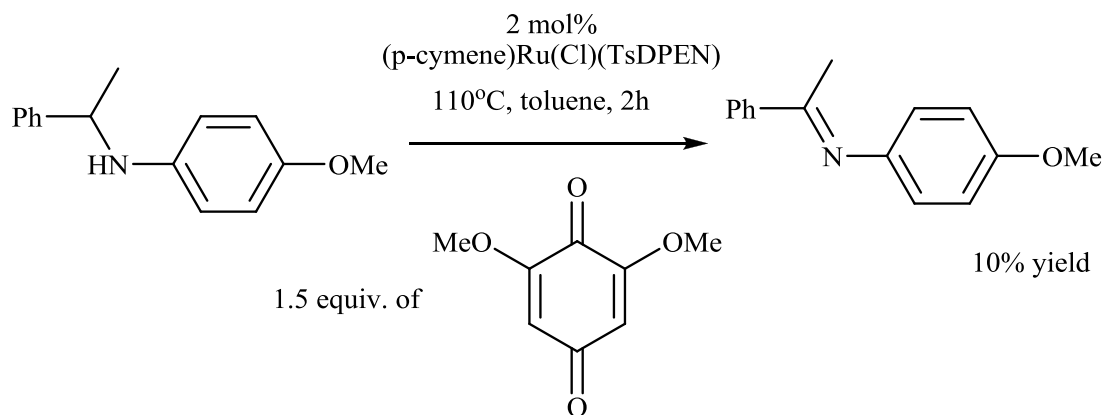


Figure 25 Dehydrogenation of amines using Noyori's ruthenium catalyst.⁷³

The same reaction with Shvo's catalyst achieved an 87% yield. During a mechanistic study of Shvo's catalyst with imines, Bäckvall *et al.* found that Shvo's catalyst, **1** together with an *N*-methyl-substituted secondary amine gave a new complex at low temperature (Figure 26). They concluded that this was most likely the first step in the dissociation of Shvo's dimer, **1**. Bäckvall extended this approach to develop an aerobic process for the oxidation of amines to imines, in which it was possible to reoxidise the dimethoxyquinone with molecular oxygen and a [Co(salen)]-type complex in a biomimetic coupled catalytic system with good to high yields under air. They proposed a mechanism for the dehydrogenation of secondary amines which is shown in Figure 27.⁶⁵ Interestingly, non-benzylic amines could also be used as

substrates giving high yields of the corresponding imine, thus drastically extending the scope of this system for organic synthesis.

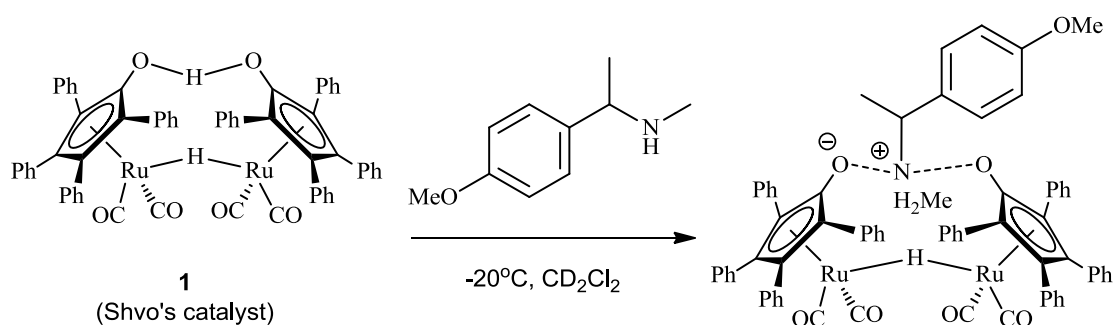


Figure 26 Shvo's catalyst and the reaction with *N*-methyl-substituted amine.⁶⁵

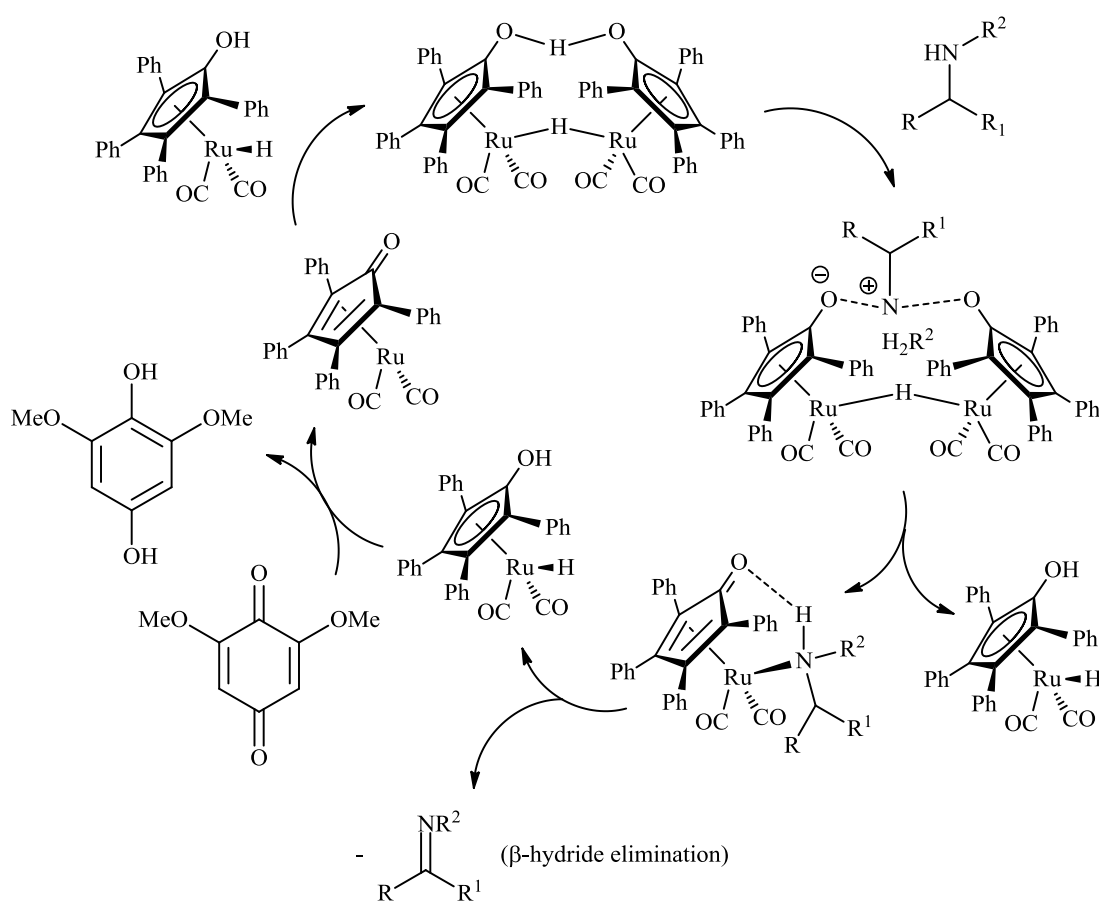


Figure 27 Proposed mechanism for the ruthenium-catalyzed dehydrogenation of secondary amines.⁶⁵

Recently, Fujita and Yamaguchi reported the oxidant-free catalytic oxidation of secondary alcohols to ketones with concomitant evolution of hydrogen, in which Cp*Ir complexes **1** and **2** containing 2-hydroxypyridine and 2-pyridonate, respectively as functional ligands have proven to be effective catalysts (Figure 28).⁷⁴

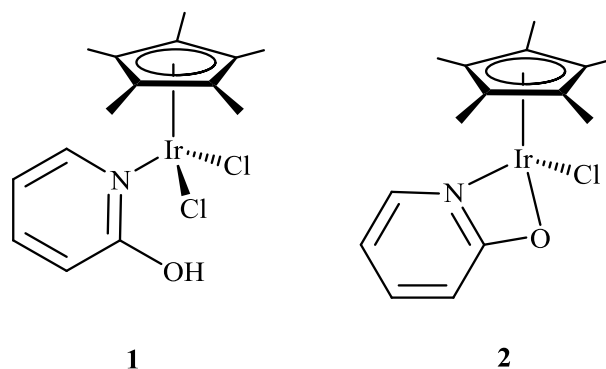


Figure 28 Cp* Iridium complexes containing (left) 2-hydroxypyridine and (right) 2-pyridonate ligands.⁷⁴

Subsequently, Fujita and Yamaguchi investigated the catalytic performance of the Cp*Ir complexes for the dehydrogenation of 1,2,3,4-tetrahydroquinoline to form quinoline.⁷⁵ Both complexes gave unsatisfactory results, although the yield of imine was increased to 69% by conducting the reaction under reflux in *p*-xylene. Next they modified the 2-pyridonate ligand by introducing electron-donating and withdrawing groups in the pyridine ring. The 5-trifluoromethylpyridonate Cp*Ir complex, **3** exhibited superior activity (Figure 29).

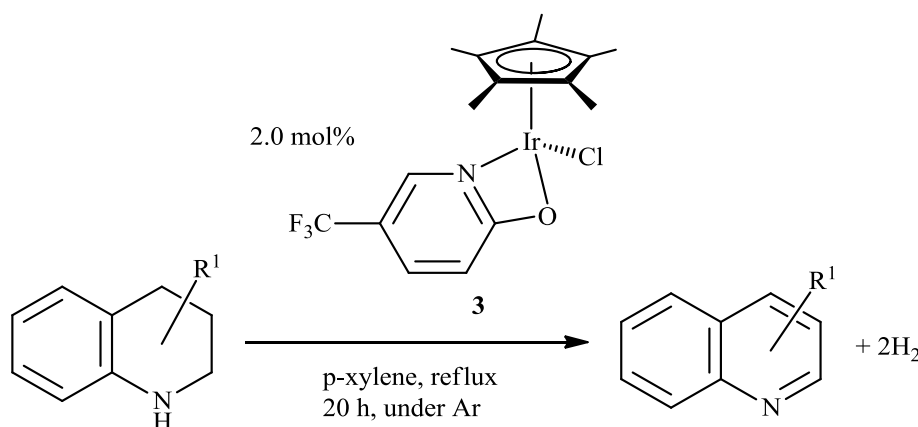


Figure 29 Dehydrogenation of 1,2,3,4-tetrahydroquinolines catalyzed by a 5-trifluoromethylpyridonate Cp*Ir complex, **3**.⁷⁵

The hydrogenation of 2-methylquinoline to the corresponding amine was achieved quantitatively using complex **3** under the same conditions as those used for the dehydrogenation reaction above, but under an atmosphere of hydrogen (Figure 30).

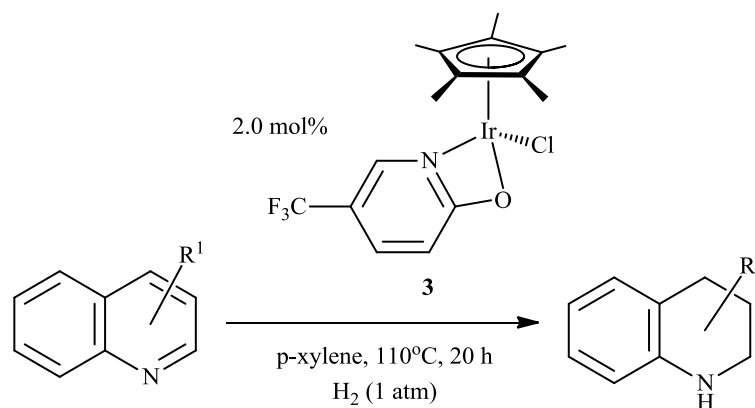


Figure 30 Hydrogenation of quinolines catalysed by complex **3**.⁷⁵

However, the pyridonate Cp*Ir complex was not found to be the common catalytic species in both the dehydrogenation and hydrogenation reactions. Instead, ¹H NMR analysis revealed that **3** was completely converted to the hydride-bridged dinuclear complex [Cp*IrHCl]₂ (**4**),⁷⁶ on reaction with gaseous H₂ at 373 K in toluene-d₈ for 5 minutes with concomitant liberation of 5-trifluoromethyl-2-hydroxypyridine in quantitative yield (Figure 31). Interestingly, heating **4** with the free ligand reformed **3** in the absence of hydrogen suggesting a reversible interconversion between **3** and **4** depending on the presence or absence of hydrogen.⁷⁵

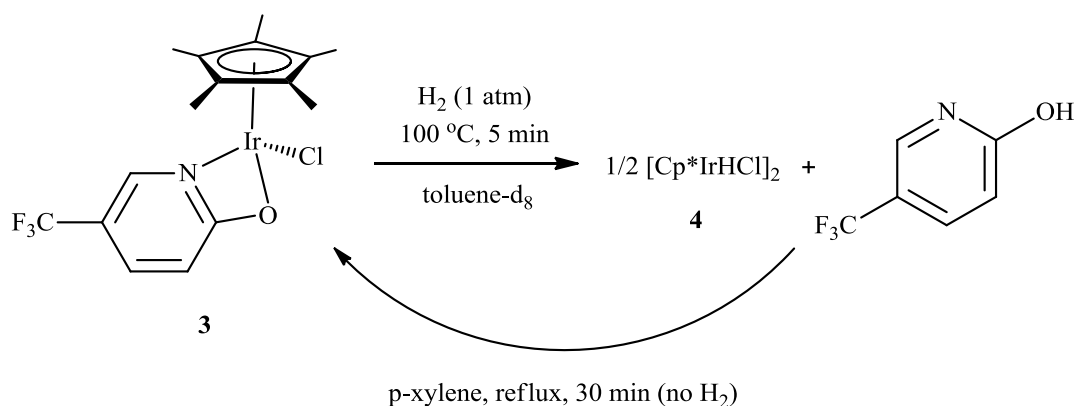


Figure 31 Formation of the hydride-bridged dinuclear Cp*Ir complex responsible for hydrogenation reaction and the formation of **3** by reaction of **4** and free ligand in the absence of hydrogen.⁷⁵

The hydrogenation of the 2-methyl substituted 1,2,3,4-tetrahydroquinoline was conducted using **4** as the catalyst and gave the amine in almost quantitative yield indicating that the catalytic species is $[\text{Cp}^*\text{IrHCl}]_2$ rather than the Cp^*Ir pyridonate complex (Figure 32).

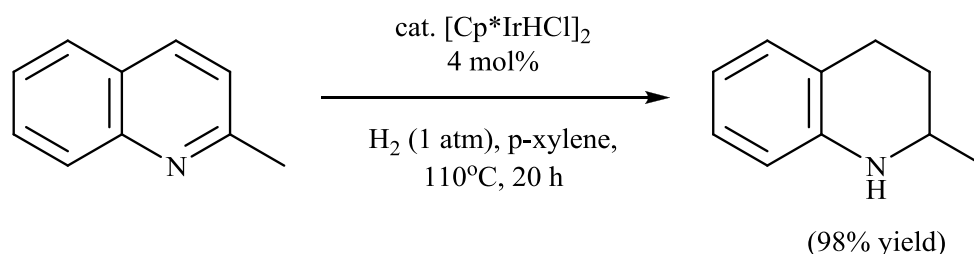


Figure 32 Hydrogenation of imine with $[\text{Cp}^*\text{IrHCl}]_2$ catalyst.⁷⁵

It is highly probable that the reversible dehydrogenation-hydrogenation reaction proceeds with reversible interconversion of catalytic species between the pyridonate Cp^*Ir complex and the hydride-bridge Cp^*Ir dinuclear complex.⁷⁵ The overall processes for the catalytic transformations are summarised in Figure 33.

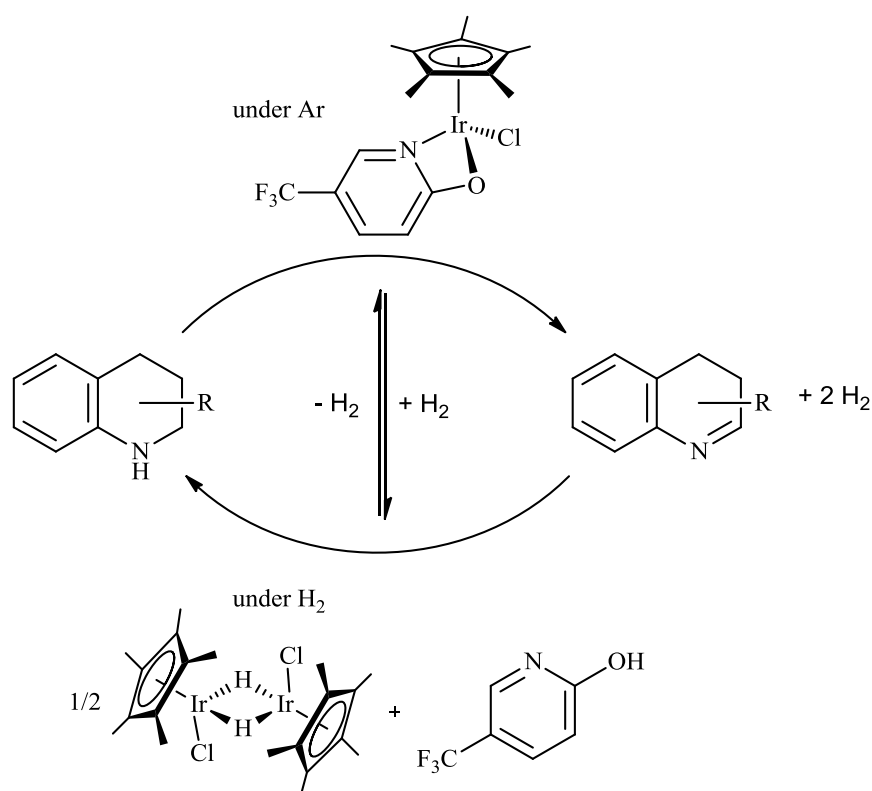


Figure 33 Overall Process for the Reversible and Repetitive Catalytic Dehydrogenation-Hydrogenation of imine using Cp^*Ir pyridinate complexes.⁷⁵

However, the selective dehydrogenation of just the C=N bond is problematic using these complexes. This is because both C-C and N-C bonds are liable to dehydrogenation. It is hard to decide whether oxidative dehydrogenation will occur at the C-C or N-C bonds, which could lead to completely different products. Calculation of the bond energy shows that the amine's dehydrogenation is found to be more thermodynamically favoured than the alkane's dehydrogenation. The large energy difference of C-N and C=N (77 kcal/mol comparing with 63 kcal/mol between C-C and C=C, and the low bond energy of N-H (93 kcal/mol comparing with 99.2 kcal/mol of C-H) make the amine dehydrogenation more favourable.

1.5 Outline of this thesis

Having provided an introduction to Chiral Asymmetric Transfer Hydrogenation, the current understanding of the mechanisms of transfer hydrogenation and transfer dehydrogenation, the rest of this thesis has been designed to develop the understanding of these powerful synthetic techniques and catalysts.

Chapter 2 describes the synthesis and characterisation of the 16-electron catalysts used for the transfer hydrogenation work in this study. A structural analysis by X-ray diffraction is supported by DFT calculations and provides an insight into the relative π -bonding abilities of the M-N bonds and other key structural features.

In Chapter 3 the 16-electron complexes isolated in the previous chapter are applied in the transfer hydrogenation of the imine substrate and differences in reactivity are discussed. This chapter also deals with the synthesis and characterisation of catalytic intermediates and includes a discussion of the mechanistic implications that arise from this study. DFT calculations on the system by Eisenstein *et al.*, are also provided to support this work.

In Chapter 4 we explore the $[\text{Cp}^*\text{Ir}(\text{I})_2]_2$ amine racemisation catalyst and key intermediates in the mechanism are observed and isolated. A method is explored to recycle the catalyst from the homogenous solution and the isolated product, $\text{Cp}^*\text{Ir}(\text{I})_2(\text{NH}_3)$ is fully characterised and its catalytic activity is compared to $[\text{Cp}^*\text{Ir}(\text{I})_2]_2$. We also look at the implications of changing variables in the system to allow transfer dehydrogenation of amines.

Chapter 5 describes a novel method for producing hyperpolarised carbon dioxide for magnetic resonance imaging purposes using the transfer hydrogenation catalysts in this study and Dynamic Nuclear Polarization (DNP) of triethylammonium formate.

Chapter 6 is a summary of the main conclusions from this work and includes suggestions for future work that could be performed. Experimental procedures are given in Chapter 7; X-ray crystallographic data tables are contained in the Appendix.

1.6 References

- 1.) P. Cintas, *Angewandte Chemie International Edition*, 2007, **46**, 4016.
- 2.) A. Lakhtakia (ed.) (1990). *Selected Papers on Natural Optical Activity* (SPIE Milestone Volume 15). SPIE.
- 3.) L. Pasteur (1848). *Researches on the molecular asymmetry of natural organic products*, English translation of French original, published by Alembic Club Reprints (Vol. 14, pp. 1-46) in 1905.
- 4.) R. Cahn, C. Ingold and V. Prelog, *Angewandte Chemie International Edition*, 1966, **5**(4), 385.
- 5.) V. Prelog and G. Helmchen, *Angewandte Chemie International Edition*, 1982, **21**(8), 567.
- 6.) A. M. Krstulovic (Ed.), *Chiral Separations by HPLC, Applications to Pharmaceutical Compounds*, Ellis Horward, 1989.
- 7.) U. J. Meierhenrich (2008) *Amino acids and the asymmetry of life*. Springer, Heidelberg, Berlin, New York, ISBN 3540768858.
- 8.) A. N. Collins and G. N. Shelldrake, J. Crosby (Ed.), *Chirality in Industry II: Developments in the Commercial Manufacture and Applications of Optically Active Compounds*, Wiley, Chichester, 1997.
- 9.) G. Blaschke, H. P. Kraft, K. Fickentscher and F. Köhler, *Arzneim.-Forsch./Drug. Res.* 1979, **29**, 1640.
- 10.) S. C. Stinson, *Chem. Eng. News* 1992, **70**(39), 46.
- 11.) (a) S. Kobayashi and H. Ishitani, *Chem. Rev.*, 1999, **99**, 1069; (b) J. M. Brunel, *Recent Res. Dev. Org. Chem.*, 2003, **7**, 155; (c) C. J. Cobley and J. P. Henschke, *Adv. Synth. Catal.*, 2003, **345**, 195; (c) S. Hashiguchi, A. Fujita, J. Takehara, T. Ikariya and R. Noyori, *J. Am. Chem. Soc.*, 1995, **117**, 7562.
- 12.) R. Noyori, *Asymmetric Catalysis in Organic Synthesis*; John Wiley & Sons: New York, 1994; Chapter 2.
- 13.) J. S. M. Samec, J. -E. Bäckvall, P. G. Andersson and P. Brandt, *Chem. Soc. Rev.*, 2006, **35**, 237.
- 14.) C. R. Graves, K. A. Scheidt and S. T. Nguyen, *Org. Lett.*, 2006, **8**(6), 1229.
- 15.) T. Ikariya, K. Murata and R. Noyori, *Org. Biomol. Chem.*, 2006, **4**, 381.

- 16.) S. E. Clapham, A. Hadzovic and R. H. Morris, *Coord. Chem. Rev.*, 2004, **248**, 2201.
- 17.) A. Basu, S. Bhaduri, K. Sharma and P. G. Jones, *Chem. Commun.* 1987, 1126.
- 18.) G. Z. Wang and J. -E. Bäckvall, *Chem. Commun.* 1992, 980.
- 19.) E. Mizushima, M. Yamaguchi and T. Yamagishi, *J. Mol. Catal. A: Chemical*, 1999, **148**, 69.
- 20.) A. Aranyos, G. Csajnyik, K. J. Kalman and J. -E. Bäckvall, *Chem Commun.*, 1999, 351.
- 21.) J. S. M. Samec and J. -E. Bäckvall, *Chem. Eur. J.* 2002, **8**, 2955.
- 22.) J. S. M. Samec, A. H. Ell and J. -E. Bäckvall, *Chem. Commun.* 2004, 2748.
- 23.) C. P. Casey and J. B. Johnson, *J. Am. Chem. Soc.*, 2005, **127**, 1883.
- 24.) J. S. M. Samec, A. H. Ell, J. B. Arberg, T. Privalov, L. Erriksson and J. -E. Bäckvall, *J. Am. Chem. Soc.* 2006, **128**, 14293.
- 25.) N. Menashe and Y. Shvo, *Organomet.* 1991, **10**, 3885.
- 26.) Y. Shvo, D. Cazarkie, Y. Rahamim and D. F. Chodosh, *J. Am. Chem. Soc.* 1986, **108**, 7400.
- 27.) J. S. M. Samec, J. Mony and J. -E. Bäckvall, *Can. J. Chem.* 2005, **83**, 909.
- 28.) J. S. M. Samec and J. -E. Bäckvall, *Chem. Eur. J.*, 2002, **8**, 2955.
- 29.) G. Z. Wang, U. Andreasson and J. -E. Bäckvall, *Chem. Commun.* 1994, 1037.
- 30.) M. L. S. Almeida, M. Beller, G. Z. Wang and J. -E. Bäckvall, *Chem. Eur. J.* 1996, **2**, 1533.
- 31.) G. Csajnyik, A. H. Ell, L. Fadini, B. Pugin and J. -E. Bäckvall, *J. Org. Chem.* 2002, **67**, 1657.
- 32.) A. H. Ell, J. B. Johnson and J. -E. Bäckvall, *Chem. Commun.* 2003, 1652.
- 33.) A. H. Ell, J. S. M. Samec, C. Brasse and J. -E. Bäckvall, *Chem. Commun.* 2002, 1144.
- 34.) A. L. E. Larsson, B. A. Persson and J. -E. Bäckvall, *Angew. Chem. Int. Edit.* 1997, **36**, 1211.
- 35.) B. A. Persson, A. L. E. Larsson, M. Le Ray and J. -E. Bäckvall, *J. Am. Chem. Soc.* 1999, **121**, 1645.
- 36.) O. Pamies, A. H. Ell, J. S. M. Samec, N. Hermanns and J. -E. Bäckvall, *Tet. Lett.*, 2002, **43**, 4699.

- 37.) C. P. Casey, S. W. Singer, D. R. Powell, R. K. Hayashi and M. Kavana, *J. Am. Chem. Soc.* 2001, **123**, 1090.
- 38.) C. P. Casey, G. A. Bikzhanova, Q. Cui and I. A. Guzei, *J. Am. Chem. Soc.* 2005, **127**, 14062 (*See also Supporting Information*).
- 39.) J. B. Johnson and J. –E Bäckvall, *J. Org. Chem.* 2003, **68**, 7681.
- 40.) J. S. M. Samec A. H. Ell and J. E. Bäckvall, *Chem. Commun.* 2004, 2748.
- 41.) C. P. Casey, G. A. Bikzhanova, J. –E. Bäckvall, L. Johansson, J. Park and Y. H. Kim, *Organometallics* 2002, **21**, 1955.
- 42.) A. Comas-Vives, G. Ujaque and A Lledós, *J. Mol. Struct.* 2009, **903**, 123.
- 43.) G. Descotes and D. Sinou, *Tetrahedron Lett.* 1976, **17**, 4083.
- 44.) K. Ohkubo, K. Hirata, K. Yoshinaga and M. Okada, *Chem. Lett.* 1976, 183.
- 45.) D. Müller, G. Umbricht, B. Weber and A. Pfaltz, *Helv. Chim. Acta.* 1991, **74**, 232.
- 46.) J. P. Genet and V. Ratovelomananavidal, C. Pinel, *Synlett* 1993, 478.
- 47.) P. Gamez, F. Fache and M. Lemaire, *Tetrahedron*, 1995, **6**, 705.
- 48.) D. A. Evans, S. G. Nelson, M. R. Gagne and A. R. Muci, *J. Am. Chem. Soc.*, 1993, **115**, 9800.
- 49.) (a) S. Hashiguchi, A. Fujii, J. Takehara, T. Ikariya and R. Noyori, *J. Am. Chem. Soc.* 1995, **117**, 7562; (b) A. Jujii, S. Hashiguchi, N. Uematsu, T. Ikariya and R. Noyori, *J. Am. Chem. Soc.* 1996, **118**, 2521; (c) J. Takehara, S. Hashiguchi, A. Fujii, S. Inoue, T. Ikariya and R. Noyori, *Chem. Commun.* 1996, 233; (d) K. J. Haack, S. Hashikuchi, A. Fujii, T. Ikariya and R. Noyori, *Angew. Chem.* 1997, **109**, 297; *Angew. Chem. Int. Ed. Engl.* 1997, **36**, 285.
- 50.) J. M. Mao and D. C. Baker, *Org. Lett.*, 1999, **1**, 841.
- 51.) US6372931, USA.
- 52.) US6545188, USA.
- 53.) S. Hashiguchi, A. Fujii, J. Takehara, T. Ikariya and R. Noyori, *J. Am. Chem. Soc.* 1995, **117**, 7562.
- 54.) D. A. Alonso, P. Brandt, S. J. M. Nordin and P. G. Andersson, *J. Am. Chem. Soc.* 1999, **121**, 9580; (b) D. G. I. Petra, J. N. H. Reek, J. W. Handgraaf, E. J. Meijer, P. Dierkes, P. C. J. Kamer, J. Brussee, H. E. Schoemaker and P. W. N. M. Van Leeuwen, *Chem. Eur. J.*, 2000, **6**, 2818; (c) M. Yamakawa, H. Ito and

- R. Noyori, *J. Am. Chem. Soc.*, 2000, **122**, 1466; (d) R. Noyori, M. Yamakawa and S. Hashiguchi, *J. Org. Chem.* 2001, **66**, 7931; (e) J. S. M. Samec, J. –E. Bäckvall, P. G. Andersson and P. Brandt, *Chem. Soc. Rev.* 2006, **35**, 237.
- 55.) S. E. Clapham, A. Hadzovic and R. H. Morris, *Coord. Chem. Rev.* 2004, **248**, 2201.
- 56.) M. Yamakawa, I. Yamada and R. Noyori, *Angew. Chem. Int. Ed.* 2001, **40**, 2818.
- 57.) T. Koike and T. Ikariya, *Adv. Synth. Catal.* 2004, **346**, 37.
- 58.) T. Koike and T. Ikariya, *J. Organomet. Chem.* 2007, **692**, 408.
- 59.) F. K. Cheang, C. Lin, F. Minissi, A. L. Criville, M. A. Graham, D. J. Fox and M. Wills, *Org. Lett.* 2007, **9**, 4659.
- 60.) J.B. Åberg, J. S. M. Samec and J. –E. Bäckvall, *Chem. Commun.* 2006, 2771.
- 61.) (a) R. M. Bullock, *Chem. –Eur. J.*, 2004, **10**, 2366; (b) M. P. Magee and J. R. Norton, *J. Am. Chem. Soc.*, 2001, **123**, 1778; (c) H. Guan, M. Iimura, M. P. Magee, J. R. Norton and G. Zhu, *J. Am. Chem. Soc.*, 2005, **127**, 7805; (d) M. Schlaf, P. Ghosh, P. J. Fagan, E. Hauptman and R. M. Bullock, *Angew. Chem. Int. Ed.*, 2001, **40**, 3887.
- 62.) J. E. D. Martins, G. J. Clarkson and M. Wills, *Org. Lett.* 2009, **11**(4), 847.
- 63.) (a) *Modern Oxidation Methods* (Ed.: J. –E. Bäckvall), Wiley-VCH, Weinheim, 2004; (b) *Industrial Organic Chemicals: Starting Materials and Intermediates, an Ullman's Encyclopedia*, Wiley-VCH, Weinheim, 1999.
- 64.) R. A. Sheldon and J. K. Kochi, *Metal Catalyzed Oxidations of Organic Compounds*, Academic Press, New York, 1981.
- 65.) J. S. M. Samec, A. H. Éll and J-E. Bäckvall, *Chem. Eur. J.*, 2005, **11**, 2327.
- 66.) N. Uematsu, A. Fujii, S. Hashiguchi, T. Ikariya and R. Noyori, *J. Am. Chem. Soc.* 1996, **118**, 4916.
- 67.) A. Córdova, *Acc. Chem. Res.* 2004, **37**, 102.
- 68.) (a) R. M. Williams and J. A. Hendrix, *Chem. Rev.* 1992, **92**, 889; (b) S. –I. Murahashi, N. Komiya, H. Terai and T. Nakae, *J. Am. Chem. Soc.* 2003, **126**, 15312.
- 69.) W. J. Drury, D. Ferraris, C. Cox, B. Young and T. Lectka, *J. Am. Chem. Soc.* 1998, **120**, 11006.

- 70.) J. S. Sandhu and B. Sain, *Heterocycles*, 1987, **26**, 777.
- 71.) (a) M. Shi and Y. -M. Xu, *Angew. Chem.* 2002, **114**, 4689; (b) D. Balan and H. Adolfsson, *J. Org. Chem.* 2002, **67**, 2329; (c) D. Balan and H. Adolfsson, *J. Org. Chem.* 2001, **66**, 6498.
- 72.) K. Hattori and H. Yamamoto, *J. Org. Chem.* 1992, **57**, 3264.
- 73.) J. S. M. Samec, A. H. Éll and J-E. Bäckvall, *Chem. Eur. J.*, 2005, **11**, 2327.
- 74.) K. Fujita, N. Tanino and R. Yamaguchi, *Org. Lett.* 2007, **9**, 109.
- 75.) R. Yamaguchi, C. Ikeda, Y. Takahashi and K. Fujita, *J. Am. Chem. Soc.*, 2009, **131**, 8410.
- 76.) D. S. Gill and P. M. Maitlis, *J. Organomet. Chem.*, 1975, **87**, 359.

SYNTHESIS AND STRUCTURE OF 16-ELECTRON Cp*Rh(III) AND Cp*Ir(III) COMPLEXES FOR TRANSFER HYDROGENATION

2.1 Introduction

Many group 8 and 9 metal catalysts for transfer hydrogenation and heterolytic hydrogenation incorporate amido ligands that are capable of metal-nitrogen π -bonding.^{1,2,3} 18-electron half-sandwich Cp*Rh(III) and Cp*Ir(III), (Cp* = η^5 -C₅Me₅) complexes with monotosylated amine or amino-alcohol ligands are examples that are used extensively as catalysts for the asymmetric transfer hydrogenation (ATH) of ketones and imines (Figure 1).

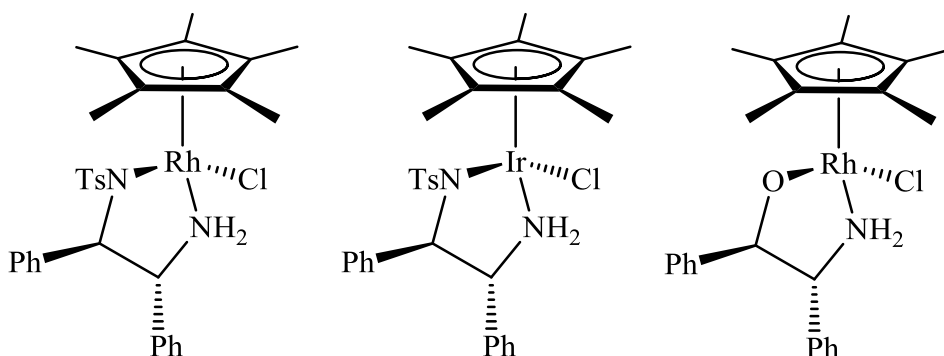


Figure 1 Cp*Rh and Cp*Ir complexes with amine or amino-alcohol ligands capable of π -bonding for ATH of ketones and imines, when HCl is eliminated.

In their base activated form, these catalysts have 16-electron configurations. In previous studies, Noyori isolated and characterised, by X-ray crystallography, all three intermediates operating for the [(*p*-cymene)RuCl(TsNCHPhCHPhNH₂)] system, including the 18-electron chloride precursor (A), the 16-electron amido complex (B) and the 18-electron hydride complex (C) which all reduce acetophenone with comparable activity and selectivity (Figure 2).⁴

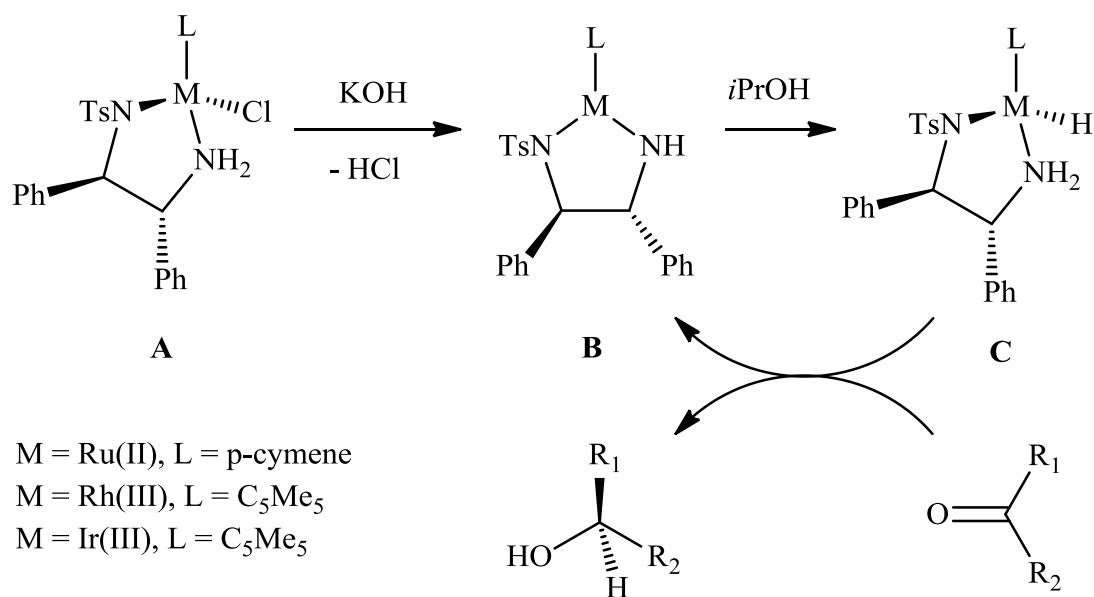


Figure 2 “Outer-sphere” bifunctional catalysis mechanism using 18-electron half-sandwich complexes. Complex B is capable of metal-nitrogen π -bonding.

Attempts to extend the approach to the Cp*Rh(III) catalyst gave a deep green product identified as the 16-electron complex Cp*Rh(TsNCHPhCHPhNH); its isolation and characterisation, including obtaining an X-ray crystallography structure, has proven difficult due to air and water instability in solution.⁵

2.1.1 16-electron Cp*Rh(III) and Cp*Ir(III) air and water stable complexes

In 1979, Maitlis *et al.* demonstrated that the reaction of catechol, *o*-aminophenol and *o*-phenylenediamine with [Cp*RhCl₂]₂ in aqueous base formed air-stable complexes with formally 16-electron configurations (Figure 3).⁶ These complexes display strong colours arising from ($\pi \rightarrow d$) ligand-to-metal charge transfer bands in the visible part of the spectrum. For the catecholate complex, the change in bond distances $r(\text{O1-C11})$, $r(\text{O2-C16})$ and $r(\text{C11-C16})$ with respect to the free ligand are insignificant. These structural parameters indicate that the Rh is in the +3 oxidation state.⁶ Interestingly, the mutually perpendicular views of the crystal structure of Cp*Rh(OC₆H₄O) in Figure 4 show that the O-Rh-O plane and the Rh-Cp* vector are almost co-planar. Similarly, Ko *et al.* demonstrated that [Cp*IrCl₂]₂ reacts with *o*-

phenylenediamine and triethylamine to form 16-electron bis(amido) Cp*Ir(HNC₆H₄NH).⁷ The complexes with O donor groups form adducts with phosphines, but the NH counterparts are less reactive which indicates that the NH group is a better ligand to the rhodium centre and forms a stronger bond.

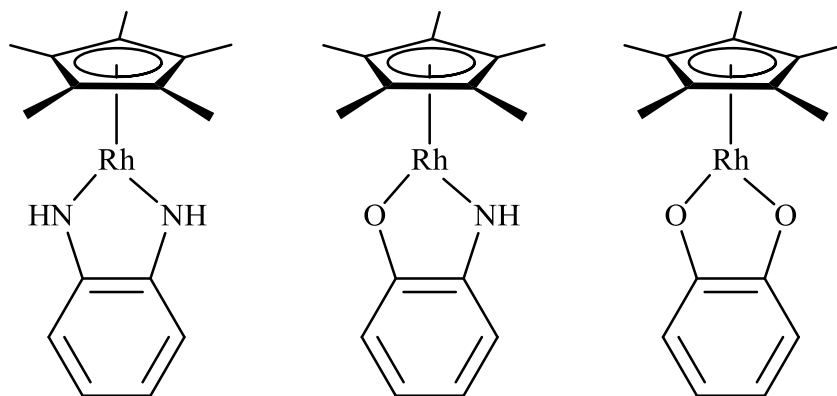


Figure 3 Three complexes first prepared by Maitlis with formally 16-electron configurations: (left) Cp*Rh(HNC₆H₄NH); (middle) Cp*Rh(OC₆H₄NH); (right) Cp*Rh(OC₆H₄O).

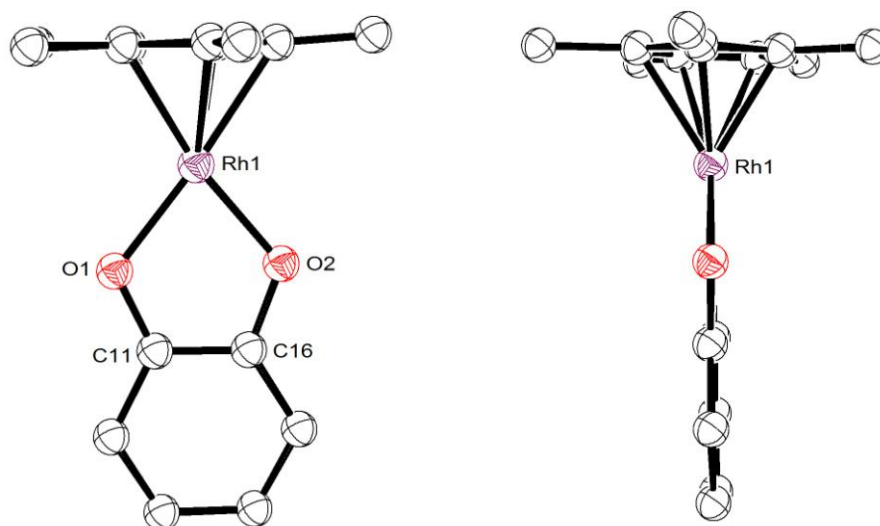


Figure 4 Two mutually perpendicular views of the molecular structure of Maitlis' Cp*Rh(OC₆H₄O) complex.⁶

2.1.2 Grace's complex, Cp*Rh(TsNC₆H₄NH) which is catalytically active

In 2006, Grace synthesised the air and water-stable 16-electron complex, Cp*Rh(TsNC₆H₄NH), using *N*-tosyl-*o*-phenylenediamine in place of the familiar TsNCHPhCHPhNH₂ (TsDPEN) series of ligands (Figure 5).⁸ This is in contrast to Noyori-type rhodium complexes which are only stable as the 18-electron precursor species.^{3,4} Furthermore, this complex was found to be catalytically active for the (non-stereo specific) transfer hydrogenation of the cyclic imine, 6,7-dimethoxy-1-methyl-3,4-dihydroisoquinoline using 2:5 triethylamine:formic acid (TEAF) in methanol-d₄.⁹ The crystal structure of this complex showed a marked asymmetry between the Rh-NH (1.9372(15) Å) and Rh-NTs (2.0796(14) Å) bond lengths (difference 0.1424(10) Å) owing to the electron withdrawing effect of the tosyl protecting group.

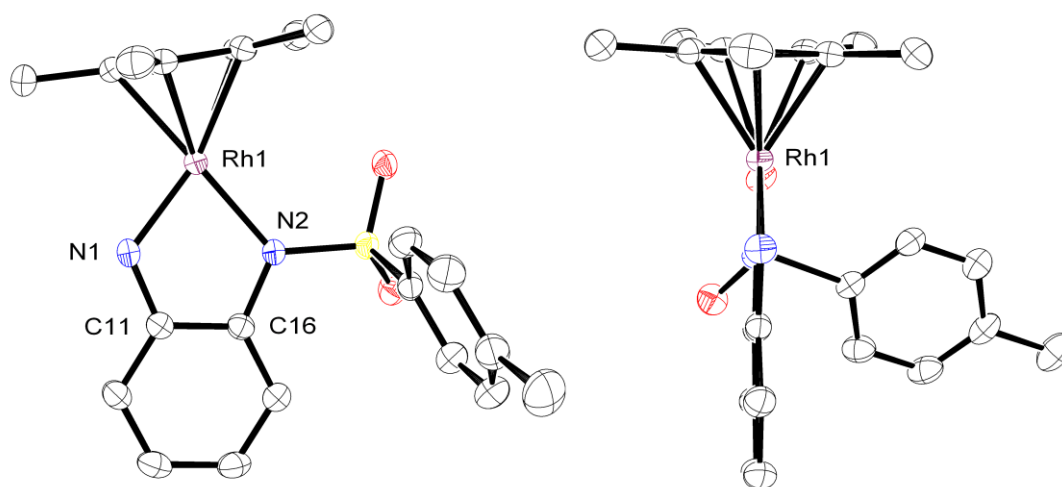
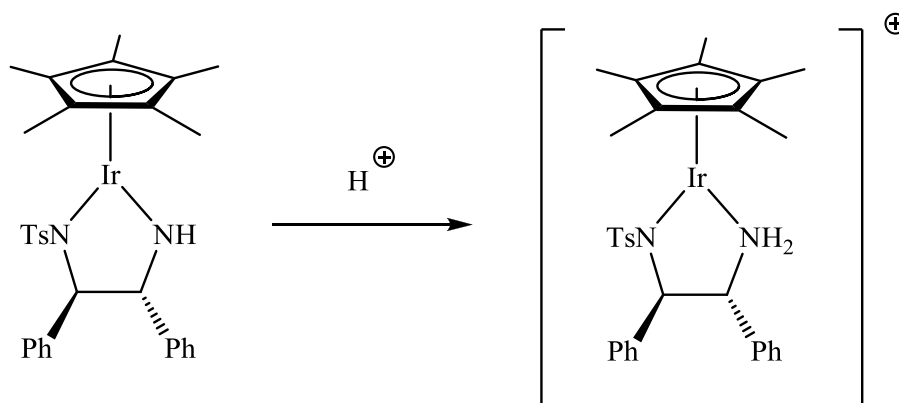


Figure 5 X-ray structure of Cp*Rh(TsNC₆H₄NH), a complex which catalyses the transfer hydrogenation of imines.

2.1.3 Evidence of redirection of π -bonding from M-NH and M-NTs groups

Rauchfuss has also previously reported that when one of the NH groups is tosylated, the bonding of the NTs and NH groups may be significantly different (where Ts = SO₂Tol). Protonation of Cp*Ir(TsNCHPhCHPhNH) at the NH group results in elongation of the Ir-NH bond by about 0.2 Å and contraction of the Ir-NTs bond by about 0.1 Å, indicating a redirection of π -bonding from one nitrogen to the other nitrogen (Figure 6). Upon binding of Lewis bases to the metal atom of the protonated 16-electron form, the Ir-NTs bond lengthens and the acidity of the amine decreases by about 3 pH units.¹⁰



	Cp*Ir[TsNCHPhCHPhNH]	Cp*Ir[TsNCHPhCHPhNH ₂] ⁺
Ir-Cp*(centroid)	1.794(6)	1.782(6)
Ir-N(1)Ts	2.058(5)	1.984(4)
Ir-N(2)H _x (x = 1, 2)	1.901(5)	2.096(5)

Figure 6 Rauchfuss' work shows the protonation of the 16-electron complex, Cp*Ir(TsNCHPhCHPhNH) at the NH group significantly changes the bonding between the iridium, NTs and NH groups.

2.1.4 Related 16-electron complexes stabilised by π -donation

Related M-O bonds are also proposed to be stabilised by π -donation. Bergman reported pinocolate complexes Cp*M(OCMe₂CMe₂O) (M = Rh, Ir) that may also be stabilised by significant π -donation from the oxygen to the metal centre.¹¹ Bergman attempted to prepare 18-electron adducts by reacting the isolated pinocolate complexes with phosphines but this led to their decomposition. This instability is consistent with favourable π -donation in the parent pinocolates, which is replaced by destabilising d π -p π repulsion in the adduct (Figure 7).¹²

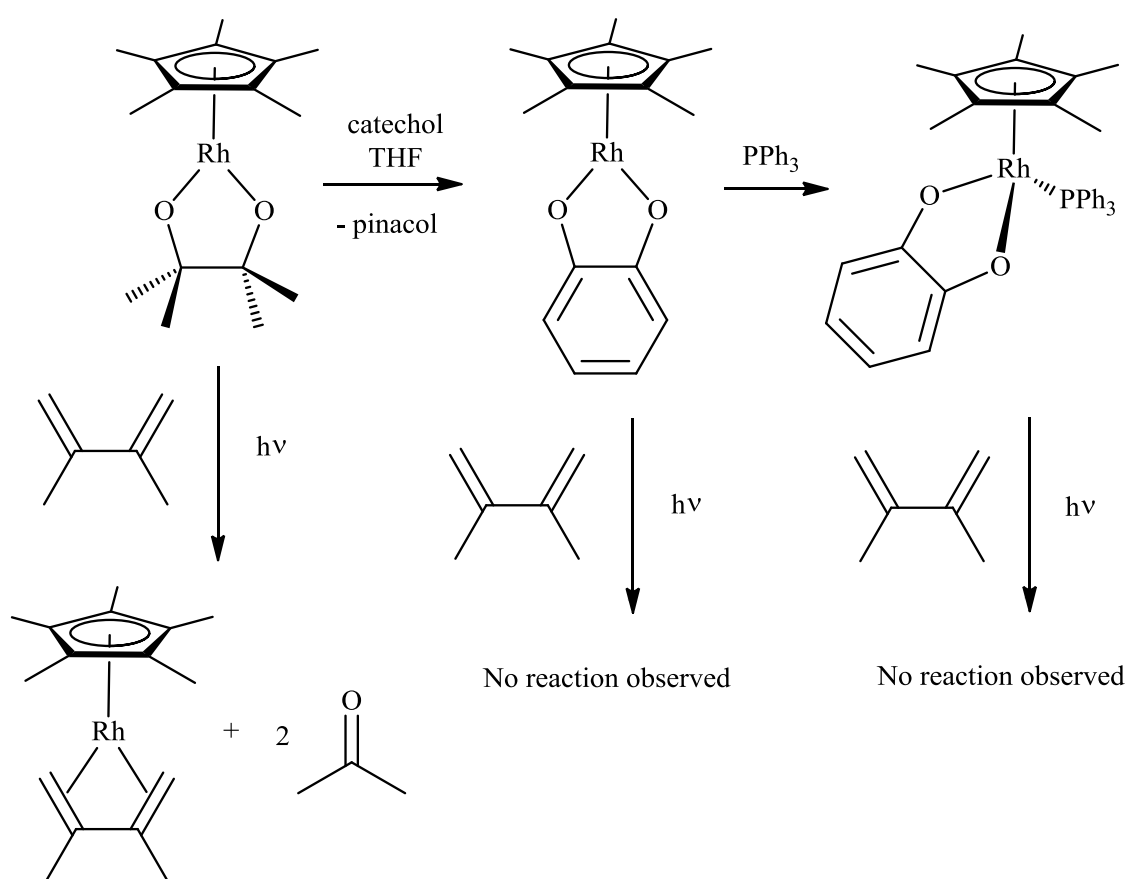


Figure 7 Cp*Rh(pin) complex and associated reactivity with catechol and 2,3-dimethylbutadiene. No reaction observed between Cp*Rh(OC₆H₄O) and 2,3-dimethylbutadiene, highlighting the stability of this 16-electron catecholate complex.

2.1.5 π -stabilised unsaturation

Compounds of the type $[\text{Cp}^*\text{RuCl}(\text{PR}_3)]$ are well established as reactive intermediates in dissociative phosphine-exchange reactions.¹³ The isolation of 16-electron complexes such as $[\text{Cp}^*\text{RuCl}(\text{PR}_3)]$ can be achieved by using bulky phosphine ligands as only bulky phosphines with a sufficiently large cone angle can allow the isolation of these 16-electron complexes.^{14,15,16} Another requirement for the stabilization of $\text{Cp}^*\text{RuX}(\text{PR}_3)$ complexes is the presence of π -electrons at the X ligand, since π -donation by lone pairs mitigates the coordinative unsaturation which would be present if the X-ligand were a pure σ -donor (Figure 8).¹ The authors coined a name for this effect, π -stabilised unsaturation. For this reason, these compounds have been referred to as *operationally* unsaturated, rather than coordinatively unsaturated.^{1,12}

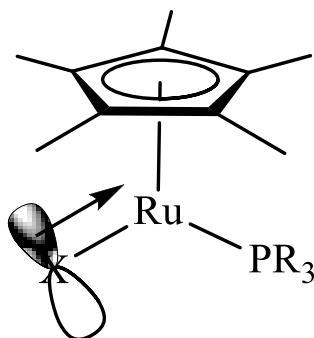


Figure 8 π -donation at the X-ligand by lone pairs mitigates the coordinative unsaturation.

Eisenstein *et al.* investigated the reason why compounds of the type Cp^*RuLX have a mirror-symmetric structure with Ru, L, X and the Cp^* centre coplanar.¹⁵ They showed that a Ru-X partial π -bond raises the LUMO energy level, increasing the HOMO-LUMO energy gap and thus disfavoring pyramidalization at the metal center. Their calculations of the behaviour of systems with X = pure σ -donor, π -donor and π -acceptor support these conclusions. Interestingly, the LUMO of Cp^*RuLX still lies low enough to give visible colour and to allow rapid addition of ‘small’ Lewis bases. In the presence of π -acceptor ligands, $\text{ML}_5 d^6$ complexes are known to have a square-pyramidal structure. Thus when Cp occupies three facial sites of a square pyramid, the metal is predicted to be pyramidal, A, e.g. $\text{CpMn}(\text{CO})_2$

(Figure 9).¹⁷ The angle between the plane L-M-X and the M-Cp vector is defined as θ , C (Figure 10). In this case, the angle between the plane L-Ru-X was found to have a bent structure with $\theta = 160^\circ$.

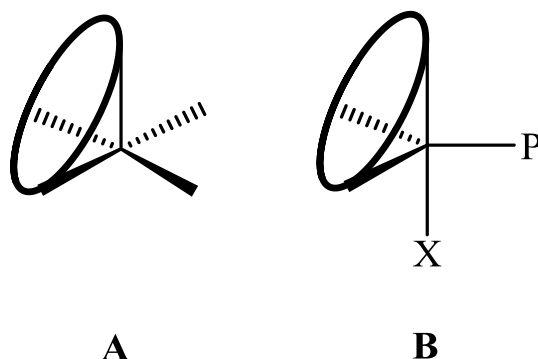


Figure 9 Pyramidal and distorted trigonal bipyramidal structure.

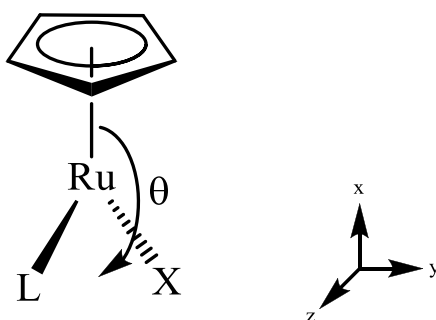


Figure 10 Angle between plane L-Ru-X and the Ru-Cp center

In contrast, ML_4X d^6 configurations, where X is a π -donor ligand are predicted to adopt a distorted trigonal bipyramidal structure with an M-X multiple bond and no stereochemically-active empty orbital. In this case, the Cp replaces three fac ligands and a planar structure is observed (**B**, Figure 9). Furthermore, Eisenstein used Extended Hückel Theory (EHT) calculations to examine the stability of $CpRuL_2$ complexes when RuL_2 was bent from the planar conformation towards the pyramidal structure. Thus, in the case of **B**, $\theta = 180^\circ$, whereas **A** $\neq 180^\circ$. As shown in Figure 11, the metal was calculated to remain planar for $CpRu(PH_3)I$ and $CpRu(PH_3)(OH)$. The calculations show there is a stronger preference for $CpRu(PH_3)I$ and $CpRu(PH_3)(OH)$ to be planar compared to $[CpRuH_2]^-$. This demonstrates that the

presence of π -donor ligands increases the preference for a planar structure over that of a σ -ligand.

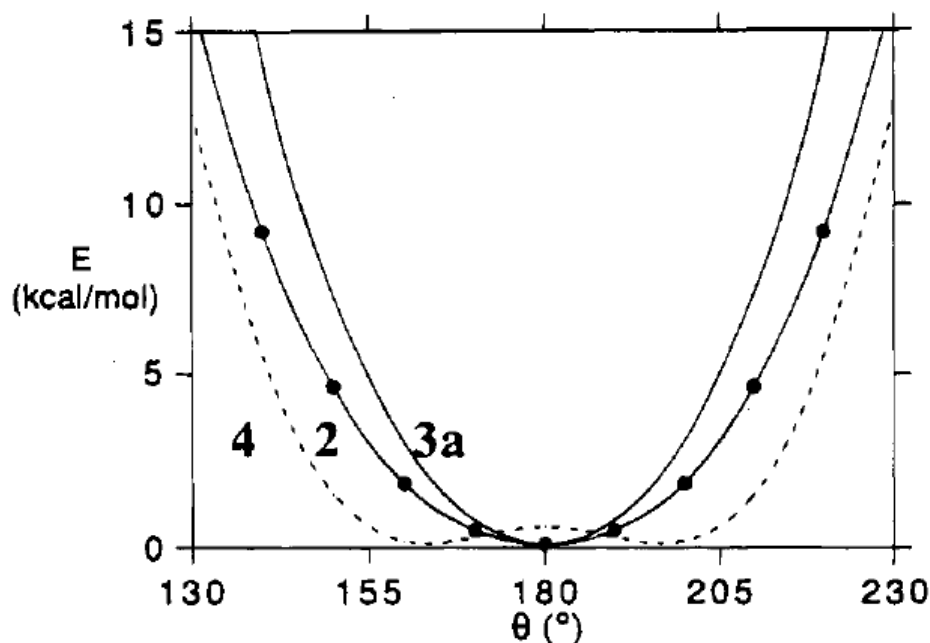


Figure 11 Total energy curves calculated by Eisenstein *et al.* for $[\text{CpRuH}_2]^-$ (**2**), $[\text{CpRu}(\text{PH}_3)\text{I}]$ (**3a**) and $[\text{CpRu}(\text{CO})_2]^+$ (**4**).¹⁵

2.1.6 Aims of the chapter

The main aim of this chapter is to synthesise and characterise a library of 16-electron complexes of the type, $\text{Cp}^*\text{M}(\text{XNC}_6\text{H}_4\text{NX}')$ (where $\text{M} = \text{Rh}, \text{Ir}$ and $\text{X}, \text{X}' = \text{H}, \text{Ts}$) and investigate in greater detail their structural features in order to gain a deeper understanding of the importance of π -bonding and deduce mechanistic implications from the study. The work is also supported then by DFT(B3PW91) calculations on these systems by Eisenstein *et al.*

2.2 Results and Analysis

2.2.1 Synthesis of monosulfonylated *o*-phenylenediamine (OPDA) ligands

The previously reported method for the synthesis of monotosylated *o*-phenylenediamine ligands was attempted initially but the reaction of *o*-phenylenediamine with tosyl chloride in the presence of triethylamine using dichloromethane as the solvent resulted in a very low yield (<30%) of pure compound. The reaction of 4,5-disubstituted *o*-phenylenediamine ligands with *p*-toluenesulfonyl chloride in the presence of triethylamine using dichloromethane as the solvent and micro-wave assistance also resulted in very low yield (< 10%) of the pure monotosylated compound and a high level of disubstituted unwanted product.⁹ A suitable process was developed for the synthesis of *unreported* monotosylated 4,5-disubstituted *o*-phenylenediamine ligands based on that reported by van Leeuwen *et al.* 2007 (Figure 12).¹⁸

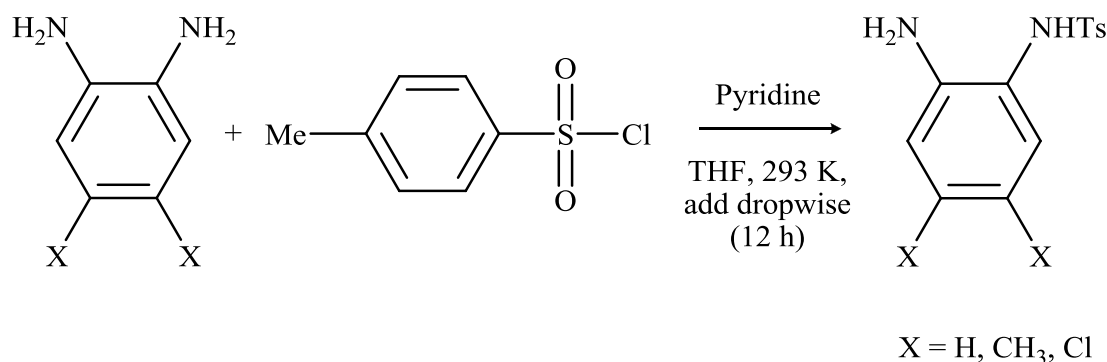


Figure 12 Synthesis of *N*-tosyl-1,2-diaminobenzene (X = H) and 4,5-disubstituted *o*-phenylenediamine ligands (X = Cl and CH₃)

To a stirred solution of the appropriate *o*-phenylenediamine ligand and pyridine in THF at 293 K, was added a solution of *p*-toluenesulfonyl chloride (0.25 equivalents) in THF over a period of 12 hours. The solution was stirred until the reaction was complete (followed by ¹H NMR) and the solvent was evaporated *in vacuo*. After workup (see experimental section), the product was crystallised using dichloromethane and pentane at 248 K. Using this method, *N*-tosyl-1,2-

diaminobenzene (X = H), 4,5-dimethyl (X = CH₃) and 4,5-dichloro ligands (X = Cl) were prepared in 82%, 68% and 53% yields, respectively. They have been characterised by ¹H and ¹³C NMR spectroscopy, KBr-IR and ESI mass spectrometry. Full details of NMR characterisation can be found in the NMR data section at the end of this chapter. The ¹H NMR spectra (500 MHz, CDCl₃, 300 K) of *N*-tosyl-1,2-diaminobenzene, 4,5-dimethyl-*N*-tosyl-1,2-diaminobenzene and 4,5-dichloro-*N*-tosyl-1,2-diaminobenzene are shown (Figure 13).

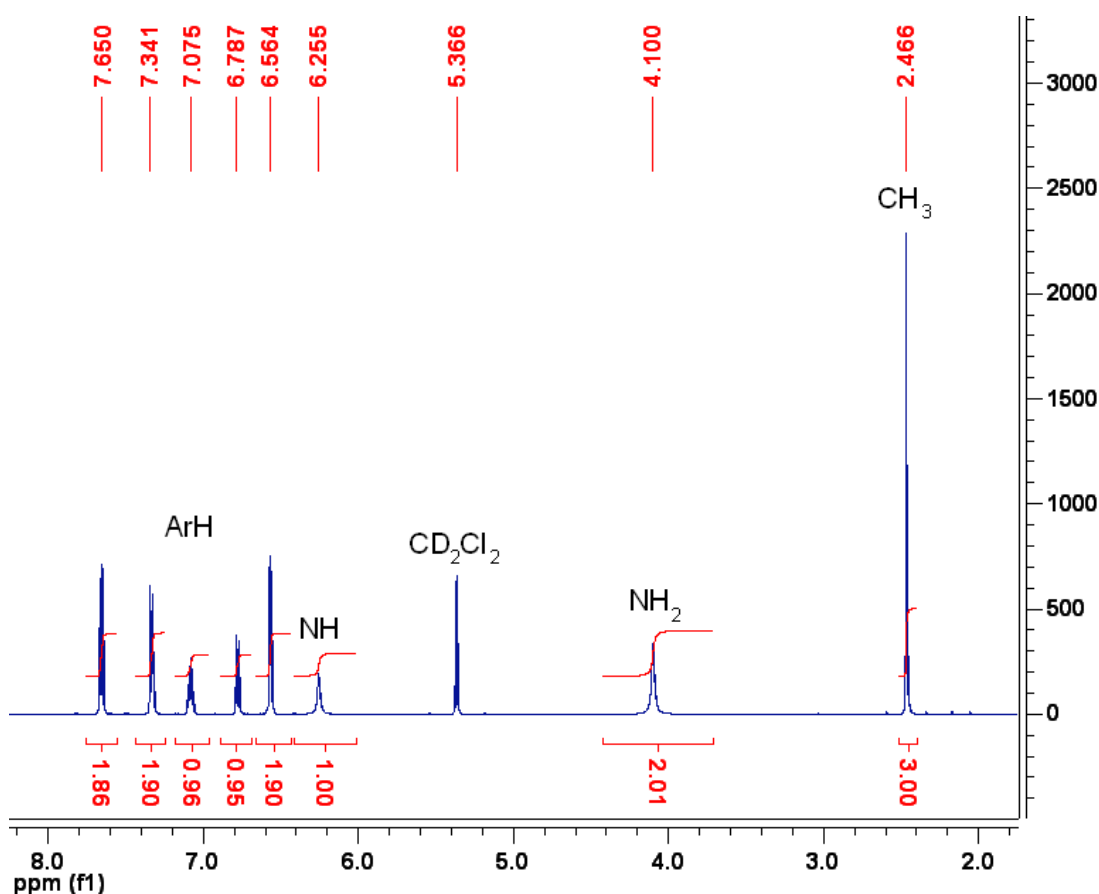
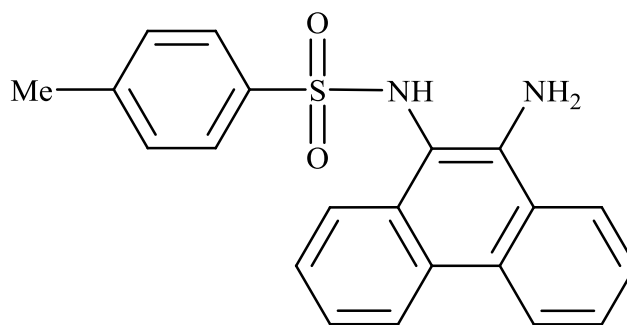
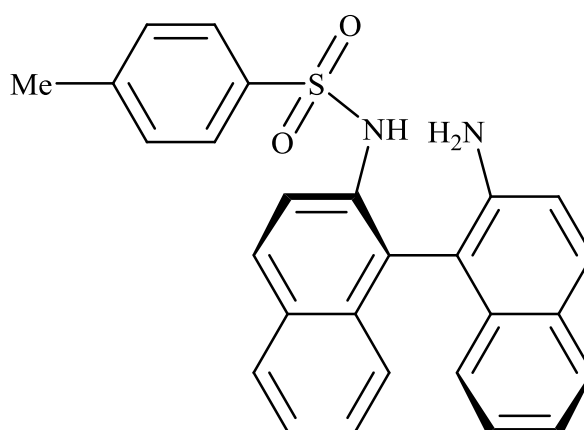


Figure 13 ¹H NMR spectrum (500 MHz, CDCl₃, 300 K) of *N*-tosyl-1,2-diaminobenzene

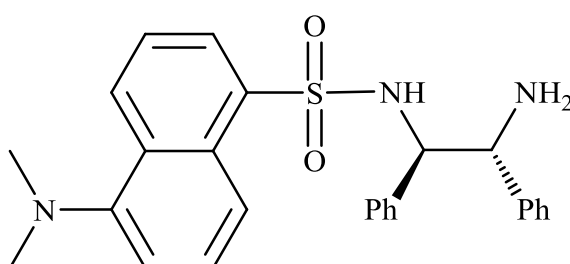
Each spectrum shows peaks consistent with the NH and NH₂ protons, the *p*-toluenesulfonyl aromatic protons and the *o*-phenylenediamine aromatic protons. Other tosylated ligands, which could be of interest for future studies, have been synthesised using this method as shown in Figure 14.



N-(10-aminophenanthren-9-yl)-4-methylbenzenesulfonamide



(R)-N-(2'-amino-1,1'-binaphthyl-2-yl)-4-methylbenzenesulfonamide



N-((1R,2R)-2-amino-1,2-diphenylethyl)-5-(dimethylamino)naphthalene-1-sulfonamide

Figure 14 Other mono-tosylated ligands synthesised during this study.

2.2.2 Synthesis of disulfonylated *o*-phenylenediamine (OPDA) ligands

In order to investigate the effect of two tosyl electron withdrawing groups on the electronic interactions of the nitrogen atoms with the rhodium centre, a disulfonylated *o*-phenylenediamine ligand was prepared using a development on the method from the previous section. Two equivalents of *p*-toluenesulfonyl chloride were reacted with the *o*-phenylenediamine ligand (Figure 15), the reaction was moderately exothermic. After removal of the solvent, the oil was dissolved in hot ethanol and allowed to cool overnight. This afforded a white solid, which was subsequently recrystallised using a supersaturated solution of ethyl acetate and layering with hexane to afford white crystals. The product was characterised by ^1H and ^{13}C NMR Spectroscopy and ESI mass spectrometry. Using this method it was also possible to form novel bistosylated ligands that maybe of interest such as ditosyl-9,10-diaminophenanthrene (see X-ray crystallography structure, Figure 16).

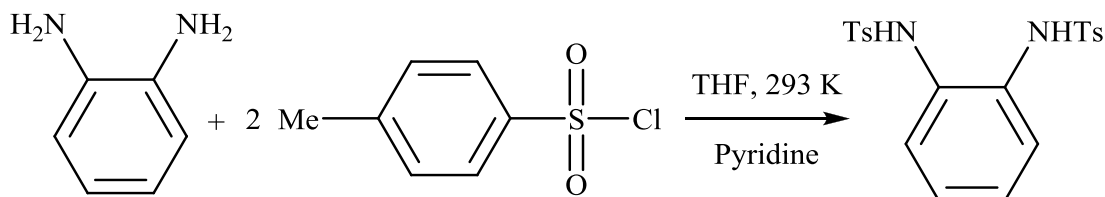


Figure 15 Synthesis of ditosylbenzene-1,2-diamine ligand.

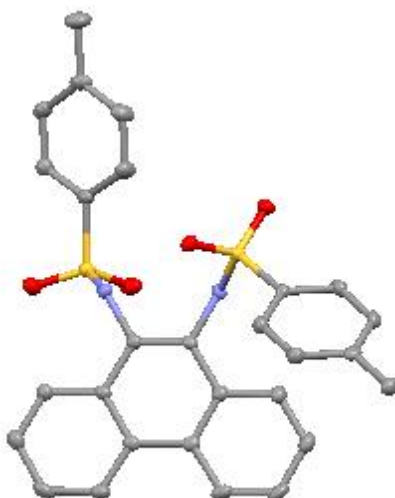


Figure 16 X-ray structure of ditosyl-9,10-diaminophenanthrene

2.2.3 Synthesis of “16-electron” rhodium and iridium(III) complexes

The 16-electron complexes Cp*Rh(TsNC₆H₄NH) (**1a**), Cp*Rh(TsNC₆H₄NTs) (**1b**), Cp*Ir(TsNC₆H₄NH) (**1d**) and Cp*Ir(TsNC₆H₄NTs) (**1e**) were prepared by treatment of [Cp*MCl₂]₂ with TsNHC₆H₄NH₂ or TsNHC₆H₄NHTs and triethylamine in dichloromethane at room temperature (Figure 17). The violet-blue air-stable rhodium products were recrystallised from dichloromethane/hexane for **1a** and from dichloromethane/methanol for **1b**. The iridium complexes are dark red air-stable products and were recrystallised from a supersaturated solution of hot toluene for **1d** and from dichloromethane/methanol for **1e**. Cp*Rh(HNC₆H₄NH) (**1c**) was prepared using the literature method and was recrystallised from toluene/pentane.⁶ These complexes were characterised by ¹H, ¹³C and ¹⁰³Rh NMR, ESI-MS, IR-KBr, UV-visible spectroscopy, CHN elemental analysis and X-ray crystallography.

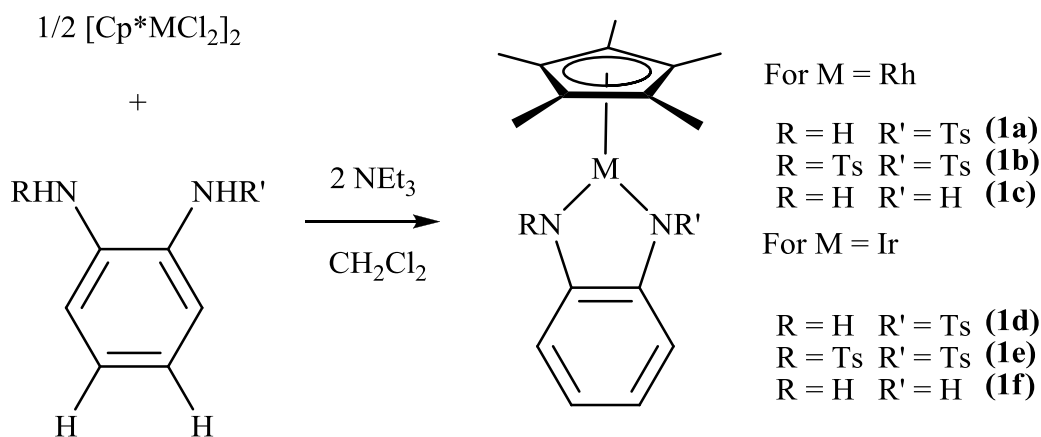


Figure 17 Synthesis of complexes **1a-1e** with formal 16e configurations.

The ¹H NMR spectra of **1a** and **1c** (dichloromethane-d₂) show broad singlets at δ 8.25 and 8.26, respectively, for the NH proton, consistent with the literature values of other related complexes (Figure 18).^{7,19,20} In methanol-d₄, the NH peak disappeared confirming the Brønsted basicity of the nitrogen. A 1-D NOESY experiment for **1a** and **1d** showed interaction between the Cp* methyl and the NH protons, confirming their proximity. ¹H/¹⁰³Rh HSQC experiments on **1a** and **1b** (chloroform-d) revealed cross peaks between the Cp* methyl protons and rhodium centres at δ 2063 (**1a**, Figure 19) and 1743, respectively. The ¹⁰³Rh chemical shifts of

16-electron **1a** and **1b** are more deshielded than that of the 18-electron chloride Cp*RhCl(TsNCHPhCHPhNH₂) we recorded previously ($\delta_{\text{Rh}} = 2551$).²¹

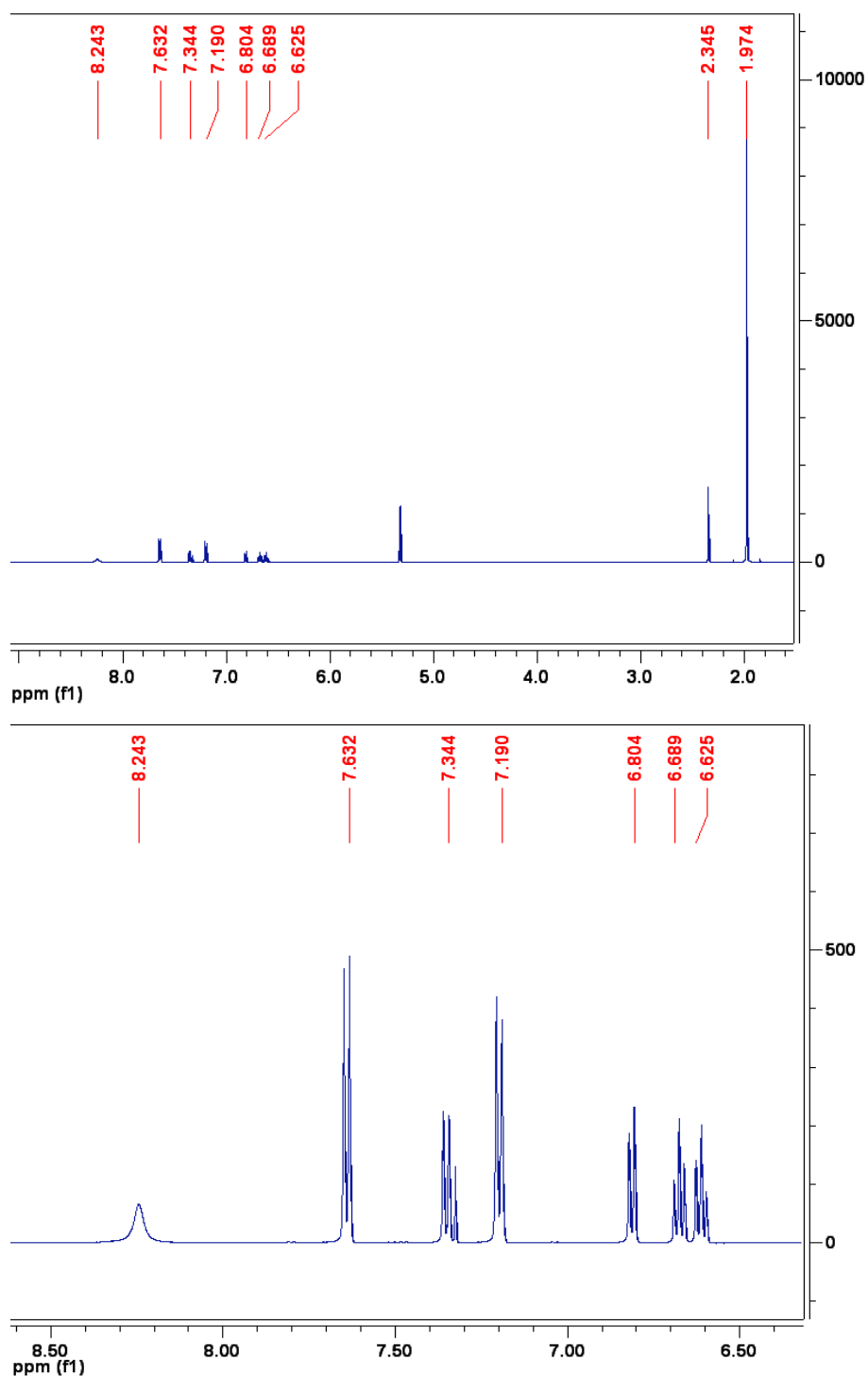


Figure 18 ¹H NMR spectrum of **1a**, Cp*Rh(TsNC₆H₄NH) in dichloromethane-d₂

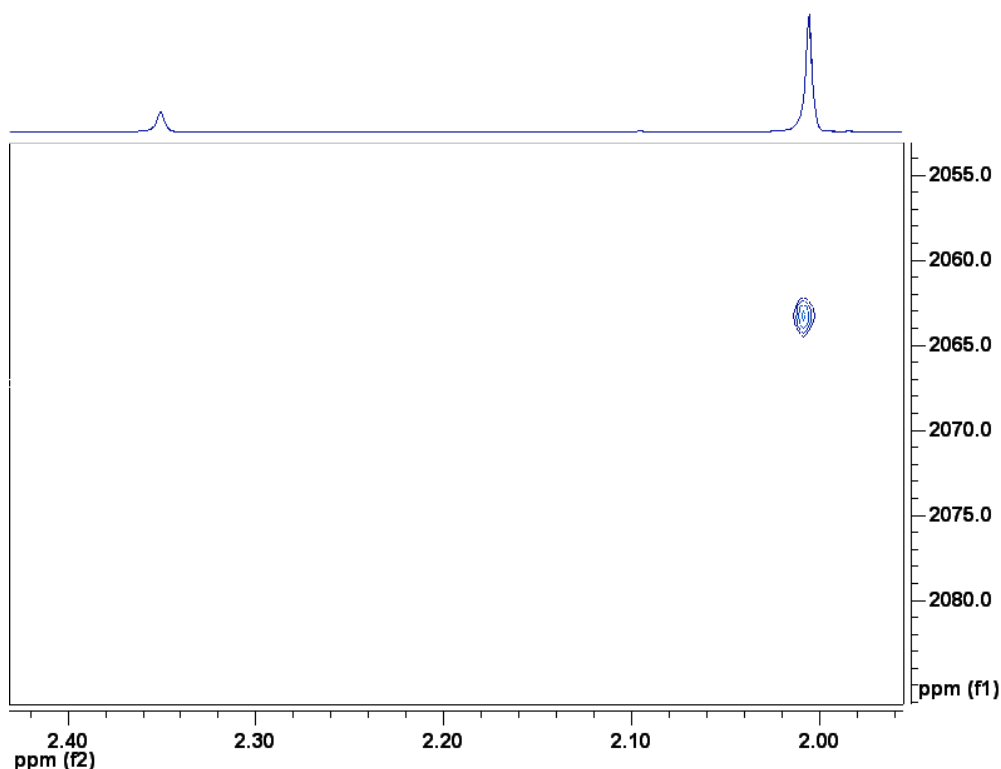


Figure 19 $^1\text{H}/^{103}\text{Rh}$ HSQC data for **1a**, $\text{Cp}^*\text{Rh}(\text{TsNC}_6\text{H}_4\text{NH})$ in chloroform-d ($\delta_{\text{Rh}} = 2063$ ppm).

The IR spectrum of **1a** shows an NH stretching band at 3318 cm^{-1} comparable to those of **1c** at 3322 and 3346 cm^{-1} and other related amido complexes.^{7,22,23}

Transitions from one electronic state to another can occur upon absorption of a photon. The energy range for these types of transition fall in the ultraviolet and visible range of the electromagnetic spectrum. The most intense type of metal-based transitions are charge transfer transitions. In a typical metal-to-ligand charge transfer transition (MLCT), an electron of one of the metal orbitals is transferred to a π^* orbital of one of the ligands on the metal. If the metal has unoccupied d-orbitals, a transfer from an orbital on the ligand to the metal is also possible, this is called ligand-to-metal charge transfer (LMCT). **1a** and **1b** display strong violet-blue colours which can be attributed to $\pi(\text{N}) \rightarrow \text{d}$ LMCT bands in the visible spectrum (Figure 20 and Table 1) (dichloromethane, $\lambda_{\text{max}}/\text{nm}$, ($\epsilon/\text{mol}^{-1}\text{ dm}^3\text{ cm}^{-1}$) **1a** 578 (7300); **1b** 554 (7400); **1c** 525 (19900)). There were no major changes in λ_{max} in

dichloromethane, methanol, or tetrahydrofuran but λ_{\max} of **1a** is shifted to slightly higher energy in acetonitrile thereby confirming a lack of solvent coordination.

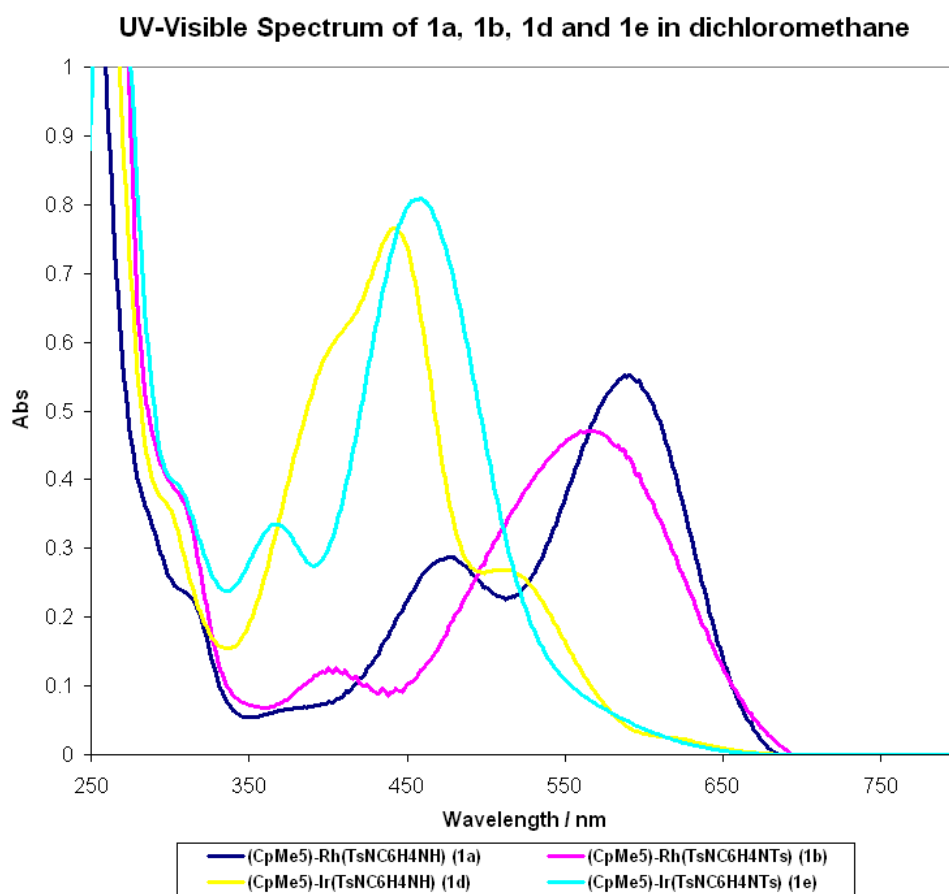


Figure 20 UV-visible spectra of complexes **1a**, **1b**, **1d** and **1e**.

	$\lambda_{\max} / \text{nm}$	$\epsilon / \text{mol}^{-1} \text{dm}^3 \text{cm}^{-1}$
Cp*Rh(TsNC ₆ H ₄ NH) (1a)	578	7300
Cp*Rh(TsNC ₆ H ₄ NTs) (1b)	554	7400
Cp*Rh(HNC ₆ H ₄ NH) (1c)	525	19900
Cp*Ir(TsNC ₆ H ₄ NH) (1d)	430	10975
Cp*Ir(TsNC ₆ H ₄ NTs) (1e)	446	8100

Table 1 UV-visible data values for **1a-1e**.

2.2.4 Molecular Orbital (MO) analysis of “16-electron” Cp*Rh(HNC₆H₄NH) and Cp*Rh(HNCHPhCHPhNH) complexesⁱ

Eisenstein *et al.* analysed the molecular orbital interactions made with the most symmetric system, Cp*Rh(HNC₆H₄NH), **1c** and a non-tosylated complex, Cp*Rh(HNCHPhCHPhNH) related to the 16-electron intermediate of the well-established ATH catalyst, Cp*RhCl(TsNCHPhCHPhNH₂). These complexes have symmetry C_{2v} and C₂, respectively. The ligand of **1c**, HNC₆H₄NH has two N lone pairs that combine with the π -orbitals of benzene leading to orbitals of a₂ and b₁ symmetry. Figure 21 shows schematically this interaction. The in phase combination of N lone pairs (N¹+N²) interacts with the benzene orbitals of b₁ symmetry; while the out of phase combination of N lone pairs (N¹-N²) interacts with those with a₂ symmetry. Consequently the orbitals b₁ and a₂ of the HNC₆H₄NH ligand are separated in energy being that b₁ is significantly lower in energy than a₂. Whereas, in the HNCHPhCHPhNH ligand there is no such interaction and the in-phase (b symmetry) and out-of phase (a symmetry) combination of N are degenerate.

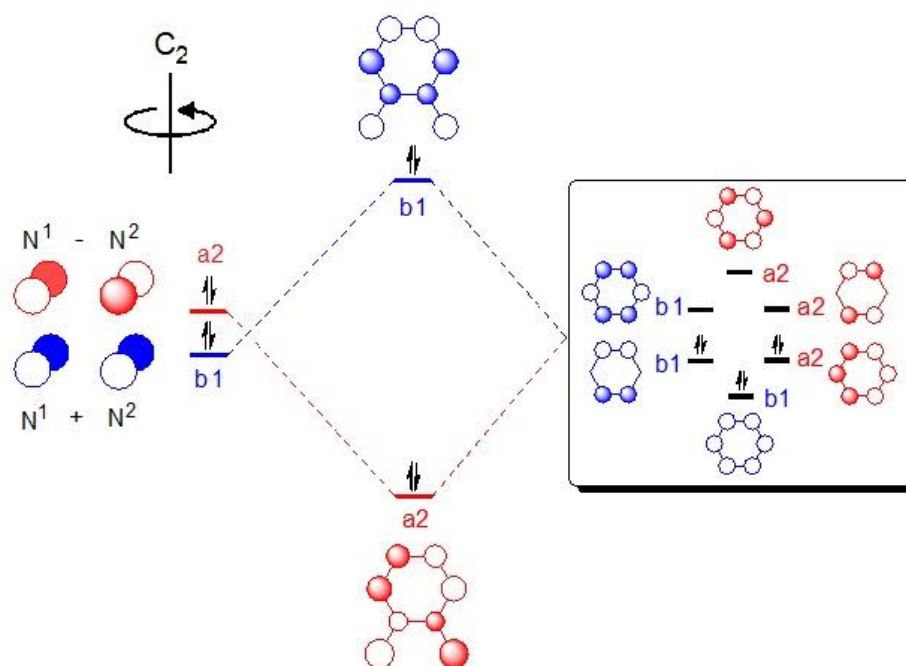


Figure 21 MO representation of in-phase / out-of-phase interactions for the HNC₆H₄NH system

ⁱ The author would like to thank Ainara Nova and Odile Eisenstein (The University of Montpellier, France) for performing the MO calculations for these systems.

The orbitals of a_2 and b_1 symmetry in the $\text{HNC}_6\text{H}_4\text{NH}$ system, and a and b symmetry in system HNCHPhCHPhNH , make a π -combination with the unoccupied d_{xz} (b_1 symmetry) and the occupied d_{xy} (a_2 symmetry) of the CpRh fragment respectively (Figure 22). The π -combination of orbitals of b_1 symmetry stabilizes the 16-electron complex; while the combination of a_2 symmetry destabilizes the complex by a 4-electron repulsion. The 4-electron repulsion should be bigger in the HNCHPhCHPhNH system where the lone pairs are more localized in the N atoms than in the $\text{HNC}_6\text{H}_4\text{NH}$ system, where they are delocalized within the Ph ring.

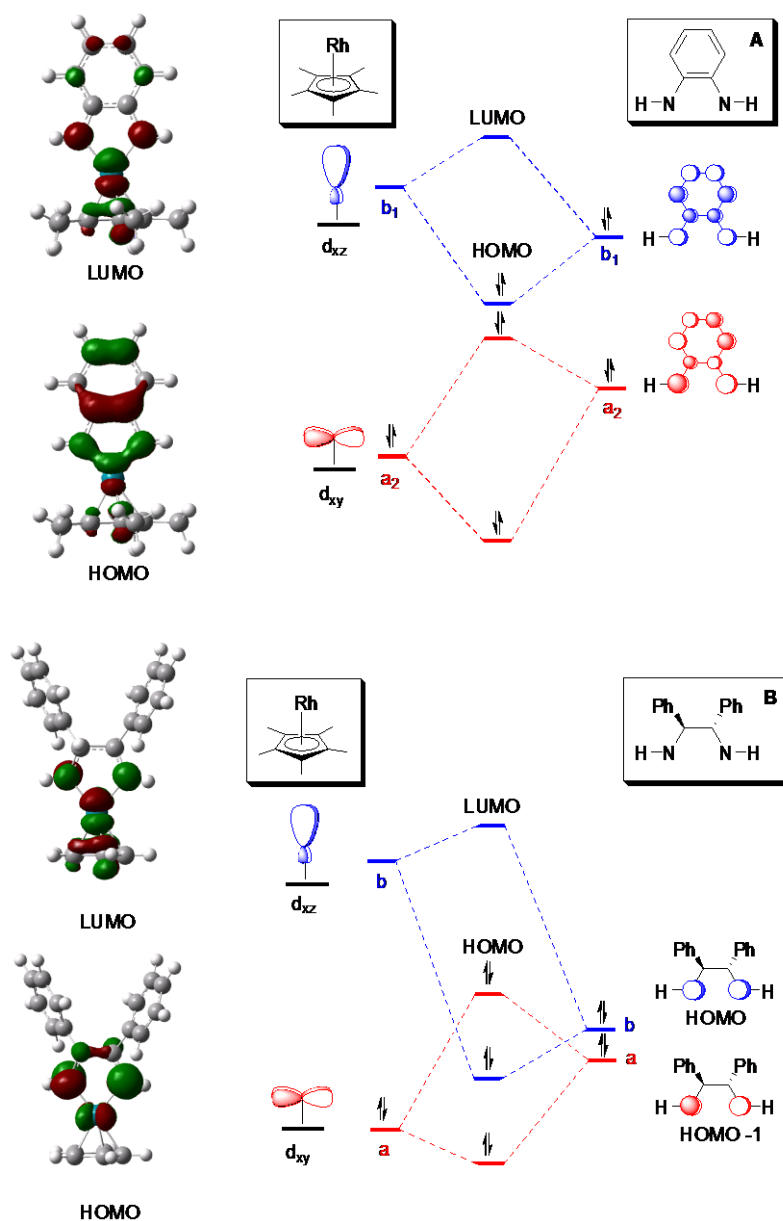


Figure 22: MO diagram to show interaction of ligands with CpRh fragment, 4-electron repulsions.

To estimate how important the 4 electron repulsion is in each system we can calculate the difference in energy between an almost pure orbital of Rh, for instance the $d_{y^2-z^2}$ and the out-of-phase combination of the orbitals with a_2 symmetry. In this way an internal reference was established to compare the energy of the orbitals in the different systems (Figure 23). This diagram shows that the 4-electron repulsion is bigger in the system using the HNCPhCHPhNH ligand than in the HNC₆H₄NH system as expected. The systems of the bistosylated complexes, Cp*Rh(TsNC₆H₄NTs) and Cp*Rh(TsNCHPhCHPhNTs), could also be investigated using this method. In these complexes the repulsion is lower than in the non-tosylated complexes because the tosyl groups on the ligand stabilise the lone pair on the nitrogen atom more than the NH groups (See Section 2.2.8, Figure 29). The 4-electron repulsion accounts for why the complexes with HNCPhCHPhNH as their ligand are more reactive than those with HNC₆H₄NH. However, this methodology cannot be used for the ranking of reactivity for each series.

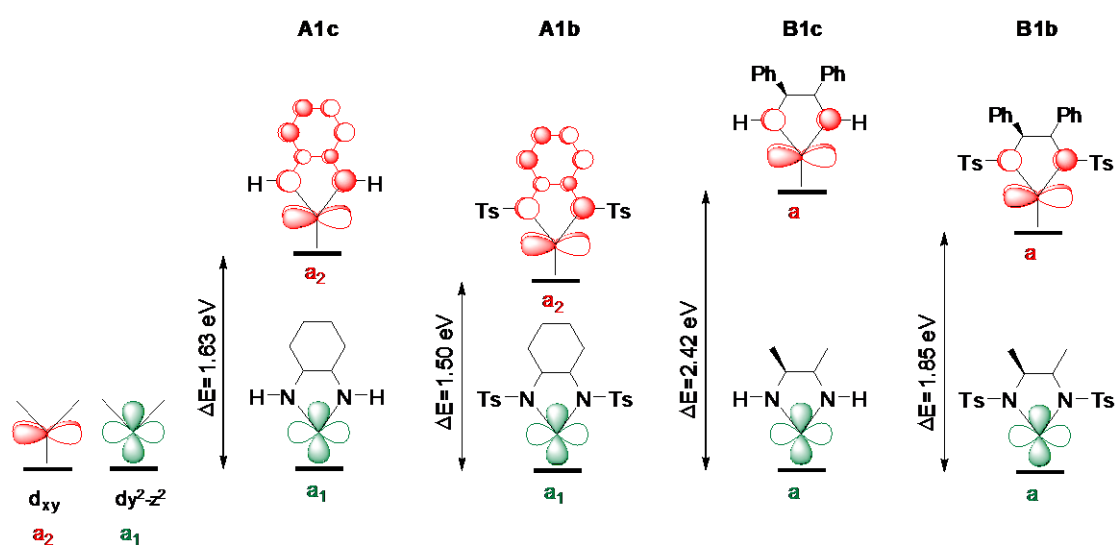
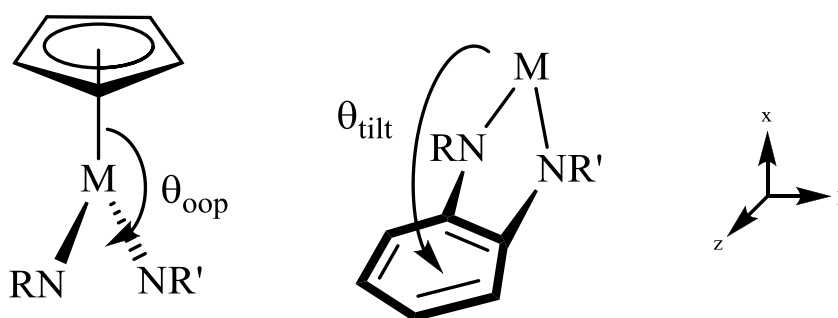


Figure 23 4-electron repulsions in **A1c**, **A1b**, **B1c**, **B1b**

2.2.5 X-ray crystallography characterisation of rhodium(III) complexes

The crystal structure of **1a** has been previously reported.⁹ For comparison, complexes **1b** and **1c** have been characterised by X-ray crystal analysis here. Suitable single crystals were grown from a solution of CH₂Cl₂ layered with methanol for **1b** and a solution of toluene layered with pentane for **1c**. The structures are shown (Figure 25) and selected bond lengths and angles are collected in Table 1 along with those for **1a** for comparison. Complexes **1a**, **1b** and **1c** show marked structural differences (Table 2). The Rh-NH bond length is much shorter than the Rh-NTs bond length for **1a** (difference 0.1424(10) Å) owing to the electron withdrawing effect of the tosyl group. **1b** and **1c** show symmetric Rh-N bond distances with long distances for the former (mean 2.0419(19) Å) and short ones for the latter (mean 1.9778(18) Å). The Rh-N distances follow the order **1a**(Rh-NH) < **1c**(Rh-NH) (mean) < **1b**(Rh-NTs) (mean) < **1a** (Rh-NTs). Complex **1a** also shows significant differences between r(N1-C11) and r(N2-C16), but the changes in r(N(1)-C(11)), r(N(2)-C(16)) and r(C11-C16) with respect to those of the free ligands²⁴ are insignificant (Table 3) which indicate the complexes are in a +3 oxidation state, as Maitlis also found for the 16-electron complex, [Cp*Rh(C₆H₄O₂)]·2C₆H₄(OH)₂.⁶ The angles θ_{oop} and θ_{tilt} (Figure 24) reveal further evidence of π -bonding.



θ_{oop} = angle between M-N1-N2 plane and M-Cp* centroid vector

θ_{tilt} = angle between M-N1-N2 plane and plane of benzene ring

Figure 24 Diagram for definition of angles θ_{oop} and θ_{tilt}

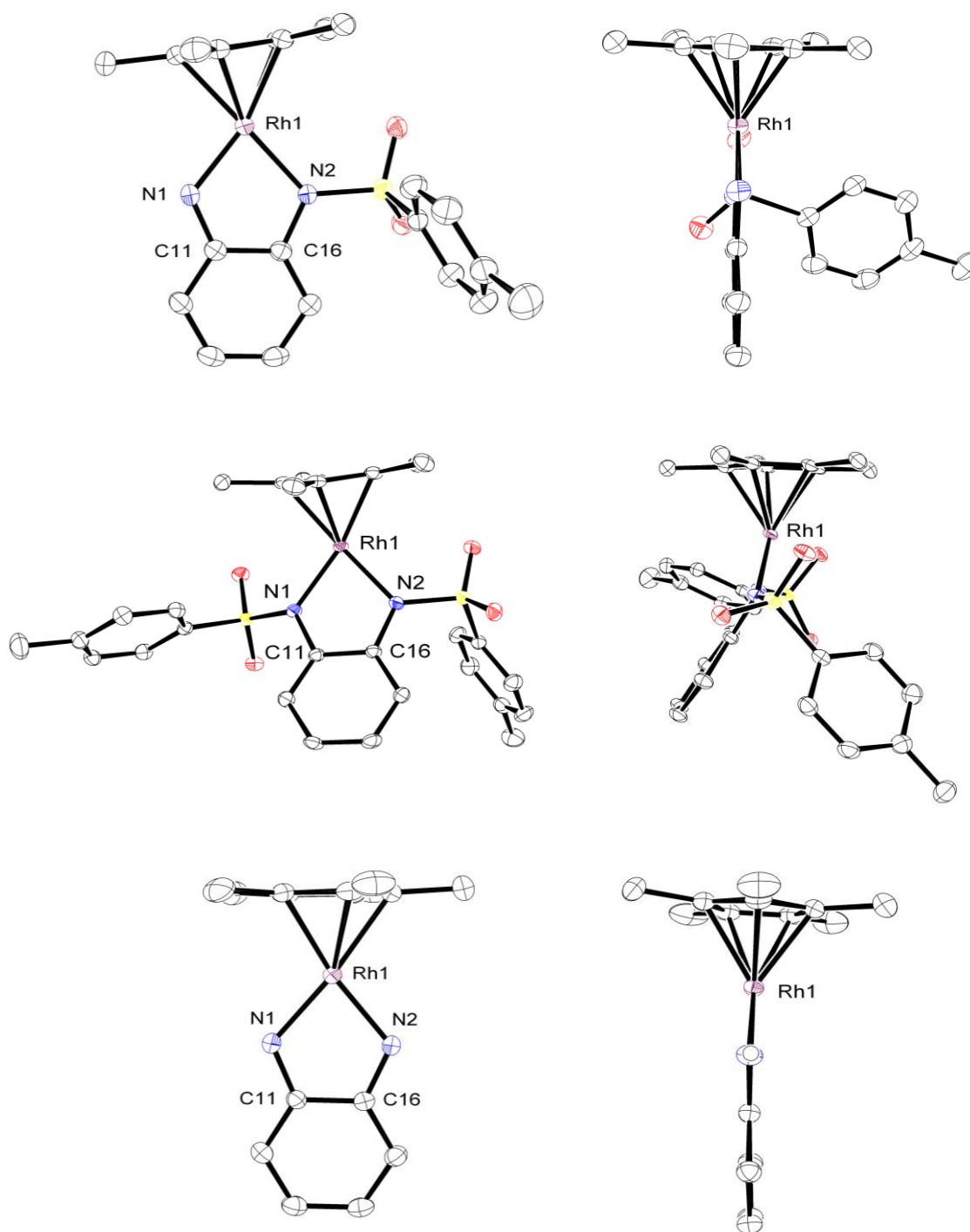


Figure 25 Two mutually perpendicular views of molecular structures of Cp*Rh(TsNC₆H₄NH), **1a** (top), Cp*Rh(TsNC₆H₄NTs), **1b** (middle) and Cp*Rh(HNC₆H₄NH), **1c** (bottom); hydrogens are omitted for clarity. Thermal ellipsoids shown at 50% probability.

Bond	Complex		
	(1a)	(1b)	(1c)
M-N(1)	1.9372(15)	2.0403(19)	1.9833(18)
M-N(2)	2.0796(14)	2.0435(19)	1.9722(19)
$\Delta r(\text{M-N})$	0.1426(10)	0.0032(13)	0.0111(13)
N(1)-C(11)	1.369(2)	1.421(3)	1.361(3)
N(2)-C(16)	1.413(2)	1.422(3)	1.364(3)
C(11)-C(16)	1.416(2)	1.404(3)	1.423(3)
$\theta_{\text{oop}}^{\text{c}}$	0.03°	8.40°	1.18°
$\theta_{\text{tilt}}^{\text{d}}$	0.82°	20.98°	2.19°

Table 2 X-ray diffraction data for **1a**, **1b** and **1c**

bond	Complex		
	H ₂ NC ₆ H ₄ NH ₂	TsNHC ₆ H ₄ NH ₂	TsNHC ₆ H ₄ NHTs
N(1)-C(11)	1.406	1.368(4)	1.417(4)
N(2)-C(16)	1.408	1.439(4)	1.431(4)
C(11)-C(16)	1.406	1.397(4)	1.388(4)

Table 3 Selected Bond Lengths (Å) and Angles (deg) for free ligands.²⁴

While **1a** and **1c** are planar ($\theta_{\text{oop}} < 2^\circ$), **1b** has lost the planar conformation, $\theta_{\text{oop}} = 8.40^\circ$. The tilt angles θ_{tilt} follow the order **1b** (20.98°) > **1c** (2.19°) > **1a** (0.82°), the last being almost planar. These data are consistent with considerable π -bonding for **1a** (Rh-NH) and **1c** but less or none for **1b** and **1a**(Rh-NTs). The structural parameters of **1a**, **1b** and **1c** show that these are Rh(III) complexes, as also identified for the 16-electron complex, [Cp*Rh(C₆H₄O₂)]·2C₆H₄(OH)₂.⁶ The marked differences on $\Delta r(\text{M-N})$, θ_{oop} and θ_{tilt} are consistent with MO arguments suggested by Morris (for related Ru amido complexes) that these bonds have partial double bond character due to π -donation from N to Ru. The locations of the hydrogen atoms in the X-ray diffraction experiments were assigned by difference map. Our studies highlight the ability of the metal to adapt to the requirements of the amido or tosylated amido ligands and the enormous electron withdrawing effect of the tosyl group on the M-N interaction in **1a**(Rh-NTs) and **1b**.

2.2.6 X-ray crystallographic characterisation of iridium(III) complexes

Grace had been successful in characterising Cp*Rh(TsNC₆H₄NH), **1a** by X-ray crystallography in 2006.⁹ It was decided that the X-ray crystallographic structures for the iridium series of complexes, Cp*Ir(XNC₆H₄NX'), where X, X' = H or Ts, should be determined. The analogous 16-electron iridium complex, Cp*Ir(TsNC₆H₄NH), **1d**, is shown in Figure 26, along with complex **1e** and **1f** for comparison (where **1f** has been previously reported).⁷ As expected, the structural parameters for the iridium series of 16-electron complexes are very similar to the rhodium series (Table 4). In agreement with the Rh-N distance trends, the Ir-NH bond length is much shorter than the Ir-NTs bond length for **1d** (difference 0.127(5) Å), also due to the electron withdrawing effect of the tosyl group. **1e** and **1f** also show near symmetric Ir-N bond distances with long distances for the former (mean 2.036(2) Å) and shorter for the latter (mean 1.971(8) Å). The Ir-N distances follow the order **1d**(Ir-NH) < **1f**(Ir-NH) (mean) < **1e**(Ir-NTs) (mean) < **1d**(Ir-NTs). The angles θ_{oop} and θ_{tilt} for the iridium complexes also follow the same trend as for the rhodium series, where **1d** and **1f** are planar ($\theta_{\text{oop}} < 4^\circ$) and **1e** has lost the planar conformation, $\theta_{\text{oop}} = 6.56^\circ$. The tilt angles also follow the same order as the rhodium series, **1e** (20.86°) > **1d** (5.06°) > **1f** (1.39°), consistent with considerable π -bonding for **1d** (Ir-NH) and **1f** but less or none for **1e** and **1d**(Ir-NTs).

Bond	Complex		
	(1d)	(1e)	(1f) ⁷
M-N(1)	1.936(3)	2.035(3)	1.985(12)
M-N(2)	2.063(3)	2.037(3)	1.957(12)
$\Delta r(\text{M-N})$	0.127(5)	0.002(5)	0.028(5)
N(1)-C(11)	1.376(4)	1.430(4)	1.35(3)
N(2)-C(16)	1.420(4)	1.422(4)	1.38(2)
C(11)-C(16)	1.412(4)	1.404(5)	1.41(3)
θ_{oop}	3.16°	6.56°	1.35°
θ_{tilt}	5.06°	20.86°	1.39°

Table 4 Selected bond lengths and angles for **1d**, **1e** and **1f**⁷

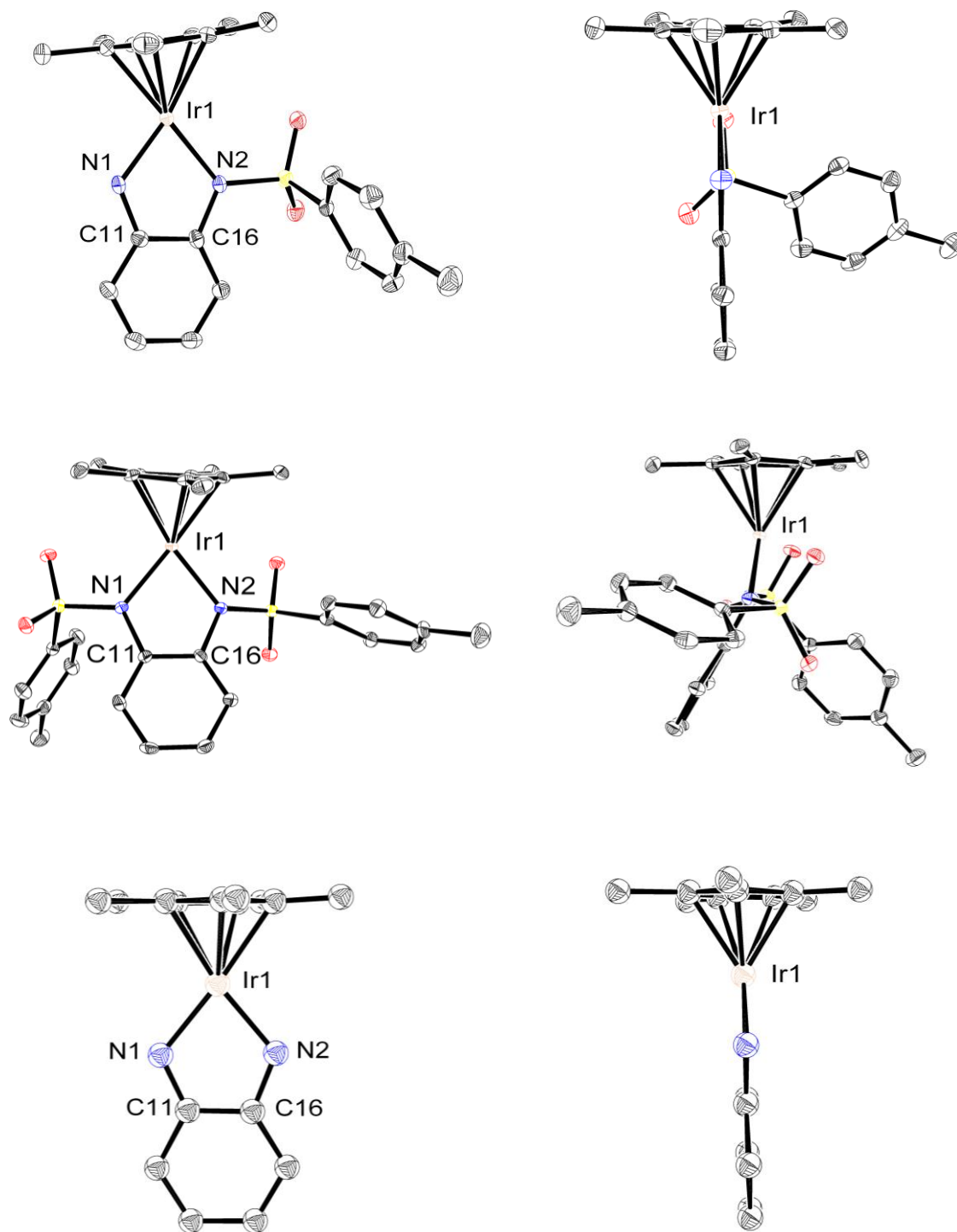


Figure 26 Two mutually perpendicular views of molecular structures of Cp*Ir(TsNC₆H₄NH), **1d** (top), Cp*Ir(TsNC₆H₄NTs), **1e** (middle) and Cp*Ir(HNC₆H₄NH), **1f** (bottom)⁷; hydrogens are omitted for clarity. Thermal ellipsoids shown at 50% probability.

2.2.7 DFT calculations supporting evidence for π -bonding in Cp*Rh(III) complexes

DFT(B3PW91) calculations by O. Eisenstein and A. Nova gave optimised structures for **1a**, **1b** and **1c**, close to the X-ray geometric parameters (Figure 27).⁸ Their calculations were performed with the Gaussian03 package²⁵ of programs with hybrid B3PW91 functional. The greater Rh-N π -bonding with NH in **1a** is evident from the calculated bond lengths and Wiberg indices. NBO analysis identifies 2p lone pairs on each nitrogen which mix with Rh(d_{xy}) and the C₆H₄ carbon to different extents for NH and NTs (Figure 28). Strikingly, the contributions of the Rh orbital to the composition of the nitrogen natural localised molecular orbital (NLMO) follow the pattern expected from the observed bond lengths: **1a**(NH) > **1c** > **1b** > **1a**(NTs) (Table 5). The delocalisation onto carbon is also greater for NH groups but follow the pattern: **1c** > **1a**(NH) > **1a**(NTs) > **1b**.

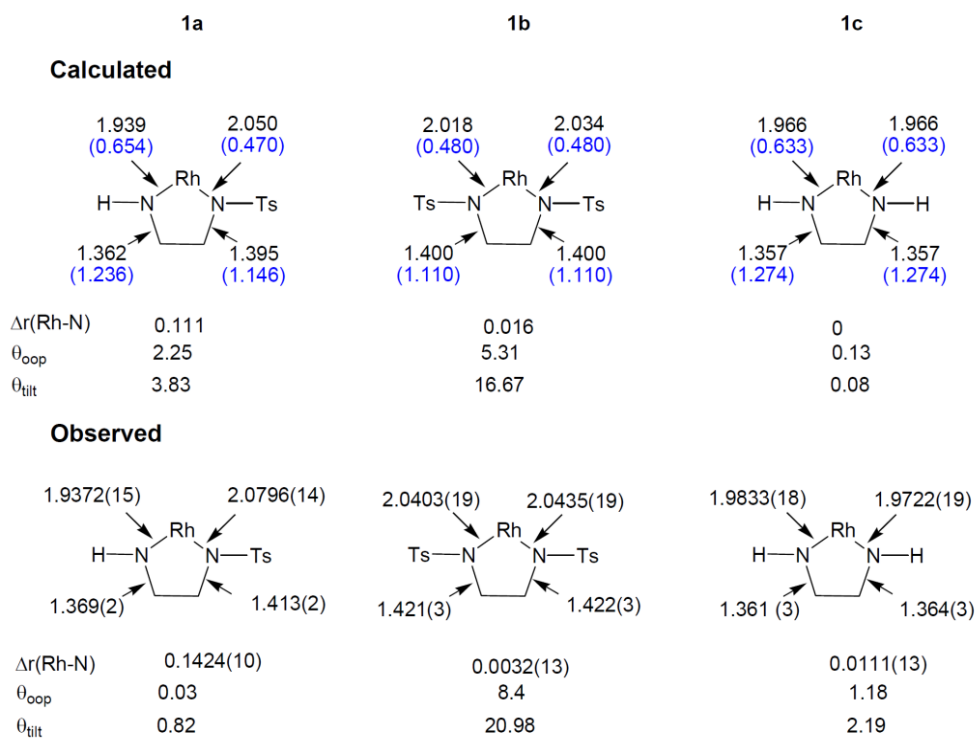


Figure 27 Comparison of calculated and observed bond lengths (Å) for **1a**, **1b** and **1c**. Wiberg indices are shown in brackets (blue). The difference between the Rh-N bond lengths is shown as Δr . Calculated and observed interplane angles θ_{oop} and θ_{tilt} also shown in degrees.

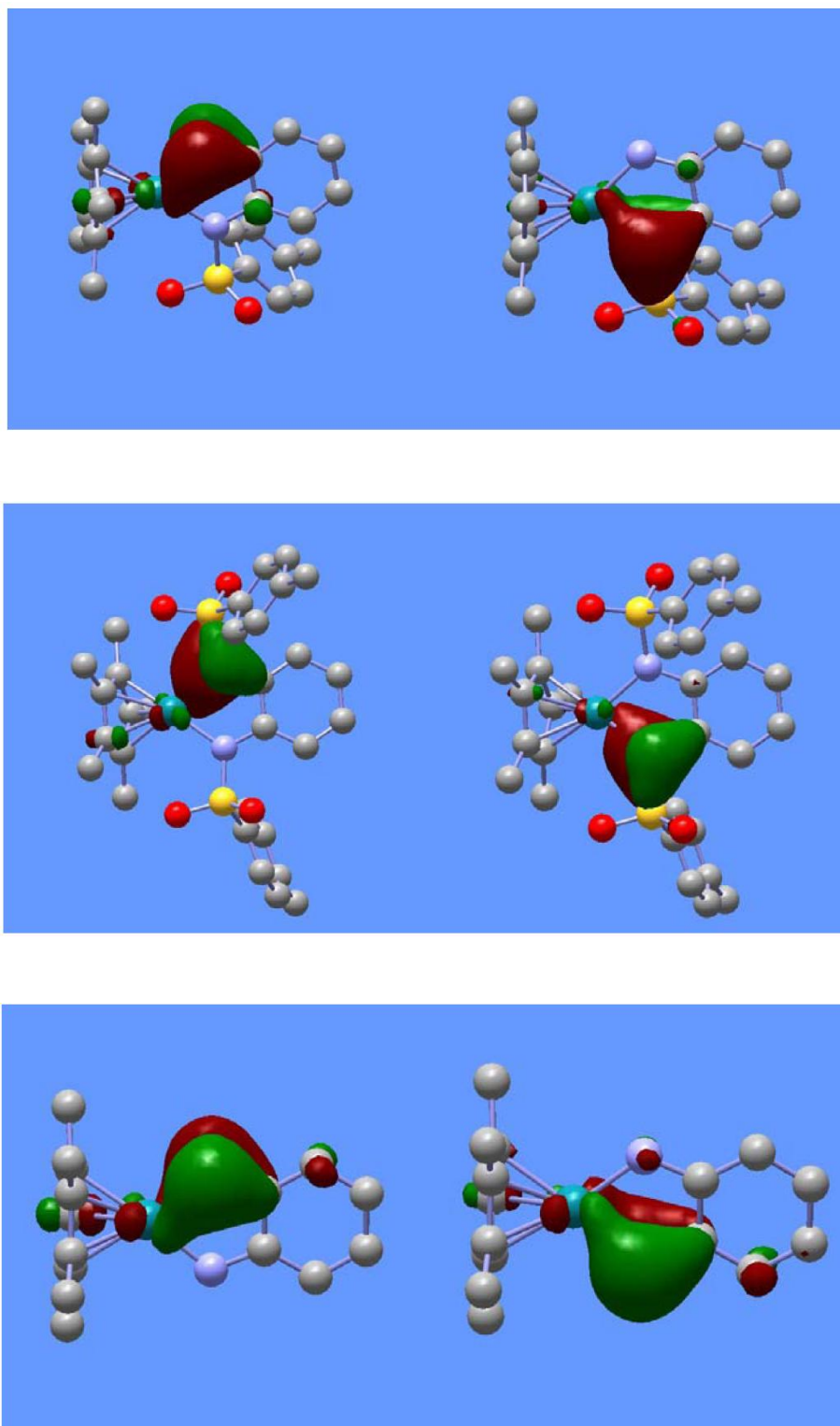


Figure 28 Optimised structures for **1a**, **1b** and **1c** showing the 2p lone pairs on each nitrogen atom mixing with the Rh(d_{xy}) orbital and the C₆H₄ carbon orbital (HOMO-1)

	N	Rh	Directly bound C	S
1a (NH)	73.4	8.5	5.8	-
1a (NTs)	80.1	3.8	4.0	2.3
1b	80.8	5.4	3.0	1.9
1c	73.9	6.8	6.8	-

Table 5 Values for the contributions of the Rh orbital to the composition of the nitrogen natural localised molecular orbital.

2.2.8 Electronic configuration of 16-electron Cp*Rh complexes 1a, 1b and 1c

From the molecular orbital diagram shown in Figure 29 we observe that the energy of the ligand's highest occupied molecular orbital decreases when the ligand has an increasing number of tosyl groups attached. On coordination to Cp*Rh, the HOMO of the ligand interacts with the metal LUMO, d_{yz} to form a M-N π -bond. The stabilisation is greatest for HNC₆H₄NH and least for TsNC₆H₄NTs, as expected considering the relative energies of the metal and ligand orbitals.

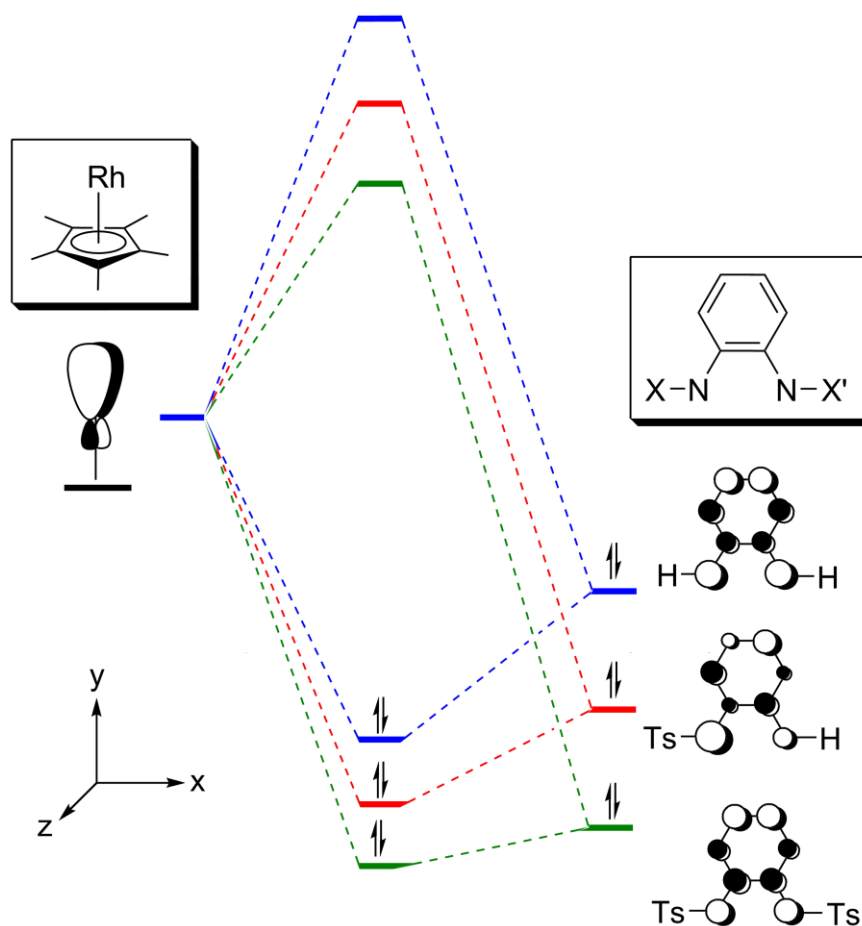


Figure 29 In-phase and out-of-phase combination between unoccupied d_{yz} of Cp*Rh and HOMO of bis(amido) ligand.

2.2.9 Synthesis and characterisation of 4,5-disubstituted 16-electron complexes

We investigated the effect of adding different substituents in the 4,5-position on the phenylenediamine ligand. These included a methyl group and a chloride group (Figure 30). The experimental method was identical to that mentioned previously. The ^1H NMR of the 4,5-dimethyl complex shows that the NH proton ($\delta = 8.22$) has an almost identical chemical shift to that of $\text{Cp}^*\text{Rh}(\text{TsNC}_6\text{H}_4\text{NH})$, **1a**. The complexes are also blue-violet and have a characteristic single NH stretch in their IR spectra (for $\text{Cp}^*\text{Rh}(\text{TsNC}_6\text{H}_2(\text{CH}_3)_2\text{NH})$, $\nu(\text{NH}) = 3320 \text{ cm}^{-1}$). High resolution mass spectral analysis of the 4,5-dimethyl complex revealed a molecular ion peak plus hydrogen with m/z of 527.1238. Attempts at growing suitable crystals for X-ray analysis were unsuccessful owing to time constraints, although the author is confident that if more time was available structural analysis would confirm similar structural features observed for **1a**, notably planarity around the Rh atom.

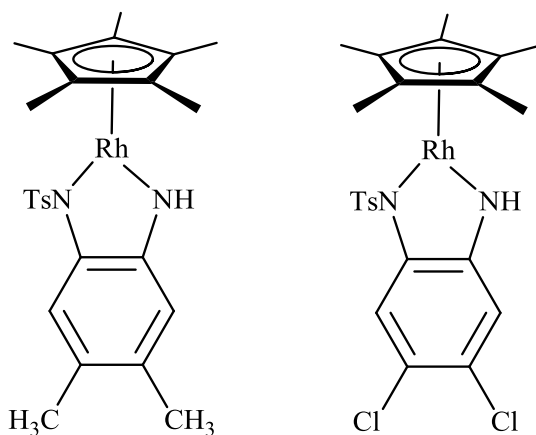


Figure 30 4,5-disubstituted complexes synthesised in this study

The 4,5-disubstituted complexes were tested as catalysts for the catalytic transfer hydrogenation of a cyclic imine, 6,7-dimethoxy-1-methyl-3,4-dihydroisoquinoline, in Chapter 3.

2.3 Summary

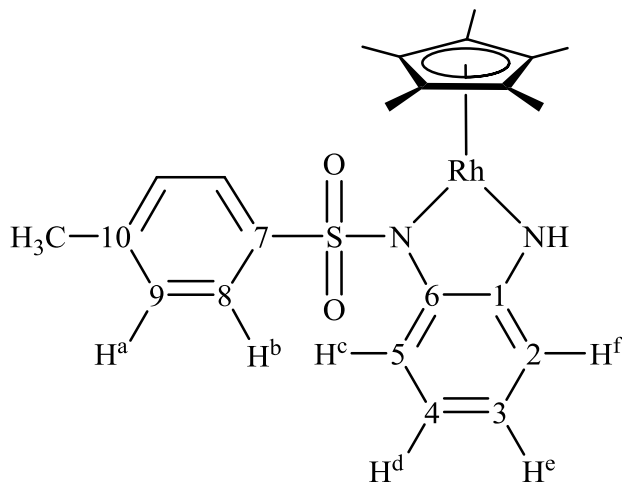
In conclusion, we have prepared a series of rhodium and iridium monotosylated and bis-tosylated complexes ($\eta^5\text{-C}_5\text{Me}_5$)M(RNC₆H₄NR') (M = Rh, Ir; X, X' = H or Ts) with formal “16-electron” configurations and demonstrated that these are in the +3 oxidation state. The complexes are postulated intermediates in the catalytic cycle for transfer hydrogenation. We have analysed their crystal structures and observed a remarkable trend in Rh-N bond lengths, indicative of M-NH π -bonding and the absence of M-NTs π -bonding in the 16-electron rhodium(III) and iridium(III) complexes. We have demonstrated that the effect of π -bonding on θ_{oop} and θ_{tilt} angles is consistent with MO arguments for ruthenium analogues. The work in this chapter also highlights the delocalisation in the bis(amido) complexes and the enormous electron withdrawing effect of the tosyl group on the M-N interaction for Cp*Rh(TsNC₆H₄NH) and Cp*Ir(TsNC₆H₄NH). DFT(B3PW91) calculations by Eisenstein *et al.* give optimised structures for **1a**, **1b** and **1c** close to the X-ray structural parameters and support our experimental observations.

During the ¹H/¹⁰³Rh HSQC NMR study, a coupling between the Cp* methyl protons and rhodium was observed; this was exploited and the ¹⁰³Rh chemical shift of **1a** and **1b** were collected, along with various related CATHyTM catalysts (in publication elsewhere). We concluded that the rhodium chemical shifts of the 16-electron complexes were more deshielded than the 18-electron chloride complex, Cp*RhCl(TsNCHPhCHPhNH₂). This could prove a useful technique for studying similar Cp*Rh complexes.

In order to probe the effect of electron donating and withdrawing substituents on the *o*-phenylenediamine ligand the rhodium 4,5-dimethyl and 4,5-dichloro complexes were prepared and characterised. The ¹H NMR spectra of these complexes show an almost identical NH proton chemical shift.

2.4 Supporting NMR data

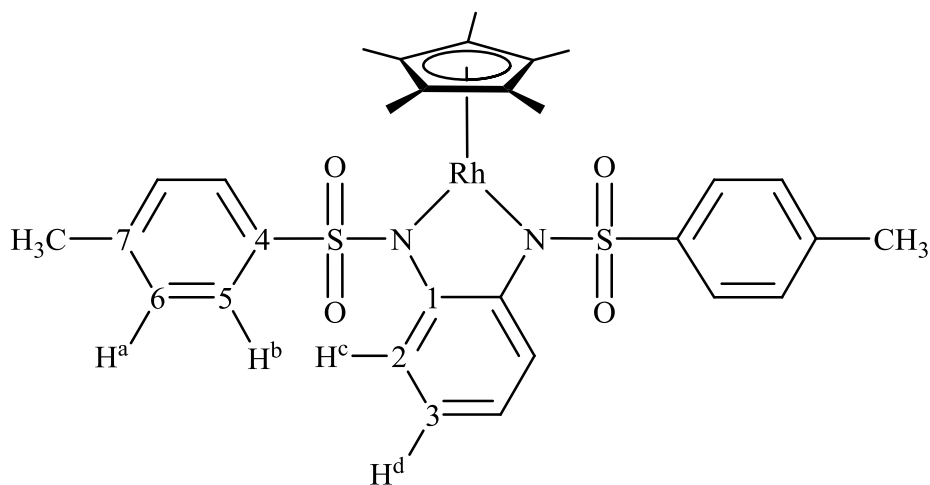
2.4.1 Cp*Rh(TsNC₆H₄NH) (1a)



	$\delta_{\text{H}} / \text{ppm}$ (area, multiplicity)	assignment	J / Hz	Assignment
¹ H NMR	1.98 (15H, s)	C ₅ (CH ₃) ₅		
500 MHz	2.35 (3H, s)	CH ₃		
(CD ₂ Cl ₂ , 300K)	6.61 (1H, t)	H ^e	8.0	³ J _{HH}
	6.68 (1H, t)	H ^d	8.0	³ J _{HH}
	6.82 (1H, d)	H ^f	8.0	³ J _{HH}
	7.20 (2H, d)	H ^a	8.2	³ J _{HH}
	7.35 (1H, d)	H ^c	8.0	³ J _{HH}
	7.64 (2H, d)	H ^b	8.2	³ J _{HH}
	8.25 (1H, br. s)	NH		
¹³ C NMR	10.67	C ₅ (CH ₃) ₅		
125 MHz	21.69	CH ₃		
(CD ₂ Cl ₂ , 300K)	94.88	C ₅ (CH ₃) ₅	8.3	J _{RhC}
	113.99	C ²		
	117.94	C ⁴		

	117.98	C ⁵
	120.85	C ³
	127.13	C ⁸
	129.76	C ⁹
	138.68	C ⁶
	141.26	C ⁷
	142.54	C ¹
	152.52	C ¹⁰
	153.70	C ¹
¹⁰³ Rh NMR	2063.0	Rh
22.18 Hz		
(CDCl ₃ , 300 K)		

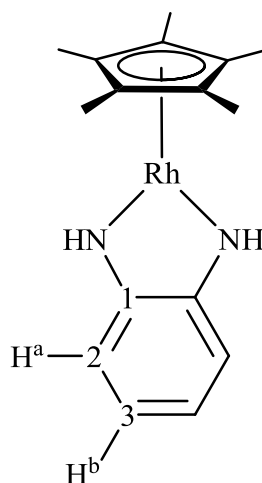
Table 2.4.1 Assigned with the aid of ¹H / ¹³C HSQC, ¹H / ¹³C HSBC, ¹H / ¹H COSY, NOESY and ¹H / ¹⁰³Rh HSQC.

2.4.2 Cp*Rh(TsNC₆H₄NTs) (1b)

	$\delta_{\text{H}} / \text{ppm}$ (area, multiplicity)	assignment	J / Hz	Assignment
¹ H NMR	1.86 (15H, s)	C ₅ (CH ₃) ₅		
500 MHz	2.33 (3H, s)	CH ₃		
(CD ₂ Cl ₂ , 300K)	6.41-6.45 (2H, m)	H ^d		
	7.13 (1H, t)	H ^a	8.0	³ J _{HH}
	7.20-7.23 (1H, m)	H ^c		
	7.50 (2H, d)	H ^b	8.0	³ J _{HH}
¹³ C NMR	11.48	C ₅ (CH ₃) ₅		
125 MHz	21.73	CH ₃		
(CD ₂ Cl ₂ , 300K)	99.34	C ₅ (CH ₃) ₅	8.9	J _{RhC}
	118.01	C ²		
	120.56	C ³		
	127.31	C ⁵		
	129.75	C ⁶		
	140.22	C ⁴		
	141.60	C ¹		
	142.83	C ⁷		

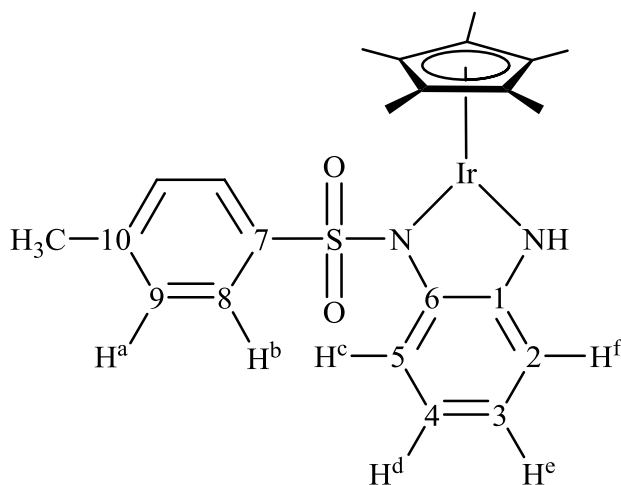
^{103}Rh NMR 1743.0 Rh
22.18 Hz
(CDCl₃, 300 K)

Table 2.4.2 Assigned with the aid of $^1\text{H} / ^{13}\text{C}$ HSQC, $^1\text{H} / ^{13}\text{C}$ HSBC, $^1\text{H} / ^1\text{H}$ COSY, NOESY and $^1\text{H} / ^{103}\text{Rh}$ HSQC.

2.4.3 Cp*Rh(HNC₆H₄NH) (1c)

	δ_{H} / ppm (area, multiplicity)	assignment	J / Hz	Assignment
¹ H NMR	2.07 (15H, s)	C ₅ (CH ₃) ₅		
500 MHz	6.66-6.69 (2H, m)	H ^a		AA'XX'
(CD ₂ Cl ₂ , 300K)	6.85-6.88 (2H, m)	H ^b		AA'XX'
	8.26 (2H, br. s)	NH		
¹³ C NMR	10.81	C ₅ (CH ₃) ₅		
125 MHz	91.54	C ₅ (CH ₃) ₅	7.3	J _{RhC}
(CD ₂ Cl ₂ , 300K)	114.56	C ³		
	117.55	C ²		
	149.63	C ¹		

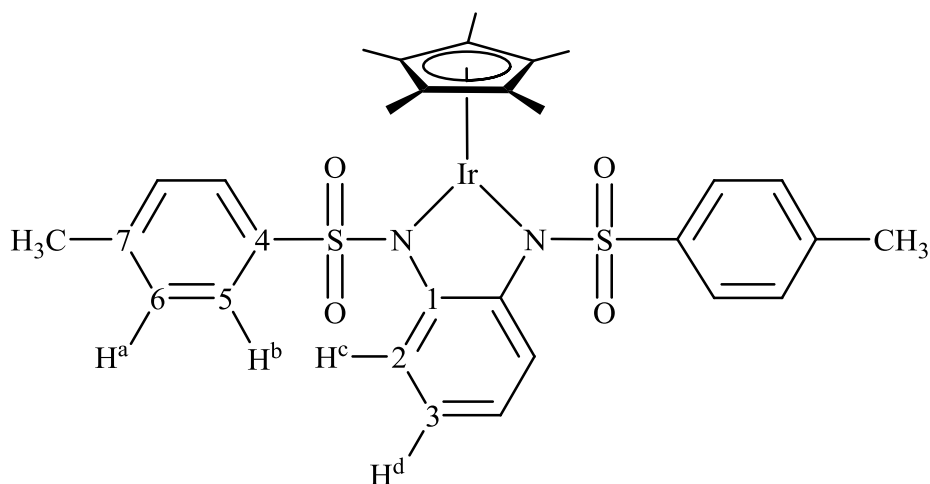
Table 2.4.3 Assigned with the aid of ¹H / ¹³C HSQC, ¹H / ¹³C HSBC, ¹H / ¹H COSY, NOESY

2.4.4 Cp*Ir(TsNC₆H₄NH) (1d)

	$\delta_{\text{H}} / \text{ppm}$ (area, multiplicity)	assignment	J / Hz	Assignment
¹ H NMR	1.99 (15H, s)	C ₅ (CH ₃) ₅		
700 MHz	2.33 (3H, s)	CH ₃		
(CD ₃ CN, 300K)	6.51 (1H, t)	H ^d	7.7	J _{HH}
	6.63 (1H, t)	H ^e	7.7	J _{HH}
	6.97 (1H, d)	H ^f	7.9	J _{HH}
	7.24 (2H, d)	H ^a	8.3	J _{HH}
	7.45 (1H, d)	H ^c	8.4	J _{HH}
	7.61 (2H, d)	H ^b	8.3	J _{HH}
	8.87 (1H, s br)	NH		
¹³ C NMR	10.66	C ₅ (CH ₃) ₅		
175 MHz	21.45	CH ₃		
(CD ₃ CN, 300K)	88.53	C ₅ (CH ₃) ₅		
	114.45	C ²		
	117.45	C ⁴		
	118.07	C ⁵		

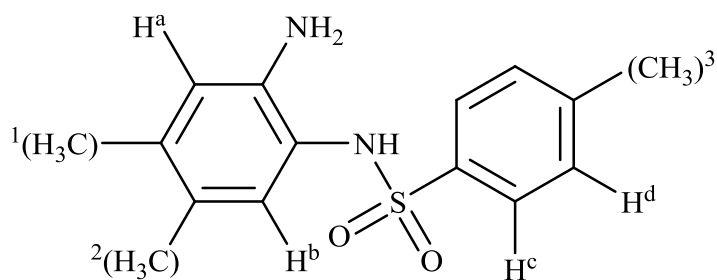
	121.60	C ³		
	127.69	C ⁸		
	130.34	C ⁹		
	140.80	C ⁶ /C ⁷		
	140.80	C ⁶ /C ⁷		
	143.32	C ¹⁰		
	154.80	C ¹		
¹ H NMR	1.99 (15H, s)	C ₅ (CH ₃) ₅		
700 MHz	2.33 (3H, s)	CH ₃		
(CD ₃ CN, 300K)	6.51 (1H, t)	H ^c	7.7	J _{HH}
	6.63 (1H, t)	H ^b	7.7	J _{HH}

Table 2.4.4 Assigned with the aid of ¹H / ¹³C HSQC, ¹H / ¹³C HSBC, ¹H / ¹H COSY and NOESY.

2.4.5 Cp*Ir(TsNC₆H₄NTs) (1e)

	δ_{H} / ppm (area, multiplicity)	assignment	J / Hz	Assignment
¹ H NMR	1.72 (15H, s)	C ₅ (CH ₃) ₅		
500 MHz	2.33 (6H, s)	CH ₃		
(CD ₃ CN, 300K)	6.40 (2H)	H ^d	3.5, 2.6	J _{HH}
	7.11 (4H, d)	H ^a	8.1	J _{HH}
	7.36 (2H)	H ^c	3.5, 2.6	J _{HH}
	7.44 (4H, d)	H ^b	8.1	J _{HH}
¹³ C NMR	10.42	C ₅ (CH ₃) ₅		
125 MHz	21.46	CH ₃		
(CD ₃ CN, 300K)	90.77	C ₅ (CH ₃) ₅		
	118.97	C ²		
	121.18	C ³		
	127.96	C ⁵		
	130.10	C ⁶		
	141.65	C ⁴		
	142.94	C ⁷		
	144.74	C ¹		

Table 2.4.5 Assigned with the aid of ¹H / ¹³C HSQC, ¹H / ¹³C HSBC, ¹H / ¹H COSY and NOESY.

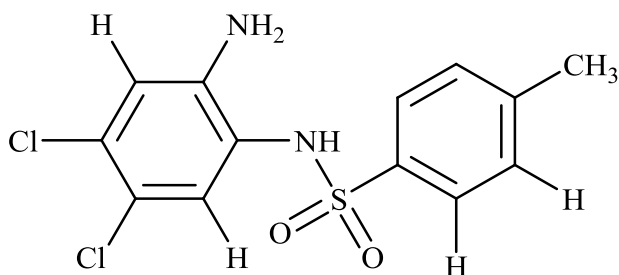
2.4.6 4,5-dimethyl-*N*¹-tosylbenzene-1,2-diamine

	δ_{H} / ppm (area, multiplicity)	assignment	J / Hz	Assignment
¹ H NMR	1.93 (3H, s)	¹ (CH ₃)		
500 MHz	2.13 (3H, s)	² (CH ₃)		
(CDCl ₃ , 300K)	2.40 (3H, s)	³ (CH ₃)		
	3.76 (2H, s br.)	NH ₂		
	5.99 (1H, s br.)	NH		
	6.27 (1H, s)	H ^a		
	6.51 (1H, s)	H ^b		
	7.24 (2H, d)	H ^d	8.2	³ J _{HH}
	7.61 (2H, d)	H ^c	8.5	³ J _{HH}
¹³ C NMR	18.73	CH ₃		
125 MHz	19.70	CH ₃		
(CDCl ₃ , 300K)	21.78	CH ₃		
	118.80	ArH		
	119.03	Q		
	127.15	Q		
	127.76	TosArH		
	129.68	ArH		
	129.72	TosArH		
	136.58	Q		
	137.70	Q		

142.12	Q
143.94	Q

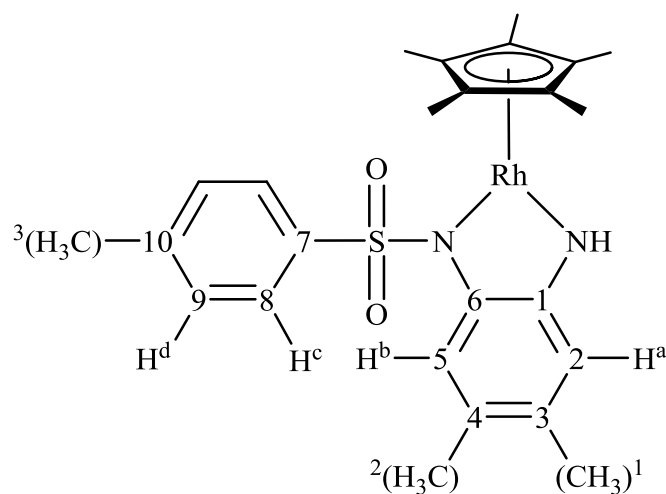
Table 2.4.6 NMR data for 4,5-dimethyl-*N*¹-tosylbenzene-1,2-diamine

Assigned with the aid of ¹H, ¹³C{¹H}, ¹H / ¹³C HSQC, ¹H / ¹³C HMBC, ¹H / ¹H COSY, ¹H NOESY experiments.

2.4.7 4,5-dichloro-*N*¹-tosylbenzene-1,2-diamine

	δ_{H} / ppm (area, multiplicity)	assignment	J / Hz	Assignment
¹ H NMR	2.43 (3H, s)	CH ₃		
500 MHz	4.12 (2H, br. s)	NH ₂		
(CDCl ₃ , 300K)	6.08 (1H, br. s)	NH		
	6.55 (1H, s)	ArH	2.0	² J _{HCl}
	6.79 (1H, s)	ArH	2.0	² J _{HCl}
	7.29 (2H, d)	TsArH	8.2	³ J _{HH}
	7.62 (2H, d)	TsArH	8.2	³ J _{HH}
¹³ C NMR	21.79			
125 MHz	117.84			
(CDCl ₃ , 300K)	120.61			
	120.68			
	127.69			
	129.80			
	130.07			
	132.63			
	135.48			
	144.29			
	144.83			

Table 2.4.7 NMR data for 4,5-dimethyl-*N*¹-tosylbenzene-1,2-diamine

2.4.8 Cp*Rh(TsNC₆H₂(CH₃)₂NH)

	δ_{H} / ppm (area, multiplicity)	assignment	J / Hz	Assignment
¹ H NMR	1.93 (3H, s)	(CH ₃) ¹		
500 MHz	1.96 (15H, s)	C ₅ (CH ₃) ₅		
(CD ₂ Cl ₂ , 300K)	2.08 (3H, s)	(CH ₃) ²		
	2.34 (3H, s)	(CH ₃) ³		
	6.60 (1H, s)	H ^a		
	7.17 (1H, s)	H ^b		
	7.19 (2H, d)	H ^d	8.2	³ J _{HH}
	7.62 (2H, d)	H ^c	8.2	³ J _{HH}
	8.22 (1H, br. s)	NH		
¹³ C NMR	10.62	C ₅ (CH ₃) ₅		
125 MHz	19.45	(CH ₃) ²		
(CD ₂ Cl ₂ , 300K)	20.26	(CH ₃) ³		
	21.68	(CH ₃) ¹		
	94.35	C ₅ (CH ₃) ₅	7.9	J _{RhC}
	114.76	C ²		

118.88	C ⁵
126.62	C ^{quart}
127.12	C ⁸
129.24	C ^{quart}
129.66	C ⁹
136.97	C ^{quart}
141.43	C ^{quart}
142.32	C ^{quart}
151.04	C ^{quart}

Table 2.4.8 Assigned with the aid of ¹H / ¹³C HSQC, ¹H / ¹³C HSBC, ¹H / ¹H COSY, NOESY and ¹H / ¹⁰³Rh HSQC.

2.5 References

- 1.) M. Jiménez-Tenorio, M. C. Puerta and P. Valerga, *Eur. J. Inorg. Chem.*, 2004, 17.
- 2.) K. Abdur-Rashid, S. E. Clapham, A. Hadzovic, J. N. Harvey, A. J. Lough and R. H. Morris, *J. Am. Chem. Soc.*, 2002, **124**, 15104.
- 3.) T. Ikariya and A. J. Blacker, *Acc. Chem. Res.*, 2007, **40**, 1300.
- 4.) K. J. Haack, S. Hashiguchi, A. Fujii, T. Ikariya and R. Noyori, *Angew. Chem., Int. Ed. Engl.*, 1997, **36**, 285.
- 5.) K. Mashima, T. Abe and K. Tani, *Chem. Lett.*, 1998, 1201.
- 6.) P. Espinet, P. M. Bailey and P. M. Maitlis, *J. Chem. Soc., Dalton Trans.*, 1979, 1542.
- 7.) C. Paek, J. J. Ko and J. K. Uhm, *Bull. Korean Chem. Soc.*, 1994, **15**, 980.
- 8.) A. J. Blacker, E. Clot, S. B. Duckett, O. Eisenstein, J. Grace, A. Nova, R. N. Perutz, D. J. Taylor and A. C. Whitwood, *Chem. Commun.*, 2009, 6801.
- 9.) J. Grace, The Rh catalysed asymmetric transfer hydrogenation of imines: a mechanistic study. PhD Thesis, University of York, York, U.K. 2007.
- 10.) Z. M. Heiden, B. J. Gorecki and T. B. Rauchfuss, *Organometallics*, 2008, **27**, 1542.
- 11.) A. W. Holland, D. S. Glueck and R. G. Bergman, *Organometallics*, 2001, **20**, 2250.
- 12.) K. G. Caulton, *New J. Chem.* 1994, **18**, 25.
- 13.) H. E. Bryndza, P. J. Domaille, R. A. Paciello and J. E. Bercaw, *Organometallics* 1989, **8**, 379.
- 14.) L. Luo and S. P. Nolan, *Organometallics* 1994, **13**, 4781.
- 15.) T. J. Johnson, K. Folting, W. E. Streib, J. D. Martin, J. C. Huffman, S. A. Jackson, O. Eisenstein and K. G. Caulton, *Inorg. Chem.* 1995, **34**, 488.
- 16.) M. Jiménez-Tenorio, M. C. Puerta and P. Valerga, *J. Organomet. Chem.* 2000, **609**, 161.
- 17.) P. Hofmann, *Angew. Chem., Int. Ed. Engl.*, 1977, **16**, 536.
- 18.) D. Rivillo, H. Gulyás, J. Benet-Buchholz, E. C. Escudero-Adán, Z. Freixa and P. W. N. M. van Leeuwen, *Angew. Chem. Int. Ed.* 2007, **46**, 7247.

- 19.) (a) R. I. Michelman, R. G. Bergman and R. A. Andersen, *Organometallics*, 1993, **12**, 2741; (b) R. I. Michelman, G. E. Ball, R. G. Bergman and R. A. Andersen, *Organometallics*, 1994, **13**, 869.
- 20.) G. S. Hall and R. H. Soderberg, *Inorg. Chem.*, 1968, **7**, 2300.
- 21.) A. J. Blacker, S. B. Duckett, J. Grace, R. N. Perutz and A. C. Whitwood, *Organometallics*, 2009, **28**, 1435.
- 22.) A. Anillo, C. Barrio, S. García-Granda and R. Obeso-Rosete, *J. Chem. Soc., Dalton Trans.*, 1993, **7**, 1125.
- 23.) A. S. Abd-El-Aziz, K. M. Epp, C. R. de Denus and G. Fisher-Smith, *Organometallics*, 1994, **13**, 2299.
- 24.) (a) C. Stalhandske, *Cryst. Struct. Commun.*, 1981, **10**, 1081; (b) C. Squires, C. W. Baxter, J. Campbell, L. F. Lindoy, H. McNab, A. Parkin, S. Parsons, P. A. Tasker, G. Wei and D. J. White, *Dalton Trans.*, 2006, 2026; (c) T. Kato, H. Masu, H. Takayanagi, E. Kaji, K. Katagiri, M. Tominaga and I. Azumaya, *Tetrahedron*, 2006, **62**, 8458.
- 25.) Gaussian 03, Revision D.01, M. J. Frisch, G. W. Trucks, H. B. Schlegel, G. E. Scuseria, M. A. Robb, J. R. Cheeseman, J. A. Montgomery, Jr., T. Vreven, K. N. Kudin, J. C. Burant, J. M. Millam, S. S. Iyengar, J. Tomasi, V. Barone, B. Mennucci, M. Cossi, G. Scalmani, N. Rega, G. A. Petersson, H. Nakatsuji, M. Hada, M. Ehara, K. Toyota, R. Fukuda, J. Hasegawa, M. Ishida, T. Nakajima, Y. Honda, O. Kitao, H. Nakai, M. Klene, X. Li, J. E. Knox, H. P. Hratchian, J. B. Cross, V. Bakken, C. Adamo, J. Jaramillo, R. Gomperts, R. E. Stratmann, O. Yazyev, A. J. Austin, R. Cammi, C. Pomelli, J. W. Ochterski, P. Y. Ayala, K. Morokuma, G. A. Voth, P. Salvador, J. J. Dannenberg, V. G. Zakrzewski, S. Dapprich, A. D. Daniels, M. C. Strain, O. Farkas, D. K. Malick, A. D., Rabuck, K. Raghavachari, J. B. Foresman, J. V. Ortiz, Q. Cui, A. G. Baboul, S. Clifford, J. Cioslowski, B. B. Stefanov, G. Liu, A. Liashenko, P. Piskorz, I. Komaromi, R. L. Martin, D. J. Fox, T. Keith, M. A. Al-Laham, C. Y. Peng, A. Nanayakkara, M. Challacombe, P. M. W. Gill, B. Johnson, W. Chen, M. W. Wong, C. Gonzalez, and J. A. Pople, Gaussian, Inc., Wallingford CT, 2004.

A MECHANISTIC STUDY INTO TRANSFER HYDROGENATION USING 16-ELECTRON Cp*Rh AND Cp*Ir COMPLEXES

3.1 Introduction

Optically active compounds are important in the fine-chemical, pharmaceutical and agrochemical industries.¹ Asymmetric transfer hydrogenation (ATH) is an outstanding method for the preparation of chiral alcohols and amines by the catalytic reduction of ketones and imines, respectively.^{2,3,4,5,6} Transfer hydrogenation is defined as the reduction of unsaturated molecules with the aid of a hydrogen donor in the presence of a catalyst.⁷ In ATH, an alcohol, *e.g.* 2-propanol, or a formate is used as the hydrogen source.^{8,9}

3.1.1 Noyori's "Outer-sphere" bifunctional mechanism

Noyori's chiral Ru(II)-TsDPEN complex **1** was used as the catalyst in transfer hydrogenation of both ketones and imines to give quantitative yields and high enantioselectivities (*ee*'s up to 97% for imines);^{6,9-11} the proposed mechanism for ATH of ketones and imines by **2**, formed from **1**, involves a cyclic transition state (**A**) (Figure 1).

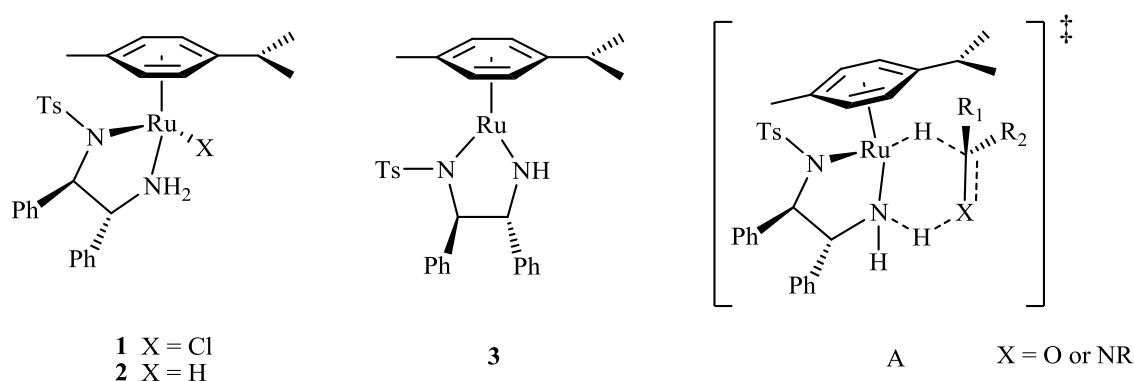


Figure 1 Ru-TsDPEN catalyst precursor **1**, true catalyst **2** and reactive intermediate **3**.

The hydride and the proton are transferred from the catalyst to the substrate in a concerted reaction without coordination of the substrate (outer-sphere mechanism).^{10,11} Mechanistic studies have proven that **2** and **3** are the active species in catalysis involving ketones and alcohols.⁹ The concerted pathway is supported by kinetic isotope measurements carried out by Casey *et al.*¹² and calculations performed by Noyori¹³, Andersson¹⁴, and van Leeuwen¹⁵. However, Bäckvall *et al.*^{16,17} and Casey *et al.*^{18,19} have shown that for Shvo's catalyst (Figure 2), a related metal-ligand bifunctional catalyst, transfer hydrogenation of imines occurs via a different mechanism to that of ketones. Furthermore, Bäckvall has reported that the concerted mechanism proposed for the addition of hydride **2** to ketones and imines is not operating for imines.²⁰ The hydride species **2**, which reacts fast with ketones, does not react with imines. However, when an acid is added in the latter case a fast reduction occurs. These results support an ionic mechanism for the reduction of imines by **1**, where the substrate is pre-activated by protonation prior to H₂-transfer (inner-sphere mechanism).

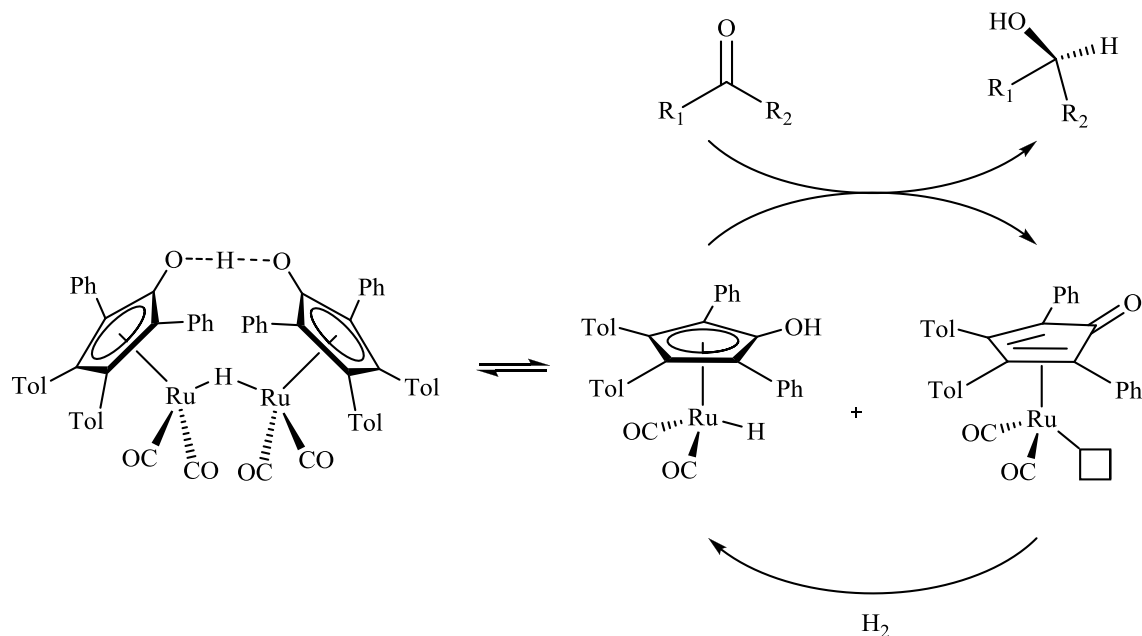


Figure 2: Shvo's catalyst and subsequent reaction with hydrogen and ketones

3.1.2 NPIL Pharma's Cp*Rh and Cp*Ir catalysts

CATHyTM (Chiral Asymmetric Transfer Hydrogenation) catalysts **4** and **5** (Figure 3) are highly efficient for the ATH of a broad range of ketones and imines to chiral alcohols and amines. An azeotropic mixture of 5:2 triethylamine and formic acid (TEAF)²¹ is used as the reducing agent, and the system can achieve similar conversions and enantioselectivities to Noyori's Ru(II)-TsDPEN catalyst.^{22,23} CATHyTM catalysts were developed at ICI's research laboratories at Huddersfield (now part of NPIL Pharma). The catalysts are prepared in-situ by combining a chiral bidentate nitrogen ligand with a Rh(III) or Ir(III) metal complex containing a substituted cyclopentadienyl ligand.²⁴

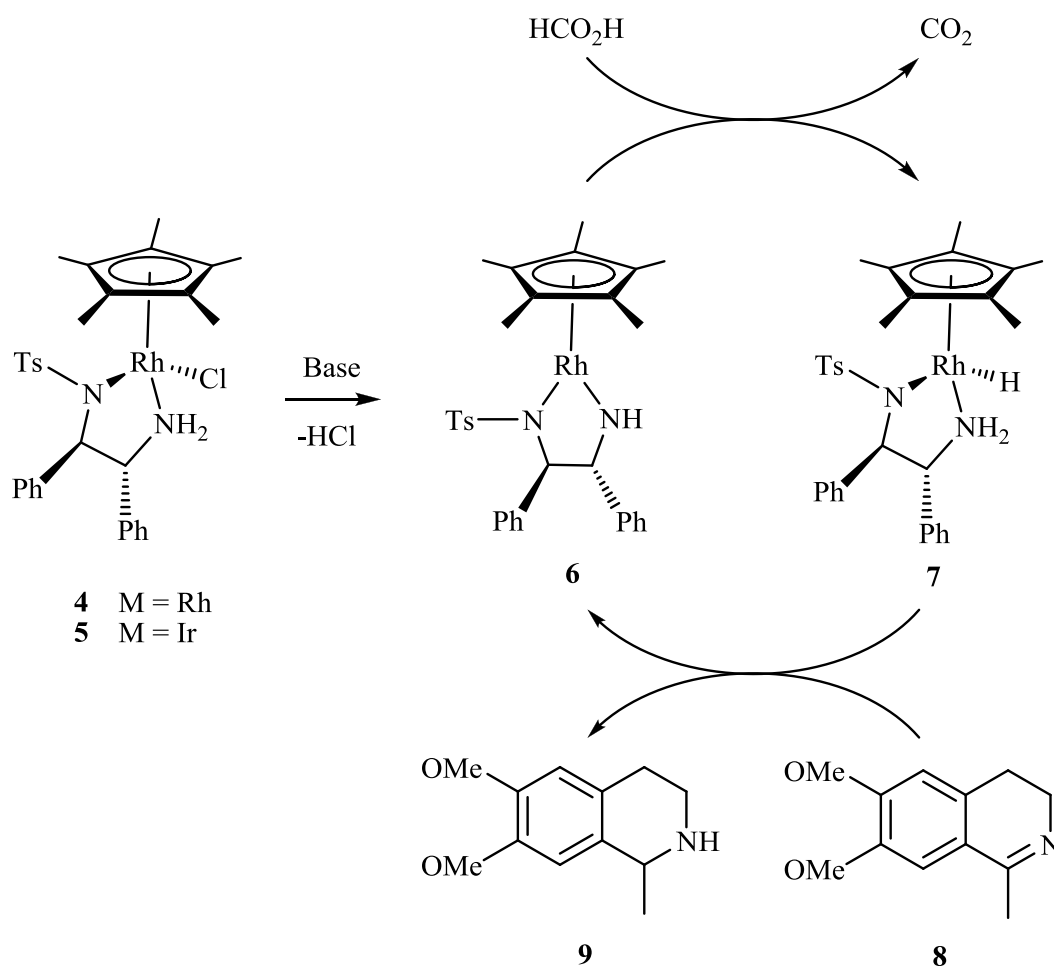


Fig. 3 Catalytic cycle for the reduction of imine **8** to amine **9** with TEAF as the reducing agent, highlighting the roles of the 16 electron 'reactive intermediate' **6** and the 18-electron 'true catalyst' **7**.

3.1.3 Reactivity of $\text{Cp}^*\text{Rh}(\text{Cl})(\text{TsNCHPhCHPhNH}_2)$ with formic acid

Grace observed that the reaction of $\text{Cp}^*\text{Rh}(\text{Cl})(\text{TsNCHPhCHPhNH}_2)$ with HCO_2H (10 equiv) in methanol at room temperature caused an immediate colour change of the solution from orange to red, and a red powder was isolated by adding 2 equiv of NaBPh_4 to a solution of the metal complex in methanol. An X-ray analysis confirmed formation of the triply bridged dimer $[\{\text{Cp}^*\text{Rh}\}_2(\mu\text{-H})(\mu\text{-Cl})(\mu\text{-HCO}_2)][\text{BPh}_4]$ (Figure 4). Related triply bridged cationic dimers of general formula $[\{\text{Cp}^*\text{Rh}\}_2(\mu\text{-H})(\mu\text{-OCOR})_2][\text{PF}_6]$ have been reported by Maitlis *et al.*²⁵

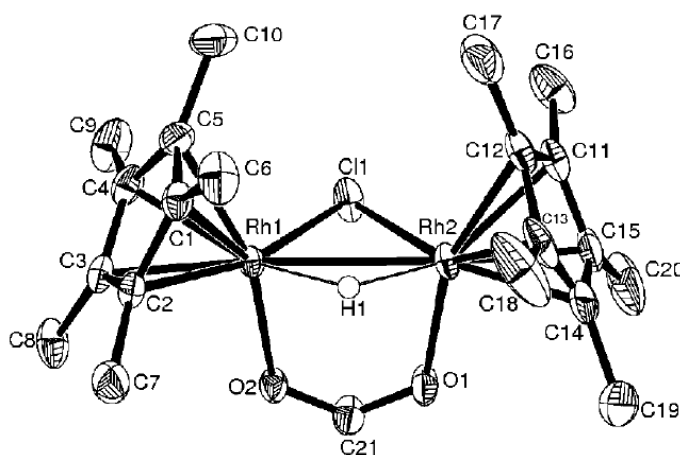


Figure 4 Molecular structure of the cation of Grace's complex, $[\{\text{Cp}^*\text{Rh}\}_2(\mu\text{-H})(\mu\text{-Cl})(\mu\text{-HCO}_2)]$.²⁶

The complex was also observed under catalytic conditions when formic acid is buffered by triethylamine. $[\{\text{Cp}^*\text{Rh}\}_2(\mu\text{-H})(\mu\text{-Cl})(\mu\text{-HCO}_2)][\text{BPh}_4]$ showed very poor activity for the transfer hydrogenation of the imine 6,7-dimethoxy-1-methyl-3,4-dihydroisoquinoline. However, the catalytic system of $[\{\text{Cp}^*\text{Rh}\}_2(\mu\text{-H})(\mu\text{-Cl})(\mu\text{-HCO}_2)]$ and free TsDPEN ligand gave activity and selectivity comparable to that of the former complex. Thus Grace *et al.* concluded that the reaction of $[\text{Cp}^*\text{Rh}(\text{Cl})(\text{TsNCHPhCHPhNH}_2)]$ with formic acid to form $[\{\text{Cp}^*\text{Rh}\}_2(\mu\text{-H})(\mu\text{-Cl})(\mu\text{-HCO}_2)]$ may occur to some extent under catalytic conditions despite the presence of triethylamine. Nevertheless, catalytic activity is not necessarily blocked because the presence of free chiral ligand may allow recovery of activity.²⁶

3.1.4 Ikariya's formato-amino complex

Ikariya *et al.* have shown that the 16-electron amide complex, (*p*-cymene)Ru[(*R,R*)-TsNCHPhCHPhNH], reacts quantitatively with formic acid at low temperature (below 243 K) to give the 18-electron formato-amino complex, (*p*-cymene)Ru(OCHO)[(*R,R*)-TsNCHPhCHPhNH₂] (**10**), as a single diastereomer as shown in Figure 5.²⁷ The ¹H NMR spectrum of the formato-amino complex, **10** displays two non-equivalent NH protons and a OCHO proton at $\delta = 6.28$, 8.96 ppm, and 8.19 ppm (THF-d₈, 243 K), respectively.

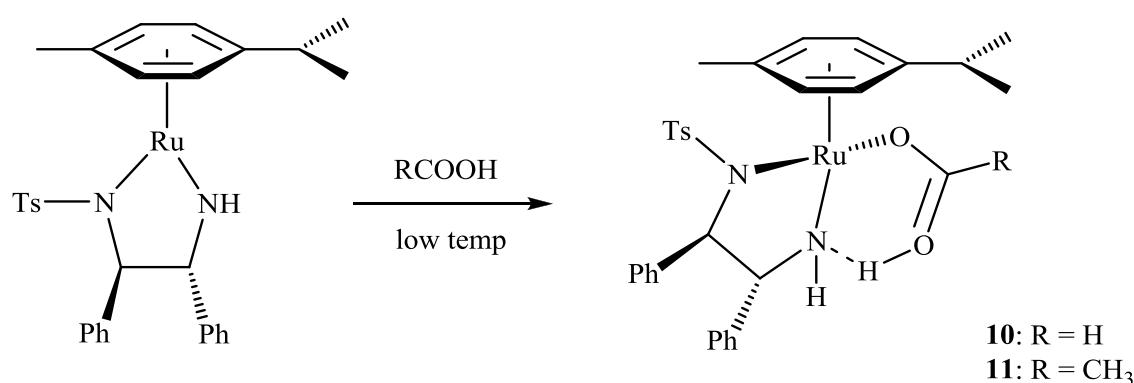


Figure 5 Reaction of 16-electron (*p*-cymene)Ru[(*R,R*)-TsNCHPhCHPhNH] with formic acid at 243 K to give the formate complex.²⁷

Their attempts to obtain single-crystal X-ray crystallographic analysis of the formate complex failed because of the thermal instability of **10**. An analogous acetate complex, (*p*-cymene)Ru(OCOCH₃)[(*R,R*)-TsNCHPhCHPhNH₂] **11**, was prepared from the reaction of the 16-electron amide complex and acetic acid in a manner similar to the synthesis of **10**. The X-ray crystallographic analysis of the acetate complex **11** is shown in Figure 6.²⁷

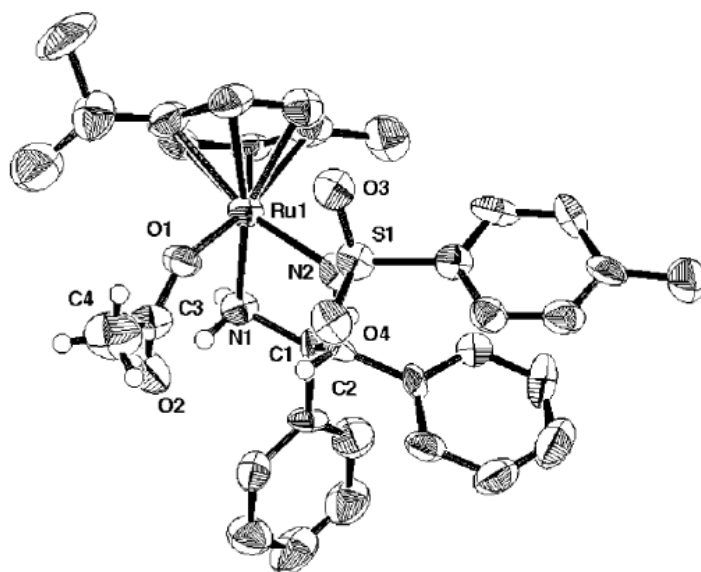


Figure 6 ORTEP of $(p\text{-cymene})\text{Ru}(\text{OCOCH}_3)[(\text{R,R-TsNCHPhCHPhNH}_2)]$.²⁷

The structure has a three-legged piano stool coordination environment and the chirality of the (R,R)-diamine ligand determines the S configuration around the central metal, as observed in the hydride complex discovered by Noyori. Interestingly, there is a short $\text{H}_2\text{N}\dots\text{O}=\text{C}$ distance of 2.77 Å, which they ascribed to an intramolecular hydrogen bond. Morris has also reported that the reaction of $\text{RuH}(\text{PPh}_3)_2(\text{NH}_2\text{CMe}_2\text{CMe}_2\text{NH})$ (Me = CH₃), with formic acid gave a similar hydrogen-bonded formate complex, *trans*- $\text{RuH}(\text{OCHO})(\text{PPh}_3)_2(\text{NH}_2\text{CMe}_2\text{CMe}_2\text{NH}_2)$, which was determined by single-crystal X-ray analysis as well as NMR and IR spectroscopy (Figure 7).

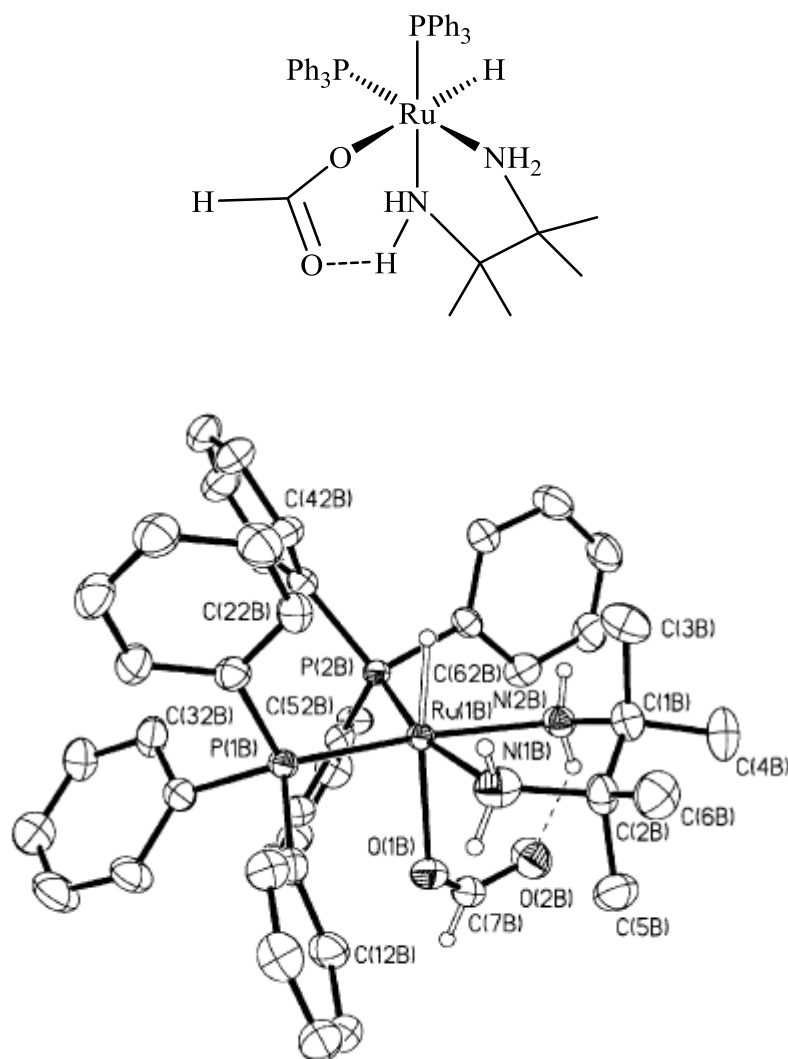
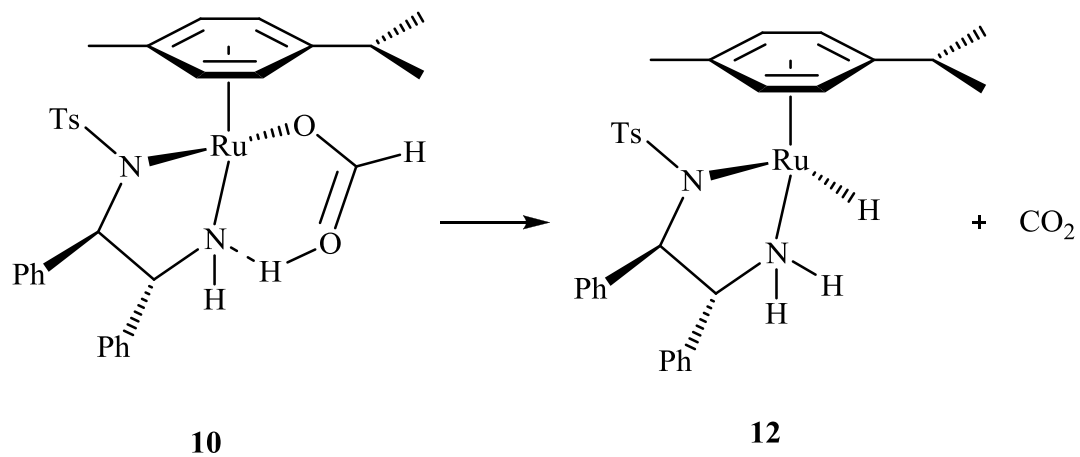


Figure 7 Morris' formate complex, $trans\text{-Ru(PPh}_3)_2(\text{H})(\text{tmen})(\text{OCHO})$.³⁹

The ^1H NMR spectrum of Ikariya's acetate complex **11** shows two non-equivalent NH protons at $\delta = 4.48$ and 9.59 ppm (CD_2Cl_2 , 273 K) similar to the formate complex **10**. The NH signal at the lower field ($\delta = 9.59$ ppm) was assigned to the NH proton that interacts with an oxygen atom of the acetate ligand in **11** possibly through hydrogen bonding as observed in related complexes.

Ikariya observed that an increase in the temperature of the formate complex **10** in THF-d_8 resulted in formation of **12** indicating that the hydride complex is formed through the decarboxylation of the intermediate **10** even under the conditions of catalytic asymmetric transfer hydrogenation (Figure 8). Based on the kinetic data involved with the negative entropy of activation value, there are three possible

pathways for the decarboxylation: formate anion dissociation leading to an ion pair; η^6 -arene ring slippage forming a η^4 -arene or NH_2 ligand dissociation, followed by β -hydrogen elimination.



$$\begin{aligned}\Delta H^\ddagger &= 76.0 \text{ kJ mol}^{-1} \\ \Delta S^\ddagger &= -37.7 \text{ J mol}^{-1} \text{ K}^{-1} \\ \Delta G^\ddagger (263.15 \text{ K}) &= 86.7 \text{ kJ mol}^{-1}\end{aligned}$$

Figure 8 Decarboxylation of the formate and kinetic data.

3.1.5 Rauchfuss and Heiden Mechanistic Work

Complexes of the type (arene)M(amido-amine) (M = Ru, Rh, Ir), developed by Noyori and co-workers have been shown to act as both transfer hydrogenation and direct hydrogenation catalysts.^{28,29} The ability of these complexes to effect both transfer hydrogenation and direct hydrogenation dramatically increases the breadth of possible substrates. Although the organic transformations performed by these catalysts have been studied for some time, little is known about their coordination chemistry.³⁰ Surprisingly, these complexes are not poisoned by water, which is the key to their recently reported catalytic activity in aqueous solution.

Heiden and Rauchfuss have demonstrated that exposure of a solution of $\text{Cp}^*\text{Ir}(\text{H})(\text{TsNCHPhCHPhNH}_2)$ to oxygen resulted in the generation of the 16-electron complex, $\text{Cp}^*\text{Ir}(\text{TsNCHPhCHPhNH})$ and one equivalent of water.³¹ The reduction of dioxygen was found to be catalytic in the presence of a hydrogen source such as alcohols and ammonia-boranes. Their discovery has been recently built-upon by Ikariya and co-workers in the area of oxidative chiral resolution of secondary alcohols.³² The reaction of the 18-electron iridium hydride complex with dioxygen is proposed to occur through a hydroperoxide intermediate (Figure 9).³³ They found that there was a direct correlation between the relative hydride donor ability of the metal complex and its reactivity toward dioxygen. The more strongly reducing metal hydride complexes³⁴ exhibited higher reaction rates with dioxygen.

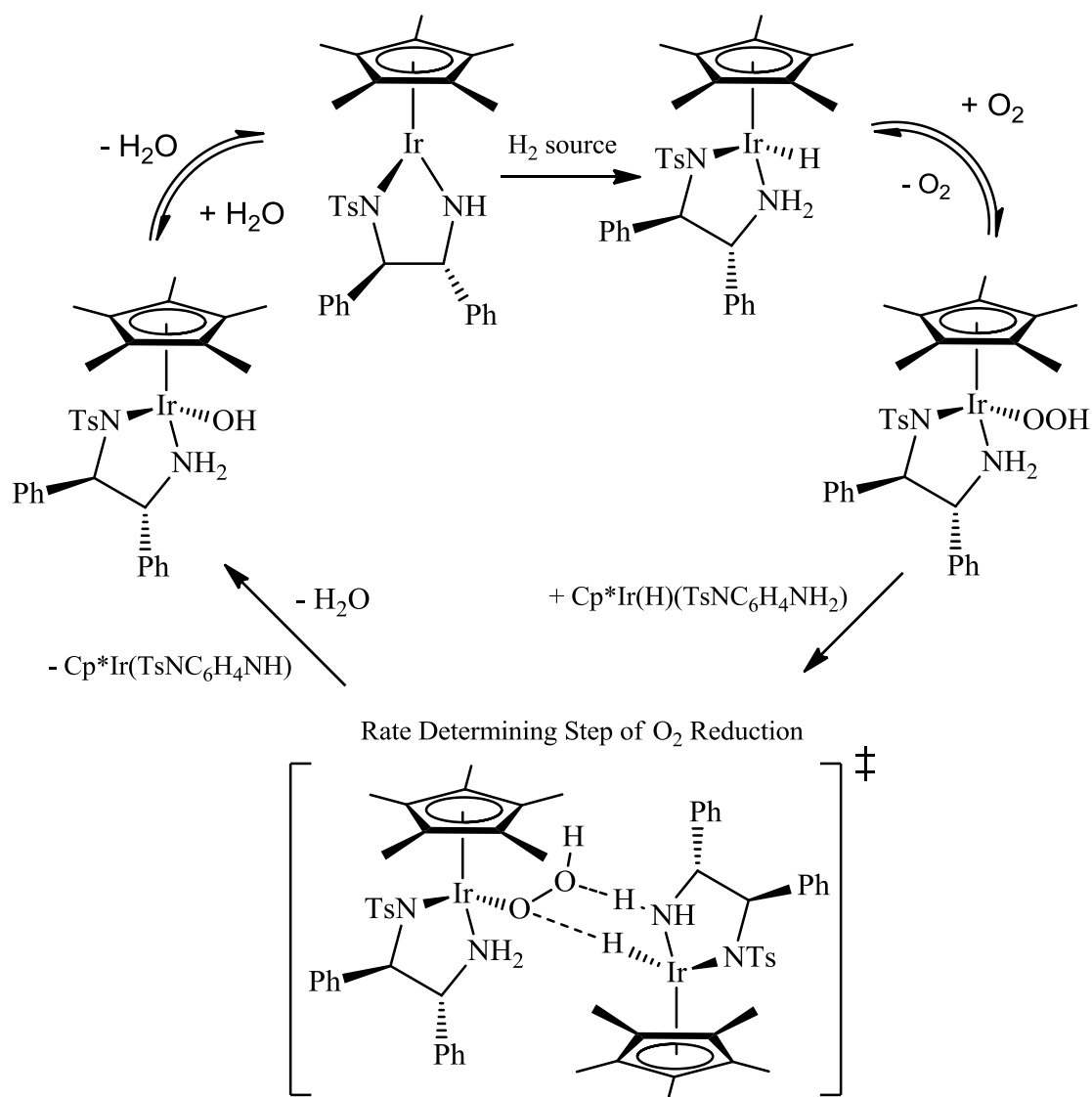


Figure 9 Proposed catalytic cycle for reduction of O₂ with Cp*IrH(TsDPEN)

Cp*Ir(TsNCHPhCHPhNH) is not Lewis acidic and does not readily react with H₂. However, the addition of a catalytic amount of acid promotes the conversion of the 16-electron complex to the 18-electron hydride. Indeed, acids with a *pK_a* three orders of magnitude less (*pK_a* about 10 in MeCN) than Cp*Ir(H₂)(TsDPEN)]⁺ (*pK_a* = 13.88 in MeCN) resulted in the fastest hydrogenation rate. Heiden and Rauchfuss used the 16-electron complex and a catalytic amount of acid to produce water from an atmosphere containing dihydrogen and dioxygen (Figure 10).

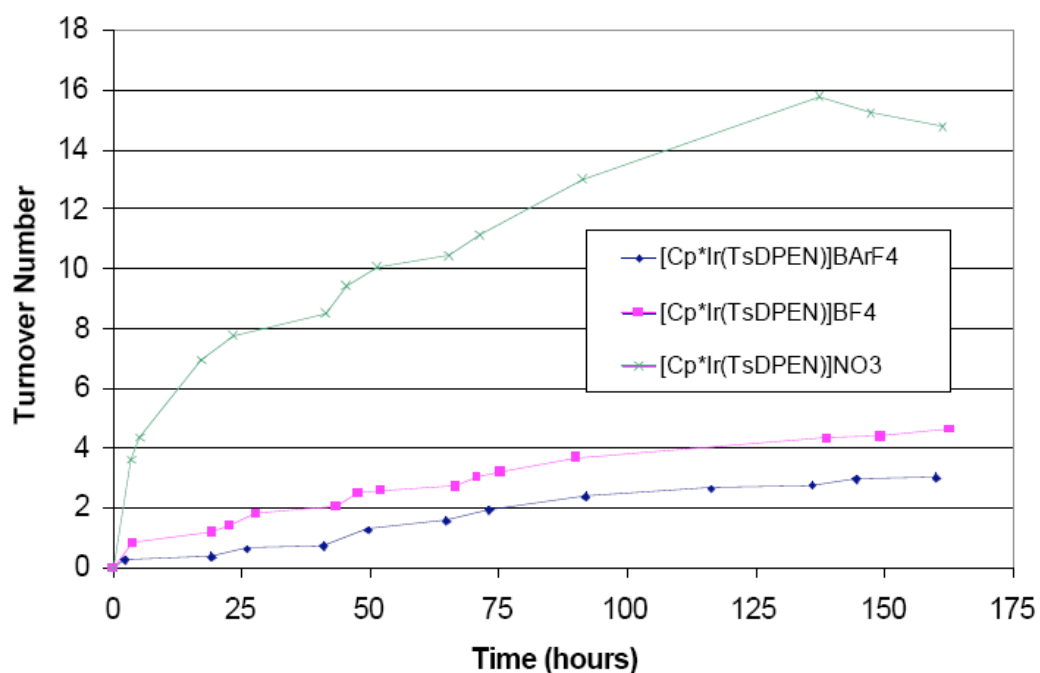


Figure 10 Turnover number against time for the production of water in methylene chloride- d_2 using 15 mol % of $[\text{Cp}^*\text{Ir}(\text{X})(\text{TsNCHPhCHPhNH}_2)]$ (where $\text{X} = \text{BARF}^{\text{F}}$, BF_4^- and NO_3^-) under an atmosphere of H_2 and O_2 .³⁵

3.1.6 Aims of Chapter

In this chapter the ability of 16-electron complexes of the type $\text{Cp}^*\text{M}(\text{XNC}_6\text{H}_4\text{NX}')$ ($\text{M} = \text{Rh}, \text{Ir}$; $\text{X}, \text{X}' = \text{H}$ or Ts) to catalyse the transfer hydrogenation of a cyclic imine was investigated. After identifying the relative rates for each complex an investigation was carried out to observe and isolate proposed key intermediates in the catalytic mechanism using $\text{Cp}^*\text{Rh}(\text{TsNC}_6\text{H}_4\text{NH})$.

3.2 Results and Analysis

3.2.1 Transfer hydrogenation of a cyclic imine with $\text{Cp}^*\text{Rh}(\text{TsNC}_6\text{H}_4\text{NH})$, $\text{Cp}^*\text{Rh}(\text{TsNC}_6\text{H}_4\text{NTs})$ and $\text{Cp}^*\text{Rh}(\text{HNC}_6\text{H}_4\text{NH})$

Grace observed that the 16-electron complex, $\text{Cp}^*\text{Rh}(\text{TsNC}_6\text{H}_4\text{NH})$ was an active catalyst for the *non-stereo specific* transfer hydrogenation of a cyclic imine, 6,7-dimethoxy-1-methyl-3,4-dihydroisoquinoline, using 1 mol equivalents of TEAF (2:5 $\text{NEt}_3:\text{HCO}_2\text{H}$) as the hydrogen donor in methanol- d_4 at 300 K (Figure 11).

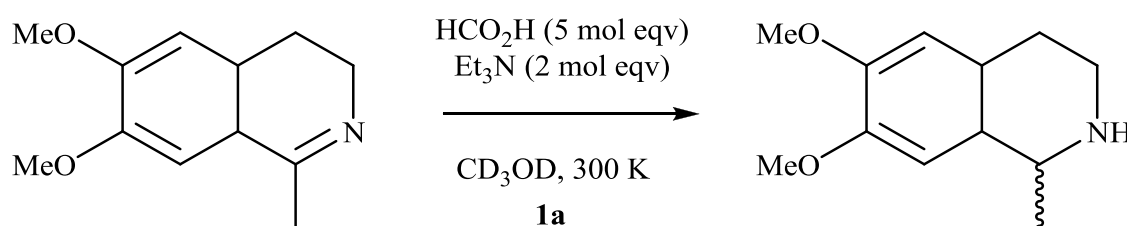


Figure 11 Transfer hydrogenation of 6,7-dimethoxy-1-methyl-3,4-dihydroisoquinoline with **1a** using 5 equivalents of triethylamine: formic acid (2:5) in methanol- d_4 at 300 K.

We examined the behaviour of the catalyst at [catalyst]/[substrate] ratios of 0.4, 0.7, 1.0, 1.5 and 2.0 mol% by following the reaction *in-situ* with ^1H NMR in methanol- d_4 at 300 K (Figure 12).³⁶ On addition of TEAF, the solution turned from violet-blue to yellow-orange. With 1 mol% catalyst, 50% of imine was converted to the amine within 40 minutes (in agreement with Grace's result). From our results in Figure 12 and Figure 13 we deduced that the reaction was first order with respect to [catalyst] but zero order with respect to [imine] up to 40% conversion.

The turnover frequency (TOF) of **1a** at 300 K was $94 \pm 5 \text{ mol h}^{-1} (\text{mol cat})^{-1}$. This value is about eight times less than that of $[\text{Cp}^*\text{RhCl}_2]_2-(\text{TsNHCHPhCHPhNH}_2)$ under the same conditions ($737 \pm 35 \text{ mol h}^{-1} (\text{mol cat})^{-1}$).³⁷ The rate for **1a** in methylene chloride- d_2 was greater than in methanol- d_4 (50% conversion within 20 minutes) (Figure 14).

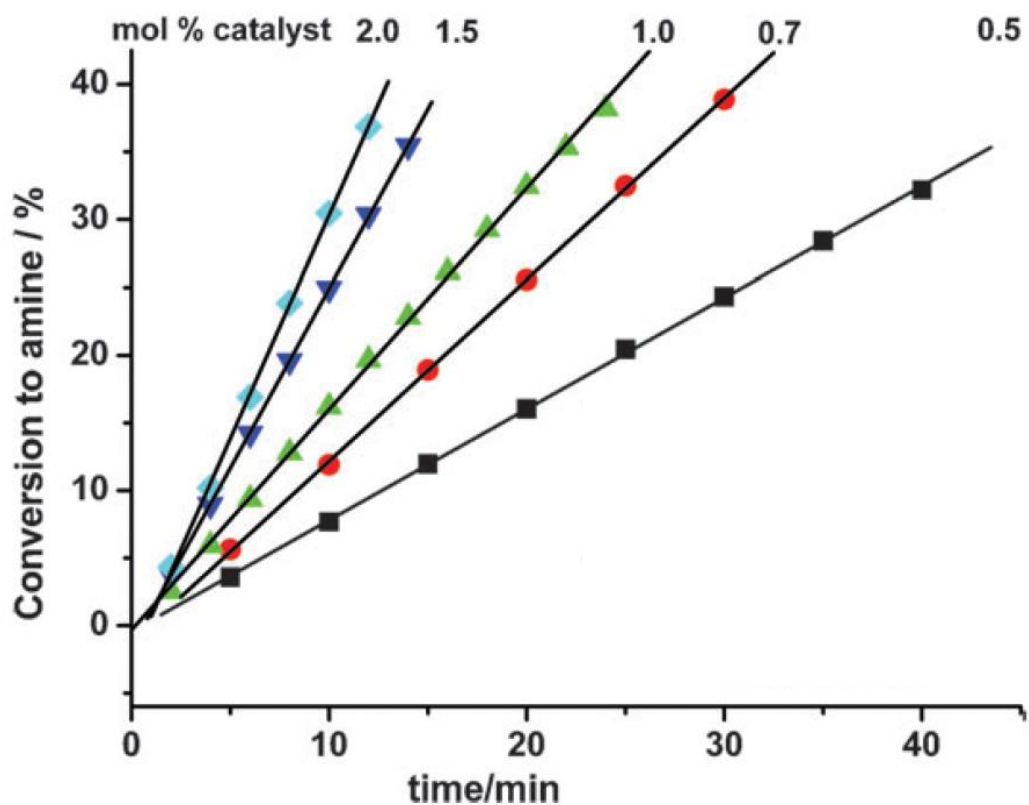


Figure 12 Conversion of imine to amine (%) against time for various [1a]/substrate ratios.³⁶

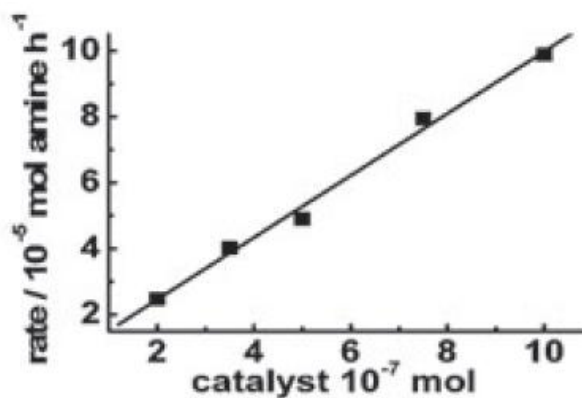


Figure 13 Rate of conversion of imine to amine against [1a] in methanol-d₄ at 300 K.³⁶

The catalytic activities of **1a**, Cp*Rh(TsNC₆H₄NTs) (**1b**) and Cp*Rh(HNC₆H₄NH) (**1c**) were compared in methylene chloride-d₂ because **1b** is insoluble in methanol-d₄ with 1 mol% catalyst and were found to be **1a** > **1b** ~ **1c**. The results are shown in Figure 14.

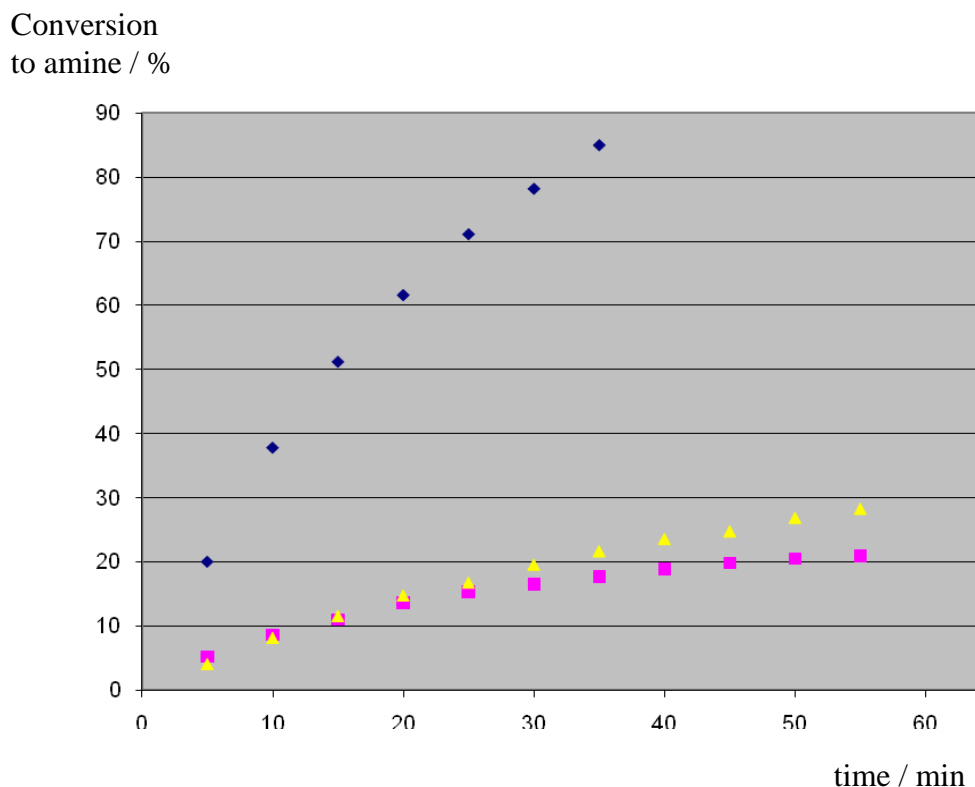


Figure 14 Rate of conversion of imine to amine using **1a** (top, blue), **1b** (middle, yellow) and **1c** (bottom, pink) in methylene chloride-d₂.

3.2.2 Transfer hydrogenation of a cyclic imine with Cp*Ir(TsNC₆H₄NH) (**1d**) and Cp*Ir(TsNC₆H₄NTs) (**1e**)

We identified that Cp*Ir(TsNC₆H₄NH) (**1d**) and Cp*Ir(TsNC₆H₄NTs) (**1e**) are both catalytically active for the transfer hydrogenation of 6,7-dimethoxy-1-methyl-3,4-dihydroisoquinoline in acetonitrile-d₃ (Figure 15). The results show that the catalytic activity for the 16-electron complexes follow the order Cp*Rh(TsNC₆H₄NH) > Cp*Ir(TsNC₆H₄NTs) > Cp*Rh(TsNC₆H₄NTs) > Cp*Ir(TsNC₆H₄NH).

Percentage conversion of an imine to an amine catalysed by 16 e⁻ Cp^{*}Rh(III) and Cp^{*}Ir(III) complexes (1 mol % catalyst loading, 5 mol eqv. of TEAF with respect to HCO₂H)

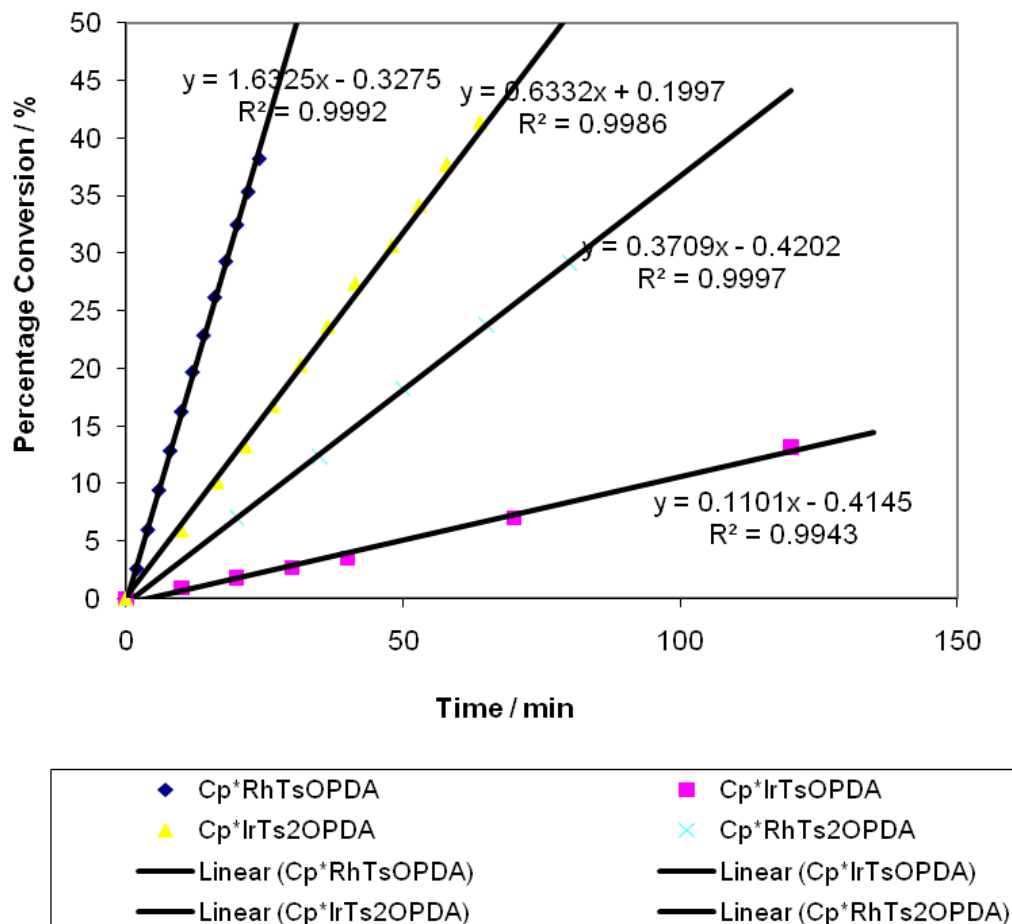


Figure 15 Rate of conversion of the cyclic imine, 6,7-dimethoxy-1-methyl-3,4-dihydroisoquinoline to the corresponding amine using **1d** and **1e** in acetonitrile-d₃

3.2.3 Catalytic decomposition of formic acid

Interestingly, after imine hydrogenation was complete, catalytic decomposition of formic acid to CO₂ and H₂ was observed. Upon completion, **1a** was recovered and the solution returned to the violet-blue colour. Since the colour of **1a** is lost during catalysis but reappears on completion (in methanol-d₄) we infer that **1a** is not the resting state.

3.2.4 Catalytic activity of 4,5-dimethyl 16-electron Rhodium complex

We examined how adding substituents on the *o*-phenylenediamine ligand affected the catalytic activity of the 16-electron rhodium complex. The 4,5-dimethyl complex, $\text{Cp}^*\text{Rh}(\text{TsNC}_6\text{H}_2(\text{Me})_2\text{NH})$ was tested at [catalyst]/[substrate] ratios of 0.4, 0.7, 1.0, 1.5 and 2.0 mol% using the same conditions as previously tested for the $\text{Cp}^*\text{Rh}(\text{TsNC}_6\text{H}_4\text{NH})$ catalyst. The catalytic activity of the 4,5-dimethyl substituted complex (125 mol amine h^{-1} per mol of catalyst) was found to be greater than the non-substituted 16e rhodium complex, $\text{Cp}^*\text{Rh}(\text{TsNC}_6\text{H}_4\text{NH})$ catalyst (90 mol amine h^{-1} per mol of catalyst) (Figure 16).

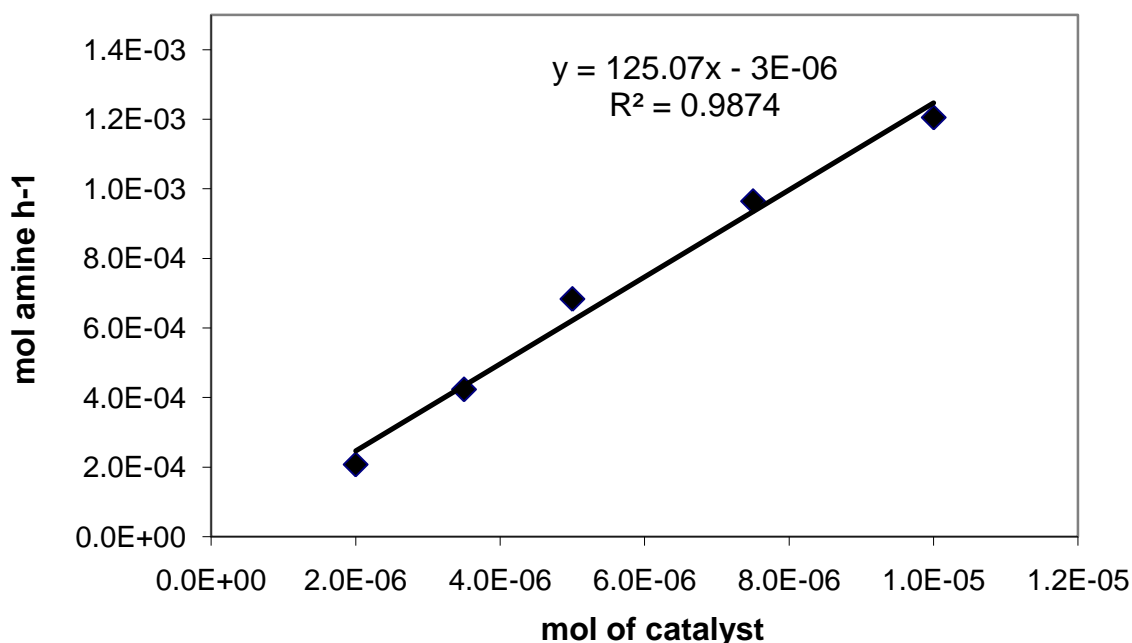


Figure 16 Rate of conversion of imine to amine against concentration of 4,5-dimethyl complex, $\text{Cp}^*\text{Rh}(\text{TsNC}_6\text{H}_2(\text{Me})_2\text{NH})$ in methanol- d_4 at 300 K (125 mol amine h^{-1} per mol of catalyst)

By adding $-I$ groups such as chlorine, the catalytic activity was slower than the unsubstituted 16-electron TsOPDA complex. Therefore it appears the rate can be increased by adding $+I$ groups such as methyl and slowed by adding $-I$ groups such as chlorine. Presumably, the increased electron density in the delocalised ring can increase the nucleophilicity of the lone pair of electrons on the nitrogen.

3.2.5 Synthesis and characterisation of 18-electron chloride, Cp*Rh(Cl)(TsNC₆H₄NH₂)

The direct synthesis of the 16-electron complex Cp*Rh(TsNC₆H₄NH), **1a** and its slower activity in transfer hydrogenation allowed us to investigate key specific steps relevant to catalysis. From Chapter Two, we have identified that Cp*Rh(TsNC₆H₄NH), **1a** incorporates π -stabilized unsaturation and consequently has a latently Lewis acidic metal centre and a coordinated nitrogen atom that is also a Brønsted base. These adjacent functionalities allow the amido complexes to react with various pronucleophiles in a concerted or stepwise manner, giving the 18-electron amine complexes with a Brønsted acidic amine proton and potentially nucleophilic ligand.

In the attempt to isolate the related 18-electron precursor complex observed for the Noyori-type ‘TsNCHPhCHPHNH₂’ series of catalysts, **1a** was reacted with 1 equivalent of hydrochloric acid in ether solution at 300 K in methylene chloride-d₂. Upon reaction at room temperature, complex **1a** reacted rapidly with the hydrochloric acid to give a mixture of the [Cp*RhCl₂]₂ dimer, free ligand and unreacted complex, **1a**. An alternative strategy was devised in which **1a** was reacted with hydrochloric acid in ether solution at low temperature. On following the reaction by ¹H and ¹³C NMR spectroscopy at 193 K, we observed quantitative formation of the 18-electron chloride, Cp*Rh(Cl)(TsNC₆H₄NH₂), **2a** (Figure 17).

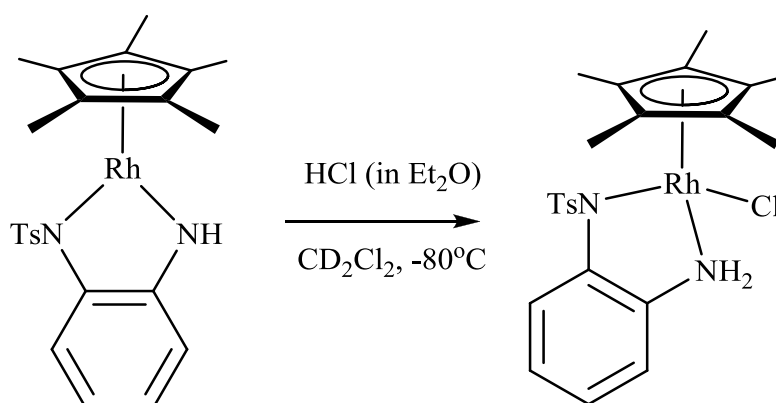


Figure 17 Synthesis of 18-electron chloride ‘precursor’ complex from **1a** and HCl in ether and methylene chloride-d₂ at 193 K.

The ^1H NMR spectrum of **2a** displays two non-equivalent NH protons at $\delta = 4.39$ and 5.27 (methylene chloride- d_2 , 193 K). The peaks are broad doublets (Figure 18). Also, the Cp* peak has shifted upfield from $\delta = 1.98$ (for the 16-electron complex, **1a**) to $\delta = 1.68$ (**2a**).

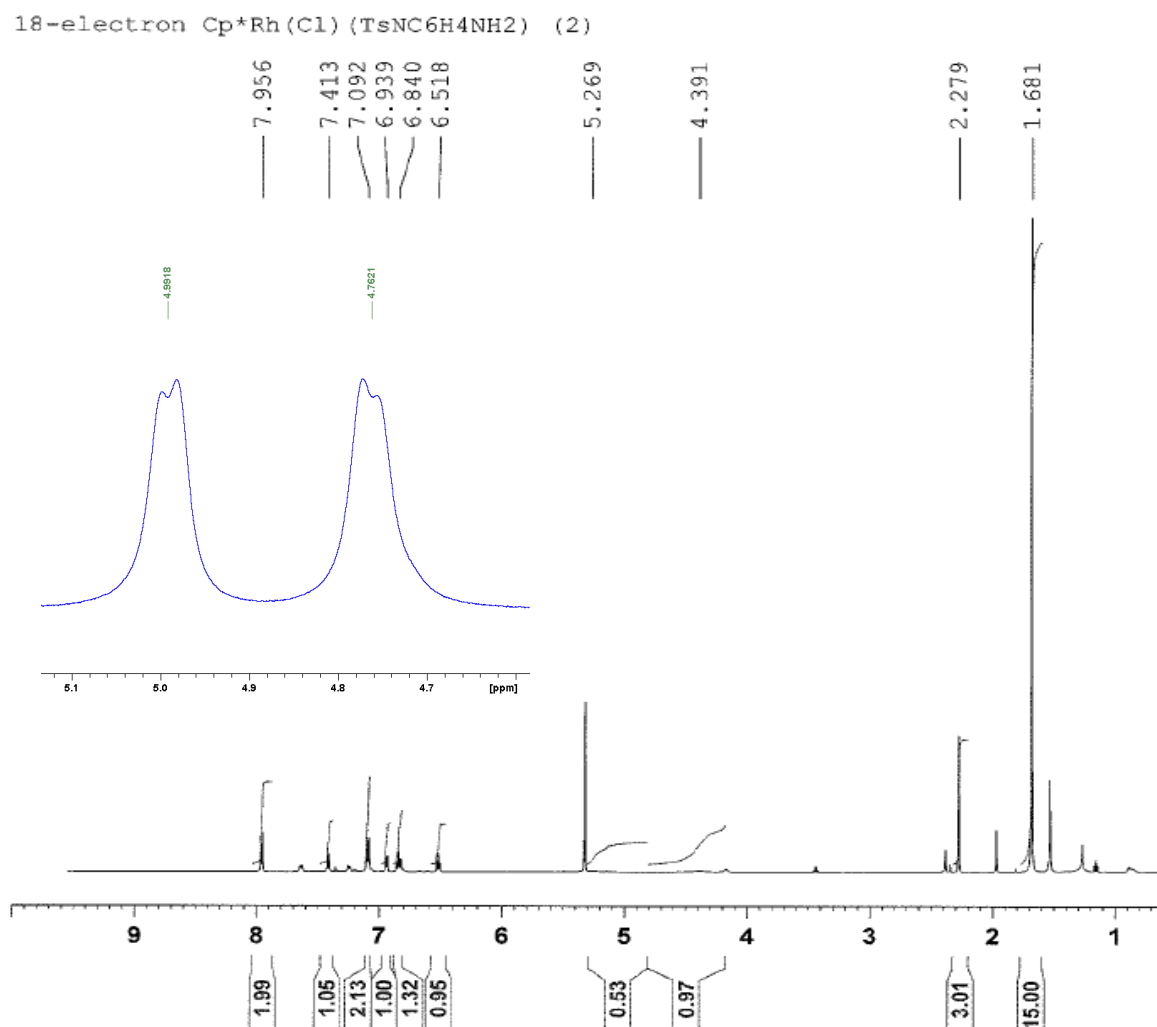


Figure 18 ^1H NMR spectrum of **2a** at 193 K, showing broad doublets for the two non-equivalent NH_2 protons.

X-ray quality crystals of **2a** were grown by layering the NMR solution with diethylether and leaving the solvents to diffuse for 5 days. Complex **2a** was characterised by X-ray crystal analysis (Figure 19). Table 1 compares its structure to those of the 16-electron complexes **1a**, **1b** and **1c**, characterised earlier in this study.

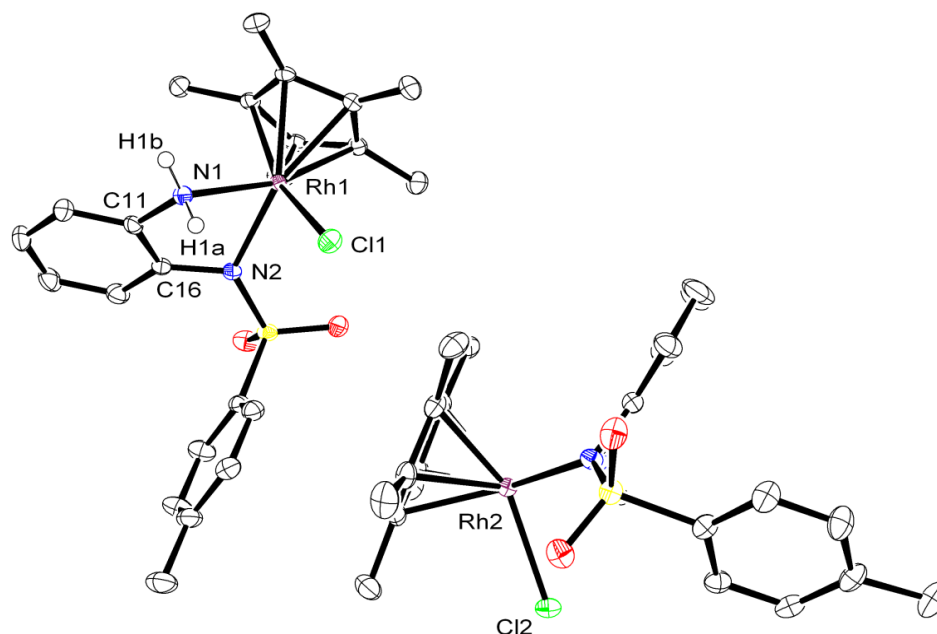


Figure 19 Molecular structure of $\text{Cp}^*\text{Rh}(\text{Cl})(\text{TsNC}_6\text{H}_4\text{NH}_2)$, **2a** (two molecules in asymmetric unit), hydrogens omitted except NH_2 .

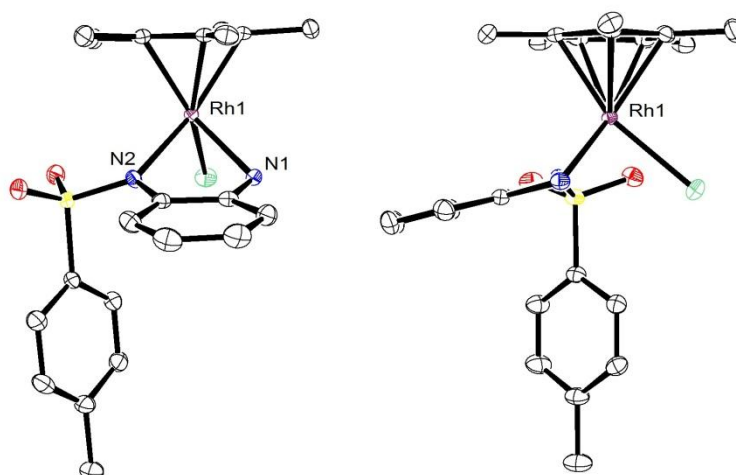


Figure 19b Two mutually perpendicular views of molecular structure of $\text{Cp}^*\text{Rh}(\text{Cl})(\text{TsNC}_6\text{H}_4\text{NH}_2)$, **2a**, hydrogens omitted for clarity.

bond	Complex			
	(1a)	(1b)	(1c)	(2a)
M-N(1)	1.9372(15)	2.0403(19)	1.9833(18)	2.1456(14)
M-N(2)	2.0796(14)	2.0435(19)	1.9722(19)	2.1515(14)
$\Delta r(\text{M-N})^a$	0.1426(10)	0.0032(13)	0.0111(13)	0.0059(10)
N(1)-C(11)	1.369(2)	1.421(3)	1.361(3)	1.448(3)
N(2)-C(16)	1.413(2)	1.422(3)	1.364(3)	1.412(3)
C(11)-C(16) ^b	1.416(2)	1.404(3)	1.423(3)	1.405(3)
θ_{oop}^c	0.03°	8.40°	1.18°	37.85°
θ_{tilt}^d	0.82°	20.98°	2.19°	39.10°

Table 1 X-ray diffraction data for Cp*Rh(Cl)(TsNC₆H₄NH₂), **2a**.

The Rh-N bond distances for **2a** are longer than in **1a** and the difference between $r(\text{Rh-N1})$ and $r(\text{Rh-N2})$ (0.0059(10) Å) is insignificant (Table 1). Moreover, θ_{oop} and θ_{tilt} deviate significantly from planarity ($\theta_{\text{oop}} = 37.85^\circ$, $\theta_{\text{tilt}} = 39.10^\circ$) consistent with the loss of Rh-N π -bonding. The amine hydrogen atoms were located in a difference map and refined isotropically, thereby demonstrating the presence of the intramolecular NH \cdots Cl hydrogen bond (average 2.63(3) Å). Table 2 compares **2a** to other related complexes.²⁶ Interestingly, when compared to the other related 18-electron ATH complexes, **2a** does not appear to have significantly longer Rh-N bonds to the amido nitrogen than the amino nitrogen. In the other complexes in Table 2 the Rh-NH₂ bond length is invariably shorter than the Rh-NTs bond length. Complex **2a** is unstable with respect to **1a** in contrast with the stabilities of their analogues that contain CHPhCHPh in place of the C₆H₄ ring.

Complex **2a** crystallizes with two independent molecules in the asymmetric unit which have opposite chirality at the Rh. In the crystal packing structure there is an extended network of hydrogen bonds between Rh-Cl \cdots HN and NH \cdots O=S (Figure 20 and Figure 21). It has been suggested that [(arene)Ru(monotosylamidoamine)] complexes form dimers in solution through hydrogen bonding between the NH

protons of one molecule and a sulfonyl oxygen of another, or between the NH protons of one molecule and the chloride of a second.³⁸

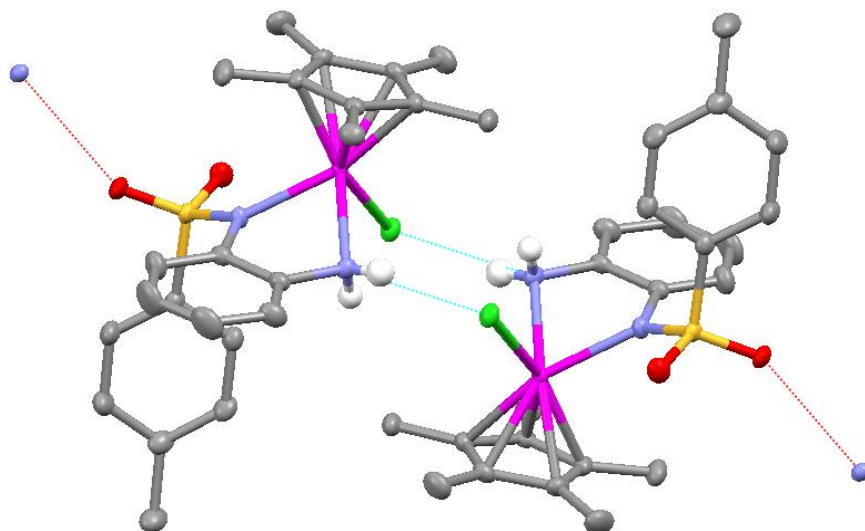


Figure 20 Hydrogen bonding in, Cp*Rh(Cl)(TsNC₆H₄NH₂), **2a**

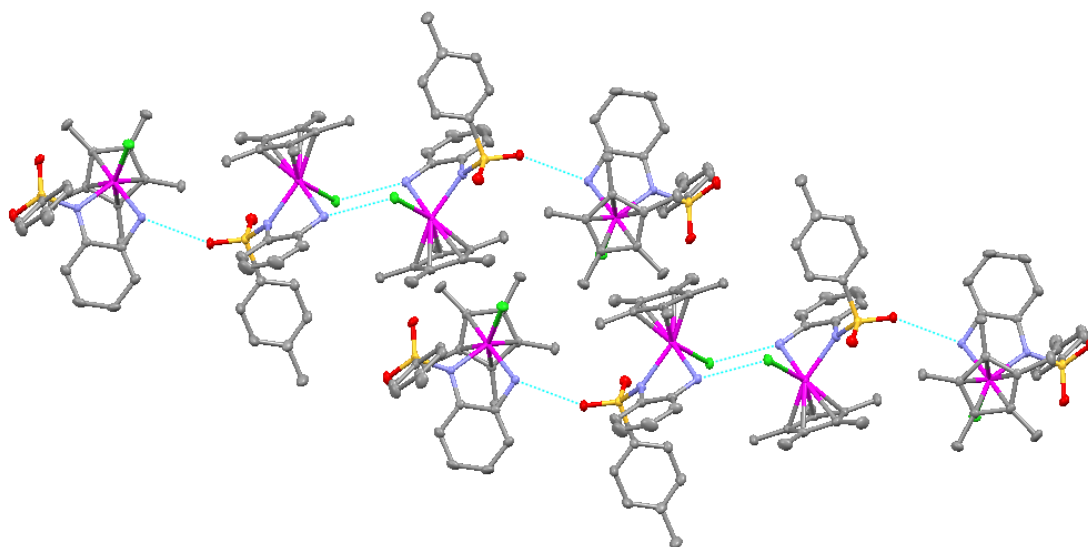


Figure 21 Extended hydrogen bonding in crystal packing structure.

3.2.6 Reactivity of $\text{Cp}^*\text{Rh}(\text{TsNC}_6\text{H}_4\text{NH})$ with HCO_2H

When complex **1a** was reacted with formic acid (1 mol equivalent) either in methylene chloride- d_2 or in methanol- d_4 at 193 K, an 18-electron formate complex, $\text{Cp}^*\text{Rh}(\text{OCHO})(\text{TsNC}_6\text{H}_4\text{NH}_2)$, **3a** was formed quantitatively (Figure 22).

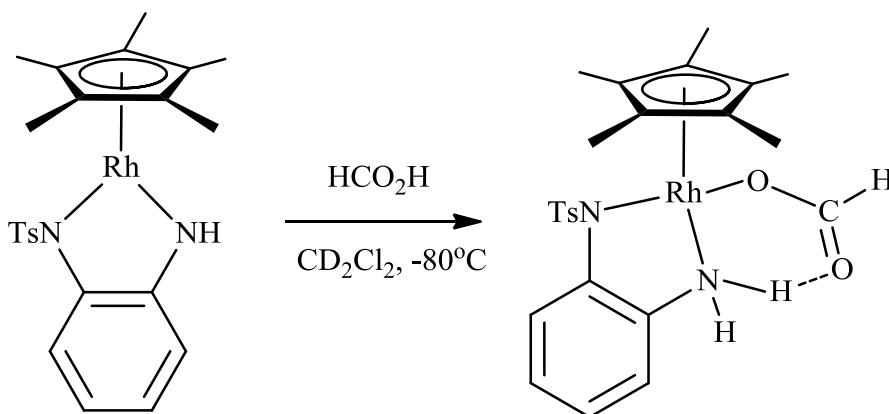


Figure 22 Synthesis of 18-electron formato-amino complex from **1a** and formic acid or TEAF solution in methylene chloride- d_2 at 193 K.

Its ^1H and ^{13}C NMR spectra at 193 K were fully consistent with those of Ikariya's ruthenium formato and acetate analogues.²⁷ The ^1H NMR spectrum of **3a** shows two inequivalent mutually coupled NH_2 protons (CD_2Cl_2 , $\delta = 4.92$ and 8.35 , $^2J_{\text{HH}} = 9$ Hz) (Figure 23). The deshielded hydrogen is presumed to interact with the formic oxygen forming a 6-membered ring as observed by Morris for *trans*- $\text{Ru}(\text{PPh}_3)_2(\text{H})(\text{tmen})(\text{OCHO})$.³⁹ The formate hydrogen is a singlet (δ 8.70), consistent with a Rh-O bond.

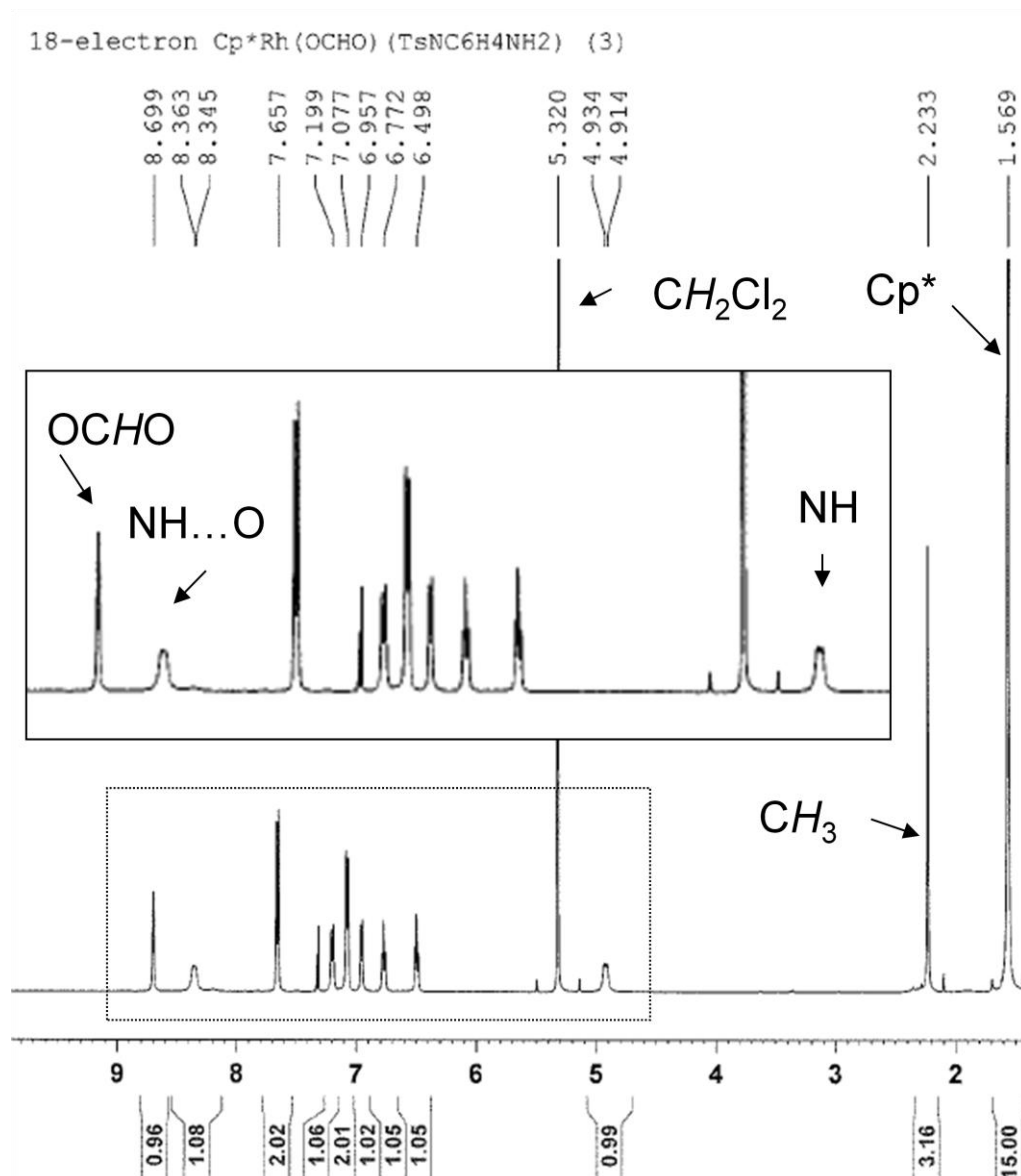


Figure 23 ^1H NMR spectrum of formato-amino complex (with expanded aromatic region).

Upon warming to 300 K, **3a** converted to **1a**, H_2 and CO_2 . Both $\text{H}_{2(\text{g})}$ (singlet at $\delta_{\text{H}} = 4.59$ ppm) and $\text{HD}_{(\text{g})}$ (triplet at $\delta_{\text{H}} = 4.55$ ppm with coupling constant $J_{\text{HD}} = 43$ Hz) were detected by ^1H NMR spectroscopy in methanol- d_4 (Figure 24). This indicates that the 16-electron complex is catalytically decomposing formic acid into hydrogen and carbon dioxide without the aid of imine or base in the system. Furthermore, when complex **1a** was reacted with 2:5 triethylamine:formic acid (TEAF) solution at 193 K, the ^1H NMR spectrum was fully consistent with the formation of the same

18-electron formate complex **3a**. Complex **3a** again regenerated **1a** and H₂ on warming to room temperature.

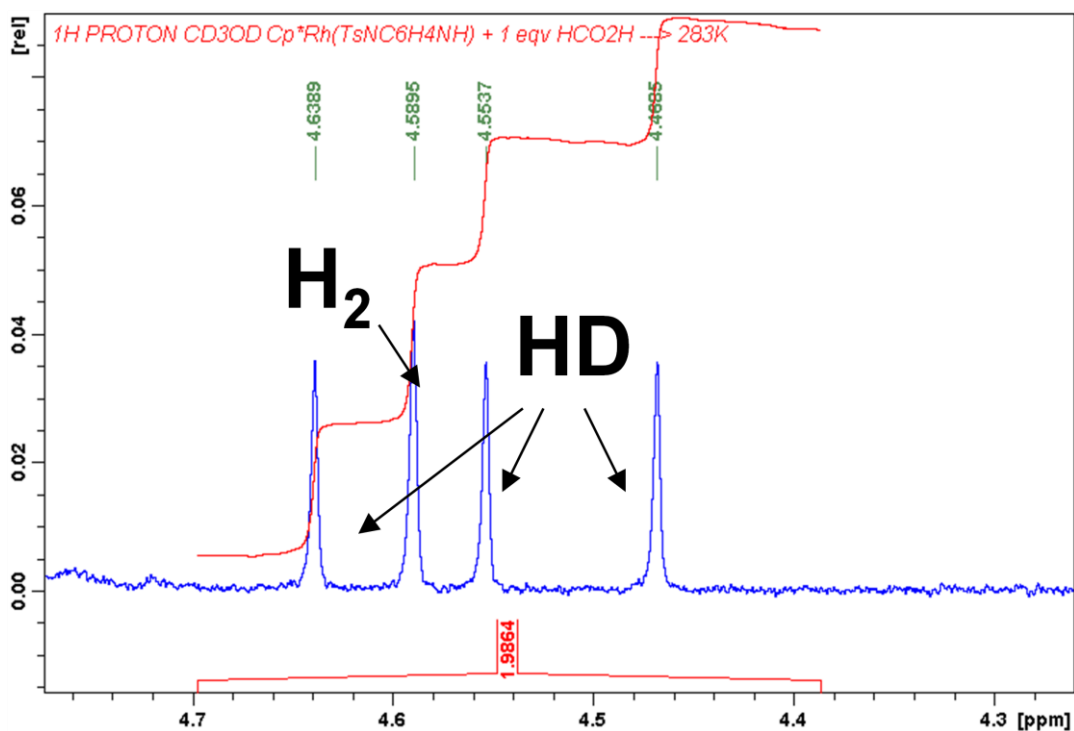


Figure 24 ¹H NMR spectrum of H_{2(g)} and HD_(g) evolved by warming formato-amino complex, **3a** from 193 K to 300 K.

The formation of the formate complex in the presence of TEAF at low temperature suggests that it has a catalytic role, in contrast to the “outer-sphere” mechanism proposed by Noyori for ruthenium ATH complexes.

3.2.7 Characterisation of 18-electron hydride, Cp**Rh*(H)(TsNC₆H₄NH₂)

When the formato-amino complex **3a** was warmed from 193 K to 273 K in methylene chloride-d₂, a doublet was detected in the hydride region of the ¹H NMR spectrum at δ -8.81 (Figure 25 and Figure 26). The hydride doublet peak has a splitting of J_{RhH} = 22 Hz, which is indicative of a rhodium-hydride coupling. A new Cp* peak at δ_H = 1.87 integrates to a 1:15 ratio with the hydride peak and subsequently disappears along with the hydride when the temperature is increased over 273 K. A new peak at δ_H = 2.45 integrates 3:1 with the hydride and is assigned

as the tosyl methyl peak. These results are consistent with other rhodium asymmetric transfer hydrogenation catalysts. Grace synthesised the 18 electron hydride complex, $\text{Cp}^*\text{Rh}(\text{H})(\text{TsNCHPhCHPhNH}_2)$, that had a hydride chemical shift at -9.42 ppm with $J_{\text{Rh-H}} = 22\text{Hz}$ which is similar to the $\text{Cp}^*\text{Rh}(\text{H})(\text{TsNC}_6\text{H}_4\text{NH}_2)$ hydride at -8.81 ppm with $J_{\text{Rh-H}} = 22\text{Hz}$.³⁷

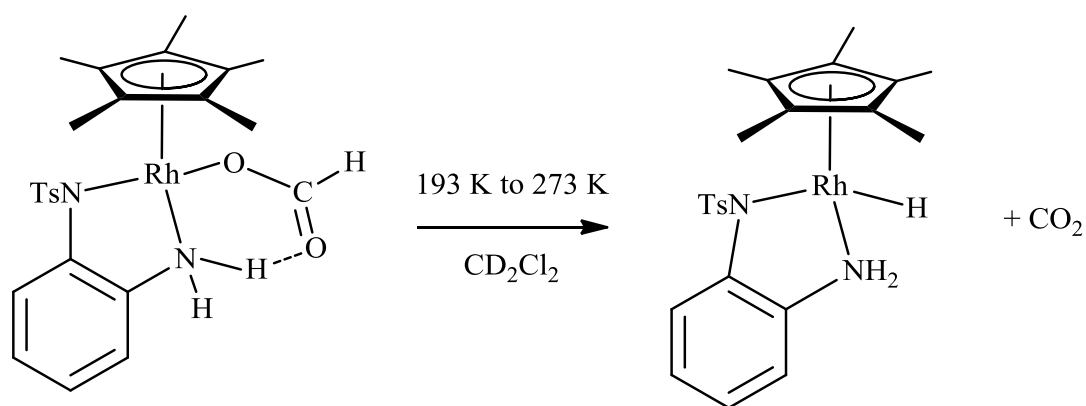


Figure 25 Conversion of formato-amino to hydride complex.

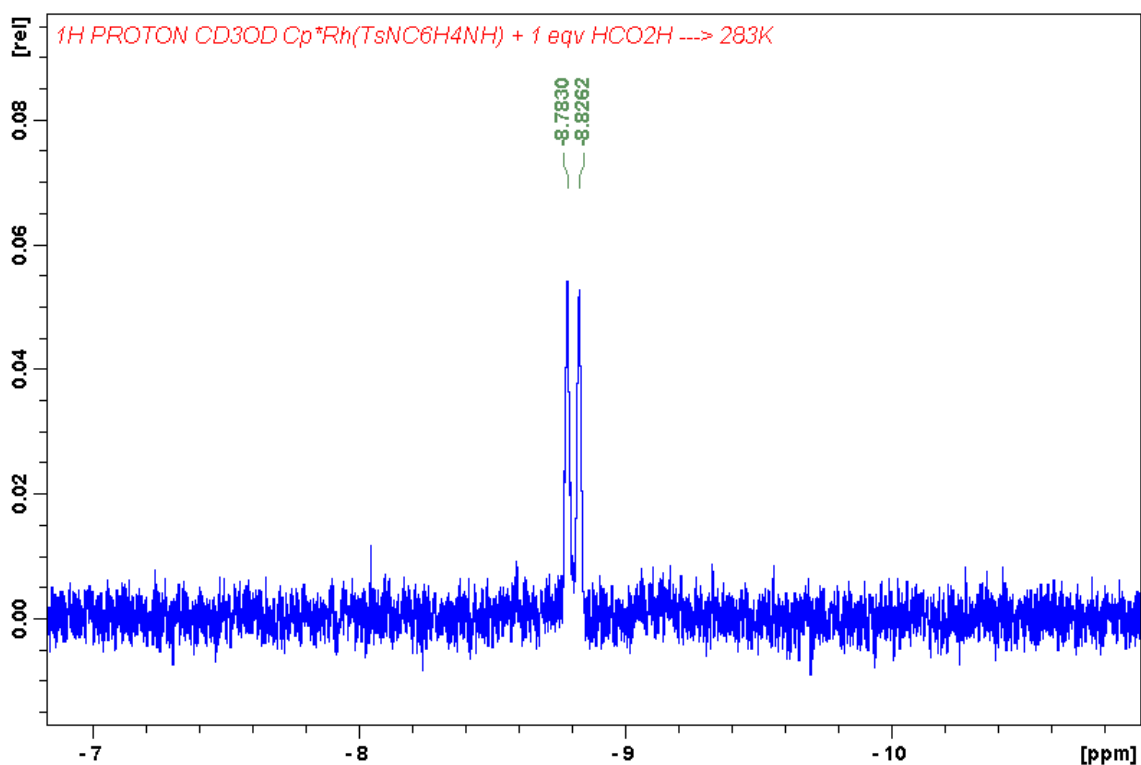


Figure 26 ^1H NMR of hydride peak for **4a** in methylene chloride- d_2 at 273 K.

An analogous experiment conducted in THF- d_8 for increased solubility at 233 K enabled us to assign the species that produces this signal *via* 2D experiments as $\text{Cp}^*\text{Rh}(\text{H})(\text{TsNC}_6\text{H}_4\text{NH}_2)$ **4a**. A ^1H - ^{103}Rh correlation established molecular connectivity of the hydride which now appeared at δ -9.51 (1H) to NH_2 (δ 5.46 and 6.05, each 1H) and Cp^* (δ 1.96, 15H) resonances (Figure 27). The ^{103}Rh peak appeared at δ 1472 ppm. The remaining ^1H resonances **4a** were also detected using ^1H - ^1H COSY.

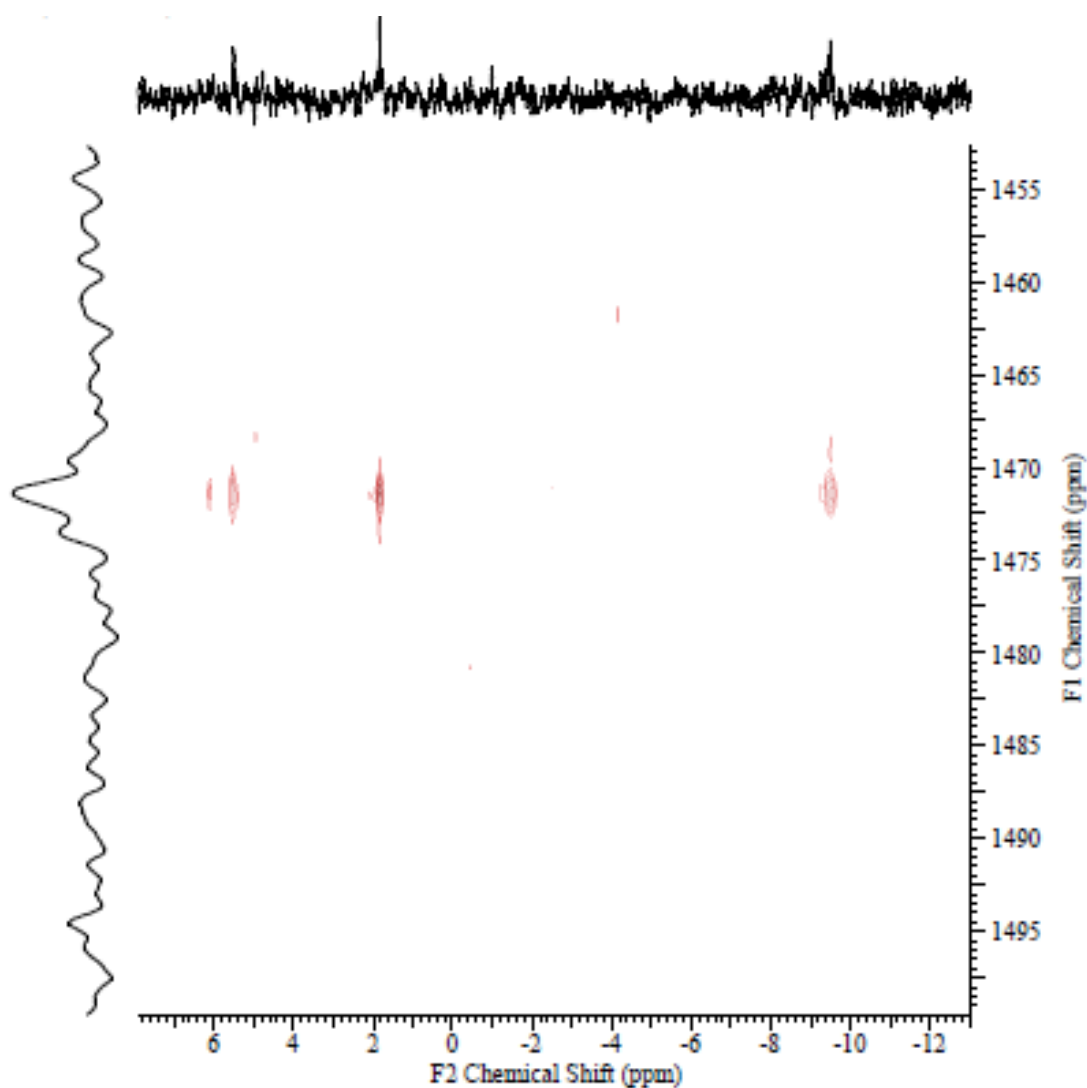


Figure 27 HSQC ^1H - ^{103}Rh for $\text{Cp}^*\text{Rh}(\text{H})(\text{TsNC}_6\text{H}_4\text{NH}_2)$, **4a**

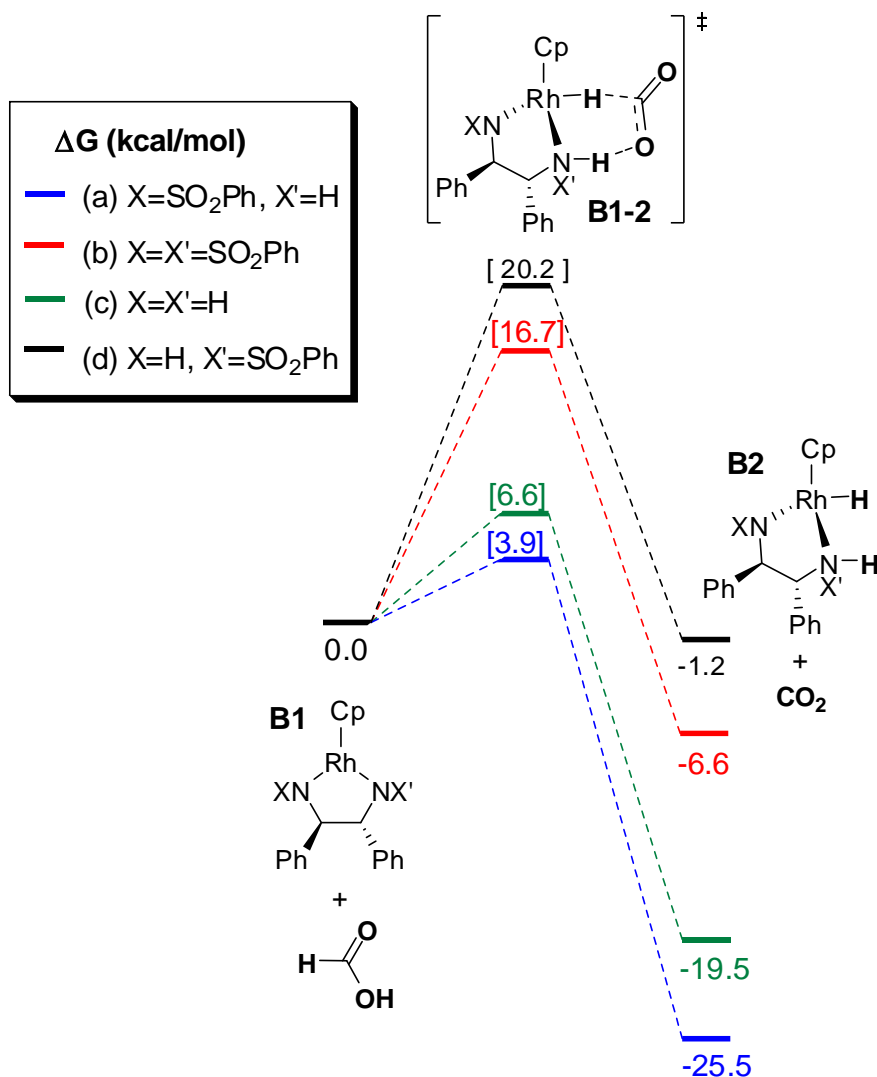


Figure 29 DFT calculation on hydrogenation of Cp*Rh(XNCHPhCHPhNX')

Odile Eisenstein has also performed similar calculations that show hydrogenation of Cp*Rh(XNCHPhCHPhNX') (where X, X' = H, Ts) (**B1**) by formic acid to form the 18-electron hydride products is thermodynamically favourable for **a** and **b**, but not as much for **c** and **d** (Figure 29). The reaction is again proposed to proceed through an outer-sphere mechanism. The barriers for the hydrogenation of Cp*Rh(XNCHPhCHPhNX) are much lower compared to that of **1a**, **1b** and **1c** which may explain the greater catalytic activity of the TsNCHPhCHPhNH ligands compared to that of the TsNC₆H₄NH ligands.

An alternative pathway was proposed in which the formate and NH_2 decoordinate from the rhodium centre to form a new reaction intermediate, **A5** (Figure 30). For this pathway we can exclude the inner sphere mechanism with **ATS4-5** due to its high energy barrier. $\text{Cp}^*\text{Rh}(\text{XNCHPhCHPhNX}') (\text{where } \text{X}, \text{X}' = \text{H}, \text{Ts})$ (**B1**) is expected to follow the same outer sphere mechanism.

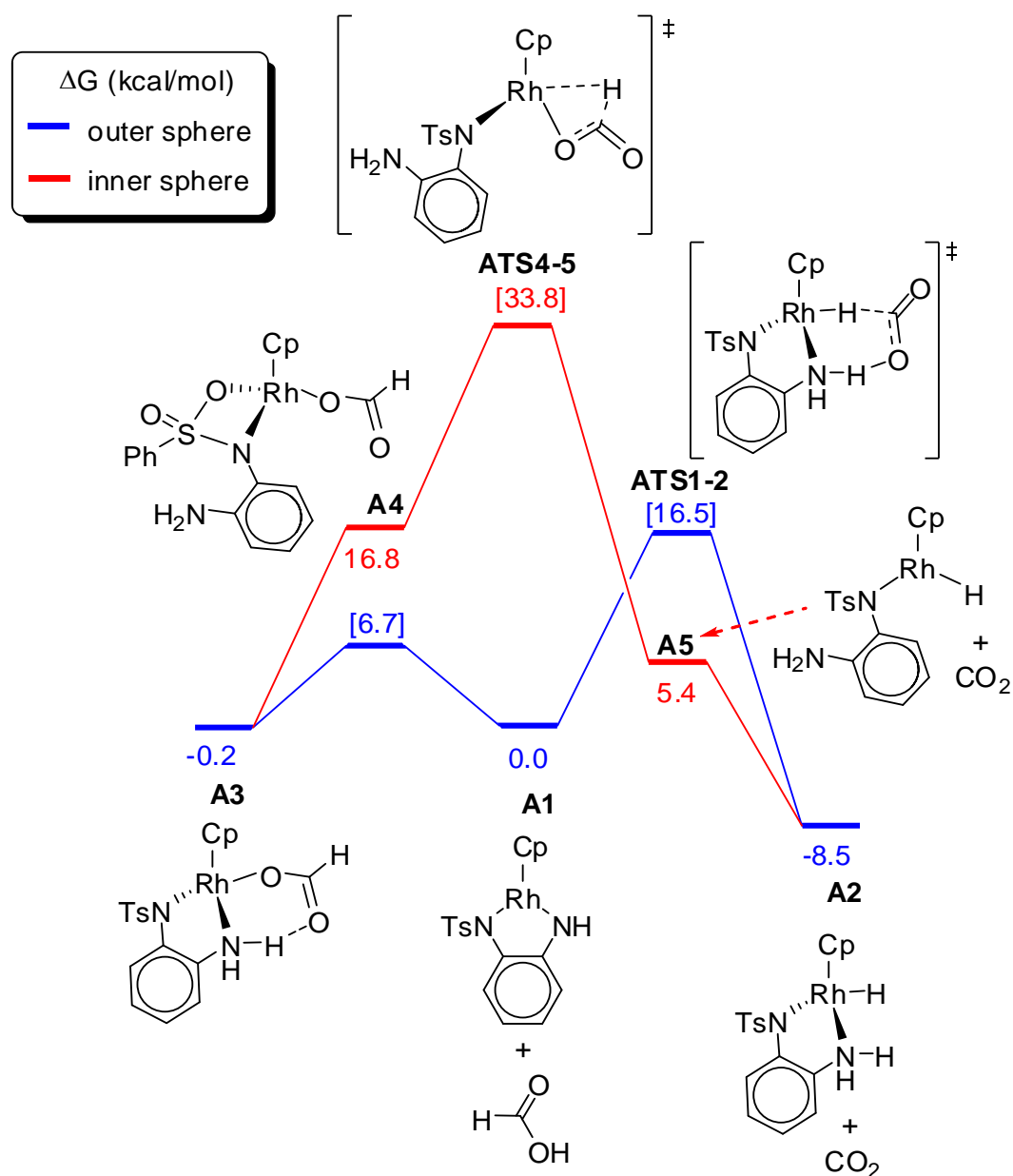


Figure 30 DFT calculation of alternative pathway to 18-electron hydride from the 18-electron formato-amino complex.

Eisenstein *et al.* have also modelled the hydrogenation process with the iridium complexes **1d**, **1e** and **1f** where Cp* has been replaced by Cp and SO₂Tol by SO₂Ph (Figure 31). These results show that hydrogenation of iridium model systems with different amido ligands (**a**, X=SO₂Ph and X'=H; **b**, X=X'=SO₂Ph; and **c**, X=X'=SO₂Ph) follows the same trend as with the rhodium XNC₆H₄NX' and XNCHPhCHPhNX' ligand systems.

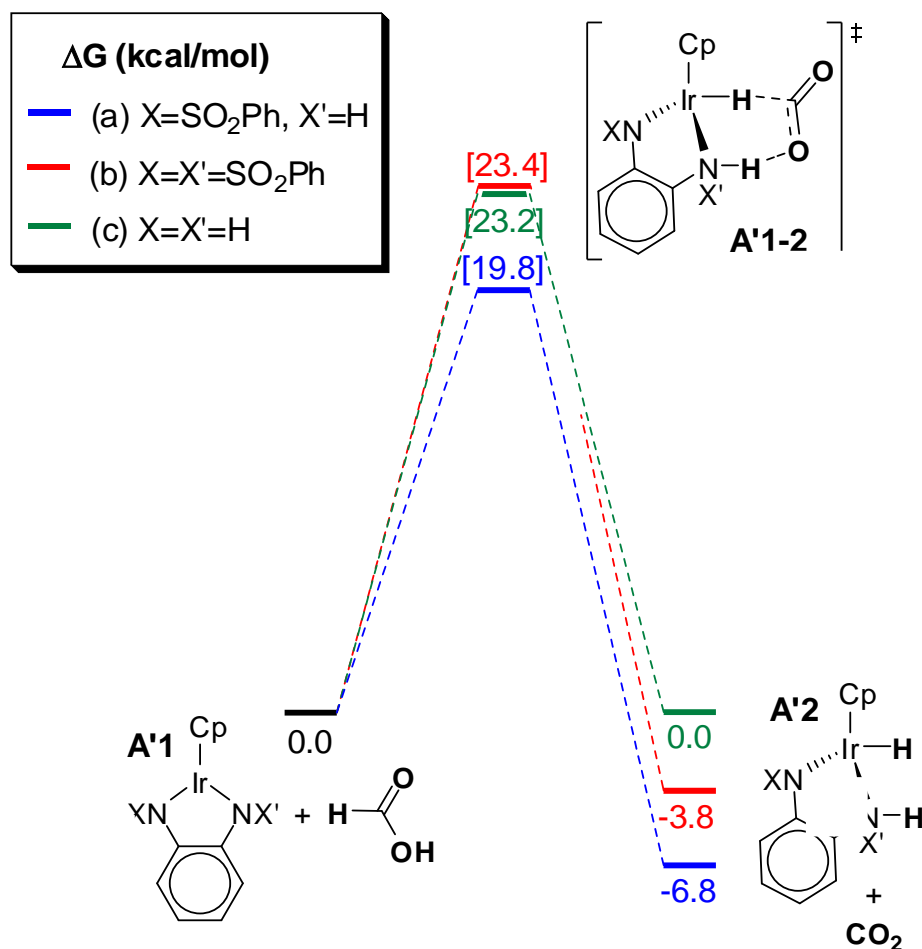


Figure 31 DFT calculation of hydrogenation of 16-electron iridium complexes by formic acid to produce 18-electron hydride complexes.

The computational results for the iridium model system do not fit with the experimental results that show Cp*Ir(TsNC₆H₄NTs) is the catalyst with highest activity for transfer hydrogenation.

3.2.9 DFT calculations on reaction of Cp*Rh complexes with methanol

Using DFT calculations, **1a** was also shown by O. Eisenstein and A. Nova to have the lowest energy barrier to the 18-electron hydride when compared to **1b** and **1c**, considering methanol as the hydrogen source (Figure 32). In this case the trend in the energy barriers is the same as with formic acid but these values are much higher. In addition this reaction is thermodynamically unfavourable. This explains why the hydrogenation of an imine does not happen with methanol as the hydrogen source, whereas it is favourable with formic acid.

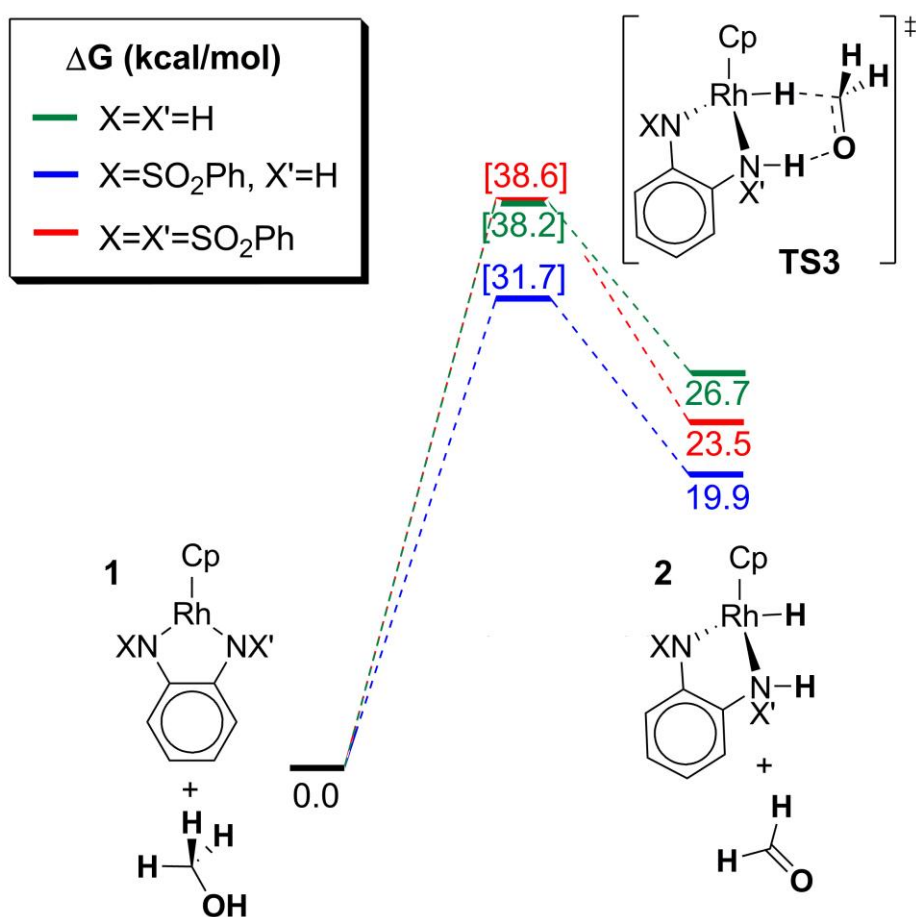


Figure 32 DFT calculations show that hydrogenation of **1a**, **1b** and **1c** with methanol-d₄ are thermodynamically unfavourable.

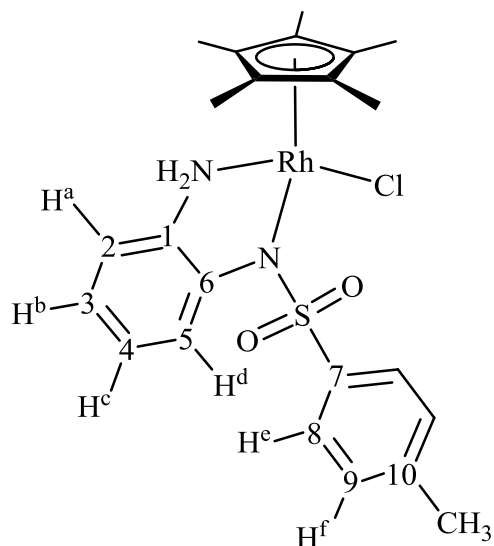
3.3 Summary

The main conclusions we can draw from this chapter are:

- These complexes allow catalytic studies without the need for 18-electron precursors, as is the case for $\text{Cp}^*\text{M}(\text{Cl})(\text{TsNCHPhCHPhNH}_2)$ (where $\text{M} = \text{Rh, Ir}$);
- The most active catalyst is the unsymmetrical, $\text{Cp}^*\text{Rh}(\text{TsNC}_6\text{H}_4\text{NH})$ for transfer hydrogenation of the cyclic imine;
- Since the colour of the 16-electron complexes are lost during catalysis and reappear after, we infer that the 16-electron intermediate is not the resting state;
- The most active 16-electron complex was the 4,5-dimethyl rhodium complex: $\text{Cp}^*\text{Rh}(\text{TsNC}_6\text{H}_2\text{Me}_2\text{NH}) > \text{Cp}^*\text{Rh}(\text{TsNC}_6\text{H}_4\text{NH}) > \text{Cp}^*\text{Ir}(\text{TsNC}_6\text{H}_4\text{NTs}) > \text{Cp}^*\text{Rh}(\text{TsNC}_6\text{H}_4\text{NTs})$, with $\text{Cp}^*\text{Ir}(\text{TsNC}_6\text{H}_4\text{NH})$ being the least active for transfer hydrogenation of the cyclic imine;
- The 18-electron chloride complex, $\text{Cp}^*\text{Rh}(\text{Cl})(\text{TsNC}_6\text{H}_4\text{NH}_2)$ is unstable with respect to $\text{Cp}^*\text{Rh}(\text{TsNC}_6\text{H}_4\text{NH})$ in contrast with the stabilities of their analogues with CHPhCHPh in place of the C_6H_4 ring;
- Formation of the formate complex, $\text{Cp}^*\text{Rh}(\text{OCHO})(\text{TsNC}_6\text{H}_4\text{NH}_2)$ in the presence of TEAF suggests a “catalytic role”. Formation of the 18-hydride complex, $\text{Cp}^*\text{Rh}(\text{H})(\text{TsNC}_6\text{H}_4\text{NH}_2)$ via $\text{Cp}^*\text{Rh}(\text{OCHO})(\text{TsNC}_6\text{H}_4\text{NH}_2)$ may be rate-determining;
- We observed $^1\text{H}/^{103}\text{Rh}$ connectivity of rhodium hydride, NH and Cp^* protons;
- DFT calculations support formic acid addition is an “outer-sphere” mechanism and explain the observed difference in catalytic activity between the rhodium and iridium CHPhCHPh and C_6H_4 complexes.

3.4 Supporting NMR data

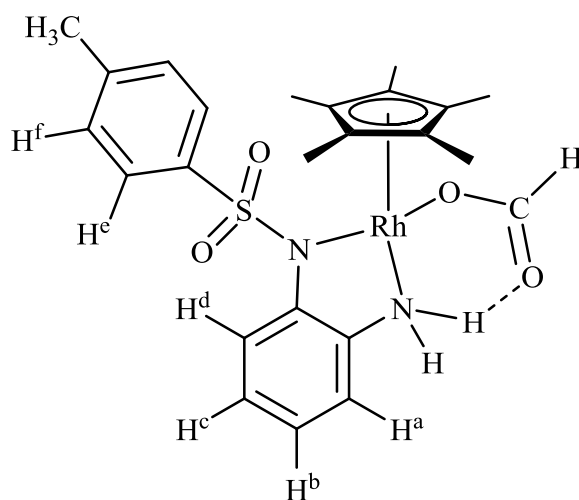
3.4.1 Cp*RhCl(TsNC₆H₄NH₂)



	δ_{H} / ppm (area, multiplicity)	assignment	J / Hz	Assignment
¹ H NMR	1.68 (15H, s)	C ₅ (CH ₃) ₅		
500 MHz	2.28 (3H, s)	CH ₃		
(CD ₂ Cl ₂ , 300K)	4.39 (1H, br. s)	NHH		
	5.27 (1H, br. s)	NHH		
	6.52 (1H, dt)	H ^b	7.5, 1	³ J _{HH} , ⁴ J _{HH}
	6.84 (1H, dt)	H ^c	8.1, 1	³ J _{HH} , ⁴ J _{HH}
	6.94 (1H, dd)	H ^a	7.5, 1	³ J _{HH} , ⁴ J _{HH}
	7.09 (2H, d)	H ^f	8.1	³ J _{HH}
	7.41 (1H, dd)	H ^d	8.3, 1	³ J _{HH} , ⁴ J _{HH}
	7.96 (2H, d)	H ^e	8.1	³ J _{HH}

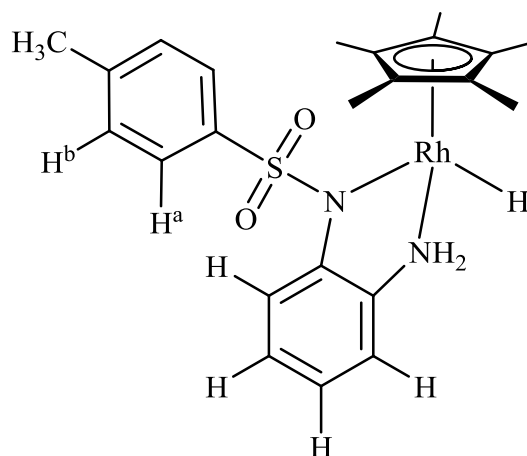
^{13}C NMR	9.80	$\text{C}_5(\text{CH}_3)_5$		
125 MHz	21.64	CH_3		
$(\text{CD}_2\text{Cl}_2, 300\text{K})$	94.82	$\text{C}_5(\text{CH}_3)_5$	8.7	J_{RhC}
	118.96	C^3		
	120.07	C^5		
	123.13	C^2		
	127.76	C^4		
	129.11	C^9		
	129.13	C^8		
	133.81	C^1		
	140.38	C^7		
	141.74	C^{10}		
	146.77	C^6		

Table 3.4.1 Assigned with the aid of $^1\text{H} / ^{13}\text{C}$ HSQC, $^1\text{H} / ^{13}\text{C}$ HSBC, $^1\text{H} / ^1\text{H}$ COSY and NOESY

3.4.2 $\text{Cp}^*\text{Rh}(\text{OCHO})(\text{TsNC}_6\text{H}_4\text{NH}_2)$ 

	δ_{H} / ppm (area, multiplicity)	assignment	J / Hz	Assignment
^1H NMR	1.57 (15H, s)	$\text{C}_5(\text{CH}_3)_5$		
500 MHz	2.23 (3H, s)	CH_3		
$(\text{CD}_2\text{Cl}_2, 213\text{K})$	4.92 (1H, br. d)	$\text{NHH}\dots\text{O}$	9	$^2J_{\text{HH}}$
	6.50 (1H, t)	H^b / H^c	7.5	$^3J_{\text{HH}}$
	6.77 (1H, t)	H^b / H^c	7.5	$^3J_{\text{HH}}$
	6.96 (1H, d)	H^a / H^d	7.5	$^3J_{\text{HH}}$
	7.08 (2H, d)	H^f	8	$^3J_{\text{HH}}$
	7.20 (1H, d)	H^a / H^d	7.5	$^3J_{\text{HH}}$
	7.66 (2H, d)	H^e	8	$^3J_{\text{HH}}$
	8.35 (1H, br. d)	$\text{NHH}\dots\text{O}$	9	$^2J_{\text{HH}}$
	8.70 (1H, s)	COOH		

Table 3.4.2 Assigned with the aid of $^1\text{H} / ^{13}\text{C}$ HSQC, $^1\text{H} / ^{13}\text{C}$ HSBC, $^1\text{H} / ^1\text{H}$ COSY and NOESY.

3.4.3 Cp*Rh(H)(TsNC₆H₄NH₂)

	δ_{H} / ppm (area, multiplicity)	assignment	J / Hz	Assignment
¹ H NMR	-9.51 (1H, d)	Rh-H	22	J_{RhH}
700 MHz	1.96 (15H, s)	C ₅ (CH ₃) ₅		
(THF-d ₈ , 233K)	2.42 (3H, s)	CH ₃		
	5.46 (1H, br. d)	NH	12	$^2J_{\text{HH}}$
	6.05 (1H, br. d)	NH	12	$^2J_{\text{HH}}$
	6.45 (1H)	ArH		
	6.69 (1H)	ArH		
	6.78 (1H)	ArH		
	6.85 (1H)	ArH		
	7.03 (2H, d)	H ^b	8.0	$^3J_{\text{HH}}$
	7.69 (2H, d)	H ^a	8.0	$^3J_{\text{HH}}$
¹⁰³ Rh NMR	1472	Rh		
22.18 Hz				
(THF-d ₈ , 233K)				

Table 3.4.3 Assigned with the aid of ¹H / ¹H COSY and ¹H / ¹⁰³Rh HSQC.

3.5 References

- 1.) A. N. Collins, G. N. Sheldrake and J. Crosby, Editors, *Chirality in Industry II: Developments in the Commercial Manufacture and Applications of Optically Active Compounds*, Wiley, Chichester, 1997.
- 2.) J. S. M. Samec, J.-E. Bäckvall, P. G. Andersson and P. Brandt, *Chem. Soc. Rev.*, 2006, **35**, 237.
- 3.) S. Gladiali and E. Alberico, *Chem. Soc. Rev.*, 2006, **35**, 226.
- 4.) H.-U. Blaser, C. Malan, B. Pugin, F. Spindler, H. Steiner and M. Studer, *Adv. Synth. Catal.*, 2003, **345**, 103
- 5.) S. E. Clapham, A. Hadzovic and R. H. Morris, *Coord. Chem. Rev.*, 2004, **248**, 2201.
- 6.) R. Noyori, M. Yamakawa and S. Hashiguchi, *J. Org. Chem.*, 2001, **66**, 7931.
- 7.) G. Brieger and T. J. Nestrück, *Chem. Rev.* 1974, **74**, 567
- 8.) G. Z. Wang and J.-E. Bäckvall, *J. Chem. Soc., Chem. Commun.*, 1992, 980.
- 9.) N. Uematsu, A. Fujii, S. Hashiguchi, T. Ikariya and R. Noyori, *J. Am. Chem. Soc.*, 1996, **118**, 4916
- 10.) K.-J. Haack, S. Hashiguchi, A. Fujii, T. Ikariya and R. Noyori, *Angew. Chem., Int. Ed. Engl.*, 1997, **36**, 285
- 11.) R. Noyori and S. Hashiguchi, *Acc. Chem. Res.*, 1997, **30**, 97
- 12.) C. P. Casey and J. B. Johnson, *J. Org. Chem.*, 2003, **68**, 1998.
- 13.) M. Yamakawa, H. Ito and R. Noyori, *J. Am. Chem. Soc.*, 2000, **122**, 1466.
- 14.) D. A. Alonso, P. Brandt, S. J. M. Nordin and P. G. Andersson, *J. Am. Chem. Soc.*, 1999, **121**, 9580.
- 15.) D. G. I. Petra, J. N. H. Reek, J.-W. Handgraaf, E. J. Meijer, P. Dierkes, P. C. J. Kamer, J. Brussee, H. E. Schoemaker and P. W. N. M. van Leeuwen, *Chem.-Eur. J.*, 2000, **6**, 2818.
- 16.) J. S. M. Samec, A. H. Ell and J.-E. Bäckvall, *Chem. Commun.*, 2004, 2748.
- 17.) A. H. Ell, J. B. Johnson and J.-E. Bäckvall, *Chem. Commun.*, 2003, 1652.
- 18.) C. P. Casey, S. W. Singer, D. R. Powell, R. K. Hayashi and M. Kavana, *J. Am. Chem. Soc.*, 2001, **123**, 1090.
- 19.) C. P. Casey and J. B. Johnson, *J. Am. Chem. Soc.*, 2005, **127**, 1883.
- 20.) J. B. Åberg, J. S. M. Samec and J.-E. Bäckvall, *Chem. Commun.*, 2006, 2771.

- 21.) K. Wagner, *Angew. Chem. Int. Edit.*, 1970, **9**, 50; (b) K. Narita and M. Sekiya, *Chem. Pharm. Bull.*, 1977, **25**, 135.
- 22.) N. Uematsu, A. Fujii, S. Hashiguchi, T. Ikariya and R. Noyori, *J. Am. Chem. Soc.*, 1996, **118**, 4916.
- 23.) J. Mao and D. C. Baker, *Organic Letters*, 1999, **1**, 841.
- 24.) A. J. Blacker and B. J. Mellor, WO 98/42643.
- 25.) J. Cook, J. E. Hamlin, A. Nutton and P. M. Maitlis, *J. Chem. Soc., Dalton. Trans.* 1981, 2342.
- 26.) A. J. Blacker, S. B. Duckett, J. Grace, R. N. Perutz and A. C. Whitwood, *Organometallics*, 2009, **28**, 1435.
- 27.) T. Koike and T. Ikariya, *Adv. Synth. Catal.*, 2004, **346**, 37.
- 28.) T. Ohkuma, N. Utsumi, K. Tsutsumi, K. Murata, C. Sandoval and R. Noyori, *J. Am. Chem. Soc.* 2006, **128**, 8724.
- 29.) C. Wang, X. Wu and J. Xiao, *Chem. Asian J.* 2008, **3**, 1750.
- 30.) (a) T. Ikariya, K. Murata and R. Noyori, *Org. Biomol. Chem.* 2006, **4**, 393; (b) T. Ikiarya, and A. J. Blacker, *Acc. Chem. Res.* 2007, **40**, 1300.
- 31.) Z. M. Heiden and T. B. Rauchfuss, *J. Am. Chem. Soc.* 2007, **129**, 14303.
- 32.) (a) M. Wills, *Angew. Chem., Int. Ed.* 2008, **47**, 4264; (b) S. Arita, T. Koike, Y. Kayaki and T. Ikariya, *Chem. Asian J.* 2008, **3**, 1479; (c) S. Arita, T. Koike, Y. Kayaki and T. Ikariya, *Angew. Chem. Int. Ed. Engl.* 2008, **47**, 2447.
- 33.) M. C. Denney, N. A. Smythe, K. L. Cetto, R. A. Kemp and K. I. Goldberg, *J. Am. Chem. Soc.* 2006, **128**, 2508 (b) M. M. Konnick, B. A. Gandhi, I. A. Guzei and S. S. Stahl, *Angew. Chem., Int. Ed.* 2006, **45**, 2904.
- 34.) C. J. Curits, A. Miedaner, J. W. Raebiger and D. L. DuBois, *Organometallics*, 2004, **23**, 511.
- 35.) Z. M. Heiden, B. J. Gorecki and T. B. Rauchfuss, *Organometallics*, 2008, **27**, 1542.
- 36.) A. J. Blacker, E. Clot, S. B. Duckett, O. Eisenstein, J. Grace, A. Nova, R. N. Perutz, D. J. Taylor and A. C. Whitwood, *Chem. Commun.*, 2009, 6801.
- 37.) J. Grace, The Rh catalysed asymmetric transfer hydrogenation of imines: a mechanistic study. PhD Thesis, University of York, York, U.K. 2007.

- 38.) P. Pelagatti, M. Carcelli, F. Calbiani, C. Cassi, L. Elviri, C. Pelizzi, U. Rizzotti and D. Rogolino, *Organometallics* 2005, **24**, 5836.
- 39.) K. Abdur-Rashid, S. E. Clapham, A. Hadzovic, J. N. Harvey, A. J. Lough and R. H. Morris, *J. Am. Chem. Soc.*, 2002, **124**, 15104.

A STUDY ON AN AMINE RACEMISATION CATALYST

4.1 Introduction

There are many reports in the scientific literature of efficient racemisation systems for optically active alcohols with a variety of different catalysts.¹ However, there is less precedent for the racemisation of homochiral amines. From an industrial perspective the scale up of amine racemisation catalysts has proved very difficult.² Bäckvall *et al.* have developed a promising solution to the problem of achieving amine racemisation under mild and widely applicable conditions through the use of Shvo's catalyst under transfer hydrogenation conditions (Figure 1).³

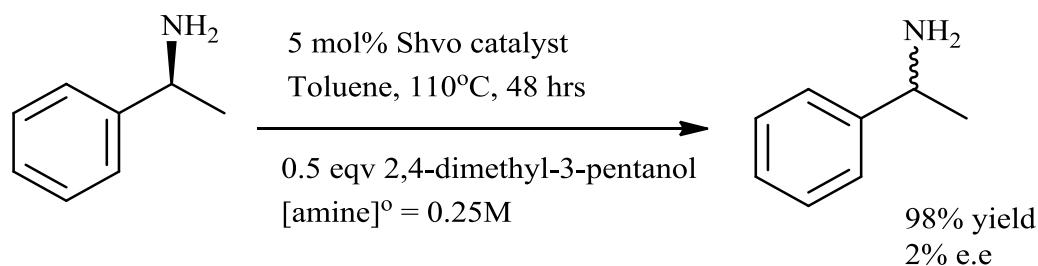


Figure 1 Racemisation of primary amines using Shvo's catalyst.³

However, it suffers from several major drawbacks including: catalyst loading (5 mol% of the dimeric ruthenium species) is too high; the high temperature of 110°C is necessary for a good rate of racemisation but the activity of the catalyst decreases dramatically with decreasing temperature.

Work at NPIL Pharma's research laboratories revealed an unusual enantiomeric excess profile for the transfer hydrogenation of 6,7-dimethoxy-1-methyl-3,4-dihydroisoquinoline using $\text{Cp}^*\text{Ir}(\text{Cl})(\text{TsNCHPhCHPhNH}_2)$ formed *in-situ* from $[\text{Cp}^*\text{IrCl}_2]_2$ and TsNHCHPhCHPhNH_2 .⁴ It was observed that enantiomeric excess decreased significantly during the reaction despite using a formate salt hydrogen donor that was expected to give an irreversible reaction. Further work by Stirling demonstrated that a small amount of racemisation of the amine was observed by stirring overnight in the presence of just iridium dimer, $[\text{Cp}^*\text{IrCl}_2]_2$.⁵ The

racemisation was accompanied by the formation of imine (11.7 %) and isoquinoline (20%), the latter presumably formed from the dehydrogenation of the imine, by the iridium catalyst. This work showed that because dehydrogenation products are observed in significant amounts, there is an alternative pathway for oxidation of the intermediate iridium hydride species, probably via loss of hydrogen gas and this pathway occurs at a comparable rate to the imine hydrogenation.

Stirling showed that changing the anionic ligand from chloride to iodide has a large effect on the rate of racemisation, resulting in a 120 fold increase. Presumably, this results from a change in the effective positive charge on the iridium metal atom and its ability to act as a Lewis acid and to donate/accept hydride ion.^{5,6} The pentamethylcyclopentadienyliridium(III) iodide dimer has previously been reported in the literature.^{7,8} The $[\text{Cp}^*\text{IrI}_2]_2$ dimer, successfully racemises 1-methyl-1,2,3,4-tetrahydroisoquinoline with a low catalyst loading (Figure 2). Racemisation was observed under extremely mild conditions, $t_{1/2} = 215$ min at 40°C using only 0.2 mol% of $[\text{Cp}^*\text{IrI}_2]_2$. Again, Stirling observed that the drop in enantiomeric excess of the corresponding amine was accompanied by the formation of a small amount of the corresponding imine, which increased with reaction time.

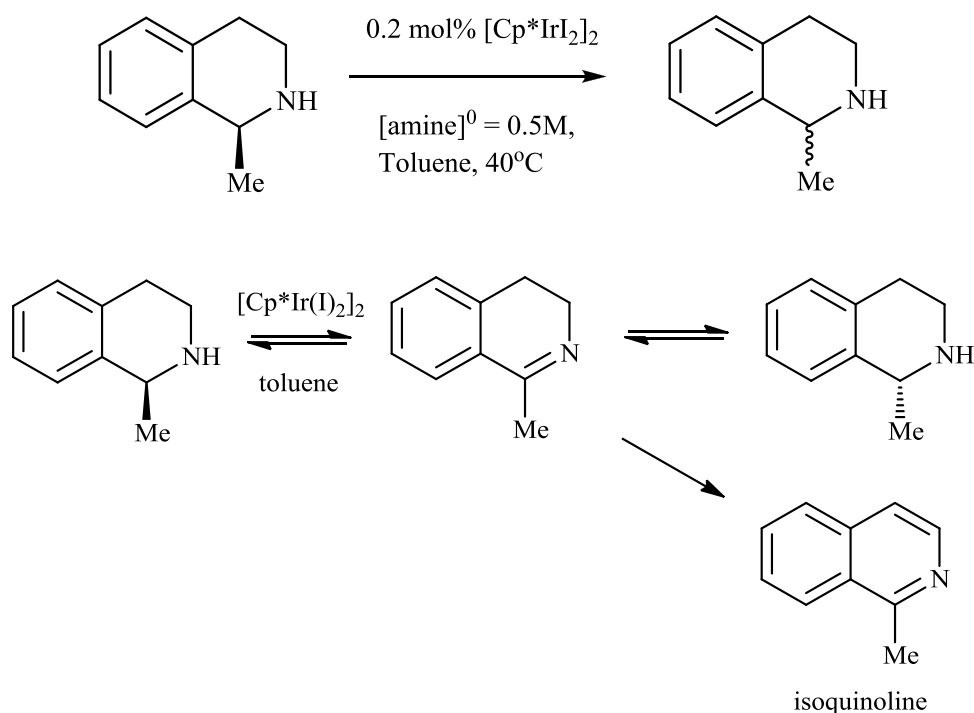


Figure 2 Racemisation of (S)-1-methyl-1,2,3,4-tetrahydroisoquinoline.⁵

4.1.1 Decomposition pathways of the amine racemisation catalyst, $[\text{Cp}^*\text{IrI}_2]_2$

Headley *et al.*, have shown that the reaction between the amine racemisation catalyst, $[\text{Cp}^*\text{Ir}(\text{I})_2]_2$ and (R)-N-methyl-2-methyl-benzylamine at high temperature led to the observation of a C-metallated species which was resistant to displacement, Figure 3.⁹ The structure was characterised by ^1H and ^{13}C NMR and by mass spectroscopy ($m/z = 720.7$). If this reaction is occurring with other amines then this represents a catalyst decomposition pathway exacerbated by high temperature.

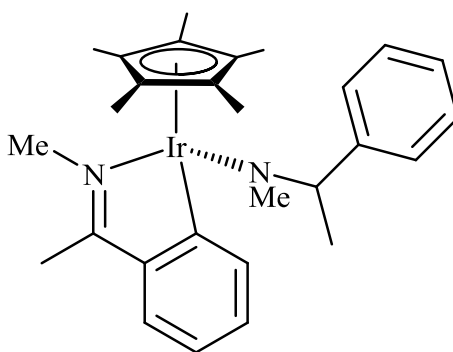


Figure 3 Structure of the Cp^*Ir cyclometallated species indicating catalyst deactivation at higher temperatures.⁹

Indeed, a method for recycling the catalyst using immobilisation of $[\text{Cp}^*\text{IrI}_2]_2$ via the cyclopentadienyl ligand was developed in conjunction with Reaxa Ltd (Figure 4); the catalyst activity fell to about half after each recycle and is perhaps related to the deactivation product described above, as the loss was greater at higher temperatures and addition of neither iodide, iodine, formic acid nor hydrogen restored activity.⁹

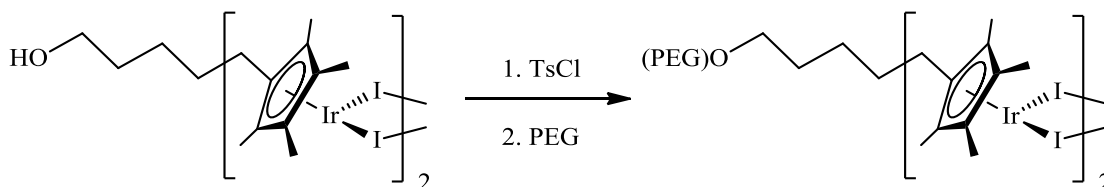


Figure 4 The immobilised $[\text{Cp}^*\text{IrI}_2]_2$ complex.^{9,10}

4.1.2 Using $[\text{Cp}^*\text{Ir}(\text{NH}_3)_3][\text{I}^-]_2$ catalyst for the synthesis of amines from NH_3

Fujita and Yamaguchi have synthesised novel-water soluble Cp^*Ir -ammine complexes from $[\text{Cp}^*\text{Ir}(\text{X})_2]_2$ (where $\text{X} = \text{Cl}, \text{Br}$ and I) (Figure 5) and have developed a new highly atom-economical system for the synthesis of organic amines using aqueous ammonia as a nitrogen source.¹¹

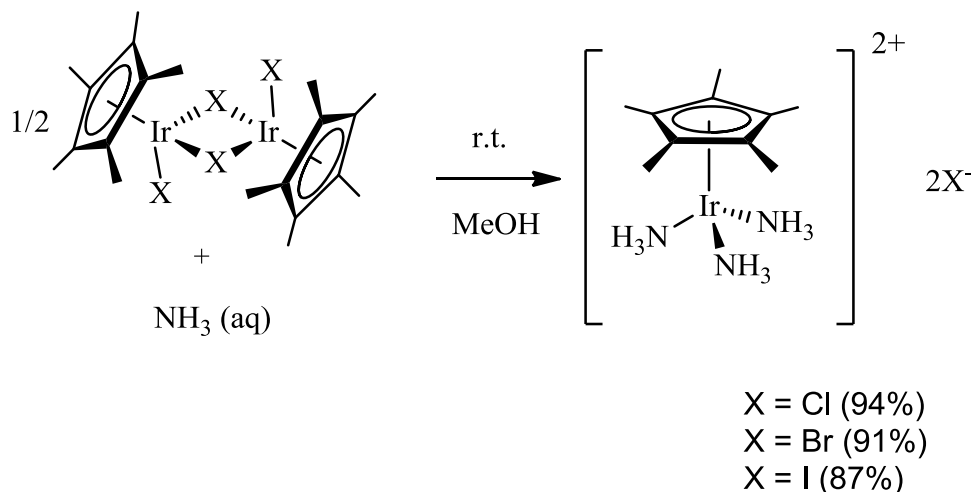
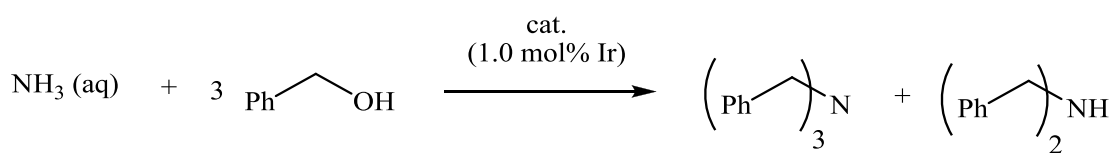


Figure 5 Synthesis of Cp^*Ir -ammine complexes from the corresponding Cp^*Ir halide dimer and aqueous ammonia.¹¹

With the water-soluble and air-stable Cp^*Ir -ammine catalyst, $[\text{Cp}^*\text{Ir}(\text{NH}_3)_3][\text{I}^-]_2$, a variety of tertiary and secondary amines were synthesised by the multi-alkylation of aqueous ammonia and benzyl alcohols (Figure 6). The superiority of the iodide complex could be attributed to the differences of activities for the hydrogenation of the iminic intermediate. When the transfer hydrogenations of *N*-benzylidenebenzylamine were carried out in the presence of the three halide ion catalysts, the highest yield was obtained in the reaction using the iodide complex (Figure 7). This is again, one of many examples that iodide often exhibits a positive effect in the transition-metal-catalyzed hydrogenation of imines. A possible mechanism is shown in Figure 8.



Catalyst	Temp (°C)	Time (h)	Yield (%)	
			(PhCH ₂) ₃ N	(PhCH ₂) ₂ NH
[Cp*IrCl ₂] ₂	140	20	29	21
[Cp*Ir(NH ₃) ₃][Cl] ₂	140	20	70	18
[Cp*Ir(NH ₃) ₃][Br] ₂	140	20	49	23
[Cp*Ir(NH ₃) ₃][I] ₂	140	20	82	7
[Cp*Ir(NH ₃) ₃][I] ₂	120	20	79	6
[Cp*Ir(NH ₃) ₃][I] ₂	140	20	76	3
[Cp*Ir(NH ₃) ₃][I] ₂	140	24	100	0

Figure 6 N-alkylation of aqueous ammonia with benzyl alcohols catalysed by Cp*Ir-ammine complexes under various conditions. The reaction was carried out with NH₃ (1.0 mmol, 28% aqueous solution). Cp*Ir catalyst (1.0 mol % Ir), and benzyl alcohol (3.0 mmol). The percentage yields were determined by GC.¹¹

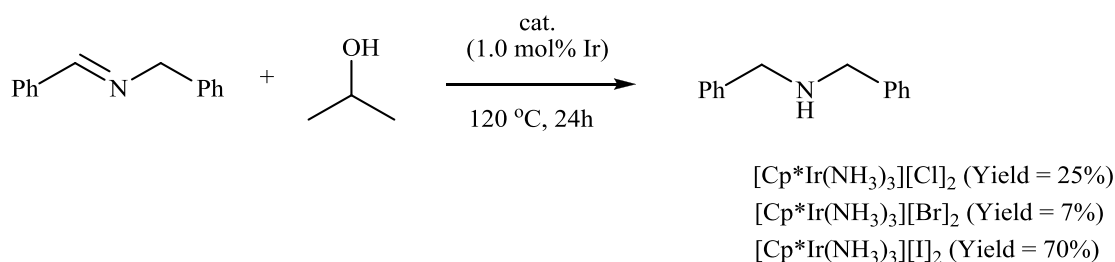


Figure 7 Transfer hydrogenation of *N*-benzylidenebenzylamine carried out in the presence of the three halide ion catalysts, the highest yield was obtained using the iodide complex (yield = 70%).¹¹

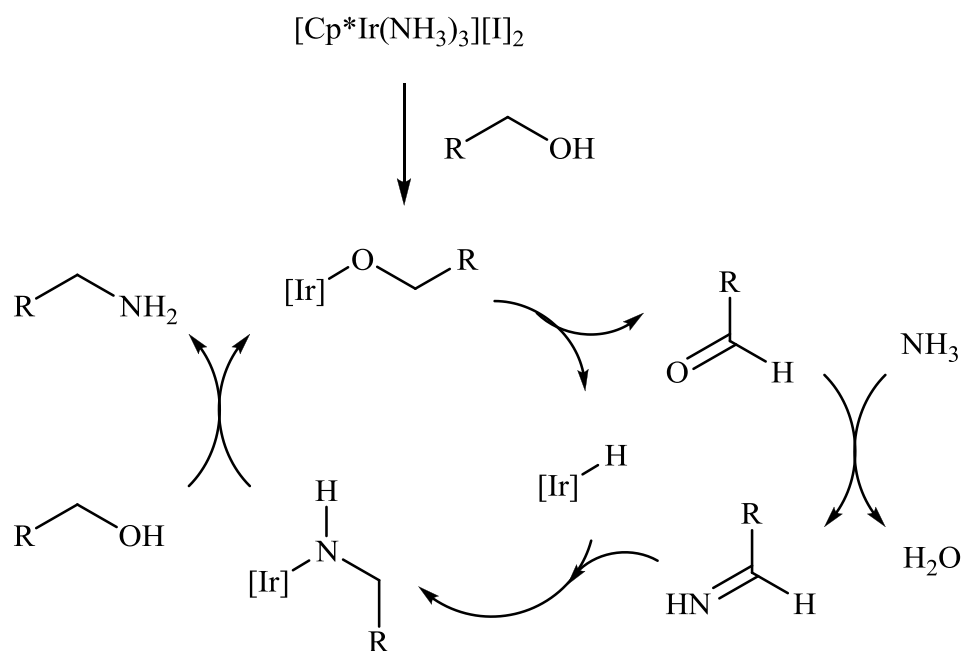
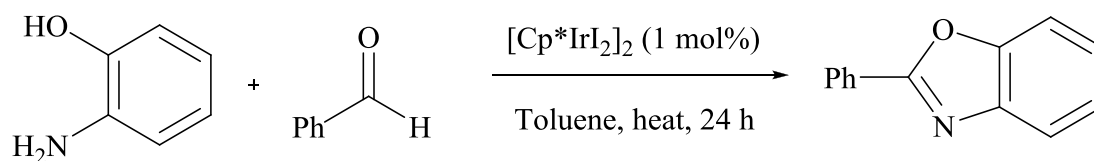


Figure 8 A possible mechanism for the N-alkylation of aqueous ammonia with an alcohol and Cp^*Ir -ammine complex.¹¹

4.1.3 Blacker et al. show that $[\text{Cp}^*\text{IrI}_2]_2$ is a versatile catalyst

Blacker *et al.* have shown that the iridium complex, $[\text{Cp}^*\text{IrI}_2]_2$ is catalytically active for the formation of benzoxazoles from benzaldehyde and 2-aminophenol under a range of conditions (Figure 9).^{12,13}



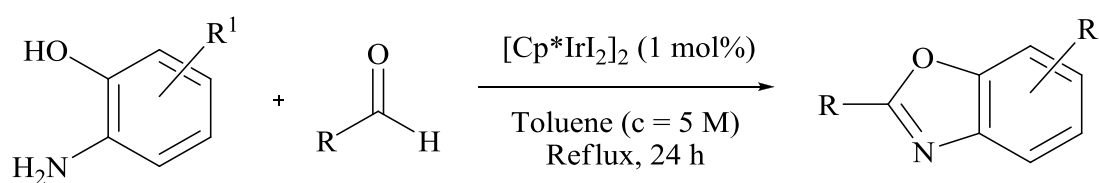
Entry	Reaction Conditions ^a	Conversion ^b (%)
1	80 °C	15
2	80 °C, styrene (1.5 eqv.)	12
3	80 °C, acetic acid (1 eqv.)	13
4	Reflux	52
5	reflux, $c = 5 \text{ M}$	100
6	reflux, styrene (1.5 eqv.)	50
7	reflux, $[\text{Cp}^*\text{IrCl}_2]_2$ as catalyst	17
8	reflux, 0.1 mol% $[\text{Cp}^*\text{IrI}_2]_2$	17
9	reflux, no catalyst	< 5

^a Conditions: benzaldehyde (1.0 mmol), *o*-aminophenol (1.0 mmol), toluene, $c = 0.5 \text{ M}$, 24 h. ^b Conversion determined by NMR ratio of Schiff base to benzoxazoles product.

Figure 9 Ir-Catalyzed Conversion of Benzaldehyde into 2-Phenylbenzoxazole using 1 mol% $[\text{Cp}^*\text{IrI}_2]_2$.¹³

Interestingly, the reactions were equally effective in the presence or absence of styrene as a sacrificial hydrogen acceptor (entries 1 and 4 versus 2 and 6). Blacker *et al.* suggest that the aromatizing oxidation is ultimately mediated by loss of H_2 (g)

from an intermediate (di)hydrido-iridium complex. The liberation of hydrogen gas was previously observed accompanying the oxidative self-dimerization of primary amines by $[\text{Cp}^*\text{IrI}_2]_2$. The diiodide was found to be superior to the dichloride (Figure 18, entry 7) as would be expected considering their known relative effectiveness seen for amine oxidation. The reaction conditions, using 1.0 mol% $[\text{Cp}^*\text{IrI}_2]_2$ was applied to the conversion of a range of aldehydes into benzoxazoles (Figure 10). Interesting, using the same reaction conditions the iridium complex was also demonstrated to be catalytically active for the synthesis of a benzothiazole from *p*-tolualdehyde and *o*-aminothiophenol.



Entry	Benzoxazole Product	Isolated Yield (%)
1		74
2		77
3		85
6		80
7		52

Figure 10 Acceptorless oxidation of Aldehydes to Benzoxazoles using the $[\text{Cp}^*\text{IrI}_2]_2$ complex.¹³

Blacker *et al.*, proposed a reaction pathway which involved condensation of the aldehyde with an ortho-heterosubstituted aniline generating an intermediate imine which would be in equilibrium with the dihydrobenzazole (Figure 11). A hydrogen transfer process between the HC-NH bond in the dihydrobenzazole and the iridium complex would then form the C=N benzazole product and produce an intermediate (di)hydrido-iridium complex similar to Fujita's process for dehydrogenation of cyclic amines (See Introduction).¹⁴

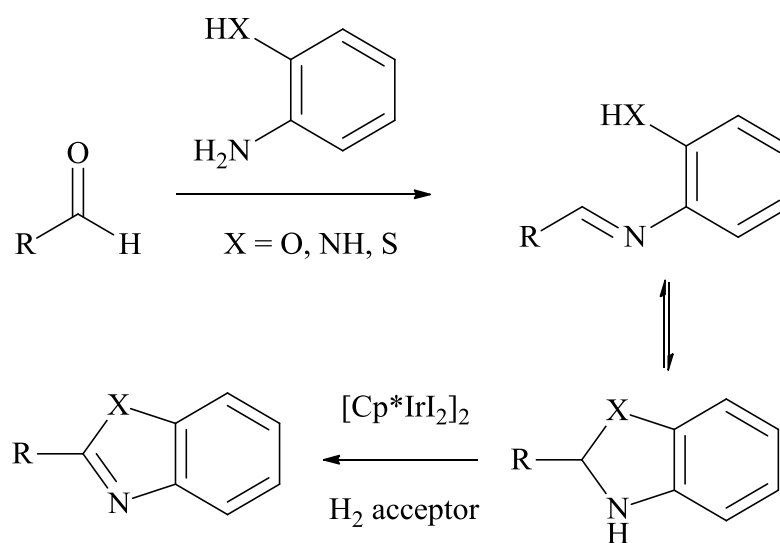


Figure 11 Mechanism proposed by Blacker *et al.* for the conversion of aldehydes into benzazoles using the $[\text{Cp}^*\text{IrI}_2]_2$ complex.¹³

4.1.4 Aims of the Chapter

Usually the most efficient way to optimise a process is to first gain an understanding of the reaction mechanism and critical parameters. Therefore, the primary aim of this chapter was to investigate the mechanism of the amine racemisation process when $[\text{Cp}^*\text{IrI}_2]_2$ is used as the catalyst. We also studied the recycling of the catalyst using ammonia and characterised and tested the resulting precipitate for the racemisation process.

4.2 Results and Analysis

4.2.1 Synthesis, Isolation and Characterisation of $\text{Cp}^*\text{Ir}(\text{I})_2(\text{NH}_3)$

After a catalytic reaction, the catalyst can sometimes be recovered.¹⁵ Catalyst reuse is of great commercial interest due to increases in overall productivity and cost effectiveness of chemical transformations while minimizing their environmental impact, ultimately contributing considerably to the sustainability of chemical processes. Catalyst recycling fits most principles of green chemistry,^{16,17,18,19} and has been included as a priority in several strategic research agendas both in the US and Europe.^{20,21}

One possible way to recover the amine racemisation catalyst, $[\text{Cp}^*\text{IrI}_2]_2$, was to purge the reaction mixture with ammonia gas (NH_3),⁹ which produced an unknown orange crystalline precipitate. In order to investigate this further, ammonia gas was bubbled through a needle directly from the cylinder into a solution of $[\text{Cp}^*\text{IrI}_2]_2$ in toluene at room temperature (Figure 12). The mixture changed colour very quickly from brown to orange and over time a bright yellow precipitate formed. The mixture was filtered through a sinter and washed twice with toluene. The resulting solid was dried under high vacuum (95% yield).⁹

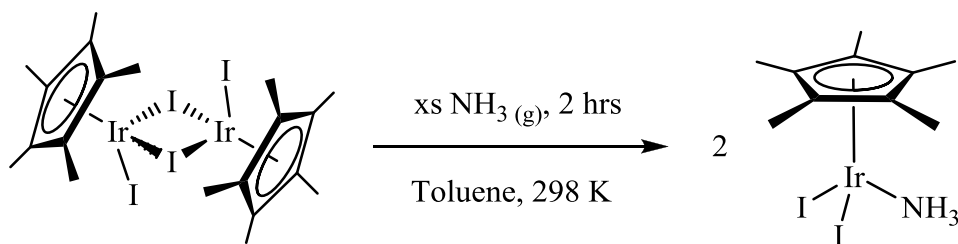


Figure 12 Preparation of $[\text{Cp}^*\text{Ir}(\text{I})_2(\text{NH}_3)]$ from the $[\text{Cp}^*\text{IrI}_2]_2$ catalyst using NH_3 (g)

The yellow solid was recrystallised by dissolving it in a minimal amount of chloroform and then layering with cyclohexane to afford a clear crystalline solid. Layering the resulting filtrate with a second equivalent of cyclohexane afforded orange crystals, which were characterised by ^1H , ^{13}C , IR-KBr, mass spectrometry, CHN analysis, UV-vis spectroscopy and X-ray crystallography. The complex was

stable in air for months without decomposition. X-ray analysis of $[\text{Cp}^*\text{Ir}(\text{I})_2(\text{NH}_3)]$ demonstrated that one ammine ligand is attached to the iridium center along with two iodine ligands, and its geometry could be described as a three-legged piano stool (Figure 13), which is common in $\text{Cp}^*\text{Ir}^{\text{III}}$ and $\text{Cp}^*\text{Rh}^{\text{III}}$ complexes (Chapter 2 and 3).

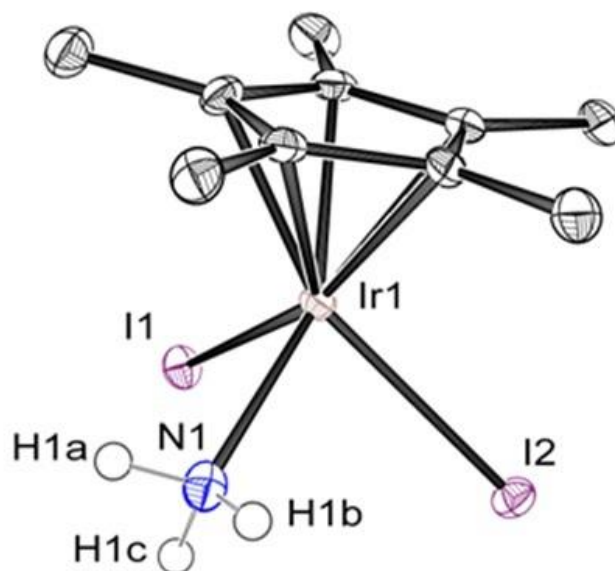


Figure 13 X-ray crystallography structure of $\text{Cp}^*\text{Ir}(\text{I})_2(\text{NH}_3)$

	$\text{Cp}^*\text{Ir}(\text{I})_2(\text{NH}_3)$	$[\text{Cp}^*\text{Ir}(\text{NH}_3)_3][\text{I}]_2^1$
Ir – N	2.133(4)	2.140(6), 2.146(7), 2.161(6) 2.141(6), 2.152(7), 2.164(7)
Ir – I(1)	2.7166(4)	-
Ir – I(2)	2.7140(4)	-
Cp(cent)-Ir	1.783(3)	1.770(3), 1.782(4)
I(1)-Ir-I(2)	91.46(1)	-
N-Ir-I(1)	85.37(14)	-
N(1)-Ir-I(2)	83.51(14)	-

Table 1 X-ray crystallographic data for $[\text{Cp}^*\text{Ir}(\text{I})_2(\text{NH}_3)]$ and $[\text{Cp}^*\text{Ir}(\text{NH}_3)_3][\text{I}]_2$.²²

¹ Values reported separately for the two molecules in the unit cell.

Subsequently, Fujita and co-workers²² cited our work when they developed $[\text{Cp}^*\text{Ir}(\text{NH}_3)_3][\text{I}]_2$ (Figure 14), a water-soluble complex for the synthesis of organic amines using aqueous ammonia as a nitrogen source. It adopts a similar geometry to that of $\text{Cp}^*\text{Ir}(\text{I})_2(\text{NH}_3)$ and the X-ray crystallographic data is shown in Table 1 for comparison.

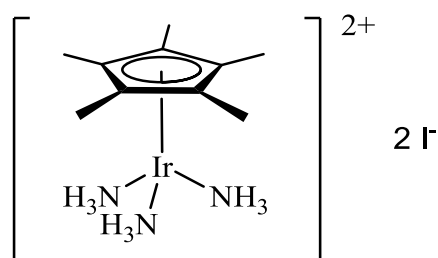


Figure 14 Structure of $[\text{Cp}^*\text{Ir}(\text{NH}_3)_3][\text{I}]_2$ developed by Fujita and co-workers.²²

The Ir-N bond length of $[\text{Cp}^*\text{Ir}(\text{I})_2(\text{NH}_3)]$ is 2.133(4) Å (slightly shorter compared to the tris-ammine complex) and the Ir-I(1) and Ir-I(2) bond lengths are 2.7166(4) Å and 2.7140(4) Å, respectively. The Cp(cent) – Ir length is 1.783(3) Å, similar to $[\text{Cp}^*\text{Ir}(\text{NH}_3)_3][\text{I}]_2$ (1.776(5) Å). The I(1)-Ir-I(2) angle is 91.46(1)°, the N-Ir-I(1) angle is 85.37(14)° and the N(1)-Ir-I(2) angle is 83.51(14)°. The complex adopts a slightly distorted octahedral geometry where the Cp* ligand occupies three adjacent coordination sites leaving the other three available *fac* sites to contain two iodide atoms and the ammonia group.

The ^1H NMR of $[\text{Cp}^*\text{Ir}(\text{I})_2(\text{NH}_3)]$ in methylene chloride- d_2 reveals Cp* methyl hydrogens at $\delta_{\text{H}} = 1.84$ ppm that integrate 15H:3H with the NH_3 protons at $\delta_{\text{H}} = 3.27$ ppm which appear as a broad singlet. The CHN microanalysis was fully consistent with a monoammine coordinated product. The UV-visible spectrum of $[\text{Cp}^*\text{Ir}(\text{I})_2(\text{NH}_3)]$ in chloroform (Figure 15 and Table 2 where $c = 8.0 \times 10^{-5}$ mol dm^{-3}), shows two peaks at $\lambda_{\text{max}} = 338$ nm and 383 nm ($\epsilon = 3.9 \times 10^3$ mol $^{-1}$ dm^3 cm^{-1} and $\epsilon = 3.9 \times 10^3$ mol $^{-1}$ dm^3 cm^{-1} , respectively). They are equally strong and can be attributed to Γ to Ir(d_{σ}) ligand-to-metal charge transfer transitions. There is also a stronger peak at $\lambda_{\text{max}} = 232$ nm ($\epsilon = 20.1 \times 10^3$ mol $^{-1}$ dm^3 cm^{-1}). This is postulated to be a π to π^* transition (as observed for the 16-electron Cp*Rh and Cp*Ir complexes in Chapter 2). There are also shoulders at $\lambda_{\text{max}} = 277$ nm, 289 nm and 463 nm ($\epsilon =$

$3.8 \times 10^3 \text{ mol}^{-1} \text{ dm}^3 \text{ cm}^{-1}$, $\epsilon = 3.4 \times 10^3 \text{ mol}^{-1} \text{ dm}^3 \text{ cm}^{-1}$ and $\epsilon = 0.5 \times 10^3 \text{ mol}^{-1} \text{ dm}^3 \text{ cm}^{-1}$, respectively), possibly from LMCT transitions from the nitrogen lone pair.

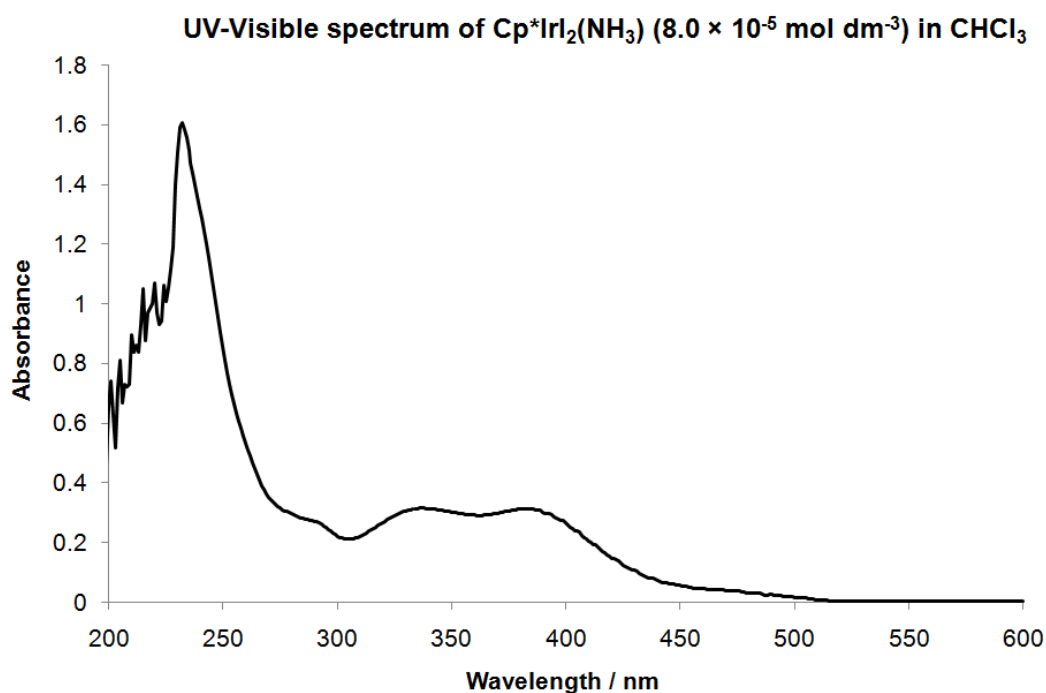


Figure 15 UV-visible spectrum of [Cp*IrI₂(NH₃)] in chloroform.

$\lambda_{\text{max}} / \text{nm}$	$\epsilon / \times 10^3 \text{ mol}^{-1} \text{ dm}^3 \text{ cm}^{-1}$	$\lambda_{\text{max}} / \text{nm}$	$\epsilon / \times 10^3 \text{ mol}^{-1} \text{ dm}^3 \text{ cm}^{-1}$
232	20.1	338	3.9
277 (sh.)	3.8	383	3.9
289 (sh.)	3.4	463 (sh.)	0.5

Table 2 Molar extinction coefficients for [Cp*Ir(NH₃)(I)₂] in chloroform

The infra-red spectrum of a KBr disc of [Cp*IrI₂(NH₃)] shows strong N-H stretches at 3151 cm^{-1} , 3196 cm^{-1} , 3258 cm^{-1} and 3329 cm^{-1} . The point group symmetry of this complex is C_s and consequently there should only be three stretching frequencies. This may be due to 2 intermolecular hydrogen bonds: N(1)-H(1A)⋯I(1) and N(1)-H(1B)⋯I(2) with distances (H⋯I) of 2.90(9) and 2.92(9) Å, respectively (Table 7.1, Appendix 8.7). Alternatively, the other stretching frequencies are likely to be from Fermi resonance, in which an overtone or combination band transforms with the same irreducible representation as the fundamental and has almost the same energy.

4.2.2 Racemisation of sertraline with purified $\text{Cp}^*\text{Ir}(\text{I})_2(\text{NH}_3)$ complex

The ammonia complex, $[\text{Cp}^*\text{Ir}(\text{I})_2(\text{NH}_3)]$ synthesised in the previous section was examined as a catalyst for the racemisation of sertraline under the same experimental conditions as would be used with the $[\text{Cp}^*\text{IrI}_2]_2$ complex (Figure 16). At Piramal Healthcare in Huddersfield, a Hewlett-Packard HP6890 gas chromatograph was used to analyse the ratio of sertraline isomers, and these were assigned using known standards. For the enantiomers a Chirasil-DEX CB chiral column was used. The racemisation of sertraline with the recycled ammonia catalyst proved to be of comparable activity to the original $[\text{Cp}^*\text{IrI}_2]_2$ catalyst (Figure 17).⁹

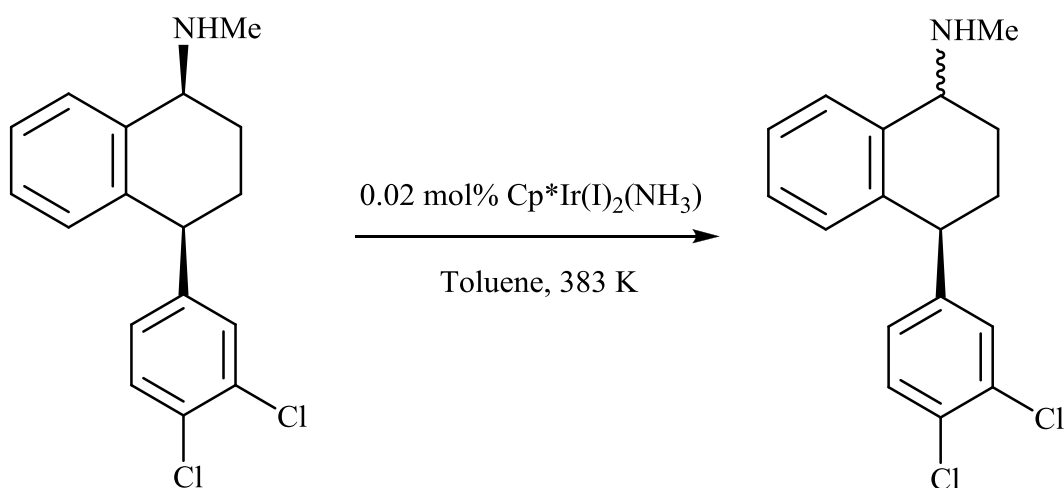


Figure 16 Reaction conditions for the racemisation of sertraline with the recycled catalyst, $[\text{Cp}^*\text{Ir}(\text{I})_2(\text{NH}_3)]$

The slightly lower activity of the recycled catalyst is possibly due to not purging the reaction mixture to remove the ammonia gas that is evolved or the decreased solubility of the ammonia complex in toluene. An experiment was run to determine the activity of the recovered $[\text{Cp}^*\text{Ir}(\text{I})_2(\text{NH}_3)]$ complex on the second addition of fresh substrate. As shown in Figure 18, there is some loss of catalytic activity on the second run with fresh substrate but the results fit consistently with the $[\text{Cp}^*\text{IrI}_2]_2$ observations.

Racemisation of Sertraline with $[\text{Cp}^*\text{Ir}(\text{I})_2]_2$ and purified recycled $[\text{Cp}^*\text{Ir}(\text{I})_2(\text{NH}_3)]$ complex

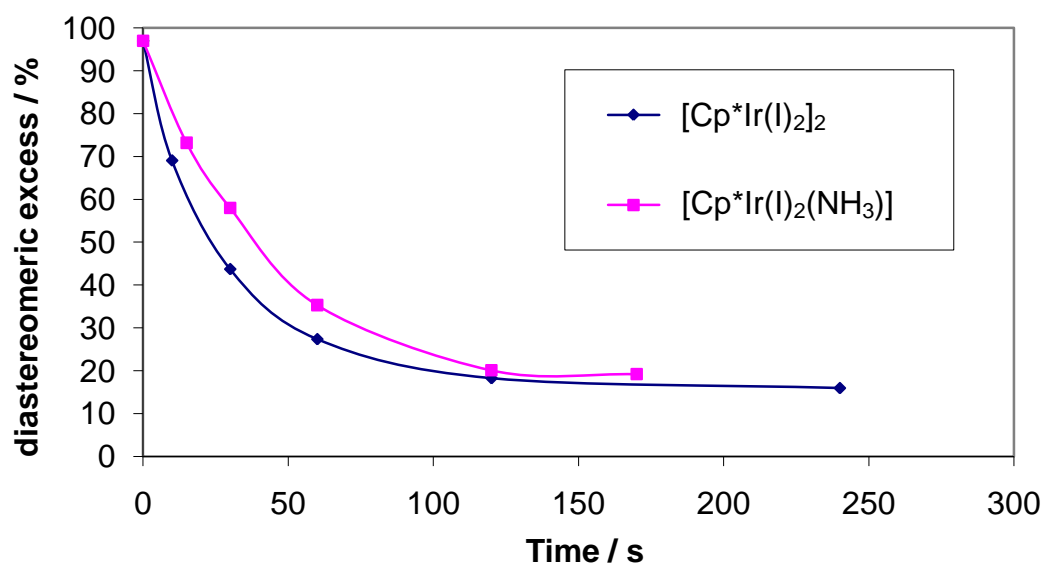


Figure 17 A graph to show the time profile of racemisation of sertraline with $[\text{Cp}^*\text{Ir}(\text{I})_2]_2$ and the recycled ammonia catalyst, $[\text{Cp}^*\text{Ir}(\text{I})_2(\text{NH}_3)]$.

Pulse Experiment for the Racemisation of Sertraline with purified recycled $[\text{Cp}^*\text{Ir}(\text{I})_2(\text{NH}_3)]$ complex

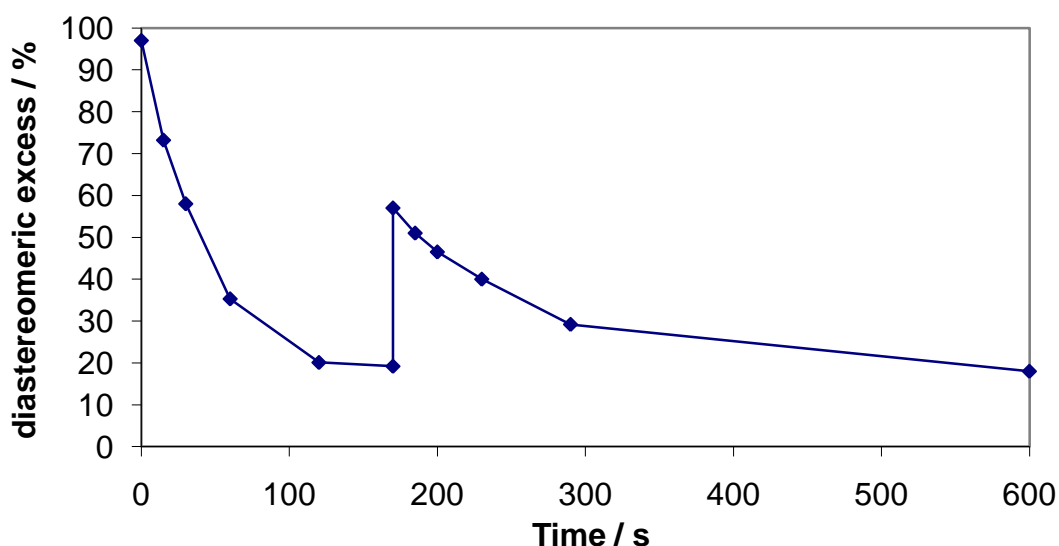


Figure 18 A graph to show time profile changes during a pulse experiment for the racemisation of sertraline with the recycled ammonia catalyst, $[\text{Cp}^*\text{Ir}(\text{I})_2(\text{NH}_3)]$, where the discontinuity corresponds to the second run with fresh substrate.

4.2.3 Reactivity of $[\text{Cp}^*\text{IrI}_2]_2$ with a secondary amine, PhCH_2NHMe

A sensible starting point for a study of the mechanism of amine racemisation catalysed by the $[\text{Cp}^*\text{IrI}_2]_2$ complex, was the isolation and characterisation of catalytic intermediates, such as the method by which the catalyst coordinates amines in preparation for subsequent transformations. To explore this first step the precursor complex $[\text{Cp}^*\text{IrI}_2]_2$ was reacted with 2 molar equivalents of a secondary amine, *N*-methylbenzylamine at 233 K in methylene chloride- d_2 (Figure 19).

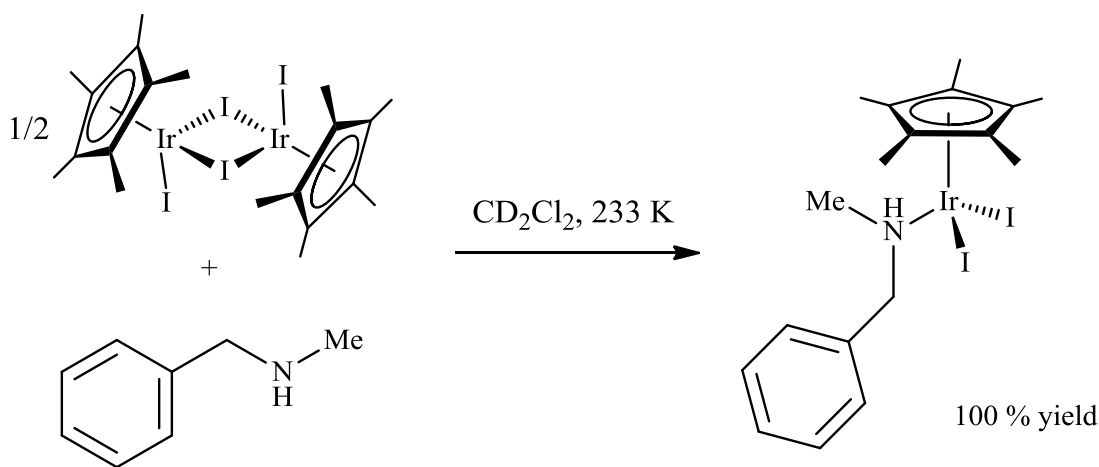


Figure 19 Reaction of $[\text{Cp}^*\text{IrI}_2]_2$ with *N*-methylbenzylamine at low temperature in methylene chloride- d_2

The reaction was followed by ^1H NMR spectroscopy at 233 K and it showed quantitative formation of $[\text{Cp}^*\text{Ir}(\text{I})_2(\text{HNMeCH}_2\text{Ph})]$ (Figure 20). ^1H NMR revealed that the NH proton was still present and had resolved into a doublet of quartets (Figure 21). The splitting can be explained by the proton on nitrogen coupling to the methyl group and one of the CH_2 protons adjacent to the nitrogen atom. This may indicate that rotation is slowed at low temperature, possible through formation of a weak hydrogen bond between NH and the iodides. The NH peak for the uncoordinated *N*-methylbenzylamine compound is a broad singlet. At 300 K, the ^1H NMR peaks become broad suggesting exchange of the amine ligand is occurring.

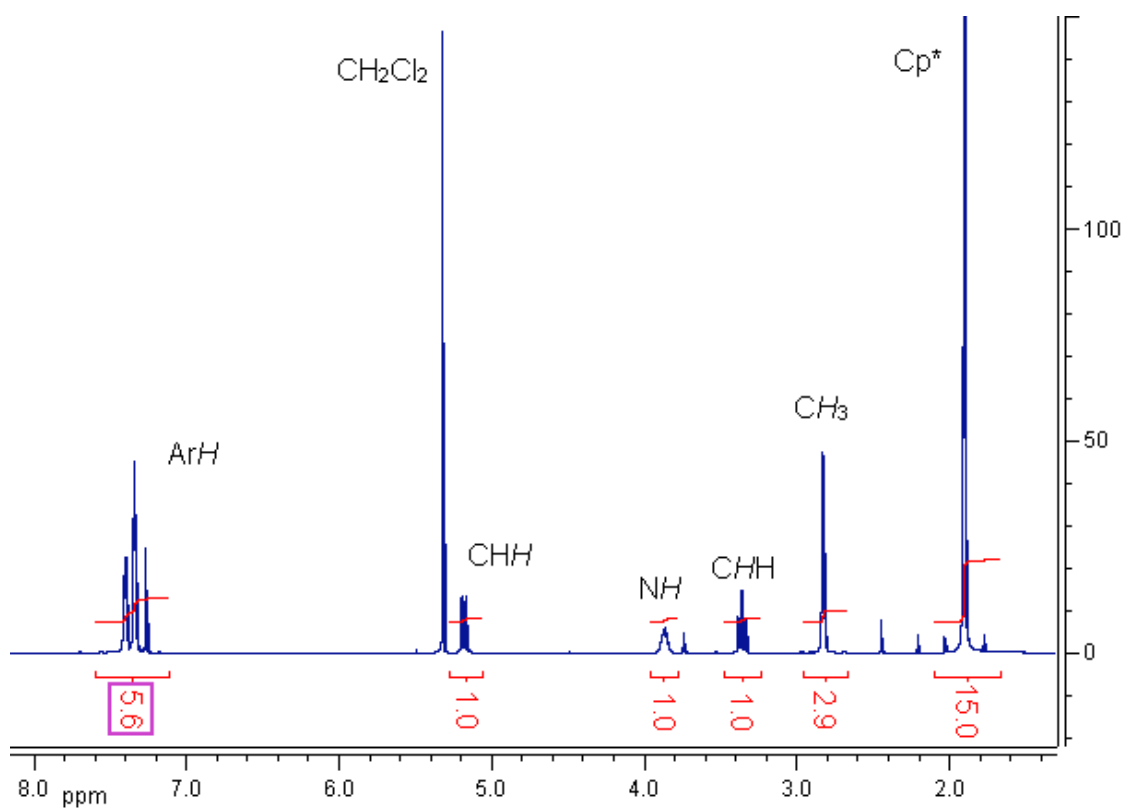


Figure 20 ^1H NMR of $[\text{Cp}^*\text{Ir}(\text{I})_2(\text{HNMeCH}_2\text{Ph})]$ in methylene chloride- d_2 at 233 K

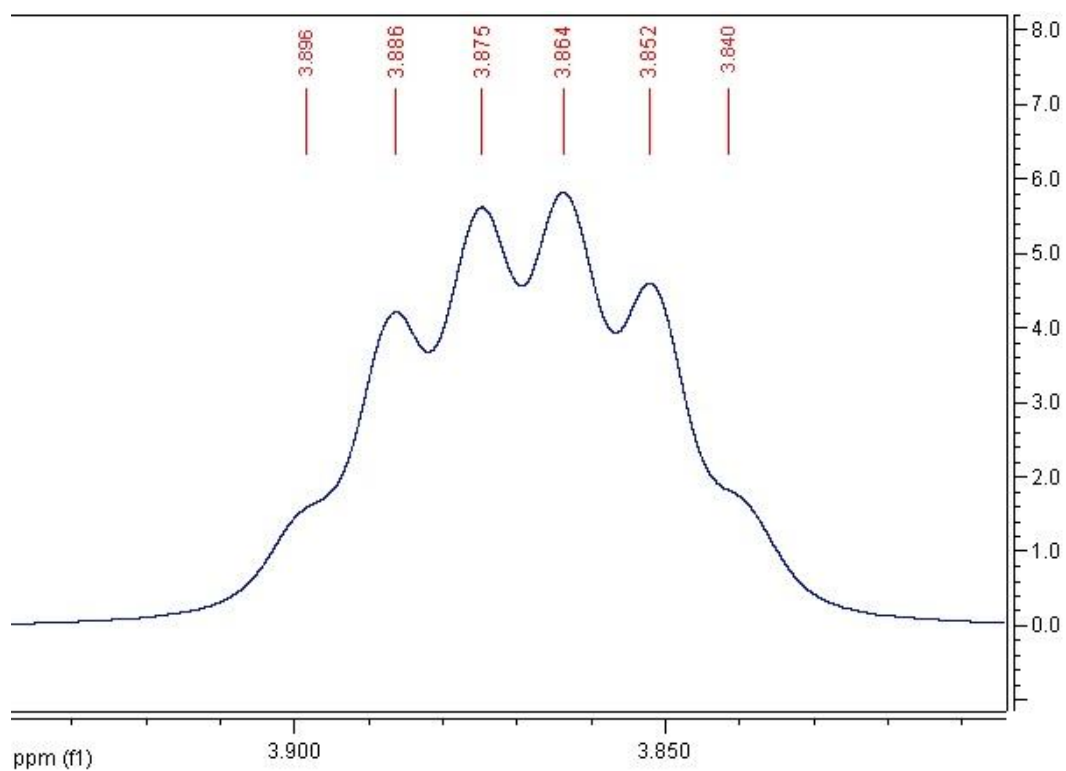


Figure 21 ^1H NMR of $[\text{Cp}^*\text{Ir}(\text{I})_2(\text{HNMeCH}_2\text{Ph})]$ in methylene chloride- d_2 showing the NH splitting pattern (doublet of quartets) at 233 K

A KBr disk of $[\text{Cp}^*\text{Ir}(\text{I})_2(\text{PhCH}_2\text{NHMe})]$ was prepared and the FT-IR spectrum revealed a single sharp peak at 3231 cm^{-1} which can be attributed to the N-H stretch of the coordinated amine. A UV-visible spectrum of the complex was also acquired in chloroform (Figure 22) and displays two strong bands at $\lambda_{\text{max}} = 358\text{ nm}$ ($\epsilon = 3.4 \times 10^3\text{ mol}^{-1}\text{ dm}^3\text{ cm}^{-1}$) and 388 nm ($\epsilon = 3.7 \times 10^3\text{ mol}^{-1}\text{ dm}^3\text{ cm}^{-1}$) and 244 nm ($\epsilon = 16.4 \times 10^3\text{ mol}^{-1}\text{ dm}^3\text{ cm}^{-1}$). The bands at $\lambda_{\text{max}} = 358\text{ nm}$ and 388 nm can be attributed as metal-to-ligand charge transfer transitions and the peak at $\lambda_{\text{max}} = 244\text{ nm}$ to π - π^* transitions, as was observed for $\text{Cp}^*\text{Ir}(\text{I})_2(\text{NH}_3)$.

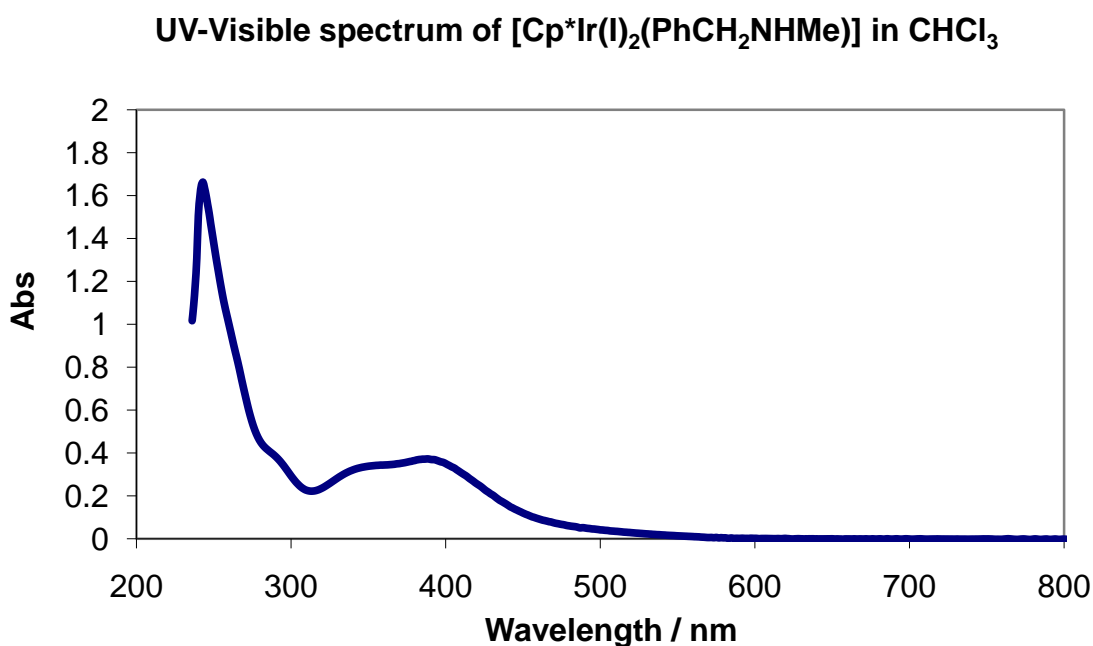


Figure 22 UV-visible spectrum of $[\text{Cp}^*\text{Ir}(\text{I})_2(\text{PhCH}_2\text{NHMe})]$ in chloroform

X-ray quality crystals of $[\text{Cp}^*\text{Ir}(\text{I})_2(\text{PhCH}_2\text{NHMe})]$ were obtained by layering the NMR solution with cyclohexane and leaving in the freezer for 72 hours. The X-ray crystallography structure was acquired and is shown in Figure 23 and Table 3. The Ir-N bond length is $2.176(4)\text{ \AA}$ which suggests that the bond has very little, if any, π -bond characteristic unlike the 16 electron catalysts investigated in Chapter 2. As expected the Ir-I(1) and Ir-I(2) bond lengths are almost equivalent, $2.7044(4)$ and $2.7052(5)\text{ \AA}$ respectively. The $\text{Cp}^{\text{cent}}\text{-Ir}$ bond length is 1.842 \AA .

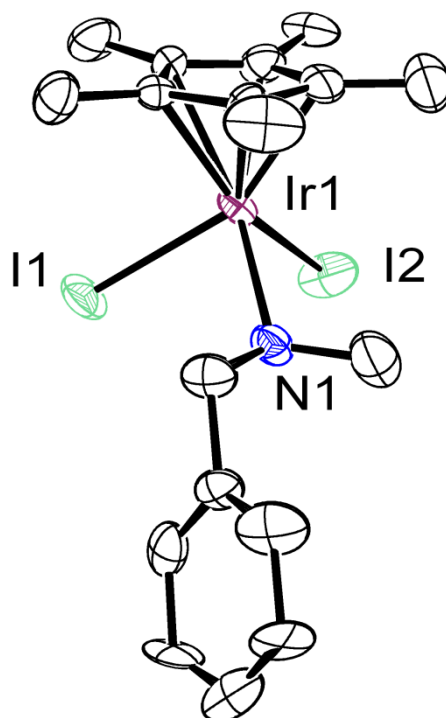


Figure 23 X-ray crystallography structure for $\text{Cp}^*\text{IrI}_2[\text{NH}(\text{Me})\text{CH}_2\text{Ph}]$.

	$\text{Cp}^*\text{Ir}(\text{I})_2(\text{NH}_3)$	$\text{Cp}^*\text{Ir}(\text{I})_2(\text{PhCH}_2\text{NHMe})$
Ir – N	2.133(4)	2.176(4)
Ir – I(1)	2.7166(4)	2.7044(4)
Ir – I(2)	2.7140(4)	2.7052(5)
Cp(cent)-Ir	1.783(3)	1.842
I(1)-Ir-I(2)	91.46(1)	89.64(2)
N-Ir-I(1)	85.37(14)	84.37(12)
N(1)-Ir-I(2)	83.51(14)	84.87(12)

Table 3 X-ray crystallographic data for $[\text{Cp}^*\text{Ir}(\text{I})_2(\text{PhCH}_2\text{NHMe})]$ and $[\text{Cp}^*\text{Ir}(\text{I})_2(\text{NH}_3)]$

4.2.4 Reactivity of $\text{Cp}^*\text{Ir}(\text{I})_2(\text{NH}_3)$ with a secondary amine, PhCH_2NHMe

The ammonia catalyst, $\text{Cp}^*\text{Ir}(\text{I})_2(\text{NH}_3)$ was reacted with 1 molar equivalent of *N*-methylbenzylamine at 233 K in methylene chloride- d_2 under the same conditions as with $[\text{Cp}^*\text{Ir}(\text{I})_2]_2$ and the reaction was again followed by ^1H NMR spectroscopy (Figure 24). The ^1H NMR data showed that the secondary amine had displaced ammonia and formed $\text{Cp}^*\text{Ir}(\text{I})_2(\text{PhCH}_2\text{NHMe})$, however the conversion was only 70% yield. It is possible that the ammonia was not purged away from the system properly and this was why only partial conversion to the amine-coordinated product was observed when using $\text{Cp}^*\text{Ir}(\text{I})_2(\text{NH}_3)$ as the starting complex.

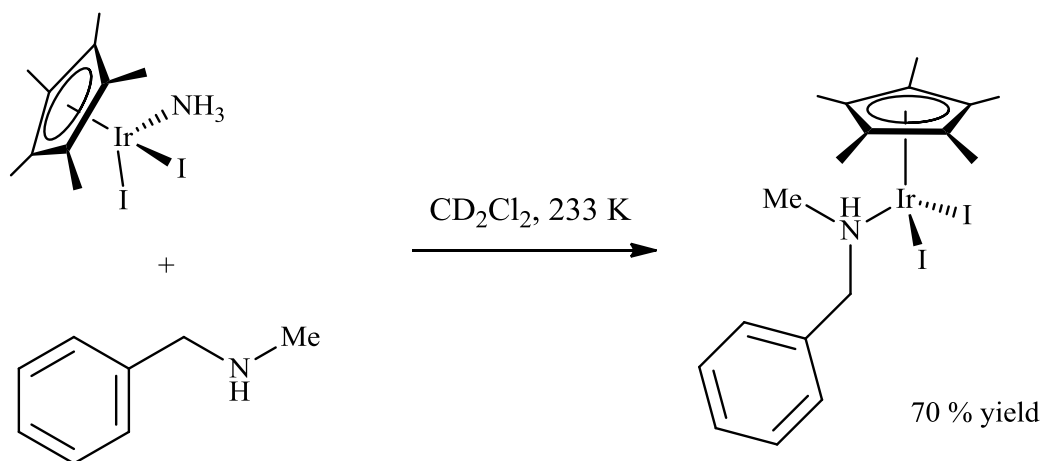


Figure 24 Reaction of $\text{Cp}^*\text{Ir}(\text{I})_2(\text{NH}_3)$ with *N*-methylbenzylamine at low temperature in methylene chloride- d_2

4.2.5 Characterisation of $\text{Cp}^*\text{Ir}(\text{Cl})_2(\text{NH}(\text{Me})\text{CH}_2\text{Ph})$ (Ir chloride analogue)

N-methylbenzylamine was reacted with the chloride analogue, $[\text{Cp}^*\text{IrCl}_2]_2$. This catalyst is known to be about 200 times less active for the racemisation of secondary amines as the iodide catalyst. The ^1H NMR spectrum showed complete conversion to the amine coordinated-metal complex. However, the resonances in the ^1H NMR spectrum were not broad as with the iodide experiment. The NMR spectrum showed sharp peaks at 300 K. It appears that the chloride analogue does not undergo exchange of the secondary amine on an NMR timescale at 300 K, whereas the iodide does, as mentioned in the previous sections.

The FTIR-KBr spectrum of $\text{Cp}^*\text{Ir}(\text{Cl})_2(\text{NH}(\text{Me})\text{CH}_2\text{Ph})$ shows a N-H stretch at 3250 cm^{-1} , which is significantly higher than 3231 cm^{-1} for the iodide complex. A crystal suitable for X-ray diffraction was grown by slow evaporation of a solution in acetone at 248 K. The crystal structure of $\text{Cp}^*\text{Ir}(\text{Cl})_2(\text{NH}(\text{Me})\text{CH}_2\text{Ph})$ is very similar to the iodide analogue (Figure 25).

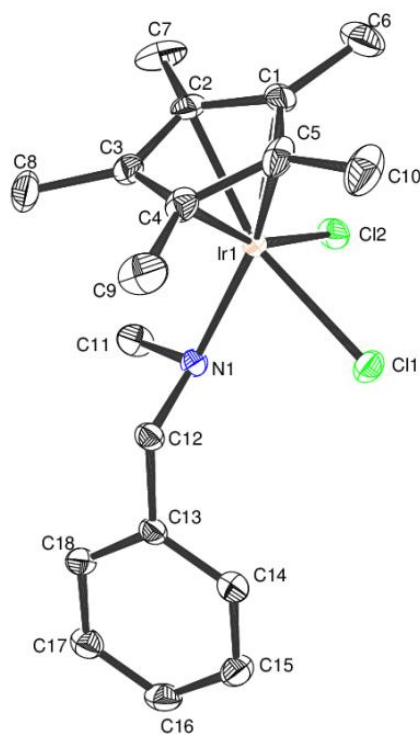


Figure 25 X-ray crystallography structure for $\text{Cp}^*\text{Ir}(\text{Cl})_2(\text{NH}(\text{Me})\text{CH}_2\text{Ph})$

The Ir-N bond length is 2.155(3) Å, which is very slightly shorter than the iridium diiodide analogue (Table 4). This may indicate that the secondary amine is bound slightly more strongly and the amine is less labile, as demonstrated in the ¹H NMR spectrum. As expected the Ir-Cl(1) and Ir-Cl(2) bond lengths are almost equivalent, 2.4129(8) Å and 2.4205(8) Å respectively. The Cp^{cent}-Ir bond length is 1.773 Å.

	Cp*Rh(Cl)₂ (PhCH₂NHMe)	Cp*Ir(Cl)₂ (PhCH₂NHMe)	Cp*Ir(I)₂ (PhCH₂NHMe)
M-N	2.1557(13)	2.155(3)	2.176(4)
M-X(1)	2.4129(4)	2.4129(8)	2.7044(4)
M-X(2)	2.4256(4)	2.4205(8)	2.7052(5)
M-Cp ^{cent}	1.774	1.773	1.842
NH...X(1)	2.667	2.606	2.995
NH...X(2)	2.764	2.688	3.024

Table 4 X-ray data for amine coordination complexes

4.2.6 Characterisation of Cp*Rh(Cl)₂(NH(Me)CH₂Ph)

N-methylbenzylamine was reacted with [Cp*RhCl₂]₂. The NMR spectrum showed complete conversion to the amine coordinated-metal complex. Like the iridium chloride amine coordinated analogue, the spectrum showed sharp peaks at 300 K. It appears that the rhodium chloride analogue also does not undergo exchange of the secondary amine on the NMR timescale at 300 K.

The FTIR-KBr spectrum of Cp*Rh(Cl)₂(PhCH₂NHMe) shows a N-H stretch at 3264 cm⁻¹, which is significantly higher compared to 3231 cm⁻¹ for the iridium iodide complex and 3250 cm⁻¹ for the iridium chloride (See Table 5).

A crystal suitable for X-ray diffraction was grown using the same method as for the iridium chloride analogous complex, by slow evaporation of an acetone solution at

248 K. The crystal structure of $\text{Cp}^*\text{Rh}(\text{Cl})_2(\text{PhCH}_2\text{NHMe})$ is similar to the iridium chloride and iodide analogues (Figure 26), but has significantly different bond lengths and angles.

	$[\text{Cp}^*\text{Rh}(\text{Cl})_2(\text{PhCH}_2\text{NHMe})]$	$[\text{Cp}^*\text{Ir}(\text{Cl})_2(\text{PhCH}_2\text{NHMe})]$	$[\text{Cp}^*\text{Ir}(\text{I})_2(\text{PhCH}_2\text{NHMe})]$
$\nu(\text{N-H}) / \text{cm}^{-1}$	3264	3250	3231

Table 5 KBr-IR data for complexes

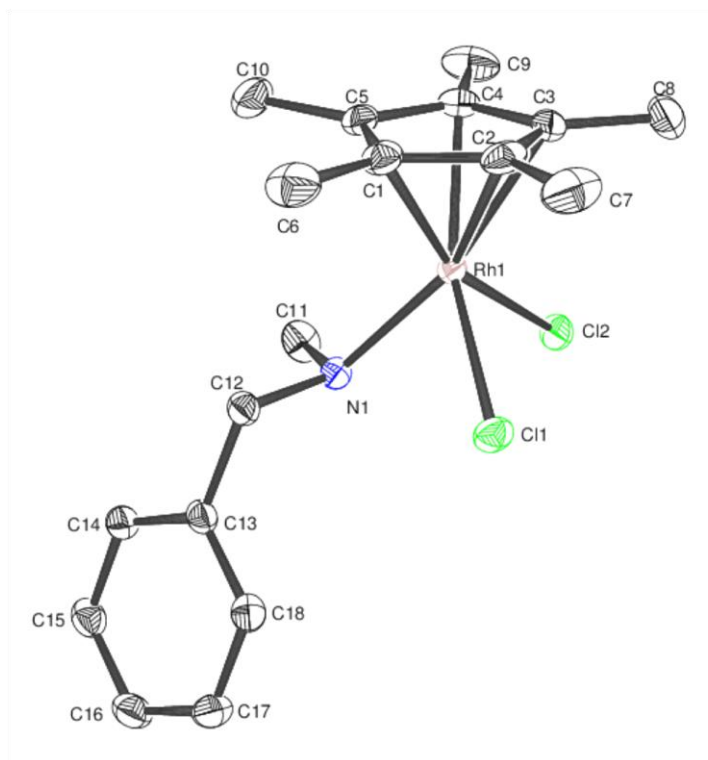


Figure 26 X-ray crystallography structure for $[\text{Cp}^*\text{Rh}(\text{Cl})_2(\text{NH}(\text{Me})\text{CH}_2\text{Ph})]$

The Rh-N bond length is $2.1557(13) \text{ \AA}$, which is slightly shorter than the iridium diiodide analogue (Ir-N $2.155(3) \text{ \AA}$). As expected the Rh-Cl(1) and Rh-Cl(2) bond lengths are almost equivalent, $2.429(4) \text{ \AA}$ and $2.4256(4) \text{ \AA}$ respectively. The $\text{Cp}^{\text{cent}}\text{-Rh}$ bond length is 1.774 .

4.2.7 Coordination of a secondary imine to the $[\text{Cp}^*\text{Ir}(\text{I})_2]_2$ catalyst

Under standard catalytic conditions, the $[\text{Cp}^*\text{Ir}(\text{I})_2]_2$ complex dehydrogenates sertraline to the corresponding imine in small quantities over time (Figure 27).⁹

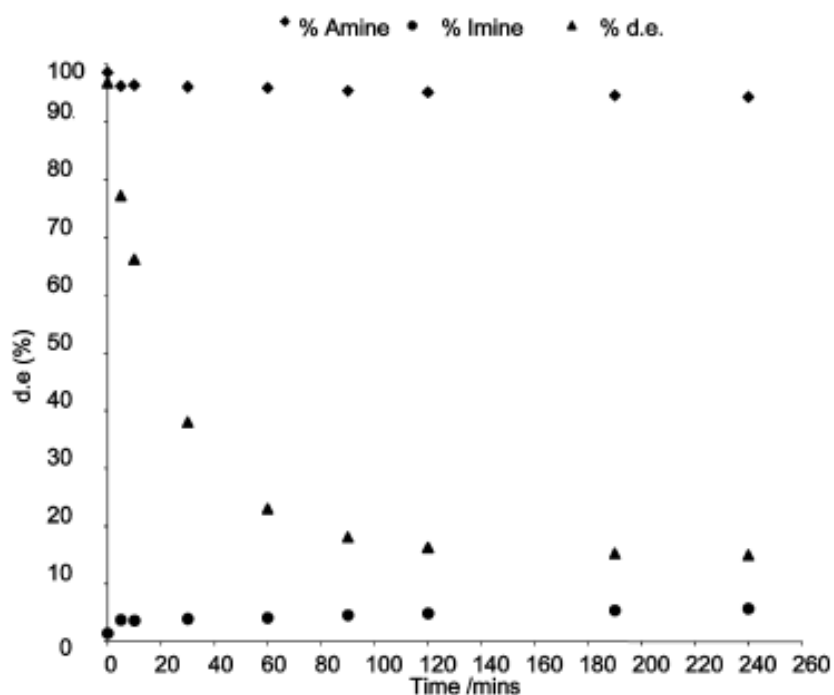


Figure 27 Epimerisation profile of (1S,4S) sertraline to (1R,S,4S)-sertraline with the $[\text{Cp}^*\text{Ir}(\text{I})_2]_2$ catalyst and evidence for formation of the corresponding imine, 6,7-dimethoxy-1-methyl-3,4-dihydroisoquinoline, over time.⁹

In an attempt to gain mechanistic insight into this process, the cyclic imine, 6,7-dimethoxy-1-methyl-3,4-dihydroisoquinoline hydrochloride, used in Chapter 3 was converted to 6,7-dimethoxy-1-methyl-3,4-dihydroisoquinoline by reaction with sodium hydroxide and after work-up it was reacted with the $[\text{Cp}^*\text{Ir}(\text{I})_2]_2$ complex in methylene chloride- d_2 in an NMR tube at 248 K under an atmosphere of argon (Figure 28). ^1H , ^{13}C , HSQC, HMBC, COSY and 1D NOESY were acquired at 248 K. The NMR spectra show the formation of a new complex in which the imine is coordinated to the iridium of $[\text{Cp}^*\text{Ir}(\text{I})_2]$ fragment.

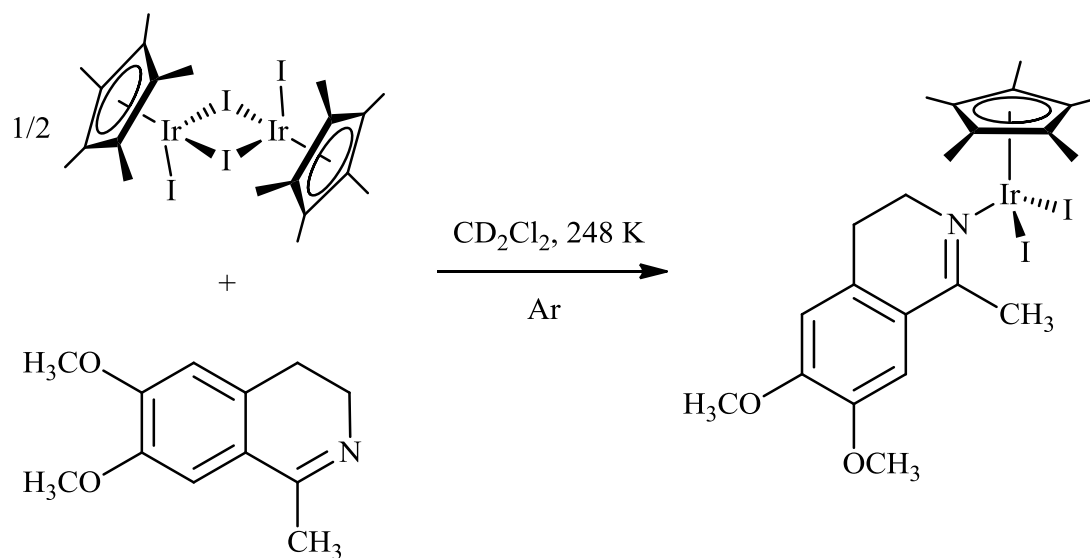


Figure 28 Coordination of a cyclic secondary imine to the $[\text{Cp}^*\text{Ir}(\text{I})_2]_2$ complex

A natural abundance $^1\text{H}/^{15}\text{N}$ HMQC correlation experiment was performed on a sample containing the coordinated imine-iridium complex (Figure 29).

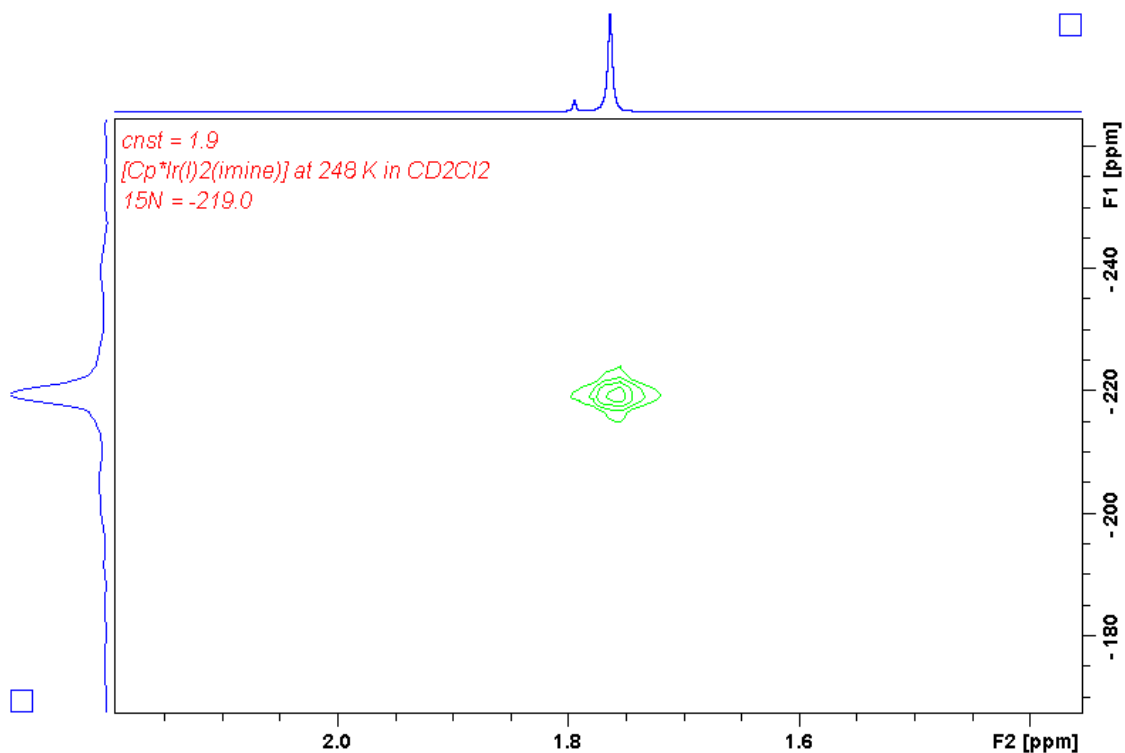


Figure 29 Portion of the $^1\text{H}/^{15}\text{N}$ HMQC spectrum showing the crosspeak of the Cp^* protons and the nitrogen of the coordinated imine at -219 ppm, (referenced to pyridine at 0 ppm).

The spectrum shows a cross peak between the nitrogen and Cp* methyl protons at $\delta_N = -219$ ppm, $\delta_H = 1.72$ ppm. For comparison, the nitrogen chemical shift of the free imine substrate was measured to be $\delta_N = -114.1$ ppm. The nitrogen chemical shift has therefore shifted upfield by a considerable amount ($\Delta\delta -104.9$ ppm) on coordination to the $[\text{Cp}^*\text{Ir}(\text{I})_2]_2$ complex. The ^1H NMR spectrum of the coordinated complex shows 4 inequivalent CH_2 protons on the isoquinoline ring at $\delta_H = 2.57$, 2.71, 4.18 and 4.41. The chemical shifts at 4.18 and 4.41 are assigned to the CH_2 protons directly next to the nitrogen (Figure 30). These protons appear downfield in the spectrum due to the electron withdrawing nature of the nitrogen atom.

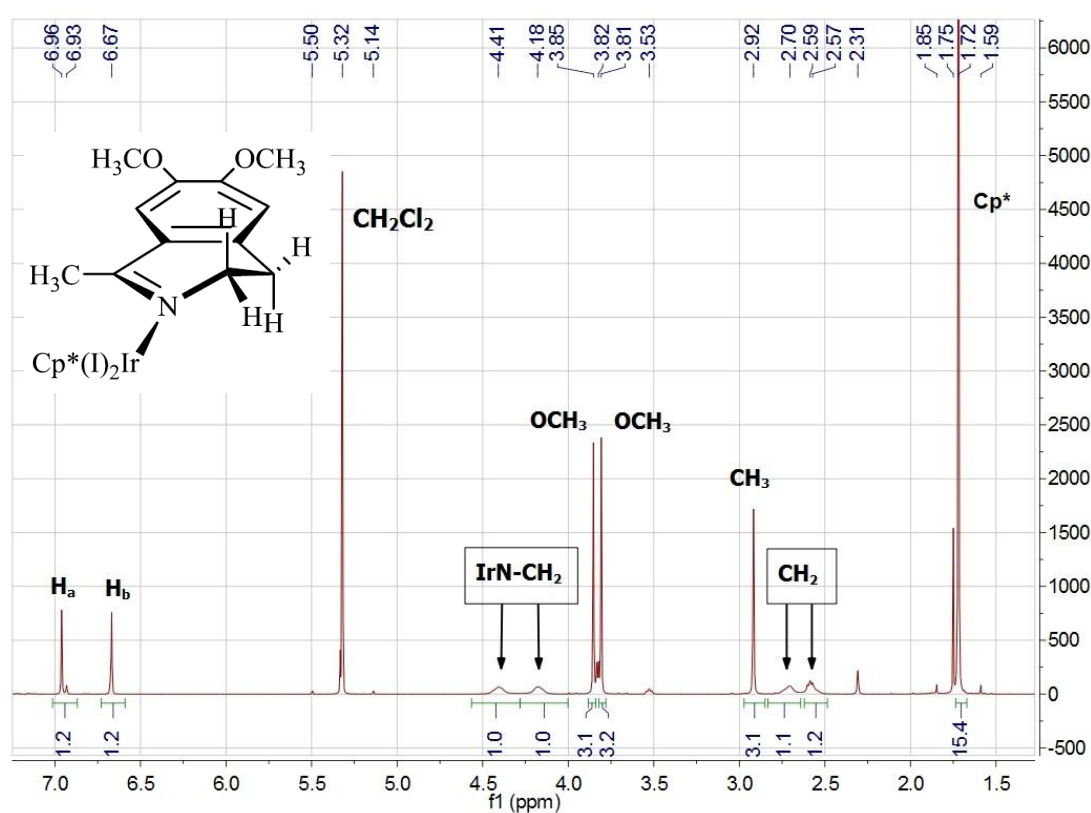


Figure 30 ^1H NMR spectrum of $\text{Cp}^*\text{Ir}(\text{I})_2[6,7\text{-dimethoxy-1-methyl-3,4-dihydroisoquinoline}]$ at 248 K in methylene chloride- d_2 and a schematic showing the anti-syn conformation the isoquinoline ring adopts.

The CH_2 protons appear broad at 248 K and become sharper when cooled to 193K. The carbon chemical shift of the quaternary carbon ($\text{C}=\text{N}$) in the free imine appears at $\delta_C = 163.46$ ppm. When coordinated to the $[\text{Cp}^*\text{Ir}(\text{I})_2]_2$ catalyst, the quaternary carbon chemical shift moves downfield to $\delta_C = 175.85$ ppm, which indicates that the

iridium is coordinating to the imine through the nitrogen at lower temperature, not the C=N double bond. However, upon warming the CH₂ peaks become broad which suggest rotation is possible.

Similar iminium ion metal complexes have been reported as important intermediates for oxidation of amines and alcohols.²³ Recently, Nagao and co-workers have synthesised and characterised an η^2 -iminium ion coordinated ruthenium(II) complex where the conversion between mer-[1] and mer-[2] can be used for the oxidation reactions of alcohols (Figure 31 and 32).²⁴ This process may be operating in the case for the coordination of imine to [Cp*Ir(I)₂]₂.

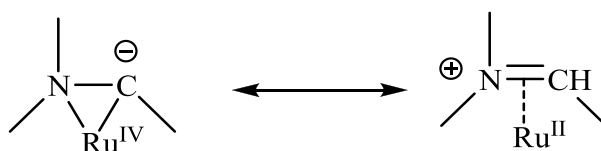


Figure 31 Resonance structures for mer-[1]

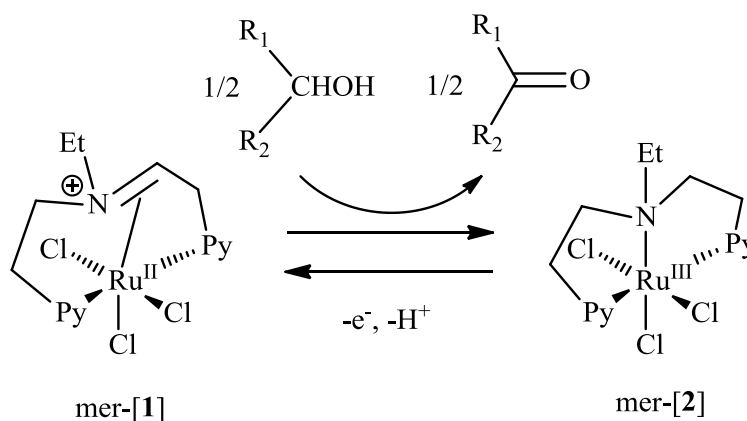


Figure 32 Conversion between mer-[1] and mer-[2]

Similarly, iminium adducts of palladium supported by a bis(phosphine)borate ligand are readily generated from β -hydride elimination of amines at a co-ordinately unsaturated Pd-(II) center.²⁵ It is rare to isolate or even observe intermediates relevant to the *in-situ* reduction of Pd(II) by amines or the Pd-(II) catalysed oxidation of alcohols. The zwitterionic palladium complex, [Ph₂BP₂]Pd(THF)₂[OTf] (where

$[\text{Ph}_2\text{BP}_2] = (\text{Ph}_2\text{B}(\text{CH}_2\text{PPh}_2)_2)^+$ reacts with trialkylamines to activate a C-H bond adjacent to the amine N atom, thereby producing iminium adduct complexes $[\text{Ph}_2\text{BP}_2]\text{Pd}(\text{N},\text{C}:\eta^2\text{-NR}_2\text{CHR}^1)$ (where N,C denotes that the $\text{R}_2\text{N}^+=\text{CHR}^1$ iminium ligand is bonded to Pd through the C=N double bond. In all cases examined the amine activation process is selective for the secondary C-H bond position adjacent to the N atom. These palladacycles undergo facile β -hydride elimination and olefin reinsertion processes.

4.2.8 Reactivity of $\text{Cp}^*\text{Ir}(\text{I})_2(6,7\text{-dimethoxy-1-methyl-3,4-dihydroisoquinoline})$ with *para*-hydrogen in-situ NMR

The coordinated imine complex that was synthesised in the previous section, was prepared again in dry and degassed methylene chloride- d_2 in a Young's tap NMR tube. At low temperature (193 K), 3 bar of *para*-hydrogen was introduced. A ^1H NMR spectrum at 193 K showed no reaction. Upon warming to 300 K, the spectra showed complete conversion to the coordinated amine, indicating that hydrogenation is possible using gaseous H_2 and the amine racemisation catalyst, $[\text{Cp}^*\text{Ir}(\text{I})_2]_2$, i.e. the reaction is reversible (Figure 33). Upon closer inspection of the reaction, a hydride peak was observed that integrated with a coordinated iminium ion that is formed between 273 K and 293 K (Figure 34).

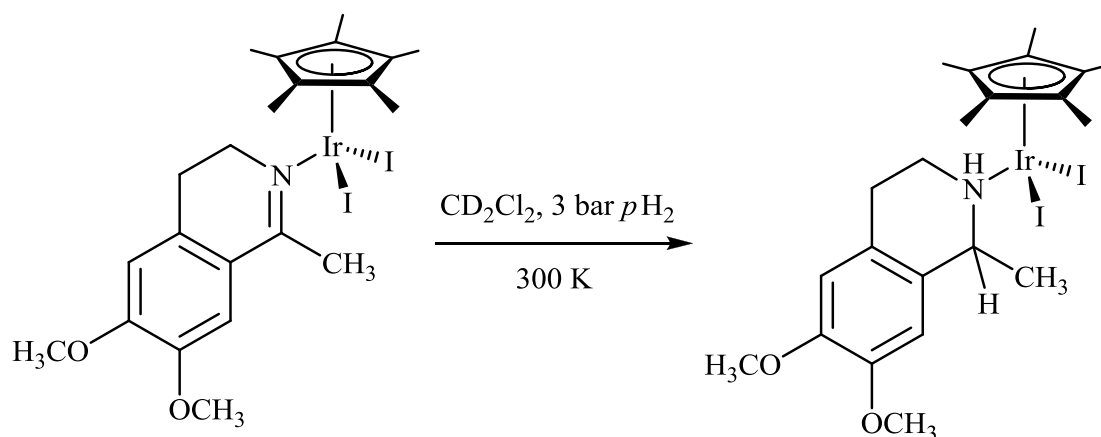


Figure 33 Reaction of coordinated imine with 3 bar of $p\text{H}_2$ in methylene chloride- d_2 at 300 K to form coordinated amine.

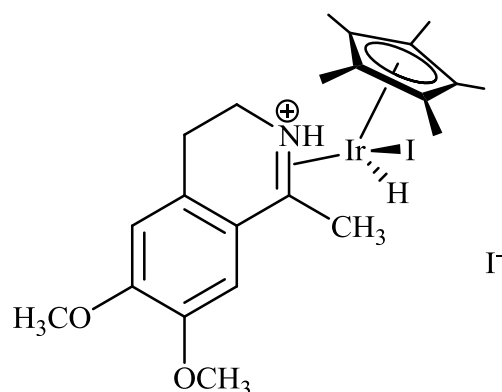


Figure 34 Postulated (iminium ion) iridium hydride intermediate

4.2.9 Dehydrogenation of a cyclic secondary amine using the $[\text{Cp}^*\text{Ir}(\text{I})_2]_2$ amine racemisation catalyst and an excess of bicyclo[2.2.1]hept-2-ene

A system has been developed to dehydrogenate a cyclic secondary amine, 1,2,3,4-tetrahydro-6,7-dimethoxy-1-methylisoquinoline, to its corresponding imine with pentamethylcyclopentadienyliridium(III) iodide dimer and an excess of bicyclo[2.2.1]hept-2-ene in toluene- d_8 at 353 K (Figure 35). The system is highly efficient and will dehydrogenate 100% of the secondary amine to imine within 1 hour at 353 K (See Figure 36). No evidence of bicyclo[2.2.1]hept-2-ane was found in the NMR. This suggests the bicyclic compound is not acting as a sacrificial alkene as originally intended and instead hydrogen gas is being formed. More probably, the ligand hampers a free coordination site on the iridium at a critical stage of the mechanism, where usually the imine would be hydrogenated back to amine.

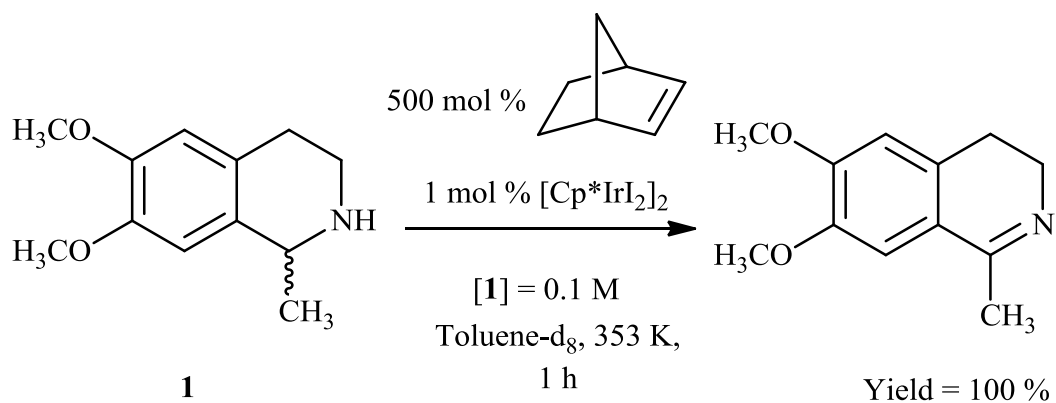


Figure 35 Quantitative conversion of amine to imine using $[\text{Cp}^*\text{Ir(I)}_2]_2$ and an excess of bicyclo[2.2.1]hept-2-ene in toluene- d_8 at 353 K.

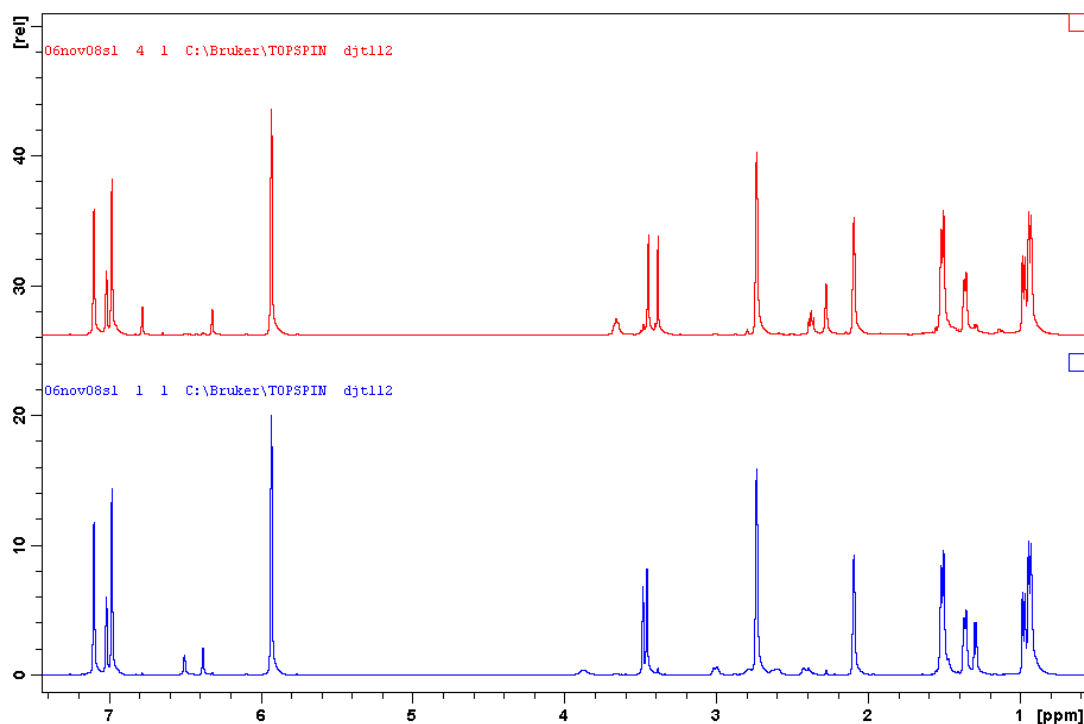


Figure 36 Secondary amine at $t = 0$ at 300 K (bottom); Conversion of amine to imine after heating in toluene- d_8 at 353K for 1 h (top).

4.2.10 Proposed Mechanism based on mechanistic studies and past work

The proposed mechanism for the racemisation of amines using the $[\text{Cp}^*\text{Ir}(\text{I})_2]_2$ catalyst, based on current evidence is shown in Figure 37. The first step is cleavage of the $[\text{Cp}^*\text{Ir}(\text{I})_2]_2$ dimer complex by a secondary amine and formation of a mononuclear Cp^*Ir diiodide complex in which the secondary amine coordinates to the iridium metal through the nitrogen (Section 4.3). Alternatively, the ammine complex, $\text{Cp}^*\text{Ir}(\text{I})_2(\text{NH}_3)$ can also react with a secondary amine in which the ammine ligand is displaced and the mononuclear amine-coordinated Cp^*Ir diiodide complex is formed (Section 4.4). The $\text{Cp}^*\text{Ir}(\text{I})_2$ intermediate can also react with ammonia gas to form an insoluble $\text{Cp}^*\text{Ir}(\text{I})_2(\text{NH}_3)$ complex in toluene, effectively recycling the catalyst (Section 4.1). Upon coordination of the amine to the iridium centre it is proposed that hydrogen iodide is formed by reaction of the NH proton and iodide to form a new Cp^*Ir hydrido iodide complex which can then reprotonate the coordinated imine or lose hydrogen and form imine and $\text{Cp}^*\text{Ir}(\text{I})_2$ which can react with a second equivalent of amine (Section 4.6 and 4.7).

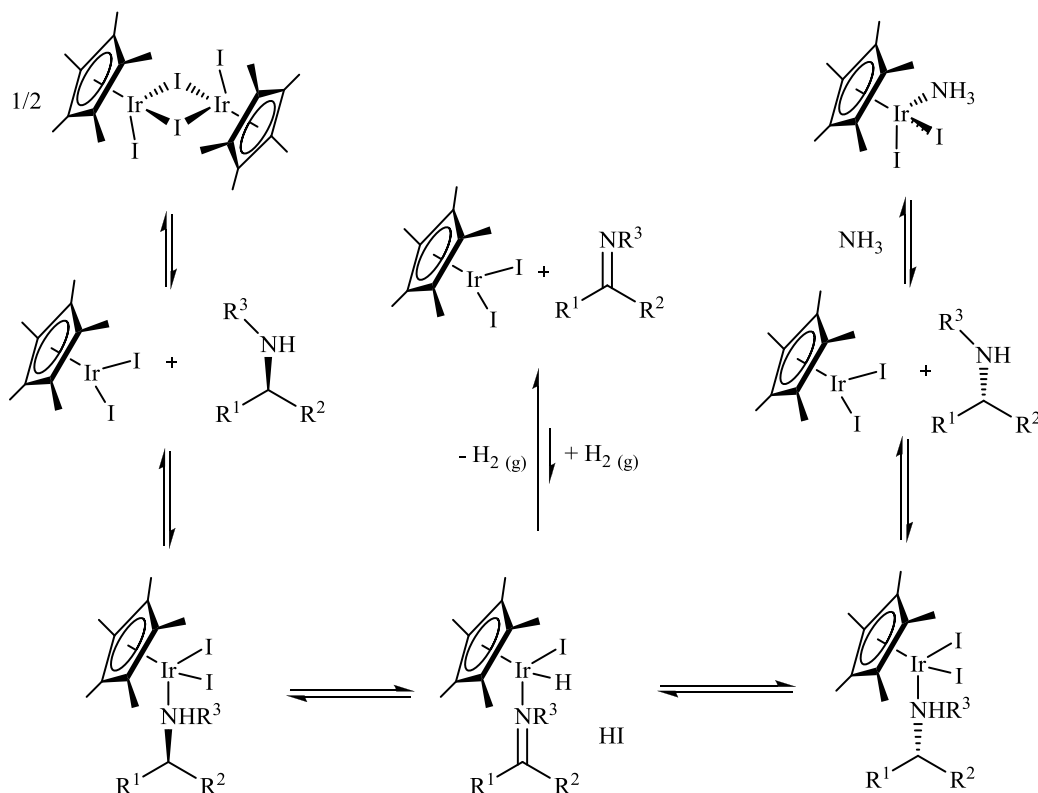


Figure 37 Proposed mechanism for racemisation of amines using $[\text{Cp}^*\text{Ir}(\text{I})_2]_2$

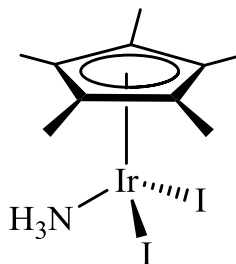
4.3 Summary

In this chapter we have:

- Synthesised and isolated the recycled ammine coordinated complex, $[\text{Cp}^*\text{Ir}(\text{I})_2(\text{NH}_3)]$ and fully characterised it by X-ray crystallography, NMR spectroscopy, UV-visible spectroscopy, IR and elemental analysis;
- Demonstrated that the $[\text{Cp}^*\text{Ir}(\text{I})_2(\text{NH}_3)]$ complex catalyses the racemisation of a secondary amine (sertraline) with comparable activity to $[\text{Cp}^*\text{Ir}(\text{I})_2]_2$;
- Explored the mechanism of the amine racemisation system using $[\text{Cp}^*\text{Ir}(\text{I})_2]_2$ and characterised key intermediates including $[\text{Cp}^*\text{Ir}(\text{I})_2(\text{PhCH}_2\text{NHMe})]$, $[\text{Cp}^*\text{Ir}(\text{Cl})_2(\text{PhCH}_2\text{NHMe})]$ and $[\text{Cp}^*\text{Rh}(\text{Cl})_2(\text{PhCH}_2\text{NHMe})]$. The X-ray crystal structures, NMR data and other spectroscopic techniques, reveal that the first step in the mechanism is the coordination of one secondary amine complex to the iridium centre of $[\text{Cp}^*\text{Ir}(\text{I})_2]$, in which the dimer has been cleaved by the secondary amine;
- Shown that a cyclic imine can coordinate with $[\text{Cp}^*\text{Ir}(\text{I})_2]_2$ at low temperature by $^1\text{H} / ^{15}\text{N}$ HSQC NMR;
- Reacted the coordinated imine with para-hydrogen to show that the reverse reaction, hydrogenation of the imine using $[\text{Cp}^*\text{Ir}(\text{I})_2]_2$ was possible;
- Identified a hydride peak which we postulate is the $[\text{Cp}^*\text{Ir}(\text{H})(\text{I})_2]$ dihydrido-bridged complex as identified by Fujita and Yamaguchi in their dehydrogenation-hydrogenation paper (see introduction);¹⁴
- Dehydrogenated a cyclic imine with 0.1 mol% $[\text{Cp}^*\text{Ir}(\text{I})_2]_2$ and norbornene in quantitative yield and within 1 hour.
- Proposed a mechanism based on the current-evidence for racemisation of amines using the $[\text{Cp}^*\text{Ir}(\text{I})_2]_2$ complex.

4.4 NMR data

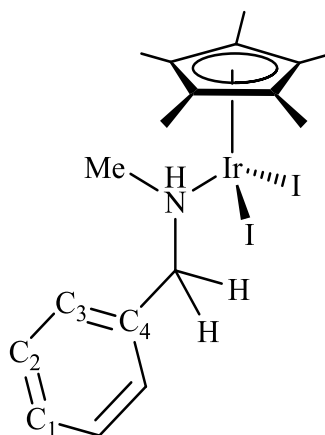
4.4.1 Cp*Ir(I)₂(NH₃)



	δ / ppm (area, multiplicity)	assignment
¹ H NMR	1.84 (15H, s)	C ₅ (CH ₃) ₅
500 MHz (CD ₂ Cl ₂), 300K	3.27 (3H, s)	NH ₃

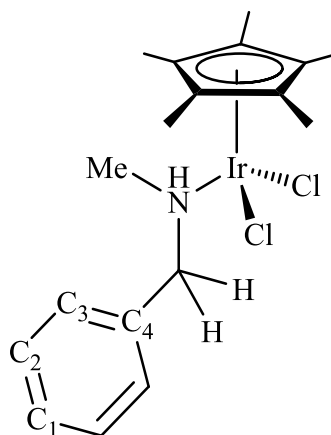
	δ / ppm (area, multiplicity)	assignment
¹³ C NMR	10.74	C ₅ (CH ₃) ₅
125 MHz (CD ₂ Cl ₂), 248K	86.91	C ₅ (CH ₃) ₅

Table 4.4.1: ¹H and ¹³C NMR data and assignments for Cp*Ir(I)₂(NH₃)

4.4.2 Cp*Ir(I)₂(PhCH₂NHMe)

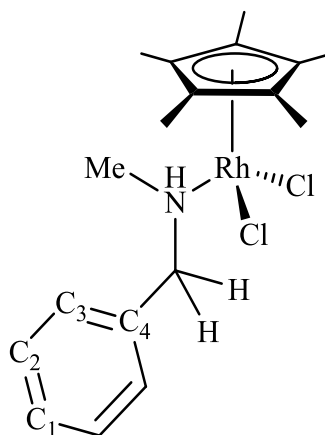
	δ / ppm (area, multiplicity)	assignment
¹ H NMR	1.90 (15H, s)	C ₅ (CH ₃) ₅
500 MHz	2.82 (3H, d)	CH ₃
(CD ₂ Cl ₂), 243K	3.38 (1H, t)	CHH
	3.87 (1H, dq)	NH
	5.18 (1H, d)	CHH
	7.26-7.40 (5H, m)	ArH
	δ / ppm (area, multiplicity)	assignment
¹³ C NMR	11.17	C ₅ (CH ₃) ₅
125 MHz	43.14	CH ₃
(CD ₂ Cl ₂), 243K	53.95	CH ₂
	86.77	C ₅ (CH ₃) ₅
	128.52	C ¹ / C ² / C ³
	128.89	C ¹ / C ² / C ³
	129.57	C ¹ / C ² / C ³
	135.99	C ⁴

Table 4.4.2: ¹H and ¹³C NMR assignments for Cp*Ir(I)₂(PhCH₂NHMe)

4.4.3 $\text{Cp}^*\text{Ir}(\text{Cl})_2(\text{PhCH}_2\text{NHMe})$ 

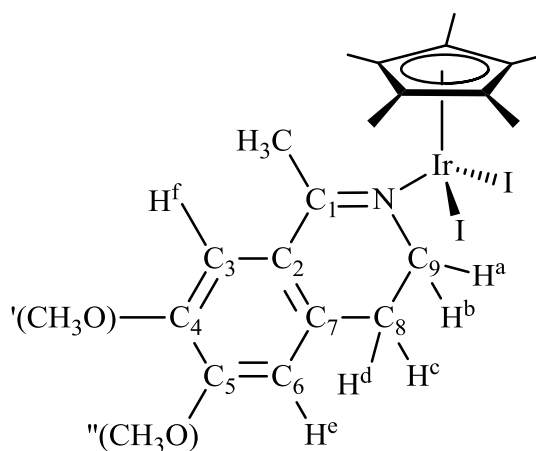
	δ / ppm (area, multiplicity)	assignment
^1H NMR	1.68 (15H, s)	$\text{C}_5(\text{CH}_3)_5$
500 MHz	2.69 (3H, d)	CH_3
(CDCl_3), 243K	3.46 (1H, t)	CHH
	3.92 (1H, dq)	NH
	4.89 (1H, d)	CHH
	7.25-7.37 (5H, m)	ArH
	δ / ppm (area, multiplicity)	assignment
^{13}C NMR	9.45	$\text{C}_5(\text{CH}_3)_5$
125 MHz	39.27	CH_3
(CDCl_3), 243K	60.64	CH_2
	84.94	$\text{C}_5(\text{CH}_3)_5$
	128.58	$\text{C}^1 / \text{C}^2 / \text{C}^3$
	128.96	$\text{C}^1 / \text{C}^2 / \text{C}^3$
	129.69	$\text{C}^1 / \text{C}^2 / \text{C}^3$
	136.18	C^4

Table 4.4.3: ^1H and ^{13}C NMR assignments for $\text{Cp}^*\text{Ir}(\text{Cl})_2(\text{PhCH}_2\text{NHMe})$

4.4.4 $\text{Cp}^*\text{Rh}(\text{Cl})_2(\text{PhCH}_2\text{NHMe})$ 

	δ / ppm (area, multiplicity)	assignment
^1H NMR	1.71 (15H, s)	$\text{C}_5(\text{CH}_3)_5$
500 MHz	2.56 (3H, d)	CH_3
(CDCl_3), 243K	2.97 (1H, dq)	NH
	3.46 (1H, t)	CHH
	4.85 (1H, d)	CHH
	7.10-7.35 (5H, m)	ArH
	δ / ppm (area, multiplicity)	assignment
^{13}C NMR	9.41	$\text{C}_5(\text{CH}_3)_5$
125 MHz	37.81	CH_3
(CDCl_3), 243K	58.93	CH_2
	93.53 (d)	$\text{C}_5(\text{CH}_3)_5$
	128.46	$\text{C}^1 / \text{C}^2 / \text{C}^3$
	129.21	$\text{C}^1 / \text{C}^2 / \text{C}^3$
	129.62	$\text{C}^1 / \text{C}^2 / \text{C}^3$
	138.04	C^4

Table 4.4.4: ^1H and ^{13}C NMR assignments for $\text{Cp}^*\text{Rh}(\text{Cl})_2(\text{PhCH}_2\text{NHMe})$

4.4.5 Cp*Ir(I)₂[6,7-dimethoxy-1-methyl-3,4-dihydroisoquinoline]

	δ / ppm (area, multiplicity)	assignment	J / Hz	assignment
¹ H NMR	1.72 (15H, s)	C ₅ (CH ₃) ₅		
500 MHz	2.57 (1H, br s)	H ^c /H ^d		
(CD ₂ Cl ₂), 248K ²	2.71 (1H, br s)	H ^c /H ^d		
	2.92 (3H, s)	CH ₃		
	3.81 (3H, s)	(OCH ₃) ["]		
	3.85 (3H, s)	(OCH ₃) [']		
	4.18 (1H, br s)	H ^a /H ^b		
	4.41 (1H, br s)	H ^a /H ^b		
	6.67 (1H, s)	H ^e		
	6.96 (1H, s)	H ^f		

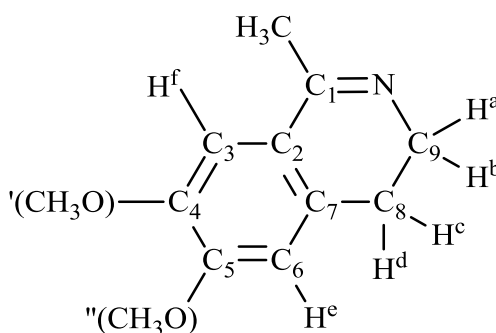
² At lower temperature (193 K) H^c and H^d resolve into sharp multiplets

	δ / ppm (area, multiplicity)	assignment	J / Hz	assignment
^{13}C NMR 125 MHz (CD_2Cl_2), 248K	10.7	$\text{C}_5(\text{CH}_3)_5$		
	28.3	C^8		
	33.1	CH_3		
	56.1	$(\text{OCH}_3)''$		
	56.2	$(\text{OCH}_3)'$		
	65.3	C^9		
	87.4	$\text{C}_5(\text{CH}_3)_5$		
	109.1	C^6		
	110.2	C^3		
	123.3	C^7		
	131.7	C^2		
	147.3	C^5		
	152.2	C^4		
	175.8	C^1		
^{15}N NMR 51 MHz (CD_2Cl_2), 248K	-219.0	Ir-N		

Table 4.4.5: ^1H , ^{13}C and ^{15}N NMR data and assignments for $\text{Cp}^*\text{Ir}(\text{I})_2[6,7\text{-dimethoxy-1-methyl-3,4-dihydroisoquinoline}]$

Assigned with the aid of ^1H , $^{13}\text{C}\{^1\text{H}\}$, $^1\text{H} / ^{13}\text{C}$ HSQC, $^1\text{H} / ^{13}\text{C}$ HMBC, $^1\text{H} / ^1\text{H}$ COSY, ^1H NOESY and $^1\text{H} / ^{15}\text{N}$ HMQC experiments.

4.4.6 6,7-dimethoxy-1-methyl-3,4-dihydroisoquinoline (free ligand) at low T



	δ / ppm (area, multiplicity)	assignment	J / Hz	assignment
¹ H NMR				
500 MHz	2.30 (3H, s)	CH ₃		
(CD ₂ Cl ₂), 248K	2.58 (2H, t)	CH ₂		
	3.52 (2H, t)	CH ₂		
	3.82 (3H, s)	OCH ₃		
	3.83 (3H, s)	OCH ₃		
	6.67 (1H, s)	H ^e		
	6.93 (1H, s)	H ^f		

	δ / ppm (area, multiplicity)	assignment	J / Hz	assignment
¹³ C NMR				
125 MHz	23.7	CH ₃		
(CD ₂ Cl ₂), 248K	25.7	CH ₂		
	47.0	N-CH ₂		
	55.9	OCH ₃		
	56.0	OCH ₃		
	108.3	C ³		

	109.9	C ⁶
	122.3	C ²
	130.9	C ⁷
	147.2	C ⁴ / C ⁵
	150.5	C ⁴ / C ⁵
	163.5	C ¹

¹⁵ N NMR	-114.1	Ir-N
51 MHz		
(CD ₂ Cl ₂), 248K		

Table 4.4.6: ¹H, ¹³C and ¹⁵N NMR data and assignments for 6,7-dimethoxy-1-methyl-3,4-dihydroisoquinoline (free ligand)

Assigned with the aid of ¹H, ¹³C{¹H}, ¹H / ¹³C HSQC, ¹H / ¹³C HMBC, ¹H / ¹H COSY, ¹H NOESY and ¹H / ¹⁵N HMQC experiments.

4.5 References

- 1.) (a) J. H. Koh, H. M. Jeong and J. Park, *Tetrahedron Lett.*, 1998, **39**, 5545; (b) G. Csajenyik, K. Bogár and J. –E. Bäckvall, *Tetrahedron Lett.*, 2004, **45**, 6799; (c) M. Ito, A. Osaku, S. Kitahara, M. Hirakawa and T. Ikariya, *Tetrahedron Lett.*, 2003, **44**, 7521; (d) K. Fujita, S. Furukawa and R. Yamaguchi, *J. Organomet. Chem.*, 2002, **649**, 289.
- 2.) H. U. Blaser and E. D. Schmidt, *Asymmetric Catalysis on Industrial Scale: Challenges, Approaches and Solutions*; Wiley-VCH: Chichester; John Wiley [distributer], Weinheim, 2004.
- 3.) A. H. Éll, J. S. M. Samec, C. Brasses and J. –E. Bäckvall, *Chem. Commun.*, 2003, 1144; O. Pamies, A. H. Éll, J. S. M. Samec, N. Hermanns and J. –E. Bäckvall, *Tetrahedron Lett.*, 2002, **43**, 4699; . S. M. Samec, A. H. Éll and J. – E. Bäckvall, *Chem. Eur. J.*, 2005, **11**, 2327.
- 4.) M. Stirling, Coupled Catalytic Cycles: Development of a Procedure for the Dynamic Kinetic Resolution of Amines. PhD Thesis, University of Huddersfield, Huddersfield, U.K. 2006.
- 5.) A. J. Blacker, M. J. Stirling and M. I. Page, *Org. Proc. Res. Dev.*, 2007, **11**, 642.
- 6.) P. M. Maitlis, A. Haynes, B. R. James, M. Catellani and G. P. Chiusoli, *Dalton Trans.*, 2004, **21**, 3409.
- 7.) M. R. Churchill and S. A. Julis, *Inorg. Chem.*, 1979, **18**, 1215.
- 8.) J. W. Kang, K. Moseley and P. M. Maitlis, *J. Am. Chem. Soc.*, 1969, **91**, 5970.
- 9.) A. J. Blacker, S. Brown, B. Clique, B. Gourlay, C. E. Headley, S. Ingham, D. Ritson, T. Screen, M. J. Stirling, D. Taylor and G. Thompson, *Org. Proc. Res. Dev.*, **2009**, 13, 1370.
- 10.) C. Kilner, University of Leeds, CCDC 724479.
- 11.) R. Kawahara, K. Fujita and R. Yamaguchi, *J. Am. Chem. Soc.* 2010, **132**, 15108.
- 12.) A. J. Blacker, M. M. Farah, S. P. Marsden, O. Saidi and J. M. J. Williams, *Tetrahedron Lett.*, 2009, **50**, 6106.
- 13.) A. J. Blacker, M. M. Farah, M. I. Hall, S. P. Marsden, O. Saidi and J. M. J. Williams, *Org. Lett.*, 2009, **11**, 2039.

- 14.) R. Yamaguchi, C. Ikeda, Y. Takahashi and K. Fujita, *J. Am. Chem. Soc.*, 2009, **131**, 8410.
- 15.) P. Barbaro and F. Liguori, *Chem. Rev.*, 2009, **109**, 515.
- 16.) P. T. Anastas and J. C. Warner, *Green Chemistry: Theory and Practice*; Oxford University Press: Oxford, 1998.
- 17.) I. T. Horváth and P. T. Anastas, *Chem. Rev.*, 2007, **107**, 2169.
- 18.) P. T. Anastas, M. M. Kirchhoff and T. C. Williamson, *Appl. Catal., A: Gen.* 2001, **221**, 3.
- 19.) R. A. Sheldon, *Green Chem.* 2008, **10**, 359.
- 20.) www.epa.gov/greenchemistry.
- 21.) (a) A European Technology Platform For Sustainable Chemistry, http://www.cefic-ustech.org/files/Publications/ETP_sustainable_chemistry.pdf.
(b) SusChem, Implementation Action Plan, 2006, <http://www.suschem.org>.
- 22.) R. Kawahara, K. Fujita and R. Yamaguchi, *J. Am. Chem. Soc.*, 2010, **132**, 15108.
- 23.) (a) S. Murahashi, N. Komiya, H. Terai and T. J. Nakae, *J. Am. Chem. Soc.*, 2003, **125**, 15312; (b) S. Murahashi, T. Naota, T. Kuwabara, T. Saito, H. Kumobayashi and S. Akutagawa, *J. Am. Chem. Soc.* 1990, **112**, 7820; (c) S. Murahashi, T. Naota and K. J. Yonemura, *J. Am. Chem. Soc.*, 1988, **110**, 8256.
- 24.) S. Fukui, N. Suzuki, T. Wada, K. Tanaka and H. Nagao, *Organometallics*, 2010, **29**, 1534.
- 25.) C. Lu and J. Peters, *J. Am. Chem. Soc.* 2004, **126**, 15818.

USING ATH CATALYSTS FOR THE PRODUCTION OF HYPERPOLARISED CARBON DIOXIDE

5.1 General Introduction

In this chapter a novel methodology for production of hyperpolarised carbon dioxide (CO_2) using metal-catalysed transfer hydrogenation complexes is discussed. The production of hyperpolarised CO_2 using metal-catalysed transfer hydrogenation complexes could open up possibilities of new mechanistic techniques that implement hyperpolarised CO_2 to study reaction mechanisms such as CO_2 insertion reactions into metal hydride complexes,¹ such as the insertion of CO_2 into the 18-electron rhodium hydride complex, $\text{Cp}^*\text{Rh}(\text{H})(\text{TsNC}_6\text{H}_4\text{NH}_2)$ to form the 18-electron formate complex, $\text{Cp}^*\text{Rh}(\text{OCHO})(\text{TsNC}_6\text{H}_4\text{NH}_2)$, see Chapter 3. Practical aspects regarding the handling of hyperpolarised CO_2 have not been investigated in this study.

Since its discovery, nuclear magnetic resonance (NMR) has rapidly evolved into an important tool in chemistry and biochemistry. After the introduction of NMR imaging by Lauterbur in 1973,² NMR techniques became used extensively in medical diagnostic imaging and biological research where they are commonly referred to as magnetic resonance imaging (MRI) and magnetic resonance spectroscopy (MRS). In the past, clinical MRI was restricted to the imaging of protons because of the insufficient sensitivity of non-proton nuclei. In recent years, hyperpolarisation techniques have been developed that can increase NMR signals by several orders of magnitude.^{3,4} The increased signal from hyperpolarised non-proton nuclei enables novel clinical examinations including imaging of the lungs and respiratory airways after inhalation of the hyperpolarised gas.⁵

5.1.1 The Nuclear Spin

The fundamental principle of NMR is based on the interaction of atomic nuclei with an external magnetic field. All nucleons (neutrons and protons) have the intrinsic property of spin, the overall spin denoted by the spin quantum number I . The nuclear spin is a purely quantum mechanical quantity; however in classical physics it may be depicted as an angular momentum where the nucleus rotates around its axis. Many atomic nuclei that have a non-zero spin quantum number can be studied with NMR spectroscopy, e.g., ^1H , ^{13}C and ^{15}N .

A rotating nucleus with positive charge has a microscopic ring current that gives rise to a microscopic magnetic moment μ , which can be thought of as a microscopic compass needle. Placing the nucleus in an external magnetic field B_0 , causes the magnetic moments to orient themselves along the magnetic field. However, in contrast to compass needles, only a discrete number of orientations are allowed given by the equation $2I+1$, whereby each orientation is associated with a distinct quantum energy E_m :

$$E_m = -\mu \cdot B_0 = m\gamma\hbar B_0$$

In the above equation, $m = -I, -I+1, \dots, +I$ is the magnetic quantum number and each atomic nucleus has a characteristic called the “gyromagnetic ratio” given by the constant γ . The magnetic moment μ cannot be oriented parallel to B_0 and therefore experiences a torque when trying to align with B_0 . In analogy with a top rotating in the earth’s gravity field, this torque will cause μ to revolve around B_0 with an angular frequency ω , denoted the Larmor frequency:

$$\omega = \gamma B_0.$$

5.1.2 Nuclear Polarisation

The number of nuclei which populate each energy state is defined by N_{up} and N_{down} , respectively. When the populations of each energy state are equal, the magnetic moments cancel, which causes zero macroscopic magnetisation and therefore no NMR signal will be observed. Under thermal equilibrium conditions the number of nuclei pointing “down” will be slightly fewer than the number of nuclei pointing “up” ($N_{\text{down}} < N_{\text{up}}$), due to a slightly higher energy associated with the “down” directions (See Figure 1).

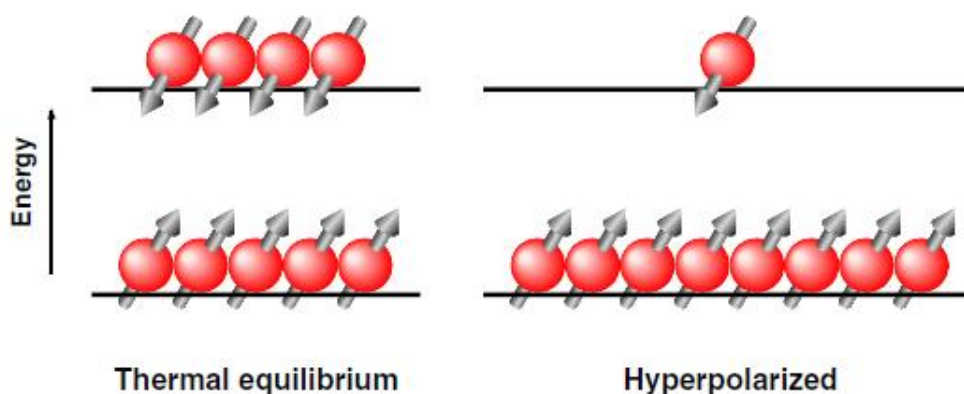


Figure 1 Pictorial description by Golman *et al.*, of the orientation of the nuclei at thermal equilibrium and in the hyperpolarised state. In the figure, the magnetic field (B_0) is directed vertically upwards.⁶

The nuclear polarisation P (for nuclei with the spin quantum number $I = 1/2$) is defined by:

$$P \equiv \frac{N_{\text{up}} - N_{\text{down}}}{N_{\text{up}} + N_{\text{down}}}$$

The magnetisation M , and thus the NMR signal, S , will be proportional to the polarization and the total number of nuclei within the sample ($N_0 = N_{\text{up}} + N_{\text{down}}$):

$$S \propto N_0 P.$$

The population of energy levels is, under thermal equilibrium conditions governed by the Boltzmann distribution:

$$N_m = \frac{\exp(E_m/k_B T)}{\sum_{i=-I}^{+I} \exp(E_i/k_B T)}$$

Where, N_m is the number of nuclei in the state m , E_m is given in Section 5.1.2 and T is the temperature. By combining these equations, P can be expressed as:

$$P = \tanh\left(\frac{\gamma \hbar B_0}{2kT}\right).$$

Where, \tanh is the hyperbolic tangens, B_0 is the magnetic field strength, γ is the gyromagnetic ratio for the nucleus, T the temperature, k the Boltzmann constant and \hbar the Planck constant (Golman *et al.*, 2003).⁶

5.1.3 Hyperpolarisation

From the above equations it is evident that increasing the magnetic field strength and decreasing the temperature will increase the total thermal polarisation of the sample.⁷ Using a simplistic “brute-force” approach, a sample which is subjected to a very strong magnetic field at very low temperature will subsequently have a greater polarisation. The polarisation of ^{13}C at 1.5 T and 310 K is 1.2×10^{-6} ; at 20 T and 4 K (the temperature of liquid helium) the polarisation is 1.3×10^{-3} ; this increases the polarisation by a factor of 1033. If the sample could be brought from 20 T, 4 K to 1.5 T, 310 K instantaneously and without loss of polarisation, it could be regarded as being “hyperpolarised”. Figure 1 illustrates the difference between thermal equilibrium and the hyperpolarised state.^{5,6}

5.1.4 The Dynamic Nuclear Polarisation (DNP) method

As described in the previous section, lower temperatures and higher magnetic fields increase the polarisation of a sample. At 1 K and 3 T, the nuclear polarisation is still too low for ^{13}C imaging purposes (polarisation $< 0.1\%$).⁸ However, electrons are highly polarised ($> 90\%$) due to the much larger gyromagnetic ratio for an electron. Using the dynamic nuclear polarisation (DNP) method, the high polarisation of the electron spins can be transferred to coupled nuclear spins.⁹ Under optimal conditions, the polarisation of the nuclear spins can be increased by the ratio between the electronic and nuclear resonance frequencies. For ^{13}C nuclear spins, the ratio is < 2600 . The DNP method has been used to increase the sensitivity of ^{13}C and ^{15}N NMR spectroscopy.^{10,11} In the method described by Ardenkjær *et al.*,¹² the material containing the nuclei to be hyperpolarized is doped with free radical. When exposed to a high magnetic field (< 3 T) and low temperature (< 1 K), the unpaired electrons of the free radical are highly polarized ($> 90\%$), whereas the ^{13}C nuclei are polarized to only $< 0.1\%$. Microwave irradiation, in a nuclear polariser (Figure 2), near the electron paramagnetic resonance frequency transfers polarization from the unpaired electrons to the nuclei, whereby the nuclear polarization in the solid material can be increased to 20%-40% (Figure 3). By rapid melting and dissolving, the solid can be transformed into an injectable liquid, with small to negligible polarization losses.



Figure 2 600 MHz NMR spectrometer and HyperSense Nuclear polariser.

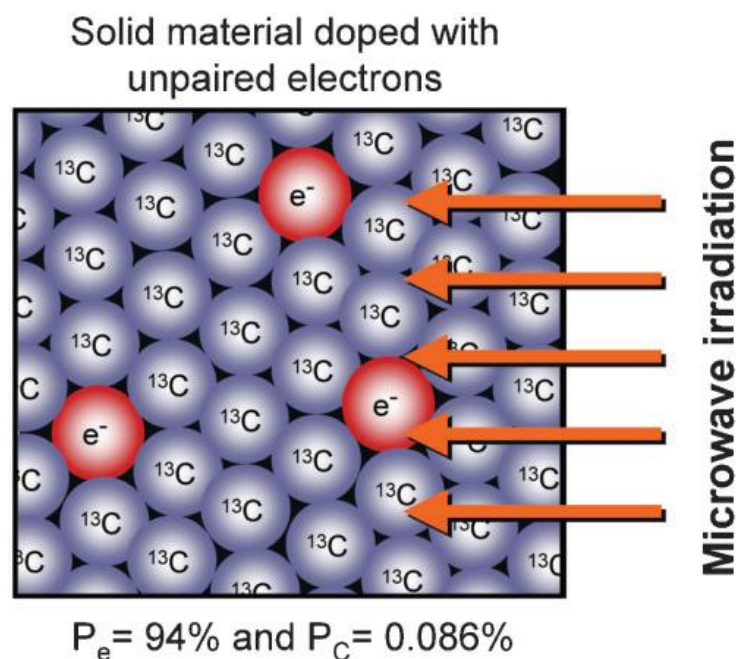


Figure 3 During the dynamic nuclear polarisation process, polarisation is transferred from the electrons of the doping material to the ^{13}C nuclei by means of microwave irradiation (Golman *et al.*).⁶

5.1.5 Properties of potential ^{13}C imaging agents

Virtually any small organic molecule containing ^{13}C can be hyperpolarized with the DNP technique, including many endogenous substances (Golman *et al.*, 2002). The main limitations are imposed by water solubility, and toxicological and relaxation time considerations. The NMR sensitivity of natural abundant ^{13}C in the body is low due to a low isotopic abundance. Isotopic enrichment of ^{13}C to $> 99\%$ is possible and can be used to increase the signal of a hyperpolarized imaging agent.⁵

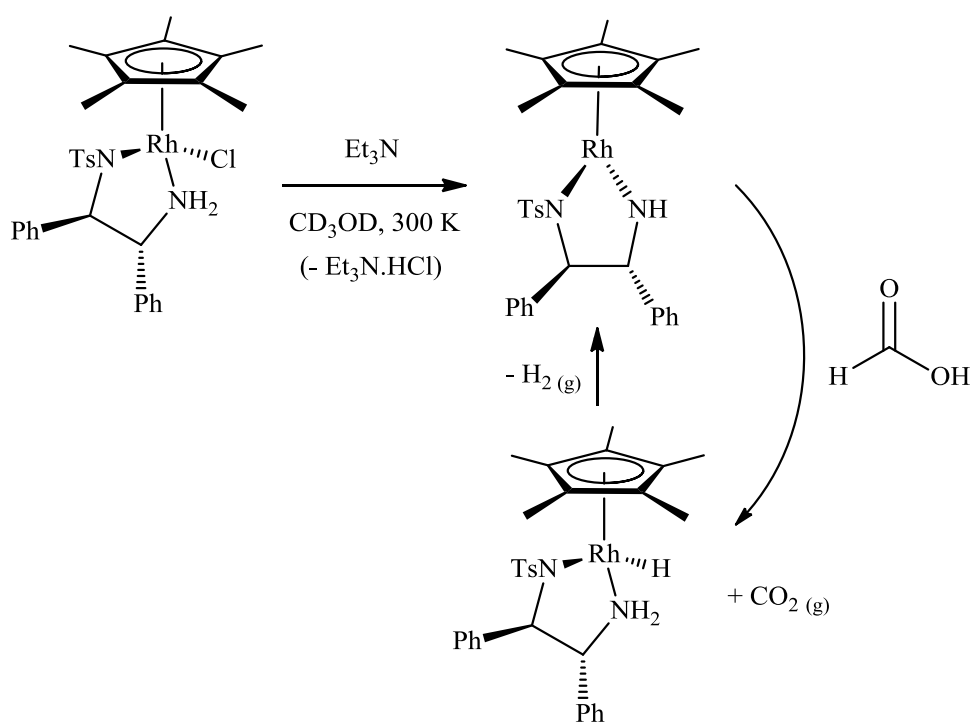
5.1.6 Aims of the Chapter

We identified that the transfer hydrogenation complexes in Chapters 2 and 3 catalytically decompose formic acid into hydrogen and carbon dioxide gas and regenerate the active catalyst upon completion. Our aim for this chapter was to exploit this reaction, attempting to produce hyperpolarised carbon dioxide from a solution of hyperpolarised triethylamine:formic acid in methanol- d_4 .

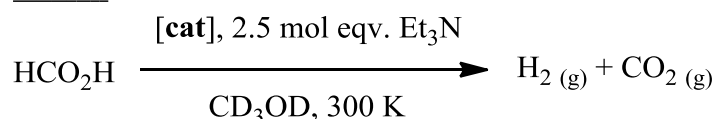
5.2 Results and Analysis

5.2.1 Decomposition of formic acid by $\text{Cp}^*\text{Rh}(\text{Cl})(\text{TsNCHPhCHPhNH}_2)$

The following reaction demonstrates the potential of using transfer hydrogenation complexes to decompose formic acid to produce hydrogen and carbon dioxide (Figure 4). In this reaction, HCl is abstracted from the 18-electron chloride complex, $\text{Cp}^*\text{Rh}(\text{Cl})(\text{TsNCHPhCHPhNH}_2)$ by triethylamine to form the 16-electron amido complex. The 16-electron amido complex can then react with formic acid to form the 18-electron hydride and evolve carbon dioxide gas. The 18-electron hydride then loses hydrogen and the 16-electron amido complex is regenerated to react further with formic acid.



Overall:



where: **cat** = $\text{Cp}^*\text{Rh}(\text{Cl})(\text{TsNCHPhCHPhNH}_2)$,
 $\text{Cp}^*\text{Ir}(\text{Cl})(\text{TsNCHPhCHPhNH}_2)$, $\text{Cp}^*\text{Rh}(\text{TsNC}_6\text{H}_4\text{NH})$, etc.

Figure 4 The decomposition of formic acid in the presence of ATH catalysts

5.2.2 Observation of CO₂ from the decomposition of H¹²CO₂H

We proposed that it may be possible to hyperpolarise a solution of triethylamine and formic acid; this solution would be reacted with the transfer hydrogenation catalyst in methanol-d₄ in an attempt to transfer the hyperpolarisation of formic acid to produce hyperpolarised carbon dioxide.

In this experiment, in collaboration with Jonathon Holmes, natural-abundance TEAF solution (5:2 H¹²CO₂H and triethylamine) was hyperpolarised in a Hypersense Dynamic Nuclear Polariser (DNP) by placing the TEAF solution inside a dissolution cup, adding a small amount of trityl radical, immersing in liquid helium (1.4 K) and irradiating with microwaves at roughly 94 Hz for eight hours. After this period, 4 mL of superheated methanol was rapidly injected into the sample and swiftly transferred over to an Avance II Bruker 600 MHz wide bore magnet into a solution of the asymmetric transfer hydrogenation catalyst, Cp*Rh(Cl)(TsNCHPhCHPhNH₂) (5 mg in 0.5 mL of methanol-d₄). Once the sample had entered the magnet and combined with the ATH catalyst solution, a series of rapid 90° ¹³C{¹H} pulses were applied. Figure 5 shows a processed acquisition from the 1D ¹³C{¹H} experiment. We observe hyperpolarised TEAF solution (triethylamine and formic acid) and a peak at δ 124.2, which corresponds to CO₂ gas (Figure 5). A control experiment was performed without catalyst and no CO₂ gas was observed in the ¹³C{¹H} NMR spectroscopy experiment.

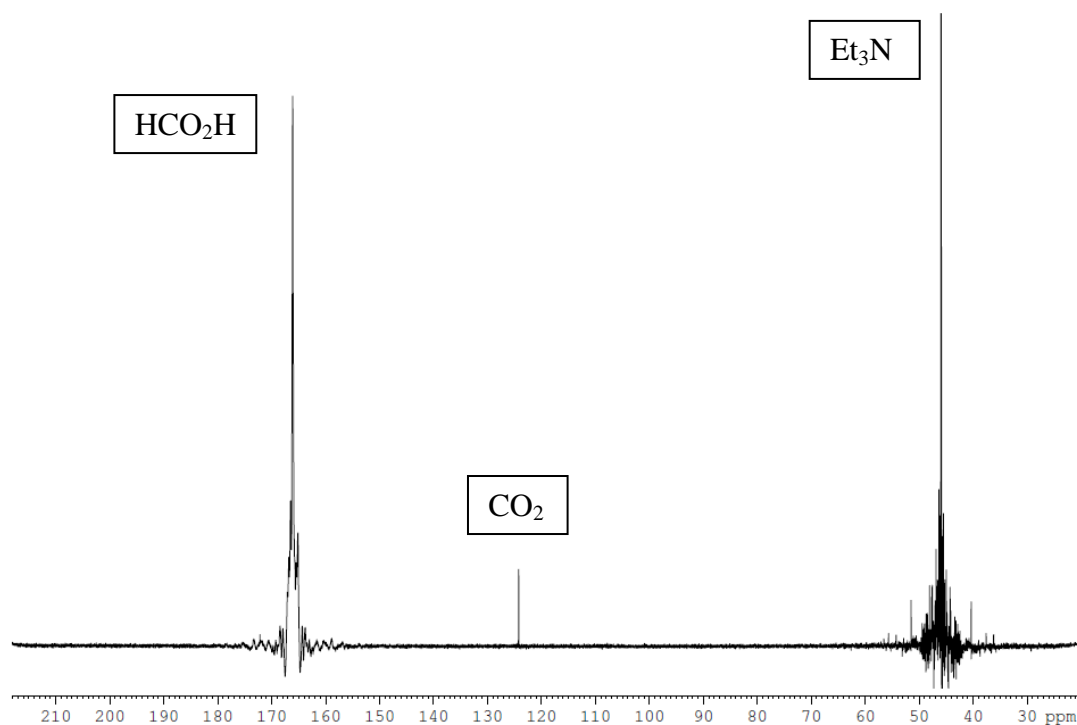


Figure 5 Observation of a ^{13}C CO_2 peak from decomposition of natural-abundance $\text{H}^{12}\text{CO}_2\text{H}$

5.2.3 Hyperpolarisation of ^{13}C -labelled $\text{H}^{13}\text{CO}_2\text{H}$ / Et_3N solution

In this experiment, also in collaboration with Jonathon Holmes, ^{13}C -labelled TEAF solution (5:2 $\text{H}^{13}\text{CO}_2\text{H}$ and triethylamine) was hyperpolarised in the Hypersense Dynamic Nuclear Polariser (DNP) by the same method used in Section 5.2.2. Once the dissolved sample had entered the magnet and combined with the solution of the $\text{Cp}^*\text{Rh}(\text{Cl})(\text{TsNCHPhCHPhNH}_2)$ ATH catalyst in methanol- d_4 , a series of rapid 90° $^{13}\text{C}\{^1\text{H}\}$ pulses were applied. Figure 6 shows a processed acquisition from the arrayed 1D $^{13}\text{C}\{^1\text{H}\}$ time-resolved experiment. We observe hyperpolarised TEAF solution (triethylamine and formic acid) and a peak at δ 124.2, which corresponds to carbon dioxide gas which decays over time (Figure 7). A plot of the signal to noise ratio for the ^{13}C resonance at δ 164.4 (hyperpolarised formic acid) and δ 124.2 (CO_2) is presented in Figure 8.

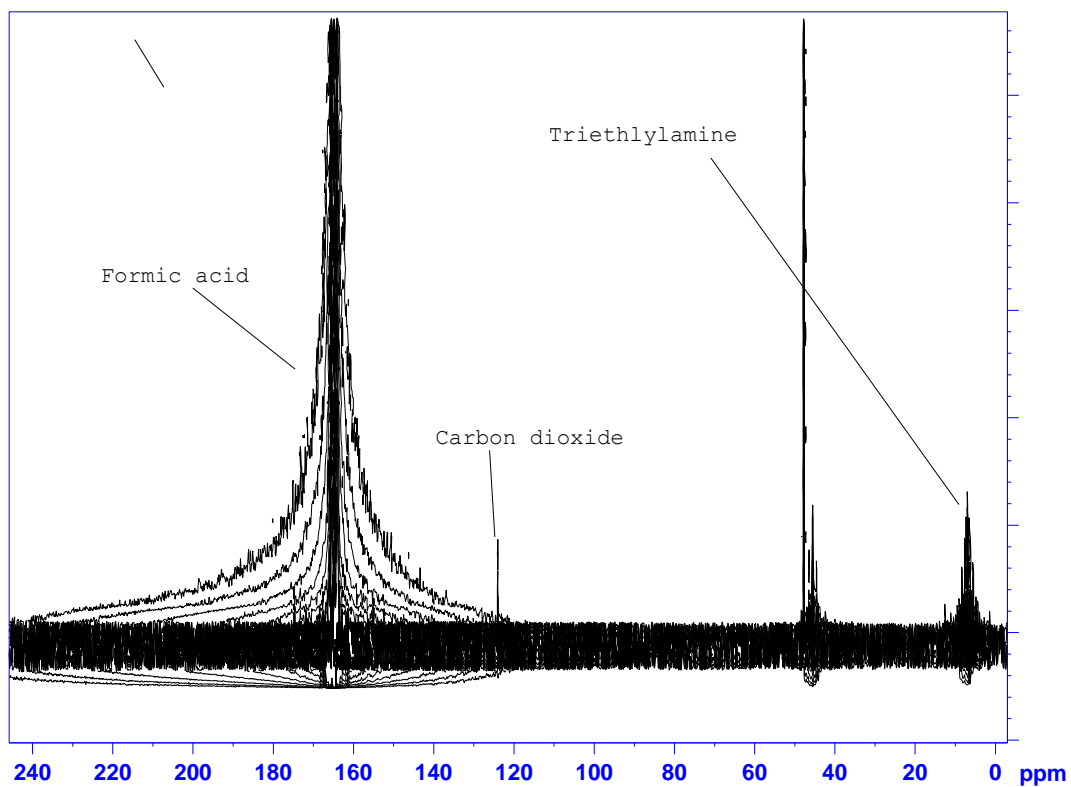


Figure 6 $^{13}\text{C}\{^1\text{H}\}$ NMR spectrum of hyperpolarised of ^{13}C -labelled $\text{H}^{13}\text{CO}_2\text{H}$ / Et_3N (2:5 TEAF solution) and $^{13}\text{CO}_2(\text{g})$

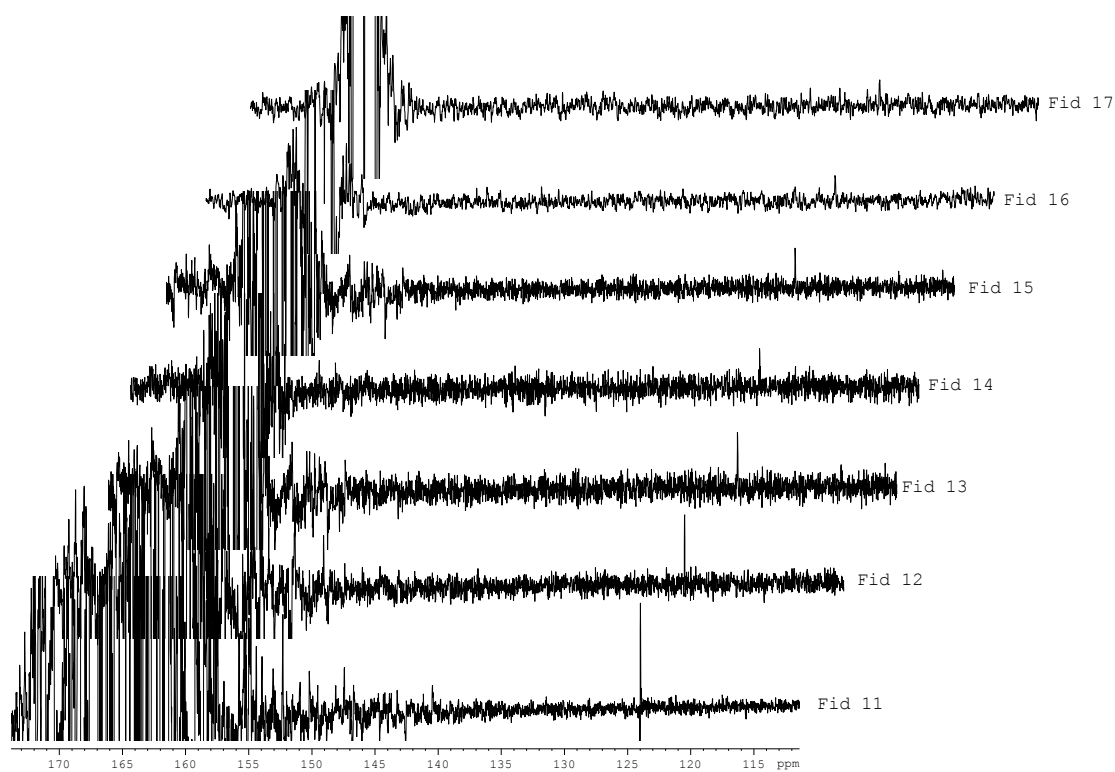


Figure 7 Arrayed 1D $^{13}\text{C}\{^1\text{H}\}$ experiment showing decay of $\text{CO}_2(\text{g})$ signal

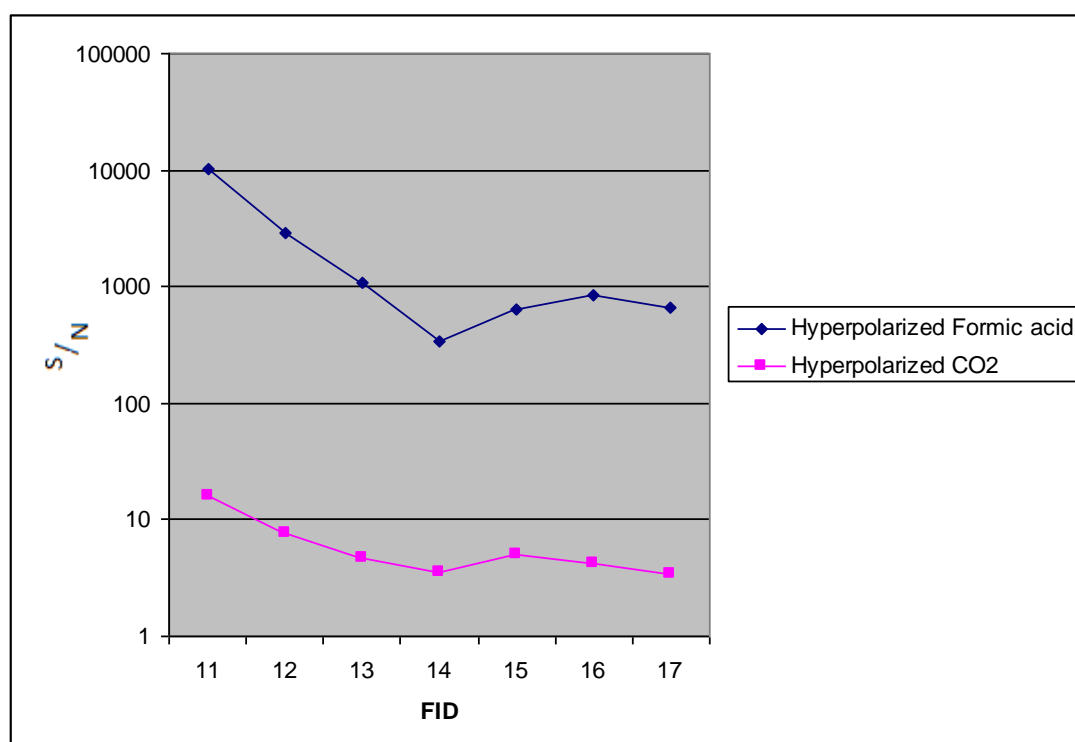


Figure 8 Plot of signal-to-noise ratio for $\text{H}^{13}\text{CO}_2\text{H}$ and $^{13}\text{CO}_2(\text{g})$

FID	S/N of $\delta 164.4$ (Hyperpolarized Formic acid)	S/N of $\delta 124.1$ (Hyperpolarized CO ₂)
11	10000	16.0
12	2900	7.5
13	1100	4.7
14	340	3.5
15	640	5.0
16	830	4.2
17	650	3.4

Table 1 Signal-to-noise calculation for the ^{13}C resonance of formic acid at $\delta 164.4$ and carbon dioxide at $\delta 124.2$.ⁱ

5.3 Summary

The results in Figure 8 and Table 1 indicate that the resonance signal strength associated with ^{13}C -labelled formic acid and the carbon dioxide decay at a similar rate. Indeed the formation of two decay curves that mirror each other leads us to consider that the resonance associated with carbon dioxide at 124.2 is hyperpolarized in nature. If carbon dioxide gas was coming from a non-hyperpolarized source then you would expect there to be no decay within the signal associated with carbon dioxide. We see a variation in signal which suggests that it is indeed highly polarised gas that is being formed not just the thermal signal. If this was not the case then this resonance would reach the maximum and remain with very little variation. The reason for this is a kinetic one; a significant concentration difference between the catalyst (3 mM) and the substrate (84 mM) produces zero order kinetics. The decay of the signal at $\delta 124.2$ cannot be due to signal saturation as the carbon dioxide within the sample is being removed from the system (it is a gas and the system is not sealed from the atmosphere), so the signal we observe comes solely from the formic acid.

ⁱ The author would like to thank Jonathon Holmes (The Duckett Group, University of York) for his contribution in calculating the signal-to-noise ratios of hyperpolarised formic acid and carbon dioxide.

5.4 References

- 1.) (a) T. Koike and T. Ikariya, *Adv. Synth. Catal.*, 2004, **346**, 37; (b) A. J. Blacker, E. Clot, S. B. Duckett, O. Eisenstein, J. Grace, A. Nova, R. N. Perutz, D. J. Taylor and A. C. Whitwood, *Chem. Commun.*, 2009, 6801.
- 2.) P. C. Lauterbur, *Nature*, 1973, **242**, 190.
- 3.) J. H. Ardenkjær-Larsen, B. Fridlund, A. Gram, G. Hansson, L. Hansson, M. H. Lerche, R. Servin, M. Thaning and K. Golman, *Proc. Nat. Acad. Sci. USA*, 2003, **100**, 10158.
- 4.) J. Wolber, F. Ellner, B. Fridlund, A. Gram, H. Jóhannesson, G. Hansson, L. H. Hansson, M. H. Lerche, S. Månsson, R. Servin, M. Thaning, K. Golman and J. H. Ardenkjær-Larsen, *Nucl. Instr. Methods A*, 2004, **526**, 173.
- 5.) Sven Månsson, Hyperpolarized Nuclei for NMR Imaging and Spectroscopy – Methodology and model studies of lung and vascular function. PhD Thesis, Lund University, Sweden, 2002.
- 6.) K. Golman, L. E. Olsson, O. Axelsson, S. Månsson, M. Karlsson and J. S. Petersson, *Br. J. Radiol.*, 2003, **76**, 118.
- 7.) W. A. Edelstein, G. H. Glover, C. J. Hardy and R. W. Redington, *Magn. Reson. Med.*, 1986, **3**, 604.
- 8.) N. G. Campeau, J. Huston, M. A. Bernstein, C. Lin and G. F. Gibbs, *Top. Magn. Reson. Imaging*, 2001, **12**, 183.
- 9.) A. Abragam and M. Goldman, *Rep. Prog. Phys.*, 1978, **41**, 395.
- 10.) R. A. Wind, M. J. Duijvestigijn, C. Van der Lugt, A. Manenschijn and J. Vriend, *Prog. Nucl. Mag. Res. Sp.*, 1985, **17**, 33.
- 11.) D. A. Hall, D. C. Maus, G. J. Gerfen, S. J. Inati, L. R. Becerra, F. W. Dahlquist and R. G. Griffin, *Science* 1997, **276**, 930.
- 12.) K. Golman, J. H. Ardenkjær-Larsen, J. Svensson, O. Axelsson, G. Hansson, L. Hansson, H. Jóhannesson, I. Leunbach, S. Månsson, J. S. Petersson, G. Pettersson, R. Servin and L. G. Wistrand, *Acad. Radio.*, 2002, **9**, S507.

CONCLUSIONS AND FUTURE WORK

In this chapter I conclude the dissertation by summarising the contributions I have made towards the understanding of transfer hydrogenation, dehydrogenation and amine racemisation. I will also suggest some future research directions.

6.1 Conclusions

In Chapter 2 we prepared a series of rhodium and iridium monotosylated and bis-tosylated complexes ($\eta^5\text{-C}_5\text{Me}_5$)M(XNC₆H₄NX') (M = Rh, Ir; X, X' = H or Ts) with formal “16-electron” configurations and demonstrated that the change in bond distances $r(\text{N1-C11})$, $r(\text{N2-C16})$ and $r(\text{C11-C16})$ with respect to the free ligand were insignificant leading us to conclude that these complexes are in the +3 oxidation state, much like the catecholate complexes characterised by Maitlis *et al.* in 1979. The complexes displayed strong colours arising from ($\pi \rightarrow d$) ligand-to-metal charge transfer bands in the visible part of the spectrum. Indeed the complexes are postulated intermediates in the catalytic cycle for transfer hydrogenation and we observed in Chapter 3 that since the colour of the 16-electron complexes was lost during catalysis and reappears after, we infer that the 16-electron intermediate is not the resting state. In Chapter 2 we have observed a remarkable trend in the M-N (where M = Rh, Ir) bond lengths through characterisation by X-ray crystallography. Owing to the electron withdrawing effect of the tosyl group, the M-NH bond length is much shorter than the M-NTs bond length for Cp*Rh(TsNC₆H₄NH) (**1a**) and Cp*Ir(TsNC₆H₄NH) (**1d**). The M-N bond lengths for Cp*Rh(TsNC₆H₄NTs) (**1b**), Cp*Rh(HNC₆H₄NH) (**1c**) and Cp*Ir(TsNC₆H₄NTs) (**1e**) were demonstrated to be symmetric with long distances for the bistosylated complexes (**1b** and **1e**) and short ones for **1c**. By analysing the angles θ_{oop} and θ_{tilt} we were able to reveal further evidence of π -bonding. Cp*M(TsNC₆H₄NH) and Cp*M(HNC₆H₄NH) were found to be almost planar ($\theta_{\text{oop}} < 4^\circ$) and Cp*M(TsNC₆H₄NTs) had lost the planar conformation. The tilt angles for the rhodium complexes followed the order **1b** (20.98°) > **1c** (2.19°) > **1a** (0.82°); the iridium complexes followed the order **1e** (20.86°) > **1d** (5.06°) > **1f** (1.39°). The marked differences on $\Delta r(\text{M-N})$, θ_{oop} and θ_{tilt} were consistent with MO arguments suggested by Morris (for related Ru amido

complexes) that these bonds have partial double bond character due to π -donation from N to Ru. The work in this chapter also demonstrates the delocalisation in the bis(amido) complexes; the ability for the metal to adapt to the requirements of the amido or tosylated amido ligands; and the enormous electron withdrawing effect of the tosyl group on the M-N interaction in **1a**(Rh-NTs), **1b** and **1c**(Ir-NTs). Eisenstein *et al.* give optimised structures for the rhodium series of complexes close to the X-ray structural parameters and support our experimental observations. Furthermore, they have shown, using NBO analysis, that 2p lone pairs on each nitrogen mix with Rh(d_{xy}) and the C₆H₄ carbon to different extents for NH and NTs. Strikingly, the contributions of the Rh orbital to the composition of the nitrogen natural localised molecular orbital (NLMO) follow the pattern expected from the observed bond lengths **1a**(NH) > **1c** > **1b** > **1a**(NTs).

In order to obtain the ¹⁰³Rh chemical shifts for the 16-electron rhodium complexes in Chapter 2 we observed a coupling between the Cp* methyl protons and rhodium using ¹H/¹⁰³Rh HSQC NMR. We exploited this method to collect the ¹⁰³Rh chemical shifts of Cp*Rh(TsNC₆H₄NH) and Cp*Rh(TsNC₆H₄NTs) and various other related 18-electron chiral asymmetric transfer hydrogenation catalysts such as Cp*Rh(Cl)(TsNCHPhCHPhNH₂). We concluded that the rhodium chemical shifts of the 16-electron complexes are more deshielded than the 18-electron chloride complexes. This could prove useful for studying similar Cp*Rh complexes.

In Chapter 3, we examined the use of the 16-electron complexes developed in Chapter 2 for the catalytic transfer hydrogenation of a cyclic imine, 6-7-dimethoxy-1-methyl-3,4-dihydroisoquinoline using NEt₃/HCO₂H (2:5) as the hydrogen donor. We found that the most active catalyst was the unsymmetrical Cp*Rh(TsNC₆H₄NH). DFT calculations for the hydrogenation of the 16-electron rhodium complexes by formic acid support this conclusion as the lowest energy barrier was obtained with Cp*Rh(TsNC₆H₄NH) and the product is the most thermodynamically stable. We did not observe any evidence for hydrogenation of imine by methanol in the presence of catalyst alone. This is supported by DFT calculations that show the hydrogenation of the 16-electron rhodium complexes by methanol to form 18-electron hydride and formaldehyde is thermodynamically unstable for Cp*Rh(TsNC₆H₄NH).

In Chapter 3, we found that adding substituent groups on the *o*-phenylenediamine ligand affected the catalytic activity of the 16-electron rhodium complexes. The catalytic activity of the 4,5-dimethyl complex, $\text{Cp}^*\text{Rh}(\text{TsNC}_6\text{H}_2(\text{Me})_2\text{NH})$ was found to be greater than the non-substituted 16-electron complex, $\text{Cp}^*\text{Rh}(\text{TsNC}_6\text{H}_4\text{NH})$ for transfer hydrogenation of the cyclic imine. By adding $-I$ groups such as chlorine, the catalytic activity was found to be slower than the $\text{Cp}^*\text{Rh}(\text{TsNC}_6\text{H}_4\text{NH})$ complex. Our results suggest that the increased electron density in the delocalised ring can increase the nucleophilicity of the lone pair of electrons in the nitrogen and therefore lead to an increase in catalytic activity for transfer hydrogenation. In conclusion, the most active 16-electron complex was the 4,5-dimethyl rhodium complex: $\text{Cp}^*\text{Rh}(\text{TsNC}_6\text{H}_2(\text{Me})_2\text{NH}) > \text{Cp}^*\text{Rh}(\text{TsNC}_6\text{H}_4\text{NH}) > \text{Cp}^*\text{Ir}(\text{TsNC}_6\text{H}_4\text{NTs}) > \text{Cp}^*\text{Rh}(\text{TsNC}_6\text{H}_4\text{NTs})$, with $\text{Cp}^*\text{Ir}(\text{TsNC}_6\text{H}_4\text{NH})$ being the least active for transfer hydrogenation of the cyclic imine. The results for the Ir series of complexes do not fit with the theoretical results by Eisenstein *et al.*, which show that $\text{Cp}^*\text{Ir}(\text{TsNC}_6\text{H}_4\text{NH})$ should lead to the faster hydrogenation reaction. This could be due to air-sensitivity of the Ir complex or anomalous experimental results.

An important finding from Chapter 3 was that these complexes allowed catalytic studies without the need for 18-electron precursors, as is the case for $\text{Cp}^*\text{M}(\text{Cl})(\text{TsNCHPhCHPhNH}_2)$ (where $\text{M} = \text{Rh}, \text{Ir}$). In fact, the direct synthesis of the 16-electron complex, $\text{Cp}^*\text{Rh}(\text{TsNC}_6\text{H}_4\text{NH})$ and its slower activity in transfer hydrogenation enabled us to investigate key specific steps relevant to catalysis. The analogous 18-electron precursor complex, $\text{Cp}^*\text{Rh}(\text{Cl})(\text{TsNC}_6\text{H}_4\text{NH}_2)$ was obtained by reaction of the 16-electron complex with HCl in ether and fully characterised by X-ray crystallography. However, the 18-electron chloride complex was found to be unstable with respect to the 16-electron complex in contrast with the stabilities of their analogues with CHPhCHPh in place of the C_6H_4 ring. We then examined the reaction of the 16-electron complex with formic acid and TEAF solution; formation of a formate complex, $\text{Cp}^*\text{Rh}(\text{OCHO})(\text{TsNC}_6\text{H}_4\text{NH}_2)$ was observed and we conclude that this has a “catalytic role”. Indeed, formation of the 18-electron hydride complex, $\text{Cp}^*\text{Rh}(\text{H})(\text{TsNC}_6\text{H}_4\text{NH}_2)$, via the 18-electron formate complex was observed *via* NMR spectroscopy and this step may be rate-determining. DFT calculations provided by Eisenstein *et al.*, could not find any direct pathway from the formate complex to the hydride: the formic acid must first dissociate. The

dissociation was calculated to proceed with a low energy barrier to the 16-electron complex, then rearrangement via an “outer-sphere” mechanism leading to the hydride complex and carbon dioxide was proposed.

In Chapter 4, we explored the mechanism of an amine dehydrogenation and racemisation system using the pentamethylcyclopentadienyliridium(III) diiodide dimer, $[\text{Cp}^*\text{IrI}_2]_2$. Initially we structurally characterised an ammine-bound iridium complex that could be recovered after the catalytic reaction by purging ammonia gas through the reaction mixture. The $[\text{Cp}^*\text{Ir}(\text{NH}_3)(\text{I})_2]$ complex was fully characterised and found to be stable in air for months without decomposition. We then examined the complex for the racemisation of sertraline, an antidepressant drug, under the same experimental conditions as would be used with the $[\text{Cp}^*\text{IrI}_2]_2$ complex at Piramal Healthcare in Huddersfield. Our results showed that the racemisation of sertraline with the recycled ammonia catalyst was of comparable activity to the original $[\text{Cp}^*\text{IrI}_2]_2$ catalyst. We suggest that the slightly lower activity of the recycled catalyst is possibly due to not purging the reaction mixture to remove the ammonia gas that was evolved or the decreased solubility of the ammonia complex in toluene. Interestingly, an experiment to determine the activity of the recovered complex on the second addition of fresh substrate fits a profile consistently with the $[\text{Cp}^*\text{IrI}_2]_2$ catalyst. We then explored the mechanism of the amine racemisation system using $[\text{Cp}^*\text{IrI}_2]_2$ and characterised monomeric 18-electron amine-bound key intermediates including $[\text{Cp}^*\text{Ir}(\text{I})_2(\text{PhCH}_2\text{NHMe})]$, $[\text{Cp}^*\text{Ir}(\text{Cl})_2(\text{PhCH}_2\text{NHMe})]$ and $[\text{Cp}^*\text{Rh}(\text{Cl})_2(\text{PhCH}_2\text{NHMe})]$. In conclusion, the X-ray crystal structures, NMR data and other spectroscopic techniques, reveal that the first step in the mechanism is the coordination of one secondary amine to the iridium centre of $\text{Cp}^*\text{Ir}(\text{I})_2$, in which the dimer has been cleaved by the secondary amine. The interesting aspect of this result is that new structural X-ray information has been provided for the first time and may facilitate further studies into how this amine-bound complex undergoes transformation to other possible complexes in the catalytic cycle.

As part of the study on the mechanism of this amine racemisation catalyst we demonstrated by $^1\text{H} / ^{15}\text{N}$ HSQC NMR spectroscopy that a cyclic imine can coordinate with the $[\text{Cp}^*\text{IrI}_2]_2$ complex at low temperature. In particular, we demonstrated that the reaction of this coordinated imine with hydrogen shows that

the reverse reaction, hydrogenation of the imine by $[\text{Cp}^*\text{IrI}_2]_2$ and hydrogen, was possible. We identified a hydride peak which we postulate is the $[\text{Cp}^*\text{Ir}(\text{H})(\text{I})_2]$ dihydrido-bridged complex as identified by Fujita and Yamaguchi in their dehydrogenation-hydrogenation work (See Chapter 4). Using these new results we were able to propose a mechanism for amine racemisation in which the dimer reacts with secondary amine to form a mononuclear amine-coordinated Cp^*Ir diiodide complex; upon coordination of the amine to the iridium centre it is proposed that hydrogen iodide is formed by reaction of the NH proton and iodide to form a new Cp^*Ir hydrido iodide complex (by β -elimination) which can then reprotonate the coordinated imine or lose hydrogen and form imine and $\text{Cp}^*\text{Ir}(\text{I})_2$ which can react with a second equivalent of amine.

In Chapter 5, we described the development of a novel method for producing hyperpolarised CO_2 . We identified that the complexes in Chapters 2 and 3 catalytically decompose formic acid into H_2 and CO_2 , regenerating active catalyst upon completion. We exploited this reaction and produced hyperpolarised CO_2 from a solution of hyperpolarised triethylammonium formate in methanol- d_4 using DNP.

6.2 Future Work

Possible future work may include further investigation of catalytic transfer hydrogenation with 16-electron iridium complexes such as $\text{Cp}^*\text{Ir}(\text{TsNC}_6\text{H}_4\text{NH})$. Synthesis and structural characterisation of the corresponding iridium 18-electron hydride, $\text{Cp}^*\text{Ir}(\text{H})(\text{TsNC}_6\text{H}_4\text{NH}_2)$ and formato-amino, $\text{Cp}^*\text{Ir}(\text{OCHO})(\text{TsNC}_6\text{H}_4\text{NH}_2)$ complexes should be attempted (they may be more stable, as is the case for the TsDPEN series of ATH catalysts). These complexes could be reacted with imine to investigate the mechanism of hydrogen transfer. Under high pressure, H_2 and CO_2 should be added to $\text{Cp}^*\text{Rh}(\text{TsNC}_6\text{H}_4\text{NH})$ in an attempt to obtain the corresponding formato-amino or hydride complexes identified in this study. It may be possible to use complexes of the type $\text{Cp}^*\text{M}(\text{XNC}_6\text{H}_4\text{NX}')$ (where $\text{M} = \text{Rh}$ or Ir , $\text{X}, \text{X}' = \text{H}$ or Ts) to dehydrogenate amines. More investigation into the dehydrogenation of secondary amines with $[\text{Cp}^*\text{IrI}_2]_2$ using sacrificial alkene donors should be performed. More work should be carried out on the characterisation of intermediates, especially the Cp^*Ir iminium and hydride complexes identified in this study.

EXPERIMENTAL

7.1 General

7.1.1 General experimental methods

Unless otherwise stated, synthetic work was carried out in air with untreated solvents. Commercially available reagents were obtained from the following sources: (R,R) and (S,S)-DPEN, (R,R) and (S,S)-TsDPEN, 6,7-dimethoxy-3,4-dihydroisoquinoline, sertraline, *N*-methylbenzylamine (donated by Piramal Healthcare); $\text{RhCl}_3 \cdot x\text{H}_2\text{O}$ and $\text{IrCl}_3 \cdot x\text{H}_2\text{O}$ (Precious Metals Online); *o*-phenylenediamine, 4,5-dimethyl-*o*-phenylenediamine, 4,5-dichloro-*o*-phenylenediamine, 1,1'-binaphthyl-2,2'-diamine, 9,10-diaminophenanthrene, pentamethylcyclopentadiene, triethylamine, formic acid, 5:2 formic acid / triethylamine (TEAF), anhydrous Hydrochloric acid in ether solution (1M) (Aldrich); tosyl chloride, dansyl chloride (Alfa Aesar); ^{13}C -labelled formic acid (Cambridge Isotopes Laboratory); Ar, N_2 and H_2 gases (BOC) were used as received without further purification. $[\text{Cp}^*\text{RhCl}_2]_2$, $[\text{Cp}^*\text{IrCl}_2]$, and $[\text{Cp}^*\text{IrI}_2]_2$, were also made as previously reported.^{1,2}

When necessary dry solvents (Fisher Scientific, AR or HPLC grade) were prepared by refluxing over Mg / I_2 (CH_3OH), CaH_2 (CH_3CN , CH_2Cl_2) or sodium / benzophenone (pentane, hexane, THF, toluene) were degassed and along with air- and moisture-sensitive materials, stored under a dry Ar atmosphere. Manipulations of these compounds were performed using standard Schlenk, high vacuum and glovebox techniques. Deuterated solvents (Aldrich) were dried using potassium (benzene, toluene, THF) or CaH_2 (CD_3OH , CD_3CN and CD_2Cl_2) and degassed by three freeze-pump-thaw cycles.

-78 °C refers to an acetone / dry ice slush bath, -40 °C refers to an acetonitrile / liquid nitrogen bath, -20 °C refers to an ice / salt slush bath, 0 °C refers to an ice / water bath.

7.1.2 Physical methods

NMR spectra were recorded on Bruker AMX500, DRX400 or BMX300 spectrometers and the chemical shift values are reported relative to the residual protons of the deuterated solvent, according to the standard Bruker list. The ^1H - ^{103}Rh HMQC were run on a Bruker Avance II 700 MHz spectrometer calibrated against $[\text{Cp}^*\text{RhCl}_2]_2$ at δ 2303.³ The hyperpolarisation experiments for the detection of hyperpolarised carbon dioxide were run on a Bruker 600 MHz spectrometer and Hypersense Dynamic Nuclear Polariser. ESI mass spectra were recorded on a Thermo Electron LCQ Classic and FAB mass spectra were recorded on a VG Auto-Spec. Microanalysis was carried out by Elemental Microanalysis Ltd., Okehampton, Devon. Infrared spectra were recorded on a Unicam RS 10000E FTIR instrument. UV-VIS spectra were recorded on a Perkin-Elmer Lambda 7 spectrophotometer and an Agilent 8453 spectrometer. X-ray crystallography structure determination was performed on a single-crystal Bruker Smart Apex CCD with Molybdenum source. GC-MS measurements were made on a Varian Saturn 2000 with a Varian FactorFour VF-5ms (CP8944) fused silica column (30 m \times 0.25 mm \times 0.25 μm). A Hewlett-Packard HP6890 gas chromatograph was used to analyse the ratio of sertraline isomers and these were assigned using known standards. For the enantiomers a Chiralsil-DEX CB chiral column was used. Microwave reactions were performed in a CEM Discover.

7.1.3 Computational Details

All calculations on the Cp^*Rh and Cp^*Ir 16-electron complexes were performed by Eisenstein *et al.*, with the Gaussian03 package⁴ of programs with the hybrid B3PW91 functional.^{5,6} The Rh atom was represented by the relativistic effective core potential (RECP) from the Stuttgart group and the associate basis set,⁷ augmented by an *f* polarization function.⁸ The remaining atoms (C, H, N, O) were represented by a 6-31G(*d,p*) basis set.⁹ The sulphur atom was represented by RECP from the Stuttgart group and the associated basis set,¹⁰ augmented by a *d* polarization function.¹¹ Full optimization of geometry was performed without any constraint, followed by analytical computation of the Hessian matrix to identify the nature of the located

the crude product was purified by crystallization (ethanol/water). The colourless crystals were washed with *n*-hexanes (Yield 1.01 g, 76% of theoretical).

NMR Spectroscopy Table 2.4.6

Mass Spectrometry 291.1165 [MH⁺]

IR Spectroscopy 3447 (m), 3421 (m), 3372 (m), 3248 (m), 3051 (m), 2921 (m), 1626 (s), 1598 (s), 1511 (s), 1493 (m), 1456 (m), 1370 (s), 1319 (s), 1184 (m), 1150 (s), 1090 (s), 1019 (m), 1001 (m), 908 (s)

7.2.3 *N*-tosyl-4,5-dichloro-1,2-diaminobenzene

p-Toluenesulfonyl chloride (0.95 g, 4.98 mmol) in THF (5 mL) was added dropwise over a period of 12 hours to a solution of 4,5-dichloro-1,2-diaminobenzene (2.64 g, 1.49 mmol) and pyridine in THF (10 mL) at room temperature. When the reaction was complete (NMR), the solvent was evaporated *in-vacuo*. Water (5 mL) was added to the dark oily residue, it was extracted with CH₂Cl₂. The organic phase was washed with brine, and dried over MgSO₄. The solvent was removed *in-vacuo*, and the crude product was purified by crystallization (ethanol/water). The colourless crystals were washed with *n*-hexanes (Yield 1.13 g, 69% of theoretical).

NMR Spectroscopy Table 2.4.7

Mass Spectrometry 331.0068 [MH⁺]

7.2.4 *N*-tosyl-9,10-diaminophenanthrene

9,10-diaminophenanthrene (250 mg, 1.20 mmol), pyridine (0.97 mL, 12 mmol), 10 mL of dichloromethane and a magnetic stirrer bar were added to a 50 mL round bottom flask. A dropping vessel was attached to the top of the flask and was charged with a solution of tosyl chloride (229 mg, 1.20 mmol) in 10 mL of dichloromethane. The reaction vessel was stirred magnetically and the tosyl chloride solution was added drop wise to the round bottom flask, that was placed in an ice-bath, over 10

minutes. After addition of the tosyl chloride solution the reaction mixture was allowed to warm to room temperature and stirred overnight. The reaction mixture was washed with 5% HCl and the organic layer was dried using magnesium sulphate. The solvent was removed under reduced pressure to afford a yellow oil. The crude oil was worked up by column chromatography using EtOAc / Pet Ether 40°C-60°C 1:3 to give the desired product. The product was recrystallized by treating with hot toluene and allowing the solution to slowly cool at room temperature. Recrystallisation from toluene gave yellow crystals (352 mg, 81% yield).

^1H NMR Spectroscopy (500 MHz, CD_2Cl_2 , 300 K): δ 2.35 (3H, s) CH_3 , δ 4.90 (2H, br. s) NH_2 , δ 6.34 (1H, s) NH , δ 7.15 (2H, d) Tosyl ArH, δ 7.19 (1H, t) ArH, δ 7.23 (1H, t) ArH, δ 7.30 (1H, t) ArH, δ 7.61 (2H, d) Tosyl ArH, δ 7.65 (1H, t) ArH, δ 7.72 (1H, t) ArH, δ 7.95 (1H, d) ArH, δ 8.50 (1H, d) ArH, δ 8.66 (1H, d) ArH. ^{13}C NMR Spectroscopy (125 MHz, CD_2Cl_2 , 300 K): δ 46.1, 21.8, 109.5, 121.5, 122.8, 123.1, 123.7, 123.8, 125.4, 126.1, 127.3, 127.4, 127.8, 128.2, 130.2, 131.2, 131.5, 137.6, 141.3, 144.7.

IR Spectroscopy 3414 (m, NH_2), 3341 (m, NH_2), 3259 (s, NH), 1636 (m), 1596 (m), 1499 (m), 1367 (m), 1312 (s), 1152 (s), 1087 (s), 1020 (m), 887 (m), 810 (s), 745 (s), 717 (s), 673 (s)

CHN analysis calculated for $\text{C}_{26}\text{H}_{27}\text{N}_3\text{O}_2\text{S}$:

Calculated	%C 70.08, %H 6.11, %N 9.43
Found	%C 70.09, %H 6.12, %N 9.44

7.2.5 Synthesis of *N*-(2'-amino-1,1'-binaphthyl-2-yl)-4-methylbenzenesulfonamide

p-toluenesulfonyl chloride solution (420 mg, 2.2 mmol) in 5.0 mL of DCM was added dropwise to a mixture of 2,2'-amino-1,1'-binaphthylene (a racemic compound, 569 mg, 2.0 mmol) and pyridine (2.0 mL, 24 mmol) in DCM (15 mL) in an ice-bath, under argon. The mixture was stirred at room temperature for 5 h. The reaction mixture was washed with 5% HCl and dried over anhydrous MgSO_4 . The

solvent was removed under reduced pressure and the residue was purified by a silica gel flash column chromatography (eluent: PE (40-60°C) / EtOAc = 6/1) to give *N*-(2'-amino-1,1'-binaphthyl-2-yl)-4-methylbenzenesulfonamide as a white crystalline solid (700 mg, 80% yield).

¹H NMR Spectroscopy (500 MHz, CD₃CN, 300 K): δ 2.27 (3H, s) CH₃, 3.98 (2H, br s) NH₂, 6.21 (1H, d, *J*_{HH} = 8.5 Hz) ArH, 6.86 (1H, br s), NH, 6.92 (1H, t, *J*_{HH} = 7.5 Hz), ArH, 6.95 (1H, d, *J*_{HH} = 8.5 Hz) ArH, 7.01 (2H, d, *J*_{HH} = 8.3 Hz) ArH, 7.16 (1H, t, *J*_{HH} = 7.5 Hz), 7.18 (1H, d, *J*_{HH} = 8.7 Hz) ArH, 7.23 (1H, t, *J*_{HH} = 7.5 Hz) ArH, 7.33 (2H, d, *J*_{HH} = 8.3 Hz) ArH, 7.40 (1H, t, *J*_{HH} = 7.5 Hz) ArH, 7.77 (1H, d, *J*_{HH} = 8.1 Hz) ArH, 7.85 (1H, d, *J*_{HH} = 8.7 Hz) ArH, 7.93 (1H, d, *J*_{HH} = 8.1 Hz) ArH, 8.00 (1H, d, *J*_{HH} = 8.5 Hz) ArH, 8.03 (1H, d, *J*_{HH} = 8.5 Hz) ArH; ¹³C NMR Spectroscopy (125 MHz, CD₃CN, 300 K): δ 21.6, 109.9, 119.4, 121.1, 124.0, 123.8, 123.9, 126.4, 126.6, 127.8, 127.9, 128.0, 128.9, 129.1, 129.3, 130.4, 130.7, 131.4, 132.6, 134.0, 134.8, 134.9, 137.4, 145.0, 145.2.

ESI Mass Spectrometry 439.15 [M+H]⁺
 284.13 (TsNHC₂₀H₁₂NHTs)

Melting Point Determination 167-170°C

7.2.6 *N*-Dansyl-1,2-diphenylethylenediamine

(1*R*, 2*R*)-*N*-dansyl-1,2-diphenylethylenediamine was prepared by the dropwise addition of a dry methylene chloride solution (20 mL) of dansyl chloride (1.16 g, 4.30 mmol) to a mixture of (R, R)-DPEN (0.91g, 4.30 mmol) and triethylamine (0.6 mL) in dry dichloromethane (30 mL) at 273 K (syringe pump addition). After the reaction mixture was stirred for 18 hours at room temperature, the solution was washed with water (2 × 20 mL) and brine (20 mL) and then dried with Na₂SO₄. The solvent was removed under reduced pressure to give 2.1g of crude yellow solid product. Recrystallisation from ethyl acetate and hexane gave 1.58 g of the desired product as yellow/white crystals. (Yield 1.58 g, 82%).

^1H NMR Spectroscopy (500 MHz, CD_3CN , 300 K): δ 2.82 (6H, s) $\text{N}(\text{CH}_3)_2$, 3.95 (1H, d) CHPhCHPh , 4.27 (1H, d) CHPhCHPh , 4.27 (1H, d) CHPhCHPh , 2.40 (3H, s) CH_3 , 6.73-6.85 (5H, m) DPEN-ArH, 6.97-7.01 (5H, m) DPEN-ArH, 7.19 (1H, d) Dansyl-ArH, 7.29 (1H, t) Dansyl-ArH, 7.54 (1H, t) Dansyl-ArH, 7.86 (1H, d) Dansyl-ArH, 8.22 (1H, d) Dansyl-ArH, 8.30 (1H, d) Dansyl-ArH. ^{13}C NMR Spectroscopy (125 MHz, CD_3CN , 300 K): δ 46.1, 61.9, 66.0, 116.3, 120.5, 124.3, 128.1, 128.3, 128.4, 128.5, 128.6, 129.2, 130.5, 130.7, 130.9, 131.1, 136.9, 140.4, 143.7, 153.2.

Mass Spectrometry (ESI) 446.1895 [MH^+]

IR Spectroscopy 3354 (m, br), 3295 (m, br), 3061 (m, br), 3001 (m), 2943 (m), 2861 (m), 2861 (m), 2826 (m), 2785 (m), 1613 (m), 1588 (m), 1570 (m), 1499 (m), 1478 (m), 1451 (s), 1405 (m), 1395 (m), 1357 (m), 1324 (s), 1310 (s), 1233 (m), 1202 (m), 1162 (s), 1145 (s), 1091 (m), 1073 (m), 1061 (m), 1029 (m), 963 (s), 896 (m), 789 (s), 766 (s), 700 (s), 623 (s), 568 (s)

CHN analysis calculated for $\text{C}_{26}\text{H}_{27}\text{N}_3\text{O}_2\text{S}$:

Calculated	%C 70.08, %H 6.11, %N 9.43
Found	%C 70.09, %H 6.12, %N 9.44

7.2.7 Bistosylated 1,2-diaminobenzene ligand - $\text{TsNHC}_6\text{H}_4\text{NHTs}$

The method for the preparation of this ligand was the same for the monotosylated ligand, however, 2 molar equivalents of tosyl chloride were used and no ice-bath was used. The tosyl chloride solution was added quickly into the diamine solution without stirring which resulted in a moderate to high exothermic reaction – the reaction mixture got very hot. Crystals were obtained by dissolving the white solid in the minimum amount of ethyl acetate and layering with twice the volume of *n*-hexanes. The crystals were filtered and washed with *n*-hexane and dried *in-vacuo* for 5 hours.

^1H NMR Spectroscopy (500 MHz, CD_3CN , 300 K): δ 2.38 (6H, s) CH_3 , δ 6.95 (2H, AA'XX', $J_{\text{HH}} = 3.5, 2.4$ Hz) ArH, δ 7.03 (2H, AA'XX', $J_{\text{HH}} = 3.5, 2.4$ Hz) ArH, δ

7.29 (4H, d, $J_{\text{HH}} = 8.1$ Hz) ArH, 7.55 (4H, d, $J_{\text{HH}} = 8.1$ Hz) ArH, 7.66 (1H, br. s) NH; ^{13}C NMR Spectroscopy (125 MHz, CD_3CN , 300 K): δ 21.7, 126.5, 128.1, 128.4, 130.7, 132.0, 136.5, 145.7.

7.2.8 $\text{Cp}^*\text{Rh}(\text{TsNC}_6\text{H}_4\text{NH})$ (**1a**)

$[\text{Cp}^*\text{RhCl}_2]_2$ (250 mg, 0.40 mmol) and *N*-tosyl-1,2-diaminobenzene (212 mg, 0.81 mmol) were added to a 250 mL round bottom flask and dissolved in 100 mL of dichloromethane at 0°C, using an ice-bath. The reaction mixture was stirred using a magnetic stirrer bar and triethylamine (225 μL , 1.62 mmol) was added dropwise. The solution turned from orange to dark purple on addition of base. The reaction mixture was stirred for a further 5 hours at room temperature before being washed with water three times and was then dried over magnesium sulfate. The solvent was removed under vacuum and the crude solid was crystallised from chloroform and hexane (or THF/hexane) to give dark purple ‘needle-like’ crystals (332 mg, 82%).

NMR data Table 2.4.1

Mass Spectrometry (FAB, m/z) 499 $[\text{MH}^+]$

Infra-red analysis (KBr / cm^{-1}) 3316 (s, NH)

CHN analysis calculated for $\text{C}_{25}\text{H}_{31}\text{N}_2\text{O}_{2.5}\text{RhS}$ (**1a**.0.5THF):

Calculated %C 56.18, %H 5.85, %N 5.24

Found %C 56.47, %H 5.99, %N 5.20

7.2.9 $\text{Cp}^*\text{Rh}(\text{TsNC}_6\text{H}_4\text{NTs})$ (**1b**)

$[\text{Cp}^*\text{RhCl}_2]_2$ (250 mg, 0.40 mmol) and ditosyl-1,2-diaminobenzene (337 mg, 0.81 mmol) were added to a 250 mL round bottom flask and dissolved in 100 mL of dichloromethane at 0°C using an ice-bath. The reaction mixture was stirred using a magnetic stirrer bar and triethylamine (225 μL , 1.62 mmol) was added dropwise. The solution turned from orange to dark purple on addition of base. The reaction mixture was stirred for a further 5 hours at room temperature before being washed

three times with water and then dried over magnesium sulfate. The solvent was removed under vacuum and the crude solid was crystallised from dichloromethane and methanol to give dark purple crystals of $\text{Cp}^*\text{Rh}(\text{TsNC}_6\text{H}_4\text{NTs})$, which were suitable for X-ray diffraction (353 mg, 67%).

NMR Spectroscopy Table 2.4.2

Mass Spectrometry (FD, m/z) 652 [M^+]

Infra-red analysis ($\text{KBr} / \text{cm}^{-1}$) 1480 (m), 1450 (m), 1314 (m), 1297 (s), 1250 (m), 1204 (w), 1152 (s), 1126 (m), 1089 (s), 1017 (m), 943 (s), 915 (m), 833 (s), 822 (m), 810 (m), 754 (m), 742 (m), 708 (w), 671 (s), 661 (s), 569 (s), 562 (s), 551 (s)

CHN analysis calculated for $\text{C}_{30}\text{H}_{33}\text{N}_2\text{O}_4\text{RhS}_2$:

Calculated %C 55.21, %H 5.10, %N 4.29

Found %C 55.02, %H 4.96, %N 4.24

X-ray crystallographic data Appendix 8.2

7.2.10 $\text{Cp}^*\text{Rh}(\text{HNC}_6\text{H}_4\text{NH})$ (**1c**)

Complex $[\text{Cp}^*\text{Rh}(\text{HNC}_6\text{H}_4\text{NH})]$, (**1c**) was prepared using the procedure outlined by Maitlis.¹³ Under argon, in a Schlenk tube, 1,2-diaminobenzene (87 mg, 0.8 mmol) was added slowly to a solution of $[\text{Cp}^*\text{RhCl}_2]_2$ (250 mg, 0.40 mmol) in deoxygenated water (30 cm^3) with stirring. The solution changed colour rapidly from yellow to dark red and a very dark red solid precipitated. The reaction mixture was stirred for a further 5 hours and the precipitate was filtered off, washed with water ($2 \times 10 \text{ cm}^3$) and dried *in vacuo*. Crystals suitable for X-ray diffraction analysis were grown by layering a saturated solution of $\text{Cp}^*\text{Rh}(\text{HNC}_6\text{H}_4\text{NH})$ in toluene with *n*-pentane.

NMR data Table 2.4.3

Infra-red analysis (KBr / cm^{-1}) 3346 (m, NH stretches), 3322 (m, NH stretches), 2904 (w), 1463 (m), 1370 (s), 1354 (s), 1209 (w), 1158 (m), 1140 (m), 1025 (m), 727 (s), 566 (m)

X-ray crystallographic data Appendix 8.3

7.2.11 $\text{Cp}^*\text{Rh}(\text{TsNC}_6\text{H}_2(\text{CH}_3)_2\text{NH})$

N-tosyl-4,5-dimethyl-1,2-diaminobenzene (47 mg) and $[\text{Cp}^*\text{RhCl}_2]_2$ (50 mg) together in a 10 mL in round bottom flask and add magnetic stirrer bar. At 273 K (in ice-bath) add 22.5 μL of triethylamine and leave to stir for 5 hours. On addition of triethylamine the solution turned green. Added a second equivalent of triethylamine 1 hour later (22.5 μL) and the solution turned blue. Wash with water 1 time, dry organic layer over magnesium sulphate for 15 minutes. Filter. Remove organic layer rotovap 20 minutes – recrystallisation of complex from chloroform and cyclohexanes.

NMR Spectroscopy Table 2.4.8

Mass Spectrometry (ESI, m/z) 527.1238 $[\text{MH}^+]$

Infra-red analysis (KBr / cm^{-1}) 3320 (m, NH stretch)

7.2.12 $\text{Cp}^*\text{Ir}(\text{TsNC}_6\text{H}_4\text{NH})$ (1d)

$[\text{Cp}^*\text{IrCl}_2]_2$ (250 mg, 0.20 mmol) and N-tosyl-1,2-diaminobenzene (212 mg, 0.81 mmol) were added to a 250 mL round bottom flask and dissolved in 100 mL of dichloromethane. The reaction mixture was stirred using a magnetic stirrer bar and 150 μL of triethylamine was added drop wise. The reaction gave a dark orange solution upon addition of the NEt_3 . Work up of the orange solution by removing CH_2Cl_2 under reduced pressure, and recrystallising from THF / Hexane gave orange crystals (202 mg, 70%).

NMR Spectroscopy	Table 2.4.4
Mass Spectrometry (ESI, m/z)	588 (57%, M+, Ir ¹⁹³), 586 (30%, M+, Ir ¹⁹¹)
Infra-red analysis (KBr / cm ⁻¹)	3332 (m, NH), 2962 (m), 2914 (m), 1459 (s), 1310.95 (s), 1155 (s), 1119 (m), 1088 (s), 1036 (s), 928 (s), 851 (s), 840 (s), 807 (m), 735 (s), 665 (s)
CHN analysis calculated for Cp*Ir(TsNC ₆ H ₄ NH).0.5Tol:	
	Calculated %C 53.00, %H 5.19, %N 4.12
	Found %C 54.25, %H 5.00, %N 4.07
X-ray crystallographic data	Appendix 8.4

7.2.13 Cp*Ir(TsNC₆H₄NTs) (1e)

[Cp*IrCl₂]₂ (500 mg, 0.63 mmol) and bistosyl-1,2-diaminobenzene (525 mg, 1.26 mmol) were added to a 250 mL round bottom flask and dissolved in 100 mL of dichloromethane. The reaction mixture was stirred using a magnetic stirrer bar and 350 μL of triethylamine was added drop wise. The reaction remained an orange solution upon addition of the NEt₃. Work up of the orange solution by removing CH₂Cl₂ under reduced pressure and recrystallising from chloroform / methanol gave orange crystals (628 mg, 67%).

NMR Spectroscopy	Table 2.4.5
Mass Spectrometry (ESI, m/z)	742, 587, 523, 432, 368, 322
Infra-red analysis (KBr / cm ⁻¹)	1598 (m), 1581 (m), 1495 (m), 1484 (m), 1451 (m), 1324 (s), 1310 (s), 1250 (m) 1157 (s), 1127 (m), 1089 (s), 1026 (m), 935 (s), 911 (m), 865 (m), 845 (s), 821 (m), 811 (m), 753 (m) 740 (m), 673 (s), 662 (s), 571 (s), 551 (s)

CHN analysis calculated for $C_{30}H_{33}N_2O_4IrS_2$:

Calculated	%C 48.56, %H 4.48, %N 3.78
Found	%C 48.32, %H 4.48, %N 3.72

X-ray crystallographic data Appendix 8.5

7.3 Experimental procedures for Chapter 3

7.3.1 Catalytic hydrogenation of a secondary imine with 16-electron rhodium and iridium catalysts and TEAF solution in methanol- d_4 and dichloromethane- d_2

Stock solutions of the imine (3,4-dihydro-6,7-dimethoxy-1-methylisoquinoline), Cp^*Rh and Cp^*Ir 16-electron complexes: $[Cp^*Rh(TsNC_6H_4NH)]$, $[Cp^*Rh(TsNC_6H_4NTs)]$, $[Cp^*Rh(HNC_6H_4NH)]$, $[Cp^*Ir(TsNC_6H_4NH)]$, $[Cp^*Ir(TsNC_6H_4NTs)]$ were prepared as described below in methanol- d_4 , methylene chloride- d_2 and acetonitrile- d_3 .

7.3.1.1 Imine

Three different stock solutions of 3,4-dihydro-6,7-dimethoxy-1-methylisoquinoline (121.0 mg, 0.5 mmol) were prepared in methanol- d_4 , methylene chloride- d_2 and acetonitrile- d_3 deuterated solvents and made up to 5 mL in a volumetric flask.

7.3.1.2 $[Cp^*Rh(TsNC_6H_4NH)]$ (1a)

Three different stock solutions of $Cp^*Rh(TsNC_6H_4NH)$ (10.0 mg, 0.02 mmol) were prepared in methanol- d_4 , methylene chloride- d_2 and acetonitrile- d_3 deuterated solvents and made up to 2 mL in a volumetric flask.

7.3.1.3 [Cp*Rh(TsNC₆H₄NTs)] (1b)

Two different stock solutions of Cp*Rh(TsNC₆H₄NTs) (13.1 mg, 0.02 mmol) were prepared in methylene chloride-d₂ and acetonitrile-d₃ deuterated solvents (as this complex was not soluble in methanol-d₄ and made up to 2 mL in a volumetric flask.

7.3.1.4 [Cp*Rh(HNC₆H₄NH)] (1c)

Three different stock solutions of Cp*Rh(HNC₆H₄NH) (6.9 mg, 0.02 mmol) were prepared in methylene chloride-d₂ and acetonitrile-d₃ deuterated solvents and made up to 2 mL in a volumetric flask.

7.3.1.5 [Cp*Ir(TsNC₆H₄NH)] (1d)

Three different stock solutions of Cp*Ir(TsNC₆H₄NH) (11.8 mg, 0.02 mmol) were prepared in methanol-d₄, methylene chloride-d₂ and acetonitrile-d₃ deuterated solvents and made up to 2 mL in a volumetric flask.

7.3.1.6 [Cp*Ir(TsNC₆H₄NTs)] (1e)

Two different stock solutions of Cp*Ir(TsNC₆H₄NTs) (14.8 mg, 0.02 mmol) were prepared in methylene chloride-d₂ and acetonitrile-d₃ deuterated solvents (as this complex was not soluble in methanol-d₄ and made up to 2 mL in a volumetric flask.

7.3.2 General procedure for catalytic runs

NMR samples were prepared by combining the imine stock solution (0.5 mL) and catalyst stock solution (50 μL for 1 mol %) and shaking the tube to afford complete mixing in the appropriate deuterated solvent. A single scan ¹H NMR spectrum was recorded (t = 0), the sample was removed from the magnet and TEAF (21 μL) was added to the tube (which was vigorously shaken) and it was returned to the spectrometer. Single scan spectra were recorded every 2 minutes until the reaction was complete. Results are reported as the average of 2 runs.

7.3.3 Catalytic run for 4,5-dimethyl substituted Cp*Rh complex

A stock solution of Cp*Rh(TsNC₆H₂(CH₃)₂NH) (10.53 mg, 0.02 mmol) was prepared in methanol-d₄ and made up to 2 mL in a volumetric flask.

7.3.4 Cp*Rh(Cl)(TsNC₆H₄NH₂) (2a)

Cp*Rh(TsNC₆H₄NH), **1a** (10.4 mg, 0.02 mmol) was added to a thoroughly cleaned and dried Young's tap NMR tube and dissolved in 0.5 mL of dry and degassed dichloromethane-d₂ on a high vacuum line. 1 mole equivalent of hydrochloric acid in ether solution (20 μL, 0.02 mmol) was added to the NMR tube, under argon at 193 K. The solution turned from purple/blue to orange. After confirming the 18-electron chloride product had been synthesised *in-situ* by NMR spectroscopy at low temperature the sample was warmed to 273 K. The deuterated solvent and ether were removed *in-vacuo* and the crude product was dissolved in dichloromethane-d₂ at room temperature. Another NMR spectrum at room temperature confirmed the 18-electron chloride was still present. Isolation of **2a** was achieved by layering approximately 1.5 mL of dry, degassed diethyl ether onto the solution containing the crude product in the NMR tube. The solvents were allowed to diffuse for 5 days and orange crystals of **2a** suitable for X-ray diffraction were obtained.

NMR Spectroscopy

Table 3.4.1

X-ray crystallographic data

Appendix 8.6

7.3.5 Cp*Rh(HCOO)(TsNC₆H₄NH₂) (3a)

Cp*Rh(TsNC₆H₄NH), **1a** (10.1 mg, 0.02 mmol) was added to a Young's tap NMR tube and dissolved in 0.5 mL of dry and degassed dichloromethane-d₂. A dry and degassed solution of formic acid (0.02 mmol) in dichloromethane-d₂ was added to the NMR tube under argon at 193 K and shaken vigorously. The solution turned from purple/blue to orange immediately. The 18-electron product was analysed by ¹H, ¹³C, HSQC, HMBC, COSY and NOESY NMR experiments at low temperature.

NMR Spectroscopy

Table 3.4.2

7.3.6 Cp*Rh(H)(TsNC₆H₄NH₂) (4a)

The sample was prepared as for [Cp*Rh(OCHO)(TsNC₆H₄NH₂)], (**3a**) but in THF-d₈. It was brought to 233 K and inserted into the NMR spectrometer at that temperature. Molecular connectivity was established by ¹H-¹⁰³Rh correlation and by ¹H COSY spectroscopy.

NMR Spectroscopy

Table 3.4.3

7.4 Experimental procedures for Chapter 4

7.4.1 Cp*Ir(I)₂(NH₃)

A solution of 500mg [Cp*IrI₂]₂ in approx 50 mL toluene at room temperature was treated with ammonia gas (bubbled through a needle directly from a cylinder into the solution), the mixture changed colour from brown to orange very quickly, however over time this formed a bright yellow precipitate. Ammonia gas was bubbled through for a further 2 hours however no other physical changes occurred. The mixture was then filtered through a sintered funnel and washed twice with toluene. The yellow solid that resulted was then dried under high vacuum.

30 mg of crude iridium ammonia complex was dissolved in 3 mL of chloroform, layered with cyclohexane and the solvents were allowed to diffuse for 6 hours. Needle-like, colourless crystalline material precipitated out and the crystals were extracted using vacuum filtration. The remaining filtrate was layered with another 6 mL of cyclohexane and allowed to stand for 3 days. Orange crystals formed and were filtered and washed 3 times with 5 mL of cyclohexane.

Mass Spectroscopy (ESI) 472.0107 [Cp*IrI(NH₃)]⁺, 454.9841 [Cp*IrI]⁺
(FD) 581.9 [M – NH₃]⁺

NMR Spectroscopy Table 4.4.1

IR Spectroscopy (KBr / v(NH) / cm⁻¹)
3329 (s), 3258 (s), 3196 (s), 3151 (s)

Other IR frequencies: 2973 (m), 2957 (m), 2912 (m), 1604 (s), 1477 (s), 1449 (s), 1381 (m), 1276 (s), 1156 (m), 1081 (m), 1037 (s), 746 (m), 612 (w), 534 (w)

Elemental Analysis for C₁₀H₁₈NIrI₂

Calculated	%C (20.08), %H (3.03), %N (2.34)
Found	%C (20.17), %H (2.97), %N (2.23)

X-ray crystallography data Appendix 8.7

7.4.2 Cp*Ir(I)₂(PhCH₂NHMe)

[Cp*IrI₂]₂ (12.7 mg, 0.011 mmol) was charged to a Young's tap NMR tube and was placed on a high vacuum line for 30 minutes. Dry and degassed chloroform (0.5mL) was transferred to the NMR tube on the high vacuum line. The NMR tube was then placed in a dry ice / acetonitrile ice bath. A stock solution of degassed N-methylbenzylamine in chloroform-d was prepared (100 μL in 1mL) in a volumetric flask. 28 μL of the stock solution (1 mol equivalent of secondary amine per iridium) was transferred to the NMR tube and ¹H and ¹³C NMR spectra were recorded. 100% conversion to the coordinated amine-metal complex was observed. The solvent was removed *in-vacuo* and the orange solid was recrystallised by dissolving in a minimal amount of acetone and slow evaporation of the solvent at 248K. The orange crystals were filtered and submitted for X-ray analysis.

NMR data Table 4.4.2

IR Spectroscopy (KBr / ν(NH) / cm⁻¹) 3231.1

CHN analysis calculated for C₁₈H₂₆NIrI₂:

Calculated	%C 30.78, %H 3.73, %N 1.99
Found	%C 30.00, %H 3.62, %N 1.90

X-ray crystallography data Appendix 8.8

7.4.3 Cp*Ir(Cl)₂(PhCH₂NHMe)

As for Cp*Ir(I)₂(PhCH₂NHMe) but using [Cp*IrCl₂]₂ dimer with 2 equivalents of N-methylbenzylamine. The solvent was removed *in-vacuo* and the orange solid was recrystallised by dissolving in a minimal amount of acetone and slow evaporation of the solvent at 248K. The orange crystals were filtered and submitted for X-ray analysis.

NMR data Table 4.4.3

IR Spectroscopy (KBr / $\nu(\text{NH})$ / cm^{-1}) 3250

CHN analysis calculated for $\text{C}_{18}\text{H}_{26}\text{N}\text{IrCl}_2$:

Calculated	%C 41.61, %H 5.04, %N 2.70
Found	%C 41.85, %H 5.04, %N 2.75

X-ray crystallography data Appendix 8.9

7.4.4 $\text{Cp}^*\text{Rh}(\text{Cl})_2(\text{PhCH}_2\text{NHMe})$

As for $\text{Cp}^*\text{Ir}(\text{I})_2(\text{PhCH}_2\text{NHMe})$ but using $[\text{Cp}^*\text{RhCl}_2]_2$ dimer with 2 equivalents of N-methylbenzylamine. The solvent was removed *in-vacuo* and the orange solid was recrystallised by dissolving in a minimal amount of acetone and slow evaporation of the solvent at 248K. The orange crystals were filtered and submitted for X-ray analysis.

NMR data Table 4.4.4

IR Spectroscopy (KBr / $\nu(\text{NH})$ / cm^{-1}) 3264

CHN analysis calculated for $\text{C}_{18}\text{H}_{26}\text{N}\text{RhCl}_2$:

Calculated	%C 50.25, %H 6.09, %N 3.26
Found	%C 50.11, %H 6.01, %N 3.25

X-ray crystallography data Appendix 8.10

7.4.5 Cp*Ir(I)₂(6,7-dimethoxy-1-methyl-3,4-dihydroisoquinoline)

[Cp*IrI₂]₂ (15 mg, 0.013 mmol) and 6,7-dimethoxy-1-methyl-3,4-dihydroisoquinoline (5.3 mg, 0.026 mmol) were added to a Young's tap NMR tube and dried *in-vacuo* for 1 hour. Dry and degassed methylene chloride-d₂ (0.9 mL) was distilled into the NMR tube on a high vacuum line., before being placed in an acetonitrile / solid CO₂ bath (248 K).

NMR data

Table 4.4.5

7.4.6 Dehydrogenation of a secondary amine with [Cp*IrI₂]₂ and norbornene

Experiment 1

1,2,3,4-tetrahydro-6,7-dimethoxy-1-methylisoquinoline (7.26 mg, 0.05 mmol), bicyclo[2.2.1]hept-2-ene (23.5 mg, 0.25 mmol) and [Cp*IrI₂]₂ (0.58mg, 0.0005 mmol) were dissolved in 0.5 cm³ of toluene-d₈ in a clean and dried NMR tube. A ¹H NMR and COSY spectrum was acquired at 300 K (t = 0). The NMR tube was heated in an oil bath at 353 K for 1 hour. After 1 hour, the NMR tube was cooled to room temperature and a ¹H NMR spectrum was acquired at 300 K. The spectrum showed almost complete conversion of the starting amine to the corresponding imine.

Experiment 2

Stock solution: 5 mg of [Cp*IrI₂]₂ in 1 mL of methylene chloride.

1,2,3,4-tetrahydro-6,7-dimethoxy-1-methylisoquinoline (7.3 mg, 0.05 mmol), bicyclo[2.2.1]hept-2-ene (23.5 mg, 0.25 mmol) and [Cp*IrI₂]₂ (11.6 μL of catalyst stock solution, 0.05 μmol) were dissolved in 0.5 cm³ of toluene-d₈ in a clean and dried NMR tube. ¹H NMR recorded at 300 K (t = 0). Heat for 30 minutes at 353 K, then take another NMR at 300 K.

7.5 Experimental procedures for Chapter 5

50 μl of ^{13}C -labelled TEAF solution was placed inside a dissolution cup and 0.7 mg of trityl radical was added (to produce roughly a 12 mM solution). This sample was then inserted into hyper sense, immersed in liquid helium and pumped upon until a temperature of 1.4 K. was reached. Once this temperature had been reached the sample was irradiated with microwaves at roughly 94 Hz for eight hours. After this period time 4 mL of superheated methanol was rapidly injected into the sample, and swiftly transferred over to an Avance II Bruker 600 MHz wide bore magnet. Once the dissolved sample has entered the magnet, a series of rapid $90^\circ \text{ }^{13}\text{C}\{^1\text{H}\}$ pulses were applied.

7.6 References

- 1.) C. White, A. Yates, P. M. Maitlis and D. M. Heinekey, *Inorg. Synth.*, **29**, 228.
- 2.) A. Millan, P. M. Bailey and P. M. Maitlis, *J. Chem. Soc., Dalton Trans.*, 1982, 73.
- 3.) V. Tedesco and W. Von Philipsborn, *Magn. Reson. Chem.*, 1996, **34**, 373.
- 4.) Gaussian 03, Revision D.01, M. J. Frisch, G. W. Trucks, H. B. Schlegel, G. E. Scuseria, M. A. Robb, J. R. Cheeseman, J. A. Montgomery, Jr., T. Vreven, K. N. Kudin, J. C. Burant, J. M. Millam, S. S. Iyengar, J. Tomasi, V. Barone, B. Mennucci, M. Cossi, G. Scalmani, N. Rega, G. A. Petersson, H. Nakatsuji, M. Hada, M. Ehara, K. Toyota, R. Fukuda, J. Hasegawa, M. Ishida, T. Nakajima, Y. Honda, O. Kitao, H. Nakai, M. Klene, X. Li, J. E. Knox, H. P. Hratchian, J. B. Cross, V. Bakken, C. Adamo, J. Jaramillo, R. Gomperts, R. E. Stratmann, O. Yazyev, A. J. Austin, R. Cammi, C. Pomelli, J. W. Ochterski, P. Y. Ayala, K. Morokuma, G. A. Voth, P. Salvador, J. J. Dannenberg, V. G. Zakrzewski, S. Dapprich, A. D. Daniels, M. C. Strain, O. Farkas, D. K. Malick, A. D., Rabuck, K. Raghavachari, J. B. Foresman, J. V. Ortiz, Q. Cui, A. G. Baboul, S. Clifford, J. Cioslowski, B. B. Stefanov, G. Liu, A. Liashenko, P. Piskorz, I. Komaromi, R. L. Martin, D. J. Fox, T. Keith, M. A. Al-Laham, C. Y. Peng, A. Nanayakkara, M. Challacombe, P. M. W. Gill, B. Johnson, W. Chen, M. W. Wong, C. Gonzalez, and J. A. Pople, Gaussian, Inc., Wallingford CT, 2004.
- 5.) A. D. Becke, *J. Chem. Phys.* 1993, **98**, 5648.
- 6.) J. P. Perdew and Y. Wang, *Phys. Rev. B*, 1992, **45**, 13244.
- 7.) D. Andrae, U. Häussermann, M. Dolg, H. Stoll and H. Preus, *Theor. Chim. Acta.*, 1990, **77**, 123.
- 8.) A. W. Ehlers, M. Böhme, S. Dapprich, A. Gobbi, A. Höllwarth, V. Jonas, K. F. Köhler, R. Stegmann, A. Veldkamp and G. Frenking, *Chem. Phys. Lett.*, 1993, **208**, 111.
- 9.) P. C. Hariharan and J. A. Pople, *Theor. Chim. Acta.*, 1973, **28**, 213.
- 10.) A. Bergner, M. Dolg W. Kuchle, H. Stoll and H. Preuss, *Mol. Phys.*, 1993, **80**, 1431.
- 11.) A. Höllwarth, H. Böhme, S. Dapprich, A. W. Ehlers, A. Gobbi, V. Jonas, K. F. Köhler, R. Stegmann, A. Veldkamp and G. Frenking, *Chem. Phys. Lett.*, 1993, **208**, 237.

- 12.) A. E. Reed, L. A. Curtis and F. Winhold, *Chem. Rev.*, 1988, **88**, 899.
- 13.) P. Espinet, P. M. Bailey and P. M. Maitlis, *J. Chem. Soc., Dalton Trans.*, 1979, 1542.

APPENDIX

8.1 Ditosyldiaminophenanthrene

Identification code	rnp0706m	
Empirical formula	$C_{28}H_{24}N_2O_4S_2$	
Formula weight	516.61 g mol ⁻¹	
Temperature	110(2) K	
Wavelength	0.71073 Å	
Crystal system	Triclinic	
Space group	P-1	
Unit cell dimensions	$a = 10.0412(9)$ Å	$\alpha = 72.719(2)^\circ$
	$b = 11.4929(10)$ Å	$\beta = 69.848(2)^\circ$
	$c = 11.5994(10)$ Å	$\gamma = 73.846(2)^\circ$
Volume	1176.60(18) Å ³	
Z	2	
Density (calculated)	1.458 Mg/m ³	
Absorption coefficient	0.267 mm ⁻¹	
F(000)	540	
Crystal size	0.18 x 0.11 x 0.10 mm ³	
Theta range for data collection	1.89 to 27.51°	
Index ranges	-13 ≤ h ≤ 13, -14 ≤ k ≤ 14, -15 ≤ l ≤ 15	
Reflections collected	11443	
Independent reflections	5345 [R(int) = 0.0293]	
Completeness to theta = 27.51°	99.0 %	
Absorption correction	Semi-empirical from equivalents	
Max. and min. transmission	0.970 and 0.826	
Refinement method	Full-matrix least-squares on F ²	
Data / restraints / parameters	5345 / 0 / 334	
Goodness-of-fit on F ²	1.044	
Final R indices [I > 2sigma(I)]	R1 = 0.0478, wR2 = 0.1242	
R indices (all data)	R1 = 0.0643, wR2 = 0.1324	
Largest diff. peak and hole	0.494 and -0.505 e.Å ⁻³	

Table 1: Atomic coordinates ($\times 10^4$) and equivalent isotropic displacement parameters ($\text{\AA}^2 \times 10^3$) for ditosyldiaminophenanthrene. $U(\text{eq})$ is defined as one third of the trace of the orthogonalized U^{ij} tensor.

	x	y	z	U(eq)
C(1)	8075(2)	5631(2)	7782(2)	15(1)
C(2)	7760(2)	6521(2)	6683(2)	16(1)
C(3)	6332(2)	7164(2)	6701(2)	20(1)
C(4)	6059(3)	8039(2)	5663(2)	24(1)
C(5)	7190(3)	8278(2)	4565(2)	25(1)
C(6)	8574(3)	7636(2)	4517(2)	22(1)
C(7)	8903(2)	6753(2)	5573(2)	17(1)
C(8)	10372(2)	6079(2)	5538(2)	16(1)
C(9)	11562(2)	6250(2)	4445(2)	20(1)
C(10)	12928(3)	5580(2)	4428(2)	22(1)
C(11)	13180(2)	4709(2)	5503(2)	21(1)
C(12)	12052(2)	4518(2)	6580(2)	18(1)
C(13)	10637(2)	5191(2)	6622(2)	16(1)
C(14)	9437(2)	4983(2)	7748(2)	15(1)
C(15)	5977(2)	7821(2)	9318(2)	15(1)
C(16)	7030(2)	8535(2)	8678(2)	20(1)
C(17)	6617(2)	9772(2)	8142(2)	21(1)
C(18)	5168(3)	10309(2)	8220(2)	20(1)
C(19)	4138(2)	9567(2)	8855(2)	22(1)
C(20)	4521(2)	8321(2)	9413(2)	19(1)
C(21)	4740(3)	11668(2)	7643(2)	26(1)
C(22)	9126(2)	2166(2)	10746(2)	19(1)
C(23)	8160(3)	2955(2)	11494(2)	27(1)
C(24)	7831(3)	2562(2)	12794(2)	29(1)
C(25)	8448(3)	1384(2)	13362(2)	24(1)
C(26)	9380(3)	602(2)	12587(2)	23(1)
C(27)	9733(2)	977(2)	11288(2)	21(1)

C(28)	8113(3)	983(2)	14778(2)	33(1)
N(1)	6925(2)	5433(2)	8922(2)	15(1)
N(2)	9715(2)	4093(2)	8845(2)	16(1)
O(1)	5325(2)	5785(1)	10964(1)	19(1)
O(2)	7833(2)	6146(1)	10274(1)	18(1)
O(3)	8429(2)	2661(2)	8621(2)	25(1)
O(4)	10967(2)	1867(2)	8612(2)	26(1)
S(1)	6527(1)	6238(1)	9978(1)	14(1)
S(2)	9596(1)	2638(1)	9082(1)	18(1)

8.2 Cp*Rh(TsNC₆H₄NTs) (1b)

Identification code	rnp0701m	
Empirical formula	C ₃₀ H ₃₃ N ₂ O ₄ RhS ₂	
Formula weight	652.61 g mol ⁻¹	
Temperature	110(2) K	
Wavelength	0.71073 Å	
Crystal system	Triclinic	
Space group	P-1	
Unit cell dimensions	a = 8.6640(8) Å	α = 76.388(2)°
	b = 12.2229(11) Å	β = 84.315(2)°
	c = 14.2366(13) Å	γ = 75.726(2)°
Volume	1418.7(2) Å ³	
Z	2	
Density (calculated)	1.528 Mg/m ³	
Absorption coefficient	0.788 mm ⁻¹	
F(000)	672	
Crystal size	0.25 x 0.12 x 0.015 mm ³	
Theta range for data collection	1.47 to 28.30°	
Index ranges	-11 ≤ h ≤ 11, -16 ≤ k ≤ 16, -18 ≤ l ≤ 18	
Reflections collected	14287	
Independent reflections	6939 [R(int) = 0.0250]	
Completeness to theta = 28.30°	98.2 %	
Absorption correction	Semi-empirical from equivalents	
Max. and min. transmission	0.99 and 0.695	
Refinement method	Full-matrix least-squares on F ²	
Data / restraints / parameters	6939 / 0 / 359	
Goodness-of-fit on F ²	1.035	
Final R indices [I > 2σ(I)]	R1 = 0.0330, wR2 = 0.0824	
R indices (all data)	R1 = 0.0419, wR2 = 0.0867	
Largest diff. peak and hole	1.186 and -1.271 e.Å ⁻³	

Table 2: Atomic coordinates ($\times 10^4$) and equivalent isotropic displacement parameters ($\text{\AA}^2 \times 10^3$) for $\text{Cp}^*\text{Rh}(\text{TsNC}_6\text{H}_4\text{NTs})$. $U(\text{eq})$ is defined as one third of the trace of the orthogonalized U^{ij} tensor.

	x	y	z	U(eq)
C(1)	7201(3)	17(2)	4085(2)	16(1)
C(2)	7229(3)	-378(2)	3221(2)	17(1)
C(3)	6315(3)	554(2)	2533(2)	17(1)
C(4)	5604(3)	1496(2)	3008(2)	17(1)
C(5)	6177(3)	1175(2)	3961(2)	16(1)
C(6)	7995(3)	-643(2)	4996(2)	21(1)
C(7)	7946(3)	-1573(2)	3070(2)	21(1)
C(8)	6111(3)	510(2)	1516(2)	23(1)
C(9)	4416(3)	2571(2)	2576(2)	23(1)
C(10)	5739(3)	1826(2)	4754(2)	21(1)
C(11)	10963(3)	1537(2)	1629(2)	14(1)
C(12)	12180(3)	1345(2)	929(2)	17(1)
C(13)	12572(3)	2282(2)	256(2)	19(1)
C(14)	11755(3)	3398(2)	295(2)	20(1)
C(15)	10511(3)	3596(2)	977(2)	18(1)
C(16)	10082(3)	2664(2)	1643(2)	14(1)
C(17)	12211(3)	-1380(2)	1941(2)	15(1)
C(18)	13648(3)	-2210(2)	2012(2)	19(1)
C(19)	14002(3)	-2967(2)	1391(2)	21(1)
C(20)	12944(3)	-2898(2)	694(2)	22(1)
C(21)	11522(3)	-2057(2)	623(2)	21(1)
C(22)	11158(3)	-1298(2)	1243(2)	17(1)
C(23)	13336(4)	-3737(3)	35(2)	35(1)
C(24)	9412(3)	4396(2)	3073(2)	17(1)
C(25)	10088(3)	3726(2)	3930(2)	22(1)
C(26)	11247(3)	4069(2)	4319(2)	25(1)
C(27)	11750(3)	5073(2)	3865(2)	23(1)

C(28)	11044(3)	5732(2)	3018(2)	25(1)
C(29)	9881(3)	5402(2)	2617(2)	22(1)
C(30)	13036(3)	5431(3)	4286(2)	33(1)
N(1)	10441(2)	657(2)	2339(1)	15(1)
N(2)	8785(2)	2714(2)	2339(1)	16(1)
O(1)	13234(2)	-195(2)	2918(1)	18(1)
O(2)	11036(2)	-1114(1)	3636(1)	18(1)
O(3)	7338(2)	4825(1)	1760(1)	19(1)
O(4)	6756(2)	3717(2)	3384(1)	20(1)
Rh(1)	8188(1)	1166(1)	2901(1)	12(1)
S(1)	11765(1)	-488(1)	2791(1)	13(1)
S(2)	7904(1)	3953(1)	2607(1)	15(1)

8.3 Cp*Rh(HNC₆H₄NH) (1c)

Identification code	rnp0832a	
Empirical formula	C ₁₆ H ₂₁ N ₂ Rh	
Formula weight	344.26 g mol ⁻¹	
Temperature	110(2) K	
Wavelength	0.71073 Å	
Crystal system	Monoclinic	
Space group	P2(1)/c	
Unit cell dimensions	a = 20.8896(6) Å	α = 90°.
	b = 13.4599(4) Å	β = 95.4840(10)°
	c = 21.1659(6) Å	γ = 90°
Volume	5924.0(3) Å ³	
Z	16	
Density (calculated)	1.544 Mg/m ³	
Absorption coefficient	1.141 mm ⁻¹	
F(000)	2816	
Crystal size	0.22 x 0.12 x 0.11 mm ³	
Theta range for data collection	0.98 to 30.11°	
Index ranges	-28<=h<=29, -18<=k<=18, -29<=l<=29	
Reflections collected	66450	
Independent reflections	17170 [R(int) = 0.0251]	
Completeness to theta = 30.11°	98.5 %	
Absorption correction	Semi-empirical from equivalents	
Max. and min. transmission	0.882 and 0.738	
Refinement method	Full-matrix least-squares on F ²	
Data / restraints / parameters	17169 / 0 / 737	
Goodness-of-fit on F ²	1.020	
Final R indices [I > 2sigma(I)]	R1 = 0.0328, wR2 = 0.0790	
R indices (all data)	R1 = 0.0461, wR2 = 0.0883	
Largest diff. peak and hole	1.707 and -0.601 e.Å ⁻³	

Table 3: Atomic coordinates ($\times 10^4$) and equivalent isotropic displacement parameters ($\text{\AA}^2 \times 10^3$) for $\text{Cp}^*\text{Rh}(\text{HNC}_6\text{H}_4\text{NH})$. $U(\text{eq})$ is defined as one third of the trace of the orthogonalized U^{ij} tensor.

	x	y	z	U(eq)
C(1)	4901(1)	-1179(2)	2118(1)	26(1)
C(2)	4443(1)	-427(2)	1955(1)	25(1)
C(3)	4225(1)	-43(2)	2530(1)	24(1)
C(4)	4552(1)	-577(2)	3050(1)	23(1)
C(5)	4967(1)	-1281(2)	2797(1)	24(1)
C(6)	5239(2)	-1802(2)	1665(2)	52(1)
C(7)	4204(2)	-116(2)	1293(1)	45(1)
C(8)	3701(1)	710(2)	2566(2)	43(1)
C(9)	4438(2)	-455(2)	3730(1)	42(1)
C(10)	5362(1)	-2047(2)	3169(2)	41(1)
C(11)	6232(1)	1584(2)	2235(1)	19(1)
C(12)	6667(1)	2158(2)	1917(1)	25(1)
C(13)	7027(1)	2889(2)	2246(1)	27(1)
C(14)	6964(1)	3060(2)	2891(1)	27(1)
C(15)	6541(1)	2504(2)	3212(1)	24(1)
N(1)	5838(1)	855(1)	1978(1)	21(1)
N(2)	5723(1)	1154(1)	3126(1)	22(1)
Rh(1)	5248(1)	215(1)	2530(1)	17(1)
C(16)	6167(1)	1761(2)	2887(1)	20(1)
C(17)	2867(1)	3835(2)	4340(1)	24(1)
C(18)	2501(1)	4538(2)	3953(1)	29(1)
C(19)	2110(1)	5085(2)	4373(1)	36(1)
C(20)	2259(1)	4719(2)	4999(1)	37(1)
C(21)	2727(1)	3952(2)	4977(1)	31(1)
C(22)	3303(1)	3083(2)	4080(2)	47(1)
C(23)	2484(2)	4683(2)	3260(1)	51(1)
C(24)	1616(2)	5837(2)	4146(2)	65(1)

C(25)	1958(2)	5009(3)	5585(2)	60(1)
C(26)	3009(2)	3346(2)	5537(1)	50(1)
C(27)	4310(1)	6406(2)	4791(1)	19(1)
C(28)	4953(1)	6709(2)	4783(1)	23(1)
C(29)	5134(1)	7656(2)	4987(1)	26(1)
C(30)	4690(1)	8315(2)	5207(1)	24(1)
N(3)	4048(1)	5515(1)	4603(1)	20(1)
N(4)	3252(1)	6690(1)	4997(1)	22(1)
Rh(2)	3115(1)	5331(1)	4667(1)	19(1)
C(31)	4053(1)	8029(2)	5221(1)	23(1)
C(32)	3856(1)	7077(2)	5014(1)	19(1)
C(33)	-381(1)	5565(2)	3016(1)	21(1)
C(34)	-761(1)	4974(2)	2562(1)	26(1)
C(35)	-594(1)	5249(2)	1939(1)	27(1)
C(36)	-117(1)	6000(2)	2013(1)	25(1)
C(37)	13(1)	6203(2)	2679(1)	22(1)
C(38)	-420(1)	5575(2)	3714(1)	33(1)
C(39)	-1276(1)	4262(2)	2699(2)	42(1)
C(40)	-902(1)	4868(2)	1320(1)	45(1)
C(41)	174(1)	6543(2)	1491(1)	40(1)
C(42)	453(1)	6995(2)	2962(1)	35(1)
C(43)	1144(1)	3084(2)	2847(1)	19(1)
C(44)	1522(1)	2347(2)	3177(1)	23(1)
C(45)	1955(1)	1802(2)	2862(1)	27(1)
N(5)	704(1)	3697(1)	3081(1)	21(1)
N(6)	824(1)	3986(1)	1935(1)	21(1)
Rh(3)	246(1)	4656(1)	2485(1)	17(1)
C(46)	2018(1)	1966(2)	2218(1)	28(1)
C(47)	1651(1)	2678(2)	1879(1)	25(1)
C(48)	1211(1)	3250(2)	2193(1)	18(1)
C(49)	2300(1)	5650(2)	1081(1)	28(1)
C(50)	2143(1)	6166(2)	500(1)	26(1)
C(51)	2521(1)	5746(2)	27(1)	28(1)
C(52)	2911(1)	4973(2)	338(1)	30(1)

C(53)	2769(1)	4914(2)	978(1)	30(1)
C(54)	2035(1)	5866(2)	1702(1)	41(1)
C(55)	1686(1)	7019(2)	395(2)	41(1)
C(56)	2539(2)	6076(2)	-645(1)	43(1)
C(57)	3401(1)	4367(2)	39(2)	51(1)
C(58)	3075(1)	4236(2)	1486(2)	48(1)
C(59)	719(1)	3513(2)	197(1)	19(1)
C(60)	85(1)	3166(2)	217(1)	24(1)
C(61)	-80(1)	2219(2)	4(1)	25(1)
C(62)	373(1)	1599(2)	-236(1)	24(1)
C(63)	1000(1)	1925(2)	-267(1)	23(1)
C(64)	1180(1)	2876(2)	-48(1)	20(1)
N(7)	969(1)	4403(1)	400(1)	21(1)
N(8)	1777(1)	3293(1)	-34(1)	23(1)
Rh(4)	1903(1)	4617(1)	357(1)	19(1)

8.4 Cp*Ir(TsNC₆H₄NH) (1d)

Identification code	rnp0803m
Empirical formula ¹	C _{26.50} H ₃₁ IrN ₂ O ₂ S
Formula weight	633.79 g mol ⁻¹
Temperature	110(2) K
Wavelength	0.71073 Å
Crystal system	Monoclinic
Space group	C2/c
Unit cell dimensions	a = 24.2794(13) Å α = 90° b = 13.1473(7) Å β = 101.0620(10)° c = 15.5482(8) Å γ = 90°
Volume	4870.9(4) Å ³
Z	8
Density (calculated)	1.729 Mg/m ³
Absorption coefficient	5.594 mm ⁻¹
F(000)	2504
Crystal size	0.20 x 0.04 x 0.02 mm ³
Theta range for data collection	1.71 to 30.02°
Index ranges	-33 ≤ h ≤ 34, -18 ≤ k ≤ 18, -21 ≤ l ≤ 21
Reflections collected	27057
Independent reflections	7054 [R(int) = 0.0415]
Completeness to theta = 30.02°	98.9 %
Absorption correction	Semi-empirical from equivalents
Max. and min. transmission	0.894 and 0.691
Refinement method	Full-matrix least-squares on F ²
Data / restraints / parameters	7054 / 0 / 333
Goodness-of-fit on F ²	1.021
Final R indices [I > 2σ(I)]	R1 = 0.0290, wR2 = 0.0633
R indices (all data)	R1 = 0.0450, wR2 = 0.0689
Largest diff. peak and hole	2.766 and -1.545 e.Å ⁻³

¹ Unit cell includes ½ equivalent of toluene, Cp*Ir(TsNC₆H₄NH).0.5Tol

Table 4: Atomic coordinates ($\times 10^4$) and equivalent isotropic displacement parameters ($\text{\AA}^2 \times 10^3$) for $\text{Cp}^*\text{Ir}(\text{TsNC}_6\text{H}_4\text{NH})$. $U(\text{eq})$ is defined as one third of the trace of the orthogonalized U^{ij} tensor.

	x	y	z	U(eq)
C(1)	2468(1)	6932(3)	2239(2)	19(1)
C(2)	2521(1)	6832(3)	3175(2)	19(1)
C(3)	2941(1)	6089(3)	3466(2)	19(1)
C(4)	3150(1)	5723(3)	2720(2)	19(1)
C(5)	2865(1)	6266(3)	1955(2)	18(1)
C(6)	2090(2)	7651(3)	1652(2)	25(1)
C(7)	2220(2)	7475(3)	3730(2)	25(1)
C(8)	3172(2)	5768(3)	4395(2)	26(1)
C(9)	3618(2)	4975(3)	2743(3)	27(1)
C(10)	2969(2)	6163(3)	1031(2)	25(1)
C(11)	1510(1)	3876(3)	1566(2)	17(1)
C(12)	1225(2)	3272(3)	883(2)	21(1)
C(13)	817(2)	2599(3)	1037(2)	24(1)
C(14)	697(2)	2512(3)	1874(2)	23(1)
C(15)	984(2)	3090(3)	2562(2)	21(1)
C(16)	1389(1)	3789(3)	2416(2)	17(1)
C(17)	900(2)	5109(3)	3857(2)	18(1)
C(18)	839(2)	6131(3)	3627(2)	22(1)
C(19)	318(2)	6590(3)	3558(2)	27(1)
C(20)	-146(2)	6040(3)	3695(2)	26(1)
C(21)	-78(2)	5021(4)	3908(3)	30(1)
C(22)	442(2)	4548(3)	4000(3)	26(1)
C(23)	-713(2)	6533(4)	3623(3)	38(1)
Ir(1)	2263(1)	5387(1)	2492(1)	14(1)
N(1)	1909(1)	4595(2)	1487(2)	17(1)
N(2)	1716(1)	4476(2)	3009(2)	16(1)
O(1)	1965(1)	5282(2)	4476(2)	21(1)

O(2)	1552(1)	3573(2)	4388(2)	24(1)
S(1)	1577(1)	4561(1)	3998(1)	17(1)
C(24)	4926(5)	5001(14)	10257(9)	53(3)
C(25)	4902(7)	5517(11)	9499(13)	60(5)
C(26)	5199(8)	5163(15)	8837(13)	71(6)
C(27)	5509(8)	4340(12)	8991(9)	47(3)
C(28)	5564(5)	3812(9)	9767(8)	49(3)
C(29)	5272(6)	4138(11)	10389(10)	48(3)
C(30)	4583(13)	5350(30)	10860(19)	140(20)

8.5 Cp*Ir(TsNC₆H₄NTs) (1e)

Identification code	rnp0702m	
Empirical formula	C ₃₀ H ₃₃ IrN ₂ O ₄ S ₂	
Formula weight	741.90 g mol ⁻¹	
Temperature	110(2) K	
Wavelength	0.71073 Å	
Crystal system	Triclinic	
Space group	P-1	
Unit cell dimensions	a = 8.7319(6) Å	α = 76.4110(10)°
	b = 12.1399(9) Å	β = 83.7960(10)°
	c = 14.2911(11) Å	γ = 75.4240(10)°
Volume	1423.19(18) Å ³	
Z	2	
Density (calculated)	1.731 Mg/m ³	
Absorption coefficient	4.876 mm ⁻¹	
F(000)	736	
Crystal size	0.27 x 0.04 x 0.01 mm ³	
Theta range for data collection	1.78 to 30.01°	
Index ranges	-12 ≤ h ≤ 12, -17 ≤ k ≤ 17, -20 ≤ l ≤ 19	
Reflections collected	15951	
Independent reflections	7960 [R(int) = 0.0325]	
Completeness to theta = 30.01°	95.7 %	
Absorption correction	Semi-empirical from equivalents	
Max. and min. transmission	0.950 and 0.659	
Refinement method	Full-matrix least-squares on F ²	
Data / restraints / parameters	7960 / 0 / 359	
Goodness-of-fit on F ²	1.033	
Final R indices [I > 2σ(I)]	R1 = 0.0342, wR2 = 0.0704	
R indices (all data)	R1 = 0.0411, wR2 = 0.0725	
Largest diff. peak and hole	2.500 and -1.698 e.Å ⁻³	

Table 5: Atomic coordinates ($\times 10^4$) and equivalent isotropic displacement parameters ($\text{\AA}^2 \times 10^3$) for $\text{Cp}^*\text{Ir}(\text{TsNC}_6\text{H}_4\text{NTs})$. $U(\text{eq})$ is defined as one third of the trace of the orthogonalized U^{ij} tensor.

	x	y	z	U(eq)
C(1)	2228(4)	15(3)	4092(3)	15(1)
C(2)	1193(4)	1182(3)	3971(3)	14(1)
C(3)	601(4)	1490(3)	3022(3)	15(1)
C(4)	1312(4)	527(3)	2553(3)	15(1)
C(5)	2235(4)	-402(3)	3237(3)	14(1)
C(6)	744(5)	1840(4)	4756(3)	20(1)
C(7)	-585(4)	2566(4)	2596(3)	20(1)
C(8)	1093(5)	468(4)	1548(3)	20(1)
C(9)	2946(5)	-1605(3)	3087(3)	17(1)
C(10)	3021(5)	-644(3)	4998(3)	17(1)
C(11)	5091(4)	2672(3)	1650(3)	12(1)
C(12)	5513(5)	3607(3)	987(3)	17(1)
C(13)	6765(4)	3404(4)	317(3)	18(1)
C(14)	7594(4)	2278(3)	286(3)	18(1)
C(15)	7209(4)	1342(3)	954(3)	15(1)
C(16)	5979(4)	1536(3)	1644(3)	12(1)
C(17)	4393(4)	4399(3)	3073(3)	15(1)
C(18)	5062(5)	3719(4)	3924(3)	21(1)
C(19)	6211(5)	4060(4)	4307(3)	22(1)
C(20)	6724(5)	5066(4)	3859(3)	20(1)
C(21)	6033(5)	5731(4)	3012(3)	23(1)
C(22)	4868(5)	5404(4)	2620(3)	20(1)
C(23)	8005(5)	5418(4)	4271(4)	29(1)
C(24)	7183(4)	-1382(3)	1923(3)	14(1)
C(25)	6131(4)	-1291(3)	1232(3)	16(1)
C(26)	6501(5)	-2029(4)	600(3)	19(1)
C(27)	7916(5)	-2874(3)	653(3)	18(1)

C(28)	8965(4)	-2961(3)	1341(3)	18(1)
C(29)	8613(4)	-2216(3)	1981(3)	16(1)
C(30)	8318(6)	-3694(4)	-30(4)	31(1)
Ir(1)	3183(1)	1167(1)	2890(1)	10(1)
N(1)	3776(4)	2718(3)	2341(2)	13(1)
N(2)	5441(3)	656(3)	2350(2)	13(1)
O(1)	1743(3)	3739(2)	3386(2)	18(1)
O(2)	2346(3)	4840(2)	1766(2)	17(1)
O(3)	8198(3)	-224(2)	2919(2)	16(1)
O(4)	6011(3)	-1142(2)	3625(2)	16(1)
S(1)	2889(1)	3970(1)	2614(1)	14(1)
S(2)	6742(1)	-512(1)	2794(1)	12(1)

8.6 Cp*Rh(Cl)(TsNC₆H₄NH₂) (2a)

Identification code	rnp0808m	
Empirical formula	C ₂₃ H ₂₈ ClN ₂ O ₂ RhS	
Formula weight	534.89 g mol ⁻¹	
Temperature	110(2) K	
Wavelength	0.71073 Å	
Crystal system	Triclinic	
Space group	P-1	
Unit cell dimensions	a = 11.0617(11) Å	α = 117.247(2)°
	b = 15.1303(15) Å	β = 104.377(2)°
	c = 16.2600(17) Å	γ = 92.805(2)°
Volume	2301.5(4) Å ³	
Z	4	
Density (calculated)	1.544 Mg/m ³	
Absorption coefficient	0.971 mm ⁻¹	
F(000)	1096	
Crystal size	0.34 x 0.23 x 0.06 mm ³	
Theta range for data collection	1.48 to 28.29°	
Index ranges	-14 ≤ h ≤ 14, -20 ≤ k ≤ 20, -21 ≤ l ≤ 21	
Reflections collected	31550	
Independent reflections	11375 [R(int) = 0.0213]	
Completeness to theta = 28.29°	99.5 %	
Absorption correction	Semi-empirical from equivalents	
Max. and min. transmission	0.943 and 0.831	
Refinement method	Full-matrix least-squares on F ²	
Data / restraints / parameters	11375 / 0 / 569	
Goodness-of-fit on F ²	1.026	
Final R indices [I > 2σ(I)]	R1 = 0.0232, wR2 = 0.0573	
R indices (all data)	R1 = 0.0282, wR2 = 0.0591	
Largest diff. peak and hole	0.701 and -0.344 e.Å ⁻³	

Table 6: Atomic coordinates ($\times 10^4$) and equivalent isotropic displacement parameters ($\text{\AA}^2 \times 10^3$) for $\text{Cp}^*\text{Rh}(\text{Cl})(\text{TsNC}_6\text{H}_4\text{NH}_2)$. $U(\text{eq})$ is defined as one third of the trace of the orthogonalized U^{ij} tensor.

	x	y	z	U(eq)
C(1)	5562(2)	3545(1)	3223(1)	16(1)
C(2)	6075(2)	3098(1)	2422(1)	16(1)
C(3)	5335(2)	2114(1)	1746(1)	14(1)
C(4)	4351(2)	1934(1)	2128(1)	15(1)
C(5)	4524(2)	2807(1)	3050(1)	16(1)
C(6)	6069(2)	4559(1)	4111(1)	25(1)
C(7)	7201(2)	3596(2)	2339(2)	24(1)
C(8)	5547(2)	1382(1)	817(1)	20(1)
C(9)	3345(2)	1001(1)	1653(1)	20(1)
C(10)	3757(2)	2929(2)	3719(1)	25(1)
C(11)	1517(2)	2202(1)	575(1)	15(1)
C(12)	636(2)	1350(1)	-137(1)	21(1)
C(13)	-500(2)	1127(2)	14(2)	25(1)
C(14)	-729(2)	1767(2)	870(2)	25(1)
C(15)	159(2)	2626(1)	1591(1)	21(1)
C(16)	1315(2)	2851(1)	1462(1)	15(1)
C(17)	1130(2)	5168(1)	2351(1)	16(1)
C(18)	-74(2)	5280(2)	2448(1)	24(1)
C(19)	-859(2)	5664(2)	1931(2)	28(1)
C(20)	-460(2)	5933(1)	1316(1)	23(1)
C(21)	755(2)	5811(1)	1232(1)	21(1)
C(22)	1551(2)	5427(1)	1740(1)	19(1)
C(23)	-1315(2)	6348(2)	756(2)	31(1)
N(1)	2734(1)	2467(1)	486(1)	14(1)
N(2)	2355(1)	3638(1)	2134(1)	15(1)
S(1)	2140(1)	4645(1)	2975(1)	16(1)
O(1)	1455(1)	4456(1)	3549(1)	22(1)

O(2)	3350(1)	5330(1)	3508(1)	21(1)
Cl(1)	4591(1)	4456(1)	1452(1)	21(1)
Rh(1)	4117(1)	3201(1)	1906(1)	11(1)
C(24)	3515(2)	7751(1)	3107(1)	17(1)
C(25)	4594(2)	7285(1)	2909(1)	17(1)
C(26)	4695(2)	7217(1)	2022(1)	18(1)
C(27)	3679(2)	7639(1)	1666(1)	20(1)
C(28)	2952(2)	7957(1)	2331(1)	20(1)
C(29)	3009(2)	7882(1)	3919(1)	23(1)
C(30)	5448(2)	6939(1)	3528(1)	22(1)
C(31)	5670(2)	6780(2)	1536(2)	27(1)
C(32)	3384(2)	7659(2)	725(1)	31(1)
C(33)	1815(2)	8447(2)	2245(2)	29(1)
C(34)	7515(2)	9171(1)	4273(1)	17(1)
C(35)	8420(2)	8963(2)	4884(2)	25(1)
C(36)	9506(2)	8675(2)	4639(2)	35(1)
C(37)	9658(2)	8605(2)	3792(2)	35(1)
C(38)	8756(2)	8824(2)	3182(2)	26(1)
C(39)	7651(2)	9096(1)	3410(1)	17(1)
C(40)	7711(2)	10884(1)	2890(1)	18(1)
C(41)	7303(2)	11623(1)	3612(1)	20(1)
C(42)	8098(2)	12556(1)	4246(1)	23(1)
C(43)	9301(2)	12767(1)	4183(1)	23(1)
C(44)	9672(2)	12026(2)	3438(2)	27(1)
C(45)	8888(2)	11086(2)	2795(1)	25(1)
C(46)	10209(2)	13748(2)	4922(2)	32(1)
N(3)	6332(2)	9448(1)	4453(1)	17(1)
N(4)	6575(1)	9245(1)	2839(1)	15(1)
S(2)	6713(1)	9672(1)	2131(1)	17(1)
O(3)	7381(1)	9084(1)	1456(1)	24(1)
O(4)	5476(1)	9791(1)	1700(1)	23(1)
Cl(2)	4317(1)	10435(1)	3662(1)	18(1)
Rh(2)	4888(1)	8774(1)	3078(1)	13(1)

Table 6.1: Analysis of Hydrogen Bonds with $d(D\cdots A) < R(D) + R(A) + 0.50$, $d(H\cdots A) < R(H) + R(A) - 0.12 \text{ \AA}$, $D-H\cdots A > 100.0^\circ$.

	D-H	H \cdots A	D \cdots A	D-H \cdots A
N(1)-H(1B) \cdots O3	0.85(2)	2.14(2)	2.9121(19)	151(2)
N(3)-H(3B) \cdots Cl2	0.84(3)	2.45(3)	3.2488(16)	160(2)
N(1)-H(1A) \cdots Cl1	0.81(3)	2.57(2)	3.0350(19)	117(2)
N(3)-H(3A) \cdots Cl2	0.83(3)	2.68(3)	3.0844(19)	112(2)

8.7 Cp*Ir(I)₂(NH₃)

Identification code	rnp0807m
Empirical formula	C ₁₀ H ₁₈ I ₂ IrN
Formula weight	598.25 g mol ⁻¹
Temperature	110(2) K
Wavelength	0.71073 Å
Crystal system	Monoclinic
Space group	P2(1)/c
Unit cell dimensions	a = 8.8106(6) Å α = 90° b = 7.9319(5) Å β = 100.5070(10)° c = 20.8261(14) Å γ = 90°
Volume	1431.02(16) Å ³
Z	4
Density (calculated)	2.777 Mg/m ³
Absorption coefficient	13.614 mm ⁻¹
F(000)	1072
Crystal size	0.17 x 0.07 x 0.03 mm ³
Theta range for data collection	1.99 to 30.01°
Index ranges	-12 ≤ h ≤ 12, -11 ≤ k ≤ 11, -28 ≤ l ≤ 29
Reflections collected	15169
Independent reflections	4119 [R(int) = 0.0329]
Completeness to theta = 30.01°	98.1 %
Absorption correction	Semi-empirical from equivalents
Max. and min. transmission	0.665 and 0.358
Refinement method	Full-matrix least-squares on F ²
Data / restraints / parameters	4119 / 0 / 141
Goodness-of-fit on F ²	1.141
Final R indices [I > 2σ(I)]	R1 = 0.0290, wR2 = 0.0744
R indices (all data)	R1 = 0.0306, wR2 = 0.0750
Largest diff. peak and hole	3.441 and -1.443 e.Å ⁻³

Table 7: Atomic coordinates ($\times 10^4$) and equivalent isotropic displacement parameters ($\text{\AA}^2 \times 10^3$) for $\text{Cp}^*\text{Ir}(\text{I})_2(\text{NH}_3)$. $U(\text{eq})$ is defined as one third of the trace of the orthogonalized U^{ij} tensor.

	x	y	z	U(eq)
C(1)	2628(6)	8042(7)	1912(3)	16(1)
C(2)	1750(6)	7253(7)	1341(3)	15(1)
C(3)	2800(6)	6732(7)	926(3)	15(1)
C(4)	4343(6)	7230(6)	1237(3)	14(1)
C(5)	4216(6)	8035(7)	1855(3)	16(1)
C(6)	1970(8)	8649(9)	2482(3)	25(1)
C(7)	50(7)	6892(8)	1228(3)	23(1)
C(8)	2427(7)	5836(7)	289(3)	18(1)
C(9)	5824(7)	6870(7)	1005(3)	20(1)
C(10)	5554(7)	8641(8)	2350(3)	22(1)
I(1)	845(1)	11881(1)	1208(1)	17(1)
I(2)	5138(1)	11763(1)	995(1)	16(1)
Ir(1)	2901(1)	9438(1)	1043(1)	11(1)
N(1)	2264(6)	9985(6)	27(2)	17(1)

Table 7.1: Analysis of Hydrogen Bonds with $d(\text{D}\cdots\text{A}) < R(\text{D}) + R(\text{A}) + 0.50$, $d(\text{H}\cdots\text{A}) < R(\text{H}) + R(\text{A}) - 0.12 \text{\AA}$, $\text{D-H}\cdots\text{A} > 100.0^\circ$.

	D-H	H \cdots A	D \cdots A	D-H \cdots A
N(1)-H(1A) \cdots I(1)	0.88(8)	2.90(9)	3.707(5)	154(7)
N(1)-H(1B) \cdots I(2)	0.78(9)	2.92(9)	3.671(5)	164(9)

8.8 Cp*Ir(I)₂(PhCH₂NHMe)

Identification code	rnp0815m	
Empirical formula	C ₁₈ H ₂₆ I ₂ IrN	
Formula weight	702.40 g mol ⁻¹	
Temperature	110(2) K	
Wavelength	0.71073 Å	
Crystal system	Orthorhombic	
Space group	P2(1)2(1)2(1)	
Unit cell dimensions	a = 7.7154(6) Å	α = 90°
	b = 11.4917(9) Å	β = 90°
	c = 23.3074(18) Å	γ = 90°
Volume	2066.5(3) Å ³	
Z	4	
Density (calculated)	2.258 Mg/m ³	
Absorption coefficient	9.446 mm ⁻¹	
F(000)	1296	
Crystal size	0.29 x 0.06 x 0.04 mm ³	
Theta range for data collection	1.75 to 28.31°	
Index ranges	-10 ≤ h ≤ 10, -15 ≤ k ≤ 15, -31 ≤ l ≤ 31	
Reflections collected	28501	
Independent reflections	5151 [R(int) = 0.0221]	
Completeness to theta = 28.31°	100.0 %	
Absorption correction	Semi-empirical from equivalents	
Max. and min. transmission	0.685 and 0.340	
Refinement method	Full-matrix least-squares on F ²	
Data / restraints / parameters	5151 / 26 / 351	
Goodness-of-fit on F ²	1.062	
Final R indices [I > 2σ(I)]	R1 = 0.0224, wR2 = 0.0484	
R indices (all data)	R1 = 0.0232, wR2 = 0.0487	
Absolute structure parameter	-0.001(5)	
Largest diff. peak and hole	2.204 and -2.062 e.Å ⁻³	

Table 8: Atomic coordinates ($\times 10^4$) and equivalent isotropic displacement parameters ($\text{\AA}^2 \times 10^3$) for $\text{Cp}^*\text{Ir}(\text{I})_2(\text{PhCH}_2\text{NHMe})$. $U(\text{eq})$ is defined as one third of the trace of the orthogonalized U^{ij} tensor.

	x	y	z	U(eq)
C(1A)	7128(16)	8300(14)	8178(7)	18(3)
C(2A)	5523(15)	8360(11)	8531(5)	25(2)
C(3A)	4238(18)	7685(14)	8281(6)	31(3)
C(4A)	4890(20)	7148(14)	7768(7)	41(4)
C(5A)	6845(8)	7542(5)	7728(2)	35(1)
C(6A)	8696(18)	8986(11)	8275(6)	47(3)
C(7A)	5369(19)	9147(10)	9046(5)	47(3)
C(8A)	2381(12)	7630(13)	8487(7)	54(4)
C(9A)	3948(17)	6422(13)	7350(5)	55(3)
C(10A)	7860(19)	7300(11)	7208(5)	39(3)
C(1B)	6600(18)	8230(18)	8234(8)	21(4)
C(2B)	4900(20)	7981(13)	8437(6)	25(3)
C(3B)	4183(16)	7131(15)	8051(8)	29(3)
C(4B)	5480(20)	6841(13)	7647(7)	27(3)
C(5B)	6845(8)	7542(5)	7728(2)	35(1)
C(6B)	7883(18)	9091(10)	8500(7)	37(3)
C(7B)	3997(18)	8569(13)	8913(5)	43(4)
C(8B)	2347(15)	6718(16)	8027(7)	54(5)
C(9B)	5250(20)	6073(11)	7129(5)	43(4)
C(10B)	8682(19)	7523(11)	7403(6)	33(3)
C(11)	4131(8)	5642(5)	9515(2)	36(1)
C(12A)	3599(18)	4686(19)	9942(9)	28(3)
C(13A)	4910(20)	4293(15)	10295(8)	36(4)
C(14A)	4460(30)	3444(19)	10706(7)	49(5)
C(15A)	2860(30)	2985(14)	10725(9)	50(5)
C(16A)	1570(30)	3385(17)	10354(8)	59(4)
C(17A)	1950(20)	4230(20)	9963(10)	53(5)

C(12B)	4130(20)	4730(30)	9970(11)	31(4)
C(13B)	5490(30)	4524(17)	10356(8)	36(4)
C(14B)	5460(40)	3610(20)	10757(9)	64(6)
C(15B)	3990(50)	2910(20)	10794(11)	76(10)
C(16B)	2560(40)	3130(20)	10450(11)	59(7)
C(17B)	2650(30)	4040(20)	10036(11)	51(5)
C(18)	4016(9)	4367(7)	8677(3)	59(2)
I(1)	8565(1)	6661(1)	9402(1)	45(1)
I(2)	8325(1)	4687(1)	8089(1)	57(1)
Ir(1)	6425(1)	6494(1)	8487(1)	24(1)
N(1)	5104(6)	5183(4)	8999(2)	30(1)

8.9 Cp*Ir(Cl)₂(PhCH₂NHMe)

Identification code	rnp0820m	
Empirical formula	C ₁₈ H ₂₆ Cl ₂ IrN	
Formula weight	519.50 g mol ⁻¹	
Temperature	110(2) K	
Wavelength	0.71073 Å	
Crystal system	Orthorhombic	
Space group	P2(1)2(1)2(1)	
Unit cell dimensions	a = 8.9124(11) Å	α = 90°
	b = 12.5778(15) Å	β = 90°
	c = 17.055(2) Å	γ = 90°
Volume	1911.8(4) Å ³	
Z	4	
Density (calculated)	1.805 Mg/m ³	
Absorption coefficient	7.260 mm ⁻¹	
F(000)	1008	
Crystal size	0.17 x 0.08 x 0.05 mm ³	
Theta range for data collection	2.01 to 28.32°	
Index ranges	-11 ≤ h ≤ 11, -16 ≤ k ≤ 16, -22 ≤ l ≤ 22	
Reflections collected	26453	
Independent reflections	4748 [R(int) = 0.0328]	
Completeness to theta = 28.32°	100.0 %	
Absorption correction	Semi-empirical from equivalents	
Max. and min. transmission	0.696 and 0.519	
Refinement method	Full-matrix least-squares on F ²	
Data / restraints / parameters	4748 / 0 / 209	
Goodness-of-fit on F ²	1.014	
Final R indices [I > 2σ(I)]	R1 = 0.0167, wR2 = 0.0363	
R indices (all data)	R1 = 0.0178, wR2 = 0.0367	
Absolute structure parameter	-0.009(5)	
Largest diff. peak and hole	1.293 and -0.552 e.Å ⁻³	

Table 9: Atomic coordinates ($\times 10^4$) and equivalent isotropic displacement parameters ($\text{\AA}^2 \times 10^3$) for $\text{Cp}^*\text{Ir}(\text{Cl})_2(\text{PhCH}_2\text{NHMe})$. $U(\text{eq})$ is defined as one third of the trace of the orthogonalized U^{ij} tensor.

	x	y	z	U(eq)
C(1)	3077(3)	6030(2)	9161(2)	22(1)
C(2)	2151(3)	5084(3)	9116(2)	21(1)
C(3)	2645(4)	4481(2)	8454(2)	21(1)
C(4)	3823(3)	5048(2)	8070(2)	21(1)
C(5)	4116(3)	5999(3)	8522(2)	26(1)
C(6)	2929(5)	6884(3)	9774(2)	40(1)
C(7)	990(4)	4762(3)	9701(2)	35(1)
C(8)	2077(4)	3399(2)	8229(2)	32(1)
C(9)	4706(4)	4679(3)	7375(2)	35(1)
C(10)	5292(4)	6812(3)	8345(2)	38(1)
C(11)	-1042(4)	4953(3)	7433(2)	25(1)
C(12)	932(3)	5147(2)	6444(2)	18(1)
C(13)	-21(3)	5365(2)	5728(2)	17(1)
C(14)	135(4)	6334(2)	5334(2)	23(1)
C(15)	-746(4)	6555(3)	4681(2)	26(1)
C(16)	-1796(4)	5812(3)	4420(2)	26(1)
C(17)	-1946(4)	4850(2)	4810(2)	24(1)
C(18)	-1066(4)	4629(3)	5459(2)	20(1)
Cl(1)	2421(1)	7382(1)	7120(1)	22(1)
Cl(2)	-236(1)	7094(1)	8519(1)	22(1)
Ir(1)	1852(1)	6023(1)	8073(1)	14(1)
N(1)	261(3)	5595(2)	7176(2)	16(1)

8.10 Cp*Rh(Cl)₂(PhCH₂NHMe)

Identification code	rnp0821a	
Empirical formula	C ₁₈ H ₂₆ Cl ₂ NRh	
Formula weight	430.21 g mol ⁻¹	
Temperature	110(2) K	
Wavelength	0.71073 Å	
Crystal system	Orthorhombic	
Space group	P2(1)2(1)2(1)	
Unit cell dimensions	a = 8.8770(5) Å	α = 90°
	b = 12.5223(8) Å	β = 90°
	c = 17.1353(10) Å	γ = 90°
Volume	1904.8(2) Å ³	
Z	4	
Density (calculated)	1.500 Mg/m ³	
Absorption coefficient	1.174 mm ⁻¹	
F(000)	880	
Crystal size	0.20 x 0.18 x 0.05 mm ³	
Theta range for data collection	2.01 to 28.33°	
Index ranges	-11 ≤ h ≤ 11, -16 ≤ k ≤ 16, -22 ≤ l ≤ 22	
Reflections collected	26194	
Independent reflections	4733 [R(int) = 0.0226]	
Completeness to theta = 28.33°	99.9 %	
Absorption correction	Semi-empirical from equivalents	
Max. and min. transmission	0.943 and 0.833	
Refinement method	Full-matrix least-squares on F ²	
Data / restraints / parameters	4733 / 0 / 209	
Goodness-of-fit on F ²	1.052	
Final R indices [I > 2σ(I)]	R1 = 0.0159, wR2 = 0.0373	
R indices (all data)	R1 = 0.0172, wR2 = 0.0378	
Absolute structure parameter	0.002(17)	
Largest diff. peak and hole	0.446 and -0.208 e.Å ⁻³	

Table 10: Atomic coordinates ($\times 10^4$) and equivalent isotropic displacement parameters ($\text{\AA}^2 \times 10^3$) for $\text{Cp}^*\text{Rh}(\text{Cl})_2(\text{PhCH}_2\text{NHMe})$. $U(\text{eq})$ is defined as one third of the trace of the orthogonalized U^{ij} tensor.

	x	y	z	U(eq)
C(1)	8826(2)	51(1)	8074(1)	23(1)
C(2)	9122(2)	1000(2)	8525(1)	25(1)
C(3)	8071(2)	1038(1)	9151(1)	24(1)
C(4)	7147(2)	83(1)	9107(1)	22(1)
C(5)	7648(2)	-522(1)	8453(1)	21(1)
C(6)	9701(2)	-316(2)	7377(1)	35(1)
C(7)	10312(2)	1808(2)	8347(1)	38(1)
C(8)	7928(3)	1896(2)	9755(1)	39(1)
C(9)	5972(2)	-230(2)	9684(1)	37(1)
C(10)	7076(2)	-1606(1)	8232(1)	34(1)
C(11)	3971(2)	-75(2)	7422(1)	26(1)
C(12)	5967(2)	136(1)	6441(1)	19(1)
C(13)	5020(2)	365(1)	5724(1)	19(1)
C(14)	3966(2)	-371(1)	5454(1)	21(1)
C(15)	3081(2)	-143(1)	4807(1)	25(1)
C(16)	3243(2)	827(1)	4425(1)	26(1)
C(17)	4295(2)	1570(2)	4688(1)	26(1)
C(18)	5174(2)	1341(1)	5336(1)	23(1)
Cl(1)	7491(1)	2378(1)	7122(1)	22(1)
Cl(2)	4740(1)	2078(1)	8534(1)	22(1)
N(1)	5278(2)	573(1)	7171(1)	17(1)
Rh(1)	6852(1)	1027(1)	8069(1)	14(1)

Synthesis and structure of “16-electron” rhodium(III) catalysts for transfer hydrogenation of a cyclic imine: mechanistic implications†

A. John Blacker,^a Eric Clot,^b Simon B. Duckett,^c Odile Eisenstein,^b Jake Grace,^c Ainara Nova,^b Robin N. Perutz,^{*c} David J. Taylor^c and Adrian C. Whitwood^c

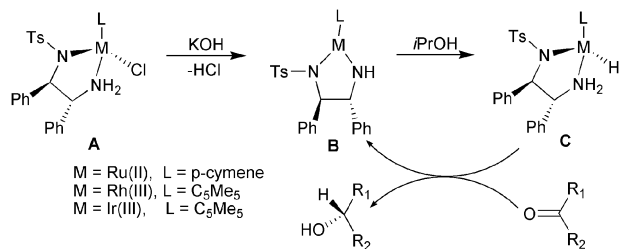
Received (in Cambridge, UK) 30th June 2009, Accepted 15th September 2009

First published as an Advance Article on the web 2nd October 2009

DOI: 10.1039/b912943j

Significant Rh–NH π -bonding in formally 16-electron (η^5 -C₅Me₅)Rh(XNC₆H₄NX') (X, X' = H or Ts) is shown by structural features and by DFT calculations; (η^5 -C₅Me₅)Rh(TsNC₆H₄NH) is the fastest transfer hydrogenation catalyst of the three complexes and generates a formate complex under catalytic conditions.

Many group 8 and 9 metal catalysts for transfer and heterolytic hydrogenation incorporate amido ligands capable of M–N π -bonding.^{1–3} The complexes Cp*M(HNC₆H₄NH) (Cp* = η^5 -C₅Me₅, M = Rh, Ir) with formal 16-electron M(III) configurations^{4,5} display strong colours arising from ($\pi \rightarrow d$) ligand-to-metal charge transfer bands. Related complexes with M–O bonds are also stabilised by π -donation.^{4,6} When one of the NH groups is tosylated, the bonding of the NTs and NH groups may be significantly different.⁷ Protonation of Cp*Ir(TsNCHPhCHPhNH) at the NH group results in elongation of the Ir–NH bond and contraction of the Ir–NTs bond, indicating redirection of π -bonding from one nitrogen to the other.⁷ Upon binding of Lewis bases⁷ to the protonated 16-electron form, the Ir–NTs bond lengthens and the acidity of the amine decreases. Half-sandwich Cp*Rh(III) and Cp*Ir(III) complexes with monotosylated amine and 16-electron configurations are proposed to be integral to the mechanism of asymmetric transfer hydrogenation (ATH, Scheme 1).³ In Noyori's system for ATH [(*p*-cymene)RuCl₂]₂–TsDPEN, all three species proposed in the outer-sphere catalysis mechanism



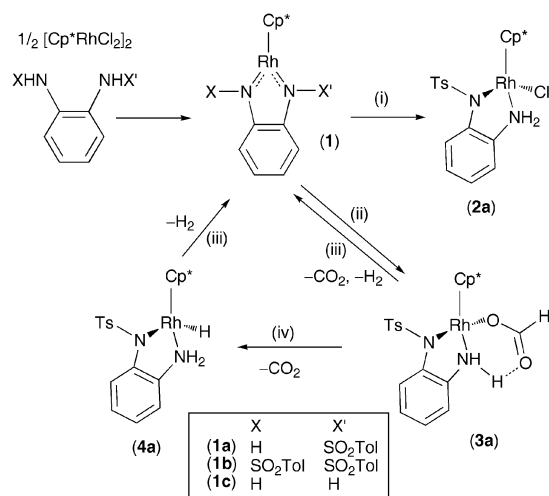
Scheme 1 “Outer-sphere” bifunctional catalysis mechanism.

^a Piramal Healthcare, Leeds Road, Huddersfield, UK HD1 9GA

^b Institut Charles Gerhardt, Université de Montpellier 2, CNRS 5253, cc 1501, Place. E. Bataillon, 34000 Montpellier, France

^c Department of Chemistry, The University of York, Heslington, York, UK YO10 5DD. E-mail: rnp1@york.ac.uk; Tel: +44 (0)1904 432549

† Electronic supplementary information (ESI) available: Synthetic procedures, spectroscopic data, X-ray data and computational details. CCDC 729047–729050. For ESI and crystallographic data in CIF or other electronic format see DOI: 10.1039/b912943j



Scheme 2 (i) 1 mol eq. HCl in ether, 193 K; (ii) 1 mol eq. HCO₂H, 193 K; (iii) warm to 300 K; (iv) warm to 233–273 K.

have been isolated: (A) the 18-electron chloride precursor, (B) the 16-electron amido complex and (C) the 18-electron hydride complex.⁸ The Noyori mechanism applies to some transfer hydrogenation catalysts but not all.⁹ Attempts to isolate 16-electron Cp*Rh(III) intermediates such as Cp*Rh(TsNCHPhCHPhNH) have met with limited success.¹⁰

We report here a range of 16-electron catalytically active Cp*Rh(III) complexes with structural evidence for the importance of π -bonding. A formate complex and a hydride complex are identified on reaction with the hydrogen donor.

The 16-electron complexes Cp*Rh(TsNC₆H₄NH) (**1a**) and Cp*Rh(TsNC₆H₄NH) (**1b**) were prepared by treatment of [Cp*RhCl₂]₂ with TsNHC₆H₄NH₂ (for **1a**) or TsNHC₆H₄NHTs (for **1b**) and triethylamine in CH₂Cl₂ at room temperature. These violet-blue air-stable products were recrystallised from CH₂Cl₂–hexane for **1a** and from CH₂Cl₂–MeOH for **1b** (Scheme 2). Cp*Rh(HNC₆H₄NH) (**1c**) was prepared by Maitlis' method⁴ and recrystallised from toluene–pentane. These complexes were characterised by ¹H, ¹³C and ¹⁰³Rh NMR, ESI-MS, IR, UV-visible spectroscopy, elemental analysis and X-ray crystallography (see ESI†).

The ¹H NMR spectra of **1a** and **1c** (CD₂Cl₂) show broad singlets at δ 8.25 and 8.26, respectively, for the NH proton, consistent with literature values.^{5,11,12} A 1D NOESY experiment showed interaction between the Cp* methyl and the NH protons, confirming their proximity. ¹H–¹⁰³Rh HSQC experiments on **1a** and **1b** (CDCl₃) revealed cross peaks between the Cp* methyl protons and rhodium centres at δ 2063 and 1743, respectively.

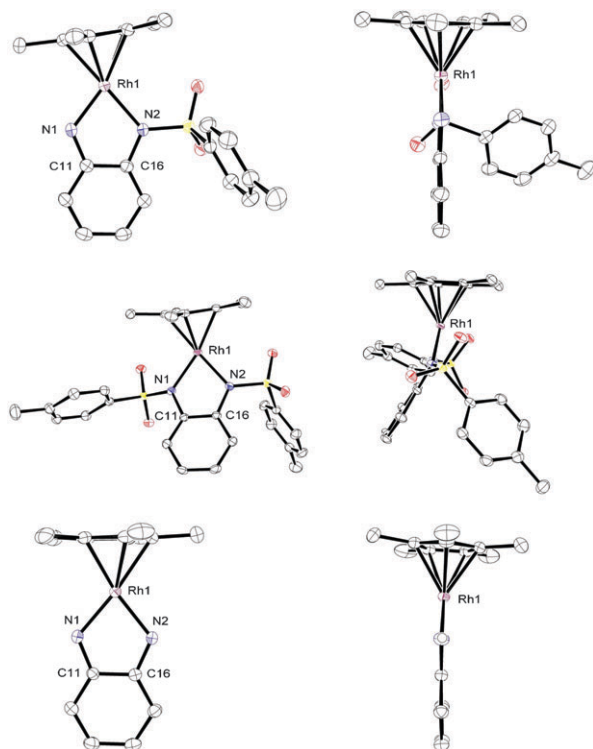


Fig. 1 Two mutually perpendicular views of molecular structures of $\text{Cp}^*\text{Rh}(\text{TsNC}_6\text{H}_4\text{NH})$, **1a** (top), $\text{Cp}^*\text{Rh}(\text{TsNC}_6\text{H}_4\text{NTs})$, **1b** (middle) and $\text{Cp}^*\text{Rh}(\text{HNC}_6\text{H}_4\text{NH})$, **1c** (bottom); hydrogens are omitted for clarity.

The ^{103}Rh chemical shifts of 16-electron **1a** and **1b** are more deshielded than that of the 18-electron chloride $\text{Cp}^*\text{RhCl}(\text{TsNCHPhCHPhNH}_2)$ ($\delta_{\text{Rh}} = 2551$).¹³ **1a** and **1b** display strong violet-blue colours arising from $\pi(\text{N}) \rightarrow \text{d}$ ligand-to-metal charge transfer bands in the visible spectrum (CH_2Cl_2 , $\lambda_{\text{max}}/\text{nm}$, ($\epsilon/\text{mol}^{-1} \text{ dm}^3 \text{ cm}^{-1}$) **1a** 578 (7300); **1b** 554 (7400); **1c** 525 (19900)). There were no major changes in λ_{max} in CH_2Cl_2 , MeOH or THF thereby confirming a lack of solvent coordination. However, λ_{max} of **1a** is shifted to slightly higher energy in MeCN.⁴

Complexes **1a**, **1b** and **1c** show marked structural differences (Table 1 and Fig. 1). The Rh–NH bond length is much shorter than the Rh–NTs bond length for **1a** (difference 0.1424(10) Å) owing to the electron withdrawing effect of the tosyl group. **1b** and **1c** show symmetric Rh–N bond distances with long distances for the former (mean 2.0419(19) Å) and short ones for the latter (mean 1.9778(18) Å). The Rh–N distances follow

Table 1 X-Ray diffraction data for **1a**, **1b**, **1c** and **2a**

Length or angle	Complex			
	1a	1b	1c ^d	2a ^d
Rh–N1/Å	1.9372(15)	2.0403(19)	1.9833(18)	2.1456(14)
Rh–N2/Å	2.0796(14)	2.0435(19)	1.9722(19)	2.1515(14)
$\Delta r(\text{M–N})^a/\text{Å}$	0.1424(10)	0.0032(13)	0.0111(13)	0.0059(10)
$\theta_{\text{oop}}^b/^\circ$	0.03	8.40	1.18	37.85
$\theta_{\text{tilt}}^c/^\circ$	0.82	20.98	2.19	39.10

^a $\Delta r(\text{M–N})$ is the difference between Rh–N1 and Rh–N2. ^b θ_{oop} = out-of-plane, θ_{oop} = angle between Rh–N1–N2 plane and Rh–Cp* centroid vector. ^c θ_{tilt} = angle between Rh–N1–N2 plane and plane of benzene ring. ^d Average of independent molecules in cell.

the order **1a**(Rh–NH) < **1c**(Rh–NH) (mean) < **1b**(Rh–NTs) (mean) < **1a**(Rh–NTs). Complex **1a** also shows significant differences between $r(\text{N1–C11})$ and $r(\text{N2–C16})$, but the changes in $r(\text{N1–C11})$, $r(\text{N2–C16})$ and $r(\text{C11–C16})$ with respect to those of the free ligands are insignificant (see ESI†).¹⁴ The angles θ_{oop} and θ_{tilt} (see Table 1 for definitions) provide a further test of π -bonding. While **1a** and **1c** are planar ($\theta_{\text{oop}} < 2^\circ$), **1b** has lost the planar conformation, $\theta_{\text{oop}} = 8.40^\circ$. The tilt angles θ_{tilt} follow the order **1b** (20.98°) > **1c** (2.19°) > **1a** (0.82°), the last being almost planar. These data are consistent with considerable π -bonding for **1a**(Rh–NH) and **1c** but less or none for **1b** and **1a**(Rh–NTs). The structural parameters of **1a**, **1b** and **1c** show that these are Rh(III) complexes, as shown for $[\text{Cp}^*\text{Rh}(\text{C}_6\text{H}_4\text{O}_2)]$.⁴

DFT(B3PW91) calculations give optimised structures for **1a**, **1b** and **1c** close to the X-ray structures; enhanced Rh–N π -bonding with NH in **1a** is evident from the calculated bond lengths and Wiberg indices. NBO analysis identifies 2p lone pairs on each nitrogen which mix with Rh(d_{xy}) and the C_6H_4 carbon to different extents for NH and NTs. Strikingly, the contributions of the Rh orbital to the composition of the nitrogen natural localised molecular orbital (NLMO) follow the pattern expected from the observed bond lengths: **1a** (NH) > **1c** > **1b** > **1a** (NTs). The delocalisation onto carbon is also greater for NH groups but follows the pattern: **1c** > **1a** (NH) > **1a** (NTs) > **1b** (for details see ESI†).

After establishing the structural characteristics of **1a–1c**, and the similarity of **1a** to the 16-electron intermediate proposed in Noyori's ATH mechanism,⁸ we examined their behaviour as transfer hydrogenation catalysts. We investigated the hydrogenation of a cyclic imine by *in situ* NMR spectroscopy in methanol- d_4 with TEAF (TEAF = $\text{NEt}_3\text{–HCO}_2\text{H}$, 2 : 5) as the hydrogen donor and [catalyst]/[substrate] ratios of 0.4, 0.7, 1.0, 1.5 and 2.0 mol% (Fig. 2).

On addition of TEAF, the solution turned from violet-blue to yellow-orange. With 1 mol% catalyst, 50% of imine was converted to amine within 40 min. The reaction proved to be first order with respect to [catalyst] but zero order with respect to [imine] up to 40% conversion (Fig. 2). The turnover frequency (TOF) of **1a** at 300 K was $94 \pm 5 \text{ mol h}^{-1} (\text{mol cat})^{-1}$; this value is about eight times less than that of $[\text{Cp}^*\text{RhCl}_2]_2\text{–}(\text{TsNHCHPhCHPhNH}_2)$ under the same conditions ($737 \pm 35 \text{ mol h}^{-1} (\text{mol cat})^{-1}$).¹⁰ The catalytic activities of **1a**, **1b**, and **1c** were compared in CD_2Cl_2 (**1b** is insoluble in CD_3OD) with 1 mol% catalyst and were found to be **1a** > **1b** ~ **1c**. The rate for **1a** in CD_2Cl_2 (50% conversion within 20 min) was greater than in CD_3OD . During consumption of the imine, catalytic decomposition of formic acid to CO_2 and H_2 is observed; **1a** recovers on completion.

The direct synthesis of 16-electron complex, **1a**, and its slower activity in transfer hydrogenation allowed us to investigate specific steps relevant to catalysis (Scheme 2). On following the reaction of complex **1a** in CD_2Cl_2 with HCl (1 mol eq. in ether) at 193 K by ^1H and ^{13}C NMR spectroscopy, we observed quantitative formation of the 18-electron chloride, $\text{Cp}^*\text{RhCl}(\text{TsNC}_6\text{H}_4\text{NH}_2)$, **2a** (δ 4.39 and 5.27 br s NH, 1.68 C_5Me_5). X-Ray quality crystals of **2a** were grown by layering with Et_2O (see ESI†). The Rh–N bond distances for **2a** are longer than in **1a** and the difference

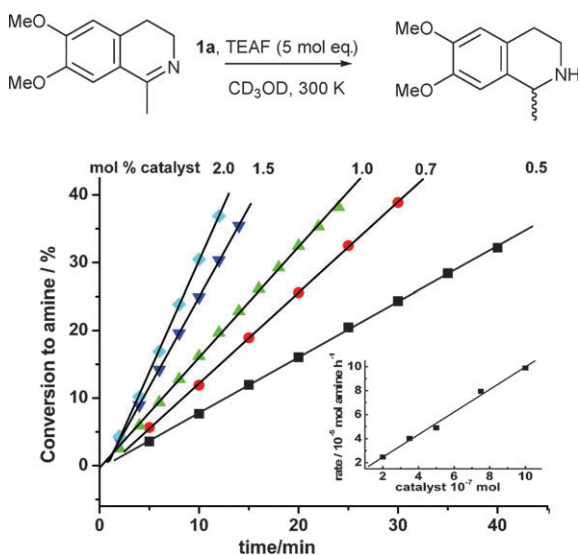


Fig. 2 Conversion of imine to amine (%) against time for various [1a]/substrate ratios. Inset: rate of conversion of imine to amine against [1a] in CD₃OD at 300 K. TOF = 94 ± 5 mol h⁻¹ (mol cat)⁻¹.

between $r(\text{Rh-N1})$ and $r(\text{Rh-N2})$ (0.0059(10) Å) is insignificant (Table 1). Moreover, θ_{oop} and θ_{tilt} deviate significantly from planarity ($\theta_{\text{oop}} = 37.85^\circ$, $\theta_{\text{tilt}} = 39.10^\circ$), consistent with the loss of Rh–N π -bonding. There is evidence for an intramolecular NH...Cl hydrogen bond (average 2.63(3) Å) by comparison with related complexes.¹⁵

When complex **1a** was reacted with formic acid (1 mol eq.) either in CD₂Cl₂ or in CD₃OD at 193 K, an 18-electron formate complex, Cp* $\text{Rh}(\text{OCHO})(\text{TsNC}_6\text{H}_4\text{NH}_2)$, **3a** was formed quantitatively. Its ¹H and ¹³C NMR spectra were fully consistent with those of ruthenium formate and acetate analogues.¹⁶ The ¹H NMR spectrum of **3a** shows inequivalent mutually coupled NH₂ protons (CD₂Cl₂, δ 4.92 and 8.35, ² $J_{\text{HH}} = 9$ Hz). The deshielded hydrogen is presumed to interact with the formate oxygen forming a 6-membered ring. The formate hydrogen is a singlet (δ 8.70), consistent with a Rh–O bond. Upon warming to 300 K, **3a** converted to **1a**, H₂ and CO₂. Both H_{2(g)} and HD_(g) were detected by NMR spectroscopy in CD₃OD. Complex **3a** was also observed in the presence of TEAF at 193 K and again regenerated **1a** and H₂ on warming.

When complex **3a** was warmed to 273 to 283 K in CD₂Cl₂, a doublet at $\delta -8.81$ ($J_{\text{RhH}} 22$ Hz) was detected. An analogous experiment conducted in THF-*d*₈ for increased solubility at 233 K enabled us to assign this species *via* 2D experiments as Cp* $\text{Rh}(\text{H})(\text{TsNC}_6\text{H}_4\text{NH}_2)$ **4a**. A ¹H–¹⁰³Rh correlation established molecular connectivity of the hydride at $\delta -9.51$ (1H) to NH₂ (δ 5.46 and 6.05, each 1H) and Cp* (δ 1.96, 15H) resonances. The remaining ¹H resonances of **4a** were also detected (see ESI†).

In conclusion, we have shown the importance of Rh–NH π -bonding in the 16-electron rhodium(III) complexes Cp* $\text{Rh}(\text{XNC}_6\text{H}_4\text{NX}')$ (X, X' = H or Ts). The considerably weaker Rh–NTs π -bond leads to a marked asymmetry between the two Rh–N amide bonds in **1a**. In the 18-electron complex, **2a**, all Rh–N π -bonding is lost. The effect of π -bonding on θ_{oop} and θ_{tilt} is consistent with MO arguments for Ru analogues.^{1,17} Our studies highlight the delocalisation

in the bis(amido) complexes and the large electron withdrawing effect of the tosyl group on the M–N interaction. These complexes allow catalytic studies without the need for 18-electron precursors. As expected considering established catalysts,³ the most active catalyst is the unsymmetrical **1a**.^{8,9} Since the colour of **1a** is lost during catalysis but reappears on completion (in CD₃OD), we infer that **1a** is not the resting state. Complex **2a** is unstable with respect to **1a** in contrast with the stabilities of their analogues that contain CHPhCHPh in place of the C₆H₄ ring. Furthermore, the formation of the formate complex **3a** in the presence of TEAF at low temperature suggests that it has a catalytic role, in contrast to the mechanism of Scheme 1. Indeed, formation of the hydride **4a** *via* **3a** may be rate determining.

We are grateful for financial support from EPSRC and Piramal Healthcare. A.N. thanks the Spanish MICINN for a MEC postdoctoral fellowship. We thank S. Matthews, C. Headley, R. Thatcher and P. Thompson for assistance.

Notes and references

- M. Jiménez-Tenorio, M. C. Puerta and P. Valerga, *Eur. J. Inorg. Chem.*, 2004, 17.
- K. Abdur-Rashid, S. E. Clapham, A. Hadzovic, J. N. Harvey, A. J. Lough and R. H. Morris, *J. Am. Chem. Soc.*, 2002, **124**, 15104.
- T. Ikariya and A. J. Blacker, *Acc. Chem. Res.*, 2007, **40**, 1300.
- P. Espinet, P. M. Bailey and P. M. Maitlis, *J. Chem. Soc., Dalton Trans.*, 1979, 1542.
- C. Paek, J. J. Ko and J. K. Uhm, *Bull. Korean Chem. Soc.*, 1994, **15**, 980.
- A. W. Holland, D. S. Glueck and R. G. Bergman, *Organometallics*, 2001, **20**, 2250.
- (a) Z. M. Heiden and T. B. Rauchfuss, *J. Am. Chem. Soc.*, 2006, **128**, 13048; (b) Z. M. Heiden and T. B. Rauchfuss, *J. Am. Chem. Soc.*, 2007, **129**, 14303; (c) Z. M. Heiden and T. B. Rauchfuss, *J. Am. Chem. Soc.*, 2009, **131**, 3593; (d) Z. M. Heiden, B. J. Gorecki and T. B. Rauchfuss, *Organometallics*, 2008, **27**, 1542.
- K. J. Haack, S. Hashiguchi, A. Fujii, T. Ikariya and R. Noyori, *Angew. Chem., Int. Ed. Engl.*, 1997, **36**, 285.
- (a) J. S. M. Samec, J.-E. Bäckvall, P. G. Andersson and P. Brandt, *Chem. Soc. Rev.*, 2006, **35**, 237; (b) J. S. M. Samec, A. H. Ell, J. B. Aberg, T. Privalov, L. Eriksson and J.-E. Bäckvall, *J. Am. Chem. Soc.*, 2006, **128**, 14293; (c) C. P. Casey and J. B. Johnson, *J. Am. Chem. Soc.*, 2005, **127**, 1883; (d) C. P. Casey, S. E. Beetner and J. B. Johnson, *J. Am. Chem. Soc.*, 2008, **130**, 2285; (e) S. E. Clapham, A. Hadzovic and R. H. Morris, *Coord. Chem. Rev.*, 2004, **248**, 2201.
- K. Mashima, T. Abe and K. Tani, *Chem. Lett.*, 1998, 1201.
- (a) R. I. Michelman, R. G. Bergman and R. A. Andersen, *Organometallics*, 1993, **12**, 2741; (b) R. I. Michelman, G. E. Ball, R. G. Bergman and R. A. Andersen, *Organometallics*, 1994, **13**, 869.
- G. S. Hall and R. H. Soderberg, *Inorg. Chem.*, 1968, **7**, 2300.
- J. Grace, PhD thesis, The University of York, 2007.
- (a) C. Stalhandske, *Cryst. Struct. Commun.*, 1981, **10**, 1081; (b) C. Squires, C. W. Baxter, J. Campbell, L. F. Lindoy, H. McNab, A. Parkin, S. Parsons, P. A. Tasker, G. Wei and D. J. White, *Dalton Trans.*, 2006, 2026; (c) T. Kato, H. Masu, H. Takayanagi, E. Kaji, K. Katagiri, M. Tominaga and I. Azumaya, *Tetrahedron*, 2006, **62**, 8458.
- A. J. Blacker, S. B. Duckett, J. Grace, R. N. Perutz and A. C. Whitwood, *Organometallics*, 2009, **28**, 1435.
- T. Koike and T. Ikariya, *Adv. Synth. Catal.*, 2004, **346**, 37.
- T. J. Johnson, K. Folting, W. E. Streib, J. D. Martin, J. C. Huffman, S. A. Jackson, O. Eisenstein and K. G. Caulton, *Inorg. Chem.*, 1995, **34**, 488.